Monte Carlo-based multi-physics analysis for transients in Light Water Reactors

Zur Erlangung des akademischen Grades eines

Doktors der Ingenieurwissenschaften (Dr.-Ing.)

von der KIT-Fakultät für Maschinenbau
des Karlsruher Instituts für Technologie (KIT)

genehmigte
Dissertation
von

M.Eng. / Dipl. Nuclear Eng. **Diego Ernesto Ferraro**
geboren in Buenos Aires, Argentina

Hauptreferent:	Prof. Dr.-Ing. Robert Stieglitz Karlsruhe Institute for Technology (KIT)
Korreferent:	Prof. Dr.-Sc.(Tech.) Jaakko Leppänen Aalto University / VTT Technical Research Centre of Finland
Tag der mündlichen Prüfung:	15.04.2021

A Eva

Acknowledgments

First of all, I would like to express my gratitude to the group of experts that agreed to supervise, coordinate, review and examine this dissertation. It was an honour for me to develop this work during the last years within the RPD - *Reactor Physics and Dynamics* group, part of the INR - *Institute of Neutron Physics* of KIT, and I would like to thank all the members for this opportunity given to me. I would like to specially thank Prof. Dr.-Ing. Robert Stieglitz and Prof. Dr. Jaakko Leppännen for their direction within this work, expressing also my gratitude to Dr. Uwe Imke for his technical guidance during this period.

My deepest gratitude for the VTT Serpent developer team, Dr. Ville Vartavirta and Dr. Riku Touminen, whose support was key to the success of this proposal. I would also like to give an special thank to Dipl-Nuc. Eng. Manu García for his insights during this process and to our CEA colleagues, specially to Margaux Faucher for the interesting discussions and analyses.

I do not want to forget to express my acknowledgments for all the RPD group, and specially for the INR secretaries Frau Petra Klug and Birgit Zagolla, for their unvaluable help during these years.

Last but not least, I would like to thank to Eva, to my friends and to my family for their support. My profound gratitude to my country and particulary to the Balseiro Institute for my education, but also to all those who played a decisive role in my career, specially to Dr. E. Villarino, Dr. J.I. Marquez-Damián, Eng. J.M. Tuñon, Eng. F. Albornoz and to Eng. A. Doval, among many others.

Karlsruhe, December 2020

Abstract

The nuclear reactor technology constitutes a mature field with several decades of evolution and key players distributed all around the world. An in-depth knowledge of this global technology is available worldwide, including well established safety principles and practices to be fulfilled in terms of its use. In this framework, the continuous improvement in nuclear industry safety standards and reactor designers' and operators' commercial goals provides a driving force for the worldwide development of highly accurate methodologies in reactor physics. These novel tools usually propose a highly detailed coupling scheme, together with a lower number of approximations within the physics modeling approach.

This is the driver for the scientific and technological question to be treated within this work, which is devoted to the investigation of advanced methodologies to develop coupled neutronic-thermal-hydraulic calculations within LWR. Here, a versatile coupled tool between Serpent Monte Carlo particle transport and SUBCHANFLOW (SCF) subchannel thermalhydraulics codes is developed, focused to tackle *transient* problems, but also suitable for *steady-state* and *burnup* calculations.

A testing, verification and validation process is developed for diverse real LWR geometries and operational conditions for *steady-state*, *burnup* and *transient* calculations, considering realistic numerical benchmarks likewise experimental data. The accuracy of the approach is assessed, showing also a consistent behavior of all involved physical phenomena at pin-wise level.

A focus is made on the study of the associated capabilities of the tool, showing its feasibility to further industry-like applications, such as safety-related analysis for *Reactivity Insertion Accidents*. Moreover, potential constrains and inherent limitations are also analyzed and diverse paths are proposed, proving that an MC-based approach represents compelling alternative path for the direct *pin-by-pin full-core* LWR calculations.

Kurzfassung

Die Kernreaktortechnologie ist ein ausgereiftes Feld mit mehreren Jahrzehnten Evolution und wichtigen Akteuren, die auf der ganzen Welt verteilt sind. Ein umfassendes Wissen über diese globale Technologie ist weltweit verfügbar, einschließlich gut etablierter Sicherheitsprinzipien und -praktiken, die hinsichtlich ihrer Verwendung vollständig ausgefüllt werden müssen. In diesem Rahmen ist die kontinuierliche Verbesserung der Sicherheitsstandards der Nuklearindustrie sowie der kommerziellen Ziele von Reaktordesignern und -betreibern eine treibende Kraft für die weltweite Entwicklung hochpräziser Methoden in der Reaktorphysik. Diese neuartigen Werkzeuge schlagen normalerweise ein sehr detailliertes Kopplungsschema zusammen mit einer geringeren Anzahl von Approximationen innerhalb des physikalischen Modellierungsansatzes vor.

Dies ist der Treiber für die wissenschaftliche und technologische Frage, die in dieser Arbeit behandelt werden soll, die sich mit der Untersuchung fortschrittlicher Methoden zur Entwicklung gekoppelter neutronisch-thermisch-hydraulischer Berechnungen innerhalb des LWR befasst. Hier, wird ein vielseitiges gekoppeltes Werkzeug zwischen Serpent Monte Carlo-Partikeltransport und SUBCHANFLOW (SCF) -Unterkanal-Thermohydraulikcodes entwickelt, das sich auf *transient*-Probleme konzentriert, aber auch für *stationäre* und *burnup* Berechnungen.

Es wird ein Test, Verifizierungs- und Validierungs-prozess bereitgestellt für verschiedene reale LWR-Geometrien und Betriebsbedingungen für *stationäre*, *burnup* und *transient* Berechnungen durchgeführt, der realistischer numerischer Benchmarks sowie experimenteller Daten berücksichtigt. Die Genauigkeit des Ansatzes wird bewertet, wobei auch ein konsistentes Verhalten aller beteiligten physikalischen Phänomene auf pin-wise-Ebene gezeigt wird.

Der Schwerpunkt liegt auf der Untersuchung der damit verbundenen Funktionen des Tools, wobei seine Durchführbarkeit für weitere industrieähnliche Anwendungen aufgezeigt wird, wie z.B. die sicherheitsrelevante Analyse für *Reactivity Insertion Accidents*. Darüber hinaus werden potenzielle Einschränkungen und inhärente Begrenzungen analysiert und verschiedene Pfade vorgeschlagen, was beweist, dass ein MC-basierter Ansatz einen überzeugenden alternativen Pfad für die direkten *pin-by-pin full-core LWR*-Berechnungen darstellt.

Declaration of Academic Integrity

I hereby declare that the work in hand is from me independently and I have used nothing other than the given sources and aids and have marked passages included from other works, whether verbatim or in content, as such and that the work in hand complies with the recent relevant version of the statutes of the Karlsruhe Institute of Technology (KIT) in assurance of good scientific practice.

Karlsruhe, December 2020 *Diego Ferraro*

Contents

Acronyms

AL	Active Length
BOC	Beginning of Cycle
BOI	Beginning of interval
BP	Burnable Poison
C_b	Boron concentration
cdf	Cummulative probability density function
CFA	Control Fuel Assembly (SPERT-IIIE)
CHF	Critical Heat Flux
CR	Control Rod
CRW	Control Rod Worth
CZP	Cold Zero Power
DNBR	Departure of Nucleate Boiling Ratio
EOC	End of Cycle
EOI	End of interval
FA	Fuel Assembly
FOM	Figure of merit
FPD	Full Power Days
FR	Fuel Rod
HZP	Hot Zero Power
HFP	Hot Full Power
HRM	Heterogeneous Response Method
IFC	Serpent Multiphysics Interface Files
IFP	Iterated Fission Probability method
INR	Institute of Neutronics and Reactor Physiscs - KIT
KIT	Karlsruhe Institute for Technology
LWR	Light Water Reactor
MC	Monte Carlo
NDL	Nuclear Data Library
NPP	Nuclear Power Plant
pdf	probability density function
PK	Point Kinetics
PWR	Pressurised Water Reactor - Used for western design (i.e. square lattice) reactor type
RIA	Reactivity Initiated Accident
SCF	SUBCHANFLOW Code
SFA	Standard Fuel Assembly (SPERT-IIIE)
SS	Stainless Steel
TR	Transient Rod (SPERT-IIIE)
TH	Thermal-hydraulics
VVER	*vodo-vodyanoi energetichesky reaktor (in russian)*, water-water power reactor - Pressurised water reactor of eastern design (i.e. hexagonal lattice)
16FA	Central Fuel Assebly with 16 pins (SPERT-IIIE)

List of publications associated to this work

As first author in peer review magazine papers

- Ferraro, D., García, M., Valtavirta, V., Imke, U., Tuominen, R., Leppänen, J., and Sanchez-Espinoza, V. 2020c. *Serpent/SUBCHANFLOW pin-by-pin coupled transient calculations for a PWR minicore. Annals of Nuclear Energy*, 137:107090

- Ferraro, D., García, M., Valtavirta, V., Imke, U., Tuominen, R., Leppänen, J., and Sanchez-Espinoza, V. 2020d. *Serpent/SUBCHANFLOW pin-by-pin coupled transient calculations for the SPERT-IIIE hot full power tests. Annals of Nuclear Energy*, 142:107387

- Ferraro, D., García, M., Imke, U., Valtavirta, V., Leppänen, J., and Sanchez-Espinoza, V. 2019b. *Serpent/SCF pin-level multiphysics solutions for the VERA Fuel Assembly benchmark. Annals of Nuclear Energy*, 128:102–114

- Ferraro, D., Valtavirta, V., García, M., Imke, U., Tuominen, R., Leppänen, J., and Sanchez-Espinoza, V. 2020e. *OECD/NRC PWR MOX/UO_2 core transient benchmark pin-by-pin solutions using Serpent/SUBCHANFLOW. Annals of Nuclear Energy*, 147:107745

As first author in peer review conference papers

- Ferraro, D., Faucher, M., Mancusi, D., Zoia, A., Valtavirta, V., Leppänen, J., and Sanchez-Espinoza, V. 2019a. *Serpent and TRIPOLI-4® transient calculations comparisons for several reactivity insertion scenarios in a 3D PWR minicore benchmark.* In *International Conference on Mathematics and Computational Methods applied to Nuclear Science and Engineering (M and C 2019)*, Portland, Oregon, USA. ISBN: 978-0-89448-769-9 / Vol. 3 / Pages 1734-1743

- Ferraro, D., Garcia, M., Mercatali, L., Sanchez-Espinoza, V. H., Leppänen, J., and Valtavirta, V. 2018. *Foreseen capabilities, bottlenecks identification and potential limitations of serpent MC transport code in large-scale full 3-D burnup calculations.* In *26th International Conference on Nuclear Engineering*, London, UK. American Society of Mechanical Engineers ASME. ISBN: 978-0-7918-5145-6 / Vol. 3 / Paper ID: V003T02A049

- Ferraro, D., García, M., Imke, U., Valtavirta, V., Tuominen, R., Bilodid, Y., Leppänen, J., and Sanchez-Espinoza, V. 2020a. *Serpent / SUBCHANFLOW coupled calculations for a VVER core at hot full power.* In *International Conference on Physics of Reactors 2020*, Cambridge, UK. ISBN: 978-1-5272-6447-2 / Paper ID: 1190

- Ferraro, D., García, M., Imke, U., Valtavirta, V., Tuominen, R., Leppänen, J., and Sanchez-Espinoza, V. 2020b. *Serpent / SUBCHANFLOW coupled burnup calculations for VVER fuel assemblies.* In *International Conference on Physics of Reactors 2020*, Cambridge, UK. ISBN: 978-1-5272-6447-2 / Paper ID: 1189

"I hope it won't take long."

—Enrico Fermi

1 Introduction

1.1 Motivation

The nuclear reactor technology counts today with more than eight decades of evolution with key players distributed all around the world. An in-depth knowledge of this technology is worldwide available, including well established safety principles and practices that condense years of operational and design experience (IAEA, 2006, 2009). A vast universe of applications are nowadays available, ranging from the basic research in fields as diverse as material sciences or technological research and development of new pharmaceutical drugs (IAEA, 2014), to the market regular production of highly demanded goods such as medical radioisotopes for treatment and diagnosis, bulk doped semiconductor production, massive scale electrical power generation and large city heating provision (IAEA, 2017).

This technology represents thus a mature field of study with established dominant designs and calculation schemes that reflect the evolution of the understanding of the physical principles, where the use of conservative and extensively validated approaches is the common rule (IAEA, 2006, 2014). Nevertheless, the continuous push for the improvement within the industry safety standards, combined with the demanding requests raising from reactor designers' and operators' commercial goals provides a driving force for the development of new methodologies, mainly oriented to offer to the stakeholders novel tools aimed to improve the level of confidence and thus diminish the conservativeness.

In this sense, a global trend to develop highly accurate methodologies in reactor physics is observed worldwide in the last years, mostly oriented to the development of a wide range of coupled state-of-the-art multi-physics tools. These new tools propose the application of highly detailed coupling schemes, using as basis novel codes that rely on a lower number of approximations in the physics modeling than the traditional conservative approaches applied in the industry. These tools allow to obtain relevant reactors' core parameters relying on new and independent approaches to the problem. An inherent benefit is the capability to tackle issues such as the increasing complexity (and heterogeneity) of modern reactor cores and the direct calculation of safety-related parameters.

This path is reflected into the innovation and research agendas worldwide, for example within European Union through its projects NURESIM (2005-2008), NURISP (2009-2012), NURESAFE (2013-2015), HPMC (2011-2014) and McSAFE (2017-2020, (Sanchez-Espinoza et al., 2020)), in USA in projects as MOOSE (Idaho National Lab, (Gaston et al., 2009)) and CASL (consortium established by the Department of Energy, (CASL, 2020)) and in China with its advanced tools developments, such as RMC package (Wang et al., 2015). A common factor of these

efforts is that they heavily rely on the availability of extensive computational resources, such as High Performance Computing (HPC) architectures, which allow to develop very demanding calculations unthinkable in former times.

Several previous efforts were held during past years within KIT in this direction, devoted both to improve the neutron physics description and the detail level of the associated TH problem. The central idea is to allow a direct pin-by-pin modeling of the reactor core physics, where suitable codes have to be considered. Unfortunately, the application of such detailed approach using industry-standard codes is not always beneficial, specially when *transient* calculations are to be analyzed (Daeubler et al., 2015b; Lee et al., 2015).

In particular, the use of Monte Carlo (MC) particle transport codes to tackle the neutronics of the combined problem is getting more impulse due to its inherent capabilities, together with its suitability for its implementation within HPC. Previous efforts have been developed within KIT in past years, providing a proof of concept for *steady-state* calculations in Light Water Reactor (LWR) square geometries (Daeubler et al., 2015a; Ivanov, 2015) through the combination of diverse MC based tools. Besides, the recent availability of functional multi-physics features and transient capabilities within reactor-oriented state-of-the-art neutronic codes (Valtavirta, 2017; Sjenitzer, 2013) unlocks a new span of interesting developments based in these MC codes.

Amid all potential applications of such methodologies, the study of coupled *transient* scenarios within LWR designs represents a compelling field of study, as far as it can provide novel calculation schemes for safety-oriented key parameters that define the operational and design limits. On top of that, the fact that most of the traditional approximations and considerations held within the standard methodologies are avoided within this MC-based tools, fully-independent and pin-wise-detailed results can be obtained for these complex scenarios.

1.2 The scientific question and its associated objectives within this work

The aptness of the use of advanced methodologies to tackle coupled *transient* problems within LWR designs represents the scientific and technological question, in particular the analysis of a MC-based neutronics plus subchannel thermal-hydraulics (TH) approach for full-core level analysis.

To provide an answer to this scientific question, a series of objectives are set. A preliminary analysis of the proposed approach is firstly required, to then develop a versatile implementation of the selected tools, which must be tested, verificated and validated to assess its suitability to accurately depict LWR phenomena. This tool must be capable to handle coupled *transient* problems likewise *steady-state* and *burnup* ones, since all *transients* start from a *steady-state* problem and several relevant LWR analysis require the consideration of burned cores. Finally, the capability of this tool to provide safety-related parameters at full-core level within realistic configurations must be also assessed.

1.3 Overview of the light water reactor designs

This study is limited to Light Water Reactors (LWR), an engineered device in which a controlled nuclear fission chain reaction can be maintained, constituting a machine capable to be turned on, operated, turned off by demand and maintained off, where all these tasks shall be done in a safe and efficient manner for justified purposes. These LWR are *thermal reactors* from the neutronics point of view, since the neutron induced fission chain reactions are maintained with neutrons having an energy spectra similar to the one that arises from vibration of the atoms composing the reactor core, where low atomic number materials are used to *moderate* the energy of the neutrons released by nuclear fission (Duderstadt and Hamilton, 1976).

The focus is put on PWR (pressurized water reactor) types, both the standard desing for western countries (named directly as PWR for simplicity) and its eastern equivalent VVER (water-water power reactor), which are historically dominant designs. For both types the fuel is arranged in form of lattices of fuel rods (FR), where pellets are encapsulated in a metallic clad of materials as *Zircalloy*. These FR are also termed as pins in reactor calculation (used indistinctively in this dissertation). They are grouped into fuel assemblies (FA) in a regular lattice, as shown in the Fig. 1.1a for a PWR (i.e. square array) and in the Fig. 1.1b for a VVER (i.e. hexagonal array) design.

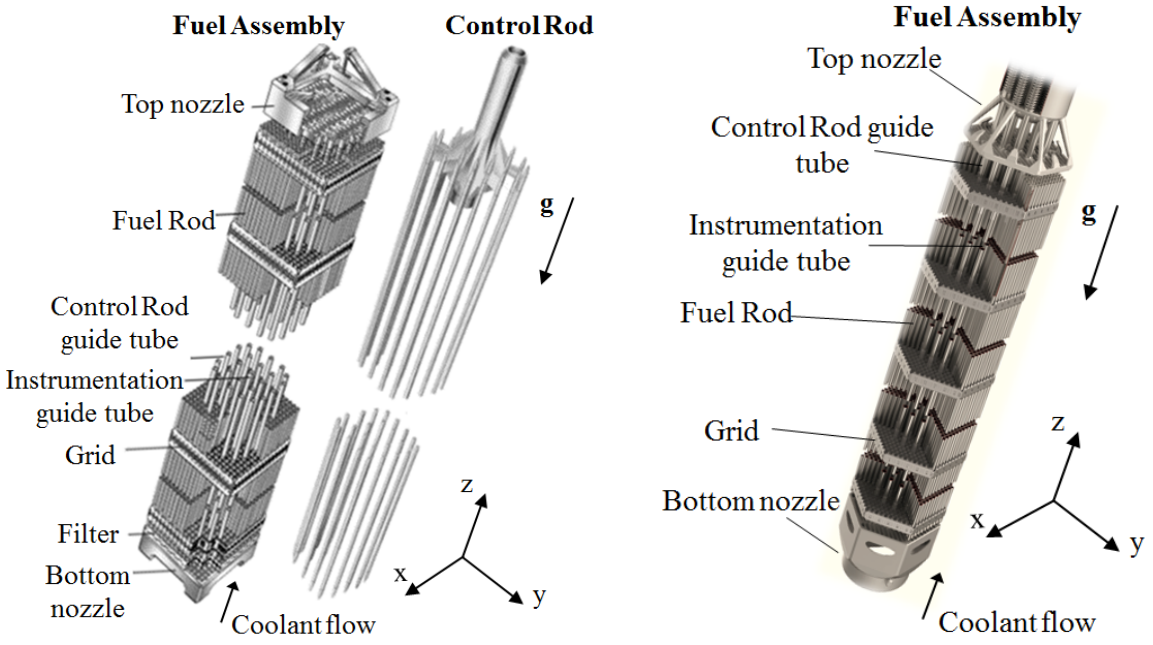

(a) PWR FA. *(b) VVER FA.*

Figure 1.1: Sketch of most common FA designs and its components for LWR.

The fuel pellets are commonly composed of UO_2 enriched in ^{235}U, where sometimes mixed oxides are considered (i.e. including ^{239}Pu). Besides, most of modern FA designs include FR with high neutron absorbent materials (such as *Gd* or *Er*), deemed to depress the neutron flux in specific zones, termed as *Burnable Poisons - BP*. Finally, the FA are also arranged using square (PWR) and hexagonal (VVER) arrays to compose the reactor core, which is both cooled

and moderated by light water at high pressure and temperature (i.e. ~ 560 $[K]$ and ~ 15.5 $[MPa]$). To achieve this, the core is placed inside a pressure vessel (RPV), where an schematic plot of its main components is presented in Fig. 1.2 for a PWR, including the gravity vector pointing downwards the axial dimension, convention that will be maintained in the rest of this dissertation.

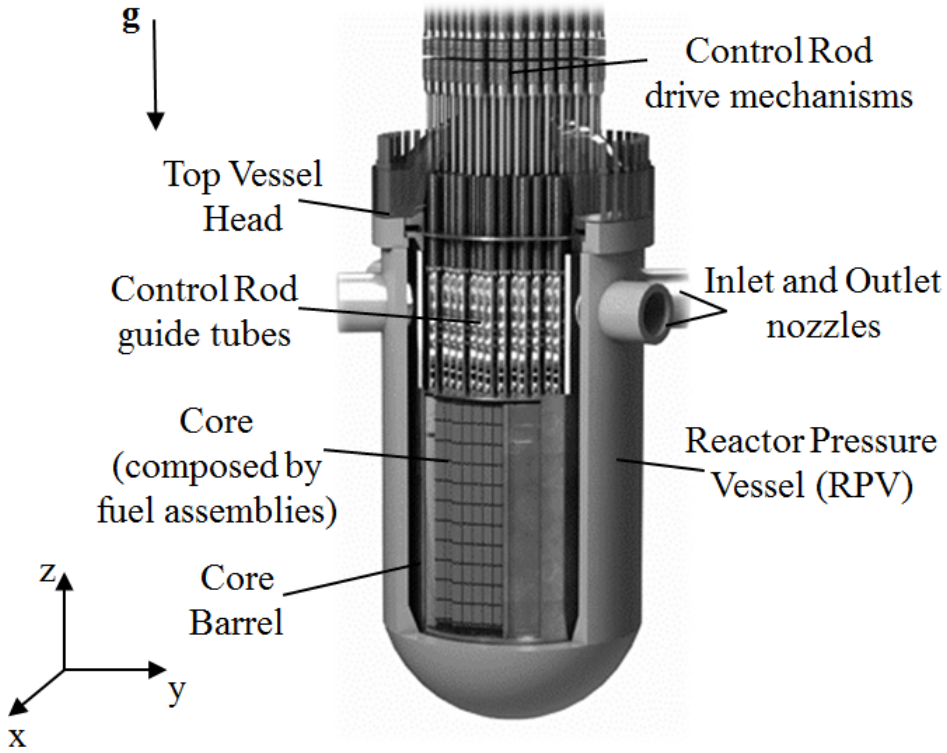

Figure 1.2: Schematic draw of main components inside a PWR reactor pressure vessel (RPV).

1.4 Structure of this dissertation

This dissertation is organized into eight Chapters. The main physical background for the phenomena occurring within the reactor core is briefly discussed in Chapter 2, followed by the description of the versatile implementation of the MC-based approach in Chapter 3. The verification and validation of the tool for *steady-state*, *burnup* and *transient* problems within realistic LWR configurations is provided in chapters 4 to 6, showing its aptness to tackle the stated scientific question. Conclusions are drawn in Chapter 7, to finalize with the proposal of future work paths in Chapter 8.

"Every body persists in its state of being at rest or of moving uniformly straight forward, except insofar as it is compelled to change its state by force impressed."

—Sir Isaac Newton

2 Fundamentals of the involved reactor physics

A brief description of the most important physical concepts commonly used to predict the behavior of neutrons in nuclear reactors is here presented, including specific aspects regarding the MC-based neutronics plus the subchannel TH scheme developed within this work.

2.1 Basics of the neutronics problem to solve

To begin with, we define most common magnitudes to be consider within the description of the neutronic problem. To characterize a neutron not only a position $\bar{r}$, but also its vector velocity $\bar{v}$ should be considered, where the direction of motion can be characterized by the unit vector $\hat{\Omega} = \frac{\bar{v}}{|\bar{v}|}$, schematically depicted in Fig. 2.1.

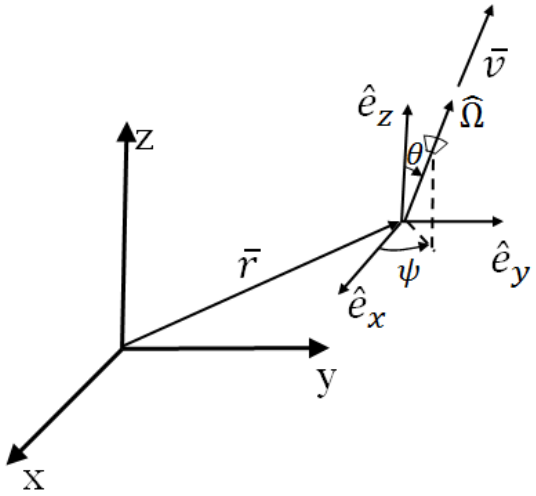

Figure 2.1: Position and direction variables to characterize the neutrons distribution.

We can then proceed to define the main magnitudes of interest from the neutronic point of view, following the convention from (Duderstadt and Hamilton, 1976):

- The angular neutron density $\bar{n}(\bar{r}, \hat{\Omega}, E, t)$, as the expected number or neutrons in a differential volume about $\bar{r}$, differential energy about E, moving in direction $\hat{\Omega}$ in a solid angle $d\hat{\Omega}$ at time t.
- The neutron speed, as $v = |\bar{v}|$.
- The neutron angular flux, as $\varphi(\bar{r}, \hat{\Omega}, E, t) = v\bar{n}(\bar{r}, \hat{\Omega}, E, t)$.
- The neutron scalar flux, as $\phi(\bar{r}, E, t) = \int_{4\pi} \varphi(\bar{r}, \hat{\Omega}, E, t) d\hat{\Omega}$, named here as neutron flux, following the standard jargon.
- The microscopic cross sections, as $\sigma_j(\bar{r}, E)$, defined in units of barns (i.e. 1e-24 cm^2), which characterize the probability of the neutron to interact with the medium. Here the

subscript j will identify different interaction channels such as fission σ_f, scattering σ_s, absorption σ_a and others or the total interactions σ_t.

- The macroscopic cross sections, as $\Sigma_j(\bar{r}, E) = N\sigma_j(\bar{r}, E)$, in units of [1/cm], where N [1/cm^3] is the number of atoms per cubic centimeters of the given interaction isotope.

The prediction of the neutronic distribution within a reactor is the basis of the core reactor physics, since it determines the capability to maintain a sustainable and controlled chain reaction and defines the power release to the system. To obtain the governing equations that describe the distribution of neutrons in the reactor, a balance of production and losses is done, where intrinsic characteristics of the neutron transport are considered. The complete derivation can be found in literature (Duderstadt and Hamilton, 1976; Bell and Glasstone, 1970), which leads to the governing equation, known as the neutron transport equation. This equation can be written in terms of the angular neutron flux $\varphi(\bar{r}, \hat{\Omega}, E, t)$ with boundary conditions for non-re-entrant surfaces as:

$$\begin{aligned} \frac{1}{v}\frac{\partial \varphi}{\partial t} + \hat{\Omega}\cdot\nabla\varphi + \Sigma_t(\bar{r}, E)\varphi(\bar{r}, E, \hat{\Omega}, t) = \int_{4\pi} d\hat{\Omega}' \int_0^\infty dE' \Sigma_s(E' \to E)\varphi(\bar{r}, \hat{\Omega}', E', t) \\ + s(\bar{r}, \hat{\Omega}, E, t); \\ \text{with an initial condition:} \quad \varphi(\bar{r}, \hat{\Omega}', E', 0) = \varphi_0(\bar{r}, \hat{\Omega}', E'); \\ \text{and a boundary condition:} \quad \varphi(r_s, \hat{\Omega}', E', t) = 0, \quad \text{if} \quad \hat{\Omega}\cdot\hat{e}_s < 0; \end{aligned} \tag{2.1}$$

where in Eq. 2.1 $\varphi(\bar{r}, \hat{\Omega}, E, t)$ represents the neutron angular flux, dependent on the position $\bar{r}$, angle $\hat{\Omega}$, energy E and time t, while $\hat{e}_s$ is the outer surface normalized vector. In addition the source term $s(\bar{r}, \hat{\Omega}, E, t)$ groups all neutrons appearing in a differential volume and solid angle at position $\hat{r}$ for a given energy. The left terms in the equation can be interpreted as change in time and losses due to leaks and collisions respectively, while right hand of it is representing the neutrons arising from scattering to the energy E and from the source term. Here the macroscopic cross sections Σ are written in terms of position and energy only, but they can also depend on time due to changes in composition or geometrical configurations.

For a nuclear reactor the source term $s(\bar{r}, \hat{\Omega}, E, t)$ can be expressed as sum of an external fixed source and a fission source, where for almost all practical core calculations only the fission source is considered. The fission process is then expressed terms of a given fission spectra $\chi(E)$, the fission cross section $\Sigma_f(E, \bar{r})$ and the number of neutrons emitted per fission $\nu(E)$ (Duderstadt and Hamilton, 1976). In addition, since the fission of a nuclei spews a variety of reaction products, including the unstable fissioned nuclei fragments and several neutrons, gammas, betas and neutrinos, special attention to the neutron generation process must be paid. In the Eq. 2.1 the emerging neutrons from fission should be discriminated, as far most of them are emitted essentially instantaneously (i.e. within 10^{-14} [s], termed as *prompt neutrons*), whereas a small fraction β of them are emitted with an appreciable delay on time, and thus are identified as *delayed neutrons* (less than 1%, e.g. 0.65 [%] for ^{235}U and 0.22 [%] for ^{239}Pu nuclei fissioned by thermal neutrons). These delayed components arise from the decay of the unstable fission fragments in times from ~ 0.2 up to ~ 55 [s] and play a major role in the involved physics. This

difference in the emission time for these *delayed* neutrons allows to control the evolution of the overall reaction in a practical engineered approach, i.e. by the aims of moving devices (such as control rod) or changes in compositions (such as Boron concentrations in the coolant).

To simplify the modeling, these *delayed* neutrons are grouped into I *decay families*, defined through a concentration of the precursors C_i and a decay constant λ_i, which leads to a new set of coupled equations to solve. If we go back to the neutron transport Eq. 2.1 and consider the fission to be an isotropic process (Lewis and Miller, 1984; Cacucci, 2010) the Eq. 2.2 is obtained:

$$\begin{aligned}
&\frac{1}{v}\frac{\partial\varphi}{\partial t}+\hat{\Omega}\cdot\nabla\varphi+\Sigma_t(\bar{r},E)\varphi(\bar{r},E,\hat{\Omega},t)=\int_{4\pi}d\hat{\Omega}'\int_0^{\infty}dE'\Sigma_s(E'\rightarrow E)\varphi(\bar{r},\hat{\Omega}',E',t)\\
&\qquad+\frac{\chi(\bar{r},E,t)}{4\pi}\int_0^{\infty}d\hat{\Omega}'dE'(1-\beta(\bar{r},E,t))\nu(E')\Sigma_f(E',r)\varphi(\bar{r},E,\Omega',t)\\
&\qquad+\frac{1}{4\pi}\sum_i^j\chi_i(E)\lambda_iC_i(\bar{r},t),\\
&\qquad\text{with initial conditions:}\quad\varphi(\bar{r},\hat{\Omega}',E',0)=\varphi_0(\bar{r},\hat{\Omega}',E');\\
&\qquad\text{and boundary conditions:}\quad\varphi(r_s,\hat{\Omega}',E',t)=0,\quad\text{if}\quad\hat{\Omega}\cdot\hat{e}_s<0;\\
&\frac{\partial C_i(\bar{r},t)}{\partial t}=\int_{4\pi}\int_0^{\infty}dE'd\hat{\Omega}\beta_i(r,E',t)\nu(E')\Sigma_f(E',\bar{r})\varphi(\bar{r},E',\hat{\omega},t)-\lambda_iC_i(\bar{r},t),\\
&\qquad\text{for:}\quad i=1,2,...,j;\\
&\qquad\text{with boundary conditions for each i:}\quad C_i(\bar{r},0)=C_{0i}(r).
\end{aligned}\tag{2.2}$$

When dealing with nuclear reactor analysis, the reaction rates (RR) are of interest. These can be defined as an integral parameter using the neutron scalar flux $\phi(\bar{r},E,t)=\int_{4\pi}\varphi(\bar{r},\hat{\Omega},E,t)d\hat{\Omega}$ as:

$$RR[1/s]=\int_V\int_E\phi(\bar{r},E)\Sigma(\bar{r},E)dEdr^3.\tag{2.3}$$

These reaction rates in Eq. 2.3 represent relevant scalar fields, such as the power density or materials activation rates when scaled with a corresponding factor (e.g. using the energy released by fission to obtain the thermal power resulting a given neutron flux level).

2.2 Aspects regarding the time dependence of the neutronic problem

From the neutronic point of view, the time dependence is tackled through the consideration of different approaches depending of the time frames where the reactor change its main characteristics. In this sense three kind of problems are solved in reactor physics core calculations, each of them identified by a specific jargon:

1. Cases where the Eq. 2.1 is solved without considering time dependence, termed as *steady-state*.
2. Cases where the Eq. 2.1 is solved without considering time dependence, but the evolution of nuclide inventory present in the reactor core is considered through the calculation of successive *steady-state* steps, identified as *burnup calculations*.

3. Cases where the Eq. 2.1 is solved considering the time dependence, including the modeling of delayed neutrons (as shown in Eq. 2.2), referred as *transient calculations* or *kinetic calculations*.

Each of these approaches has its own modeling complexity and its main aspects are here discussed in view of the work path of this dissertation. It is key to note here that *transient* calculations within a nuclear reactor require an initial *steady-state* calculation. On top of that, several safety-related parameters must consider *burned* fuel compositions within the core, since the delayed components described above show a dependence with the fissioned nuclei (Duderstadt and Hamilton, 1976).

2.2.1 Steady-state problems

The spatial dependence of the neutron distribution over a reactor core and all its safety characteristics related to its capability to be turned on, operated and turned off are obtained considering a static problem, i.e. eliminating the temporal dependence. To do this, the balance of productions and losses represented in such equation has to be arbitrary altered. There are several ways to do this (Duderstadt and Hamilton, 1976; Bell and Glasstone, 1970; Lewis and Miller, 1984), but the most common is to alter the rate of productions by a factor k, which converts our problem into a eigenvalue problem. As an example of that, if we take the Eq. 2.1 and we alter the production term dividing by k at the same time that we avoid the existence of external sources we arrive to a problem in the form:

$$\begin{aligned}\hat{\Omega}\cdot\nabla\varphi+\Sigma_t(\bar{r},E)\varphi(\hat{\Omega},\bar{r},E) = &\int_{4\pi}\int_0^\infty d\hat{\Omega}'dE'\Sigma_s(E'\to E,\hat{\Omega}'\cdot\hat{\Omega})\varphi(\hat{\Omega}',\bar{r},E')\\ &+\frac{1}{k}\chi(E)\int_0^\infty dE'\nu(E')\Sigma_f(E',r)\int_{4\pi}d\hat{\Omega}'\varphi(\hat{\Omega}',\bar{r},E);\\ &\text{with a boundary condition:}\quad \varphi(\bar{r_s})=\varphi_{rs}.\end{aligned} \tag{2.4}$$

The factor k in Eq. 2.4 is defined as multiplication factor. The capability of a reactor to maintain a stationary chain reactor in time is then referred as critical reactor (i.e. $k=1$), where higher values are indicating an excess of neutrons causing fission (i.e. $k>1$, supercritical reactor) and lower values are indicating a defect of neutrons causing fission (i.e. $k<1$, subcritical reactor). Besides, the associated magnitude named as reactivity ρ is useful to define the behavior of the reactor, as stated in Eq. 2.5.

$$\rho=\frac{(k-1)}{k}. \tag{2.5}$$

Due to its low values, ρ is commonly defined as percent-mille (pcm) likewise in *dollars* units (\$), dividing its value by the delayed fraction ($\rho[\$]=\frac{(k-1)}{k\beta}$), conventions that will be also used in this work.

It is key to note that the solution for the neutron flux distribution $\varphi(\hat{\Omega},\bar{r},E)$ for the criticality problem is not dependent on the absolute level (which means that the solution is floated in power). Obviously the existence of TH feedbacks will modify this statement within a real reactor, as seen in further sections. In addition, it can be proved that the temporal solution

of a critical reactor that suffers from a perturbation on its neutron population will decay to its fundamental mode (Duderstadt and Hamilton, 1976), ruled by the solution to this associated problem.

Finally, the total thermal power produced in the reactor arises from the summation of all energy released by fission. With disregard of the specific components of such energy release (basically the energy of a fission is mostly released as kinetic energy of fission fragments, but there is also a contribution from emerging particles (Duderstadt and Hamilton, 1976)), the thermal power represents then a normalization factor as:

$$P[W] = \int_V \int_0^{E_{max}} dE' E_{fiss}(E') \Sigma_f(E', \bar{r}) \phi(\bar{r}, E) dr^3; \tag{2.6}$$

where in Eq. 2.6 the energy release per fission is defined as $E_{fiss}(E)$.

2.2.2 Burnup problems

If a reactor is operated at a significant power or for enough time, changes in the fuel composition within the core due to the fission and absorption processes that occur (and subsequent fission product decay). As far as these changes affect the components of Eq. 2.4 they are mandatory to be considered. These changes can be interpreted as a modification of macroscopic cross sections Σ, both from the consumption of fissile nuclide concentrations (referred as *fuel burnup*) or by the appearance of new isotopes that increase or decrease the production vs. losses balance, such as ^{239}Pu or ^{135}Xe.

These changes in compositions appear in relative long time periods (i.e. hours to months), hence the traditional approach is to solve the problem as for the *steady-state* case and evolve the composition independently. This evolution is usually done through the solution of the set of time dependent equations for selected nuclides for each position in space, known as *Bateman equations* (Bateman, 1910). These equations can be written for a reactor as (Cacucci, 2010):

$$\frac{dN_i}{dt} = \underbrace{\sum_j \gamma_{ji} \sigma_{f,j} N_j \phi + \sigma_{c,i-1} N_{i-1} \phi + \sum_k \lambda_{ki} N_k}_{\text{production}} - \underbrace{\sigma_{a,i} N_i \phi}_{\text{absorption}} - \underbrace{\lambda_i N_i}_{\text{decay}}; \quad \text{for:} \quad i = 1, 2, ..., j; \tag{2.7}$$

where N_i is the number density of the isotope i to consider $[cm^{-3}]$, γ_{ji} is the yield of nuclide j from a fission of nuclide i, $\sigma_{f,j}$ represents the microscopic fission cross section of nuclide j $[cm^2]$, ϕ represents the scalar neutron flux $[cm^{-2}s^{-1}]$ in a given position, $\sigma_{c,i-1}$ is the capture cross section of nuclide $i-1$ $[cm^2]$, λ_{ki} is the decay constant of nuclide k to nuclide i $[s^{-1}]$, λ_i represents the decay constant of nuclide i $[s^{-1}]$ and $\sigma_{a,i}$ is the absorption cross section of nuclide i $[cm^2]$. It should be noted here that the energy dependence was avoided to enhance comprehension, but the terms $\phi\sigma$ are to be interpreted as energy integrals over a portion of space. To solve the Eq. 2.7 the neutron fluxes are required over the reactor zones where the

composition are known to be changing, which typically corresponds to the fuel zone. It should be regarded that this problem can be interpreted as a matrix differential equation of first order, where diverse solution schemes are applicable (Leppänen et al., 2015):

$$\frac{d\bar{N}}{dt} = A\bar{N}; \tag{2.8}$$

where vector $\bar{N}$ contains the concentrations of the isotopes and the matrix A the coefficients from the Eq. 2.7. The solution of the Eq. 2.8 is assuming that the fluxes ϕ and the cross sections σ are not changing with time. This is not the case in reality, since changing nuclide compositions affect the level of self-shielding experienced by the materials under irradiation. To tackle this issue the burnup interval is divided in a number of steps (i.e. burnup steps), where ϕ and σ are assumed to be constant (or to have a simple dependence, such as linear). This process is iterative, where the common option is to solve the *steady-state* problem and then advance in these burnup steps, constituting the so-called *Predictor-Corrector* schemes. Diverse options of successive calculation of steady-states with modified nuclide compositions are proven to be suitable to obtain an accurate description of the fuel composition evolution (Leppänen and Isotalo, 2012), where the most common is to consider a constant extrapolation in the prediction step and a linear interpolation in the corrector one.

2.2.3 Transient problems

The transient problems are analyzed for time scopes where the main compositions are considered to be constant and the effect of delayed neutrons is modeled through the condensation of the complex decay in precursor families, (see Eq. 2.2). As a result, the solution for these transient problems provides a neutron distribution evolution in time and space, which implies an increased complexity. Moreover, it should be regarded that a dynamic reactivity based on the neutron multiplication in time can be obtained for such problems as a derived parameter that also identifies the excess of neutron production to losses in the system, but does not mathematically equals the definition from Eq. 2.4 (Cullen et al., 2003).

2.3 Industry standard approach to solve the neutronics

Unfortunately, the Eq. 2.1 has almost no solution for practical geometries due to its mathematical complexity, since this differential equation depends on energy, time, position and angular direction, totaling eight variables. As a result, the standard approach is to develop a series of approximations to obtain a sufficiently accurate representation of the problem dealing with a reduced number of variables (Duderstadt and Hamilton, 1976; Bell and Glasstone, 1970). These simplifications and approximations can be done either in time, spatial, angular or energy dependencies, where a combination of all of them is often developed, defining the *deterministic* calculation methods.

The traditional industry-approach proposes to divide this problem in two steps (namely cell-core approach (Duderstadt and Hamilton, 1976)), where the first tackle the main aspects that

govern the involved neutron physics, while the second one models the whole core level problem using parameters obtained from the first one.

In the former step a simplification in the angular dependence is usually held, together with a discretization in energy (the so-called *energy groups*). Several techniques are available for this purpose, such as *Discrete Ordinates - S_n*, *Spherical Harmonics - P_n*, *Collision Probabilities - CP* or *Heterogeneous Response Methods - HRM* (Duderstadt and Hamilton, 1976; Bell and Glasstone, 1970). This step provides an accurate modeling of the physics involved, using reflected 2D detailed models at pin or fuel assembly levels that represent relevant portions of the problem. Key features governing the problem such as neutron spectra, power distribution and inventory burnup (among others) are then represented in detail. Here the energy discretization commonly considers several tens to few hundreds of *energy groups*, where cross section data for the involved isotopes (i.e. the *Nuclear Data Library - NDL*) is specifically developed in a previous step and only accurate for a given span of problems. Finally, the outcome is a set of condensed parameters (i.e. the energy discretization is collapsed to few groups) that represent homogeneous zones of the reactor, which will be used in the following step.

In the second step the whole reactor core is modeled, considering big homogenized portions in terms of neutronics. The most common approximation in eq. 2.1 is to develop an angular integration over $d\hat{\Omega}$ and then apply the Fick's diffusion law to the leakage term (Duderstadt and Hamilton, 1976). Thereby a differential equation for the scalar flux $\phi(\bar{r}, E, t)$ is obtained, termed as the *diffusion equation*, being the industry-standard to describe the neutron distribution at core level:

$$\begin{aligned} \frac{1}{v}\frac{\partial \phi}{\partial t} - \nabla \cdot D(\bar{r}, E)\nabla\phi + \Sigma_t(\bar{r}, E)\phi(\bar{r}, E, t) = \int_0^\infty dE' \Sigma_s(E' \rightarrow E)\phi(\bar{r}, E', t) \\ + S(\bar{r}, E, t); \\ \text{with initial condition:} \quad \phi(\bar{r}, 0) = \phi_0(r); \\ \text{and boundary condition:} \quad \phi(\bar{r}_s, t) = \phi_s; \end{aligned} \tag{2.9}$$

where $D(\bar{r}, E)$ is referred as the diffusion coefficient (usually obtained as $D(\bar{r}, E) = \frac{1}{3\Sigma_{tr}(\bar{r},E)}$). Here, the boundary conditions are to be defined in terms of physical considerations (i.e. continuity of flux or currents and non re-entrant neutrons, among others). It is important to note that the approximations considered to obtain 2.9 are not valid near the boundaries, near localized sources or in strongly absorbing media. In spite of this, if homogenized zones are correctly defined (such as different axial zones of each FA), the diffusion approximation is accurate enough to provide an adequate description of main core characteristics (Duderstadt and Hamilton, 1976). It is key to note here that these homogenized zones are represented by macroscopic parameters (such as cross sections and diffusion coefficients) calculated in the first step described above. If we develop the same approach as for Eq. 2.2, we arrive to Eq. 2.10 (Lewis and Miller, 1984;

Cacucci, 2010):

$$\begin{aligned}
&\frac{1}{v}\frac{\partial\phi}{\partial t} - \nabla\cdot D(\bar{r},E)\nabla\phi + \Sigma_t(\bar{r},E)\phi(\bar{r},E,t) = \int_0^\infty dE'\Sigma_s(E'\to E)\varphi(\bar{r},E',t) \\
&\quad + \chi(E)(1-\beta)\int_0^\infty dE'\nu(E')\Sigma_f(E',r)\phi(\bar{r},E,t) \\
&\quad + \sum_i^j \chi_i(E)\lambda_i C_i(\bar{r},t) + S_{ext}(\bar{r},E,t); \\
&\quad \text{with an initial condition:} \quad \phi(\bar{r},0) = \phi_0(r); \\
&\quad \text{and a boundary condition:} \quad \phi(\bar{r}_s,t) = \phi_s; \\
&\frac{\partial C_i(\bar{r},t)}{\partial t} = \int_0^\infty \beta_i dE'\nu(E')\Sigma_f(E',r)\phi(\bar{r},E',t) - \lambda_i C_i(\bar{r},t); \text{for:} \quad i = 1,2,...,I; \\
&\quad \text{with boundary conditions for each i:} \quad C_i(\bar{r},0) = C0_i(r).
\end{aligned} \tag{2.10}$$

In this point we arrived to set of equations to solve, where the diffusion approximation and the collapsing in precursor families has been done. Besides, when dealing with the calculation of reactor cores, the external source term is not considered, even though it is always present. These simplified forms that represent the neutron distribution behavior at a reactor core-level (eqs. 2.9 and 2.10) also consider a non-continuous energy approach, thus the energy variable is again discretized, leading to an energy condensation scheme with a lower number of *energy groups* as the previous steps (i.e. two to five). As a final step, these equations are solved spatially using diverse techniques such as nodal approximations or finite-differences, where the first one is the most common one within LWR (Duderstadt and Hamilton, 1976).

To summarize, the process to attain the eqs. 2.9 and 2.10 used to describe the reactor core develops successive considerations over the spatial and energy variables, termed as an *homogenization* and *condensation* process, where:

- Condensation is the process of instead considering a continuous energy dependence, use cross sections and fluxes condensed into a few-group structure, defined to preserve relevant reaction rates (Duderstadt and Hamilton, 1976).
- Homogenization is the process of instead considering the typical highly-detailed spatial heterogeneity of a reactor, homogenize macroscopic parameters (such as macroscopic cross-sections and diffusion coefficients) using detailed models that represent relevant zones (such as each axial slice of a FA or the core reflector). These parameters are then used in further core-level calculations that do not take into account these peculiarities.

This homogenization-condensation process implies a loss of detail in the problem solution and when pin-wise results are required, a *reconstruction* process has to be applied to recover the details lost. It will be seen in further sections that several of these approximations can be evaded through a MC-based full-core oriented approach.

Regarding transient calculations, despite being the industry-standard approach to solve this

problem with traditional nodal or finite difference methodologies, it is a common practice to develop additional simplifications to Eq. 2.10. This is basically aimed to get a simplified set of equations that allows to model the global time behavior of the transient problem. If we integrate in energy and space Eq. 2.10, considering the neutron flux solutions expressed into separable functions of space and time, a simplified time description of the problem can be obtained (Duderstadt and Hamilton, 1976; Bell and Glasstone, 1970). This set of differential equations are then only expressed in terms of the global power $P(t)$, the precursors concentration C_i and the system reactivity $\rho(t)$ as:

$$\begin{aligned} \frac{dP}{dt} &= \left(\frac{\rho(t) - \beta_{eff}}{\Lambda_{eff}} \right) P(t) + \sum_{i=1}^{j} \lambda_i C_i; \\ \frac{dC_i}{dt} &= \frac{\beta^i_{eff}}{\Lambda_{eff}} P(t) - \lambda_i C_i \quad ; \text{for precursor groups:} \quad i = 1, 2, ..., j; \\ &\text{with boundary conditions for:} \quad C_i(0) = C0_i \quad and \quad P(0) = P_0. \end{aligned} \tag{2.11}$$

This approximation is known as *Point Kinetics model* (PK), where it should be regarded that in Eq. 2.11 the kinetics parameters such as β_{eff}, β^i_{eff} and Λ_{eff} are obtained by the proper neutron flux weighting of nuclear constants (Bell and Glasstone, 1970), defining thus *effective* values (i.e. for the stated configuration, where commonly $\beta_{eff} > \beta$ for reflected reactor cores). The importance of the Eq. 2.11 relies in the fact that it represents a powerful tool to analyze the global evolution of the power of reactor for a given reactivity insertion in the system. The presence of the delayed contributions represents a key factor, since the behavior changes dramatically when these delayed neutrons are not required for the criticality of the system (known as a *prompt supercritical* configurations, i.e. where the reactivity is higher than β_{eff} (Duderstadt and Hamilton, 1976)), as depicted in the Fig. 2.2

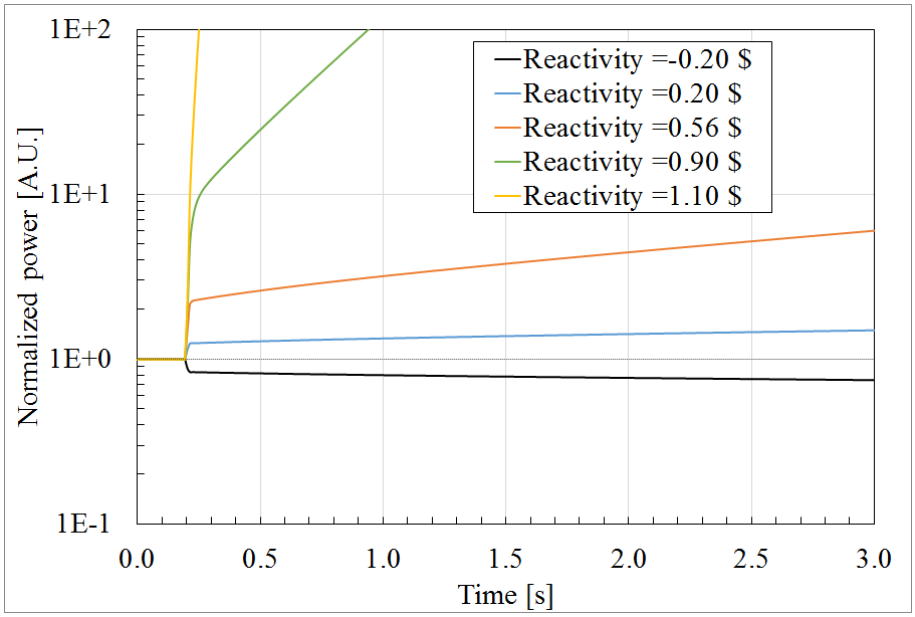

Figure 2.2: Normalized power evolution as a function of inserted reactivity (expressed as ratio to β_{eff}), calculated using Eq. 2.11 (no TH feedbacks). Using condensed constants for a PWR-minicore geometry with 8 delayed neutron groups from (Ferraro et al., 2019a).

The Fig. 2.2 presents solutions to the Eq. 2.11 for diverse values of reactivity. These cases, obtained using eight-precursors group data weighted for a PWR-kind realistic geometry (Ferraro et al., 2019a), represent a sudden step reactivity insertion that occurs at a time t =0.2s, where the values are normalized to β_{eff} (i.e. represented in [$]). The relevance of these delayed components is thus appreciated in the temporal evolution of the normalized power. For the reactivity insertions below 1 β_{eff}, an initial rapid change in the power is observed, characteristic of the prompt lifetime, followed by more slowly response governed by the delayed neutron behavior (this evolution is known as *prompt-jump* (Duderstadt and Hamilton, 1976)). It is important to note that for reactivity insertions above β (i.e. *prompt supercritical*) the power increase is entirely governed by the *prompt* constants, thus resulting in the fast power evolution observed in Fig. 2.2. These fast-transients are no controllable by external means (e.g. a control rod movement o a change in the core composition), where the feedbacks from the rest of the involved physics (such as the TH) will play a relevant role in the evolution. In a reactor core these increments of power will generate a change in the TH scalar fields (named here directly as fields for compactness) which will affect the cross sections, thus generating a reactivity compensation (in case this feedback is negative), as discussed in the following sections. It is also important to note that when there is a increment of power due to a positive reactivity insertion in the system, the precursors population will be also affected (i.e. increased), thus the system will not recover its initial power level if the reactivity is set back to a zero value. To show this effect, Fig. 2.3 presents the results of the same case with 0.56 β_{eff} reactivity insertion, but here the step reactivity is maintained during 2 s and then set back to zero.

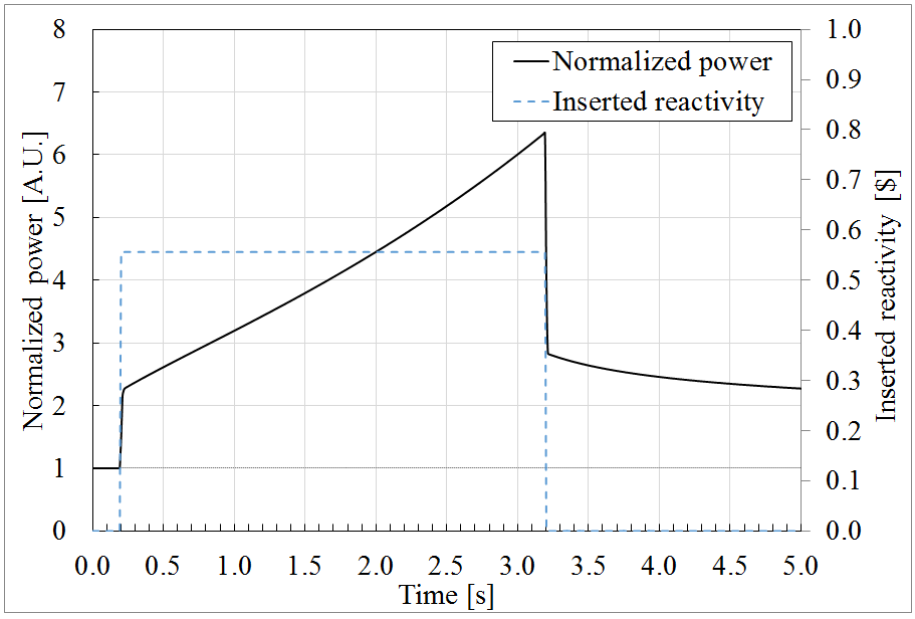

Figure 2.3: Normalized power evolution for a positive 2 [s] step reactivity insertion (expressed as ratio to β_{eff}), calculated using Eq. 2.11 (no TH feedbacks). Using condensed constants for a PWR-minicore geometry with 8 delayed neutron groups from (Ferraro et al., 2019a).

It can be seen from Fig. 2.3 that the initial power evolution is the same as the one depicted in Fig. 2.2, but when the reactivity excess is eliminated the reactor gradually sets its power to a new (and higher value) due to the increased precursors population concentration. This time response behavior is actually the common practice to set the power of a real reactor, where as a

first step a critical configuration is obtained with almost no power, to then proceed to increase the power through successive steps of power increase, where small amounts of reactivity are applied on each.

Finally, it is important to note that the models from Eq. 2.11 can also incorporate additional terms to represent main reactor feedbacks (i.e. the reactivity introduced in the system due to the change in power), and thus develop a rough model of the global behavior reactor transients. These analyses have the limitation of not being able to take into account spatial effects, such as the change of the flux shape in time due to the fast movement of a control rod in a small portion of a big reactor core (Duderstadt and Hamilton, 1976).

2.4 Highly detailed neutronics: the use of the Monte Carlo method

The Monte Carlo (MC) method is a statistical technique developed in late eighteen century that allows to simulate mathematical or physical problems. The main concept behind the MC technique is to obtain the expectation value of a given variable through the successive simulation of individual processes with known or assumed probability density functions (*pdf*), thus constituting a *stochastic* approach to the problem. To do this, pseudo-random numbers (nowadays generated by a computer) are used to simulate these processes, where the repetition is required to achieve a small relative statistical uncertainty over the expected values. In particular, the use of MC techniques to solve the neutron transport problem has its origins in the nuclear laboratories of United States during late 1940s (X-5 Team, 2008), but the increase of the use of such methodologies is related with the availability of extensive computational resources in the last decades.

2.4.1 Basics of the Monte Carlo method

In a MC simulation, the goal is to simulate a physical process in which the related physics relations are known. As a consequence, the probability density functions (*pdf*, identified here as $p(x)$) of the processes to be modeled can be defined. Assuming that random numbers are available, the idea is to sample the outcome of the random process x for a given *pdf* $p(x)$, sampling random numbers as cumulative probability density function output (*cdf*, named here as $P(x)$).

To illustrate the concept, we can suppose that we want to sample x for a given *pdf* $p(x)$, which is assumed to be correctly normalized. Then we know that the cumulative probability can be expressed as:

$$P(a < x < b) = \int_a^b p(x)dx. \tag{2.12}$$

But we also know that $P(a < x < b)$ will have values between 0 and 1. So the method proposes to associate this *cdf* $P(x)$ to an uniform distributed variable that will be sampled, as it is schematically shown in Fig. 2.4.

This association can be proved using the rule of transformation of variables (Lewis and Miller,

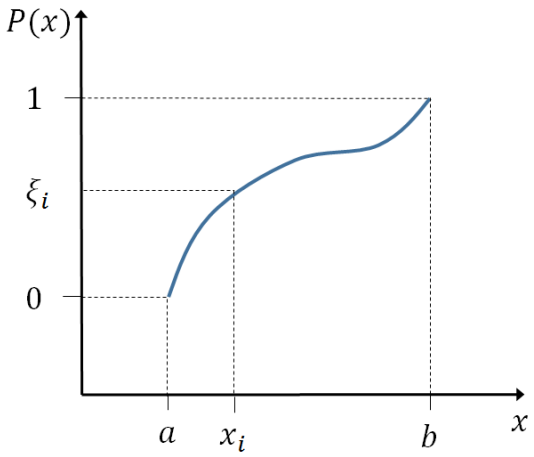

Figure 2.4: Sketch of the sampling of a random variable x.

1984), that will lead us to the equality:

$$P(a < x < b) = \xi \quad \rightarrow \quad x = \xi^{-1}. \tag{2.13}$$

The selection of these random values ξ from probability distributions is called sampling, and is highly dependent on the capability to provide random and uniformly distributed values for ξ and the proper representation over the *pdf* $p(x)$. It should be noted that the scheme proposed in Eq. 2.13, referred as *inversion-method*, is not always possible. Nevertheless alternative techniques are available that always somehow relies in the same idea (Leppänen, 2007).

As a second step, the definitions of expected values $E(x)$ and variance σ^2 through eqs. 2.14 and 2.15 can be used:

$$E(x) = \int x f(x) dx; \tag{2.14}$$

$$\sigma^2 = \int (x - E(x))^2 f(x) dx = E(x^2) - (E(x))^2. \tag{2.15}$$

Both definitions do not depend on any restriction on the distribution of x, beyond requiring that $E(x)$ and σ^2 exist and are finite. The final step is then to take advantage of the theory of large numbers, that states that the accuracy of an estimate of a quantity tends to improve as one averages larger and larger samples of observations of the value of the quantity (X-5 Team, 2008). Accordingly, it can be considered x_i as sample values of the random variable x. If the sample mean is formed, the law of large numbers states that the sample mean, with a probability that approaches to 1 as n increases to infinity, approximates the population mean (or true mean), $E(x)$ (Lewis and Miller, 1984; X-5 Team, 2008):

$$E(x) \approx \bar{X}_N = \frac{1}{N} \sum_{i=1}^{N} x_i. \tag{2.16}$$

Finally, the square root of the variance is σ, which is called the standard deviation of the population of scores. In a practical calculation, one should keep in mind not only that the true mean is unknown but also that the variance σ must be estimated in order to apply the central limit theorem. If we have sampled x, the random variable, N times, we can estimate the sample

variance $\bar{\sigma}$ as (Lewis and Miller, 1984; X-5 Team, 2008):

$$\sigma(x)^2 \approx \bar{\sigma}(\bar{X}_N)^2 = \frac{1}{N-1}\left(\frac{1}{N}\sum_{i=1}^{N} {x_i}^2 - {\bar{X}_n}^2\right). \tag{2.17}$$

When dealing with MC calculations, it is common to report the standard deviation $\bar{\sigma}(\bar{X}_N)$ in terms of its relative statistical error $R(\bar{X}_N)$, which is a convenient number because it represents statistical precision as a fractional result with respect to the estimated mean. This parameter will be used here too, which can be defined in terms of the $\bar{\sigma}(\bar{X}_N)$ and the mean value $\bar{X}_N$ as shown in Eq. 2.18 :

$$R(\bar{X}_N) = \frac{\bar{\sigma}(\bar{X}_N)}{\bar{X}_N}. \tag{2.18}$$

Both $R(\bar{X}_N)$ or $\bar{\sigma}(\bar{X}_N)$ are proportional to $1/\sqrt{N}$, which is the inherent drawback to the Monte Carlo method. As a consequence, to halve $\bar{\sigma}(\bar{X}_N)$, four times more of histories must be calculated, which shows that a converged MC calculation can lead easily to a computationally expensive problem.

2.4.2 Using MC to solve the neutron transport

In MC-based neutronics instead of solving the Eq. 2.1 through approximations such as those described in Eq. 2.9, the main behavior is inferred taking advantage of the knowledge over the *pdfs* ruling the neutron transport process. As a result, in a MC neutronic calculation a direct sample of random particles is recorded to finally obtain expected values as in Eq. 2.17 (with its associated statistical uncertainty). In this sense MC for neutron transport is conceptually different from deterministic transport methods described in previous sections, since the obtained answers are guessed in terms of the average behavior of the parameters obtained using estimators that represent the physical process we are looking for.

To illustrate this, the estimation of a neutron track length can be discussed. As a first step, the *pdf* of a neutron suffering a collision within a distance dx around x is known to be $p(x) = \Sigma_t e^{-\Sigma_t x}$ (Duderstadt and Hamilton, 1976; Lewis and Miller, 1984). If we proceed to integrate to obtain the *cdf* (as in Eq. 2.13) and associate it to a uniform distributed random number ξ with values between 0 and 1 we arrive to:

$$p(x)dx = \Sigma_t e^{-\Sigma_t x}dx \rightarrow \xi = F(x) = \int_0^x p(x\prime)dx\prime = \int_0^x \Sigma_t e^{-\Sigma_t x\prime}dx\prime = \left(1 - e^{-\Sigma_t x}\right). \tag{2.19}$$

If we proceed with the inversion method, the track length x as a function of the uniform variable ξ can be obtained:

$$\ln(1-\xi) = -\Sigma_t x \rightarrow \quad x = -\frac{\ln(1-\xi)}{\Sigma_t} = -\frac{\ln(\xi)}{\Sigma_t}; \tag{2.20}$$

where we considered that ξ and $1-\xi$ have the same distribution. If N random numbers ξ are

sampled, the average track length can be estimated using 2.14:

$$\bar{x} = \frac{1}{N}\sum_{i=1}^{N} -\frac{\ln(\xi_i)}{\Sigma_t}. \tag{2.21}$$

Since the physical processes that govern the neutron physics are clearly understood in terms of being able to define the sampling *pdf*, the interactions of a traveling neutron with matter (e.g. fission, scattering, capture, etc.) can be modeled (X-5 Team, 2008). Once the track length is obtained (eq. 2.20), the interaction that occurs can be sampled. If for example we have a purely absorbing and scattering media, we can decide to terminate the tracking of this particle comparing another sampled random number to the ratio of the absorption to the total cross sections (or sample an scattering reaction otherwise). This approach, called analog absorption, just considers that the particle history ends if the absorption occurs, deposits its energy in that position and a new history is to be sampled. But being this analog scheme far from the optimum (from the point of view of computing efficiency), an alternative approach is commonly applied, called implicit absorption. For this case, a statistical *weight* W_n is assigned to the each particle sampled, which basically determines its importance (or the number of neutrons the simulated history actually represents). In this case, instead of terminating the neutron history at the capture site, this *weight* is reduced according to the capture probability, as shown in Eq. 2.22.

$$W_n^{\text{new}} = (1 - \frac{\sigma_a}{\sigma_t})W_n^{\text{old}}. \tag{2.22}$$

where σ_a and σ_t are the absorption and total cross sections where the interaction occurs. As a result, within a MC neutronic code a particle *weight* will be tracked together with its position, direction, energy and time (if applicable). It is clear that values too big or too low of W_n will affect the statistic behavior of the sampling, as far as will over-represent some events (in the first case) or expend too much computational time be tracking particles that will not produce an appreciable contribution to the result (in the latter case). To avoid such problems, a common practice in MC codes is to develop *splitting* and *Russian roulette* techniques to handle these particle weights. In the former, a particle of weight W_0 is splitted into n independent particles, each having a weight which is $1/n$ times the original weight. On the contrary, the *Russian roulette* takes a particle at of weight W_0 and turns it into a particle of weight $W_1 > W_0$ with probability $\frac{W_0}{W_1}$ and terminates it with a probability of $1 - \frac{W_0}{W_1}$ (X-5 Team, 2008).

Finally, a difference must be made regarding how the histories of the sampled particles are managed, which basically arises from the way fission is considered. Almost all MC codes consider two kinds of problems, namely *criticality* and *fixed-source* problems (Leppänen et al., 2020; X-5 Team, 2008).

In *fixed-source* problems the particles are considered as an initial fixed source with a user-defined shape in terms of spatial, angular an energetic distributions. Using this information, a number of histories are run, sampling the diverse processes involved. This scheme is usually used for shielding and *transient* calculations, each of them with specific details to be considered.

On the contrary, *criticality* problems are analogous to an eigenvalue problem from Eq. 2.4, where the chain reaction is artificially balanced. This scheme is used for steady-state and burnup calculations. In this mode, the simulation is developed for a given number N of particles distributed in M cycles. The source distribution for each cycle is defined by the random sampling of N fission sources from P points stored from the preceding one. As far as the number of new source neutrons generated by fission at the end of each cycle generally differs from N, the multiplication factor k automatically arises as the scaling factor. Specific convergence aspects arise here, as far as the spatial and energy convergence of the sampled fission source is more difficult than the multiplication factor. Several techniques are available to assess this issue (such the evaluation of the Shannon Entropy of the fission source distribution (X-5 Team, 2008)). On top on that, some assumption over how fission source sites are initially distributed is mandatory, where a good first guess improves the convergence process.

Regardless of the case, the collection of results from the simulated events is done using diverse estimators that save the information from the history sampling. Diverse methods are available within MC codes that lead to the definition of diverse accumulators (i.e. *tallies* or *detectors* (X-5 Team, 2008; Leppänen et al., 2020)), where the results will be always expressed both in terms of its expected value and its associated uncertainty (in terms of $\bar{\sigma}$ or R, as defined in eqs. 2.15 and 2.18).

2.4.3 Accuracy vs precision in MC neutronics

The MC method samples particles and infers relevant results from the collection of discrete events, where the deviation over this estimation will diminish as $1/\sqrt{N}$, being N the number of particles simulated (see Eq. 2.15). If we consider an un-biased estimator, the reduction of this uncertainty through the increase of simulated histories will not improve the description of the physical problem. In this sense, it is key to understand that there is an important difference between precision and accuracy within MC calculations (X-5 Team, 2008).

If the physical description of the problem is not correct (e.g. the materials or the geometries are not properly considered in the model), a lack of accuracy remains independently of the number N selected. As a result, MC allows to obtain a highly precise result that is far from the physical truth because of poor modeling of the nature of the problem. On the opposite sense, if N is too low, there will be a lack of precision on the results. These two effects are schematically depicted in Fig. 2.5.

It is evident from Fig. 2.5 that in case the physical problem is not properly modeled, the results will be bad regardless the number of particles considered. Furthermore, the results provided by an MC calculation shall include their associated uncertainty (named as *statistical convergence* or *stdev*) in order to verify the level of convergence reached in the estimators. Consequently, the error bars presented for the calculations held with the developed tool in the diverse sections of this work are representing this *statistical convergence*.

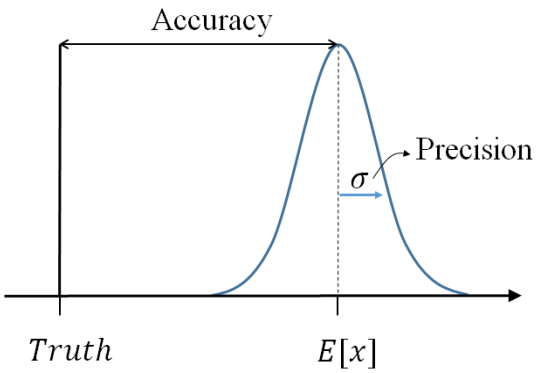

Figure 2.5: Sketch of the difference between accuracy vs. precision in MC neutronics.

2.4.4 Some remarks about statistical convergence

Following the analysis of Fig. 2.5, the quantification of the level of statistical convergence required to be confident on the results obtained by an MC approach arises. There is not a general rule for all the estimators within a MC neutronic code, but a guideline for identifying the level of confidence on the tallies is commonly considered (X-5 Team, 2008), presented in Table 1 in terms of the relative statistical uncertainty R (see Eq. 2.18).

Range of R	Quality of the Tally
0.5 to 1.0	Not meaningful
0.2 to 0.5	Factor of a few
0.1 to 0.2	Questionable
< 0.10	Generally reliable

Table 1: Guidelines for interpreting the relative statistical error R (X-5 Team, 2008)

It can be seen from these guidelines on Table 1 that if the statistical convergence of the problem is too poor the results are of limited trust. To improve this convergence the options are to increase the number of histories N or to try to improve the contribution of each history to the tally we are dealing with (even if the computer time spent is increased). The latter process is somehow mandatory for MC codes dealing with complex (of neutronically big) problems, which is usually named as *Variance Reduction*. In that sense it is important to define an additional terminology, known as Figure or Merit (FOM):

$$\text{FOM} = \frac{1}{R^2 T}; \tag{2.23}$$

where T is the computer time and R represents the relative error. This FOM will represent the level of efficiency of a MC calculation has, being a larger FOM an indicator that less computer time is required to reach a given value of R.

2.4.5 The use of MC neutronics within *transient* calculations

From the example of Eq. 2.20 it is clear that the track length of each neutron is obtained in the MC modeling process. For each calculated track length, the energy of the neutron (and thus the velocity) is also known. Having the velocity and the distance, the elapsed time is

obtained. In spite of that, specific aspects of the implementation of this approach for MC *transient* calculations in nuclear reactors arise.

The *transient* problems within MC are analogous to a *fixed-source* calculation, where a time-binning is added to record the involved times associated to the particle histories. But when dealing with multiplying media, several aspects have to be considered related to the control of population in either subcritical and supercritical problems to maintain a reasonable number of particles on each time bin (Leppänen, 2013a). Besides, for reactor-oriented calculations, the *delayed* neutrons contribution must be also handled, which represents a problem since their characteristic time differs from the *prompt* ones.

The strategy to deal with this issue is somehow dependent in the MC code implementation, but most of them rely on the idea of creating *delayed* neutron precursors instead of sampling delayed neutrons (Sjenitzer, 2013). When a fission occurs, instead of sampling the *delayed* neutron that can appear up to several seconds later, the precursors population that produces the delayed neutrons is tracked. These delayed neutrons are modeled as waiting in precursor atoms (also grouped in j families) at a certain position with its given decay constant λ_i (see Eq. 2.2). This approach has several advantages from the global performance point of view and hence is applied in several MC codes (Valtavirta et al., 2016).

The scheme constitutes a two-step approach, for which an initial distribution of neutrons and precursors must be previously obtained through a *criticality* problem representing the starting configuration, to then proceed to the time-dependent *fixed-source* calculation. As a result two external sources are to be simultaneously considered; one with neutrons traveling with a given position, direction and energy (identified in the jargon as *live* neutrons) and another one with the information of the precursors population that will generate the delayed neutrons (including a given decay constant per group obtained from the selected *NDL* (Valtavirta et al., 2016)).

To finally develop the *transient* simulation the time domain is divided into n bins, where the idea is thus to develop a series of steps considering the available information for the beginning of the interval (BOI) to reach the end of interval (EOI), handling the behavior of precursors within the calculation during each time bin. Besides, if changes in the compositions or geometries occur (such as the change in temperatures and densities or movement of Control Rods), these are to be also considered. It must be noted that this scheme is known to have slight differences implementations depending on the chosen MC-based neutronic code, where the further description will be done using Serpent code as basis (Valtavirta et al., 2016) (see details in the Algorithm 2 in Appendix B).

When modeling the behavior of the delayed neutrons arising from the precursors source for a given time bin, it is important to note that not all of them survive up to the EOI. Consequently, only a part of their weight (as defined in Eq. 2.22) is allowed to survive until EOI due to decay. It can be supposed then that a precursor is produced from an interaction that occurs at time t_* with weight w_0, and only a part of its weight will survive until the end of the interval, as

schematically depicted in Fig. 2.6, where the emitted w_{emit} and surviving w_{tal} weight portions are shown (using t_0 as BOI and t_1 as EOI).

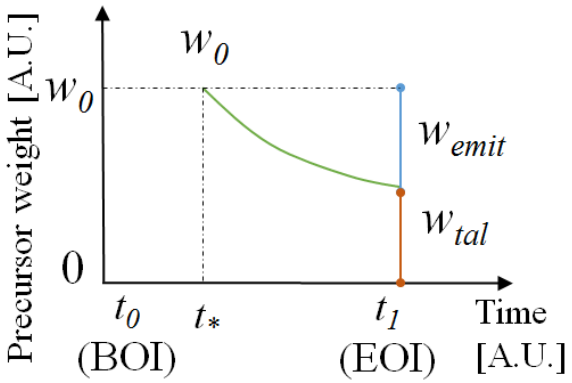

Figure 2.6: Scheme of precursors decay approach within Serpent. Modified from (Leppänen et al., 2020).

The associated weight of the surviving portion can be calculated using the decay law, as presented in Eq. 2.24 of this then added to the end-of-interval precursors source, as shown in Eq. 2.24:

$$w_{\text{tal}} = w_0 e^{-\lambda_g (t_* - t_0)}; \tag{2.24}$$

where λ is representing the decay constant of the precursor. The remaining part must decay during the interval, which should be emitted as a delayed neutron:

$$w_{\text{emit}} = w_0 \left(1 - e^{-\lambda_g (t_* - t_0)}\right). \tag{2.25}$$

It should be noted that, being w_{emit} small compared to w_0, the common approach is to represent the emission of the correspondent delayed neutron applying *Russian roulette* to either increase its weight to a more reasonable level or not emit it at all.

Finally, regarding the required initial distribution for *live* neutrons and precursors, it is key that these sources represent correctly the distributions within the initial reactor configuration. The generation of these requires a previous *criticality* calculation that accurately represents the initial configuration. The common approach applied for *live* neutrons is to define tentative interaction sites and store neutrons at random times during their life, since the intention is to avoid recording all histories from the *criticality* calculations. Besides, regarding the precursors, point-wise positions are commonly stored using implicit estimators during the active cycles of the criticality. These sources are saved as specific files for further linking in *transient* calculations, as schematically depicted in Fig. 2.7.

In case of a coupled transient calculation starting from a state that requires an initial coupled neutronic-TH calculation, this scheme is slightly modified. Nevertheless, this two-step scheme is executed in all MC *transient* calculations within this work.

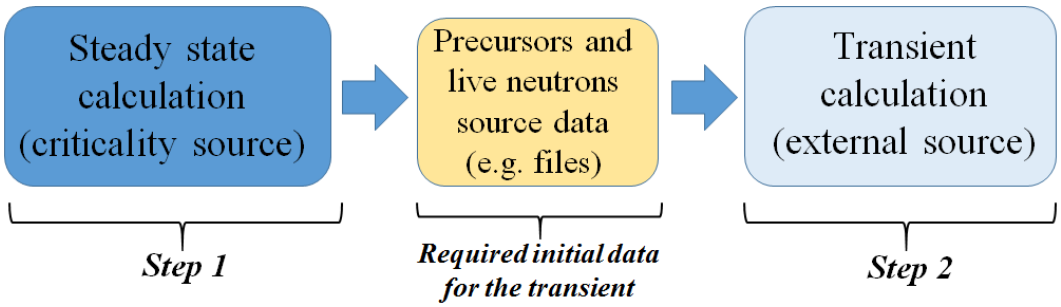

Figure 2.7: Two-step approach for transient calculations

2.5 The feedbacks to the neutronic problem: the core thermal-hydraulics (TH)

Depending on the specific reactor design, the distribution of neutrons within the core suffers from feedbacks related to the characteristics of the materials involved. For the LWR types, the most relevant ones are those related to changes in the thermal-hydraulic scalar fields (such as temperatures and densities distributions) with the total generated power. Having the LWR a *thermal neutron spectra* due to the moderation of neutrons released by fission that occurs mainly in the coolant, changes in the associated TH fields modify the global neutronic solution since they impact in the moderation and absorption processes.

The neutrons released by fission have an energy distribution $\chi(E)$, that can be modeled as a *Maxwellian* spectra with an average energy around 2 MeV (Duderstadt and Hamilton, 1976). In a *thermal reactor* these highly-energetic neutrons must be *moderated* (i.e. decrease their energies to the range of $\sim$ eV) to produce a sustainable chain reaction, for example from fission in ^{235}U isotopes in the fuel rods. This is achieved through the successive scattering with light elements (mainly the Hydrogen in the water), but in this process the neutrons pass through energies ranges where the heavy fissile elements also present in the fuel exhibit big absorption resonances (e.g. ^{238}U). Most of these are present in the so-called epi-thermal region, where the neutron distribution is inversely proportional to its velocity (Duderstadt and Hamilton, 1976). This process of thermalization is dependent on the number of neutrons that are not absorbed in these resonances and can finally reach the *thermal* region, where the probability to undergo fission is higher. Besides, the kinetic energy for thermal neutrons is comparable to the thermal energy of the atomic-motion, which means that the structure of molecules (and temperatures) plays an important role for these low-energies.

To schematically depict this phenomena within a thermal power reactor, the Fig. 2.8 presents the energy distribution of the neutron flux within a VVER reactor at Hot Full Power (HFP), spatially averaged over the whole core. This neutron flux was calculated with the tools and models developed within this work, where the main aspects are discussed in the next chapters. In the plot the three zones described above (i.e. the *thermal*, the *epi-thermal* and *fast* neutron spectra ranges) are indicated, including also the microscopic cross sections for fission of ^{235}U and absorption of ^{238}U, obtained from ENDF/B VII Nuclear Data Libraries (NDL) (Chadwick et al., 2011).

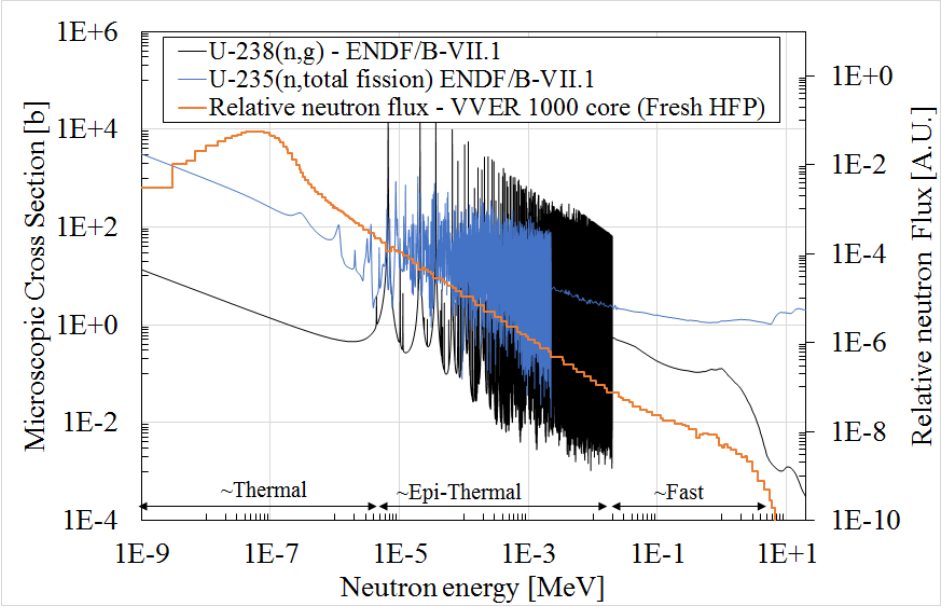

Figure 2.8: Energy dependence of the neutron flux, integrated in the whole core for a VVER at HFP and most relevant nuclear cross sections (from (Chadwick et al., 2011)).

The importance of the absorption resonances from ^{238}U is clear in Fig. 2.8, since they act as a neutron absorber, thus degrading the neutron production vs. losses balance within the core.

For LWR, the feedbacks to the neutronics arise from the temperature and density changes occurring in the materials present in the reactor core. These can be analyzed considering two separated physics, i.e. the change in the neutron moderation process and the effect on the non-fission absorptions. If we focus on density changes (ocurring in the coolant), a decrease in coolant density leads to a loss on the moderation capability, which in turn produces an increment of absorption in the epithermal zone (see Fig. 2.8). Besides, in case diluted burnable poisons are used, changes in the coolant density also alters the amount of neutrons absorbed in non-fission reactions (e.g. the absorption in Boron when boron acid is used). These effects are modeled just altering the density of the coolant in the problem.

Conversely, the temperature feedbacks are relevant both for the coolant and fuel, since for LWR they affect both the neutronics moderation process and the resonance absorption. Regarding the moderation process, the slowing down of the fission neutrons in a thermal reactor is treated in two parts, considering a representation of the scattering cross sections that take into account the involved physical phenomena. For neutron energy that exceeds values in the order of ~10 eV, the thermal motion of the scattering nucleus may be neglected and it can be assumed to be at rest. In this case it may be treated as being free and the effect of temperature can be modeled quite straightforward with ad-hoc models. On the opposite sense, for lower energies, this approximation is not valid. This is due to the fact that the neutron energy starts to be comparable with the binding energy of the molecule that is interacting with the neutron. In such case, an special treatment must be considered, that requires a consideration of the scattering upon molecules and its dependence with the temperature (commonly termed as $S(\alpha, \beta)$, which represents scattering data with angular and energy dependence (X-5 Team, 2008) as a function of the target nuclide temperature).

Regarding absorption cross sections, several structural and fissionable materials suffer temperature changes that affect the rate of non-fission interactions. The absorption of neutrons by heavy nuclei in the epi-thermal region occurs at relatively sharply defined resonance energies (see Fig. 2.8). For these reactions that mainly remove neutrons from the system, the most important effect of the temperature is the broadening of such resonances in the energy domain due to the thermal motion the the target nuclei, called *Doppler effect*. To schematically show this process, an example of the resonance broadening is presented in Fig. 2.9, obtained using the Doppler-broadened Breit-Wigner formula for resonances (Duderstadt and Hamilton, 1976).

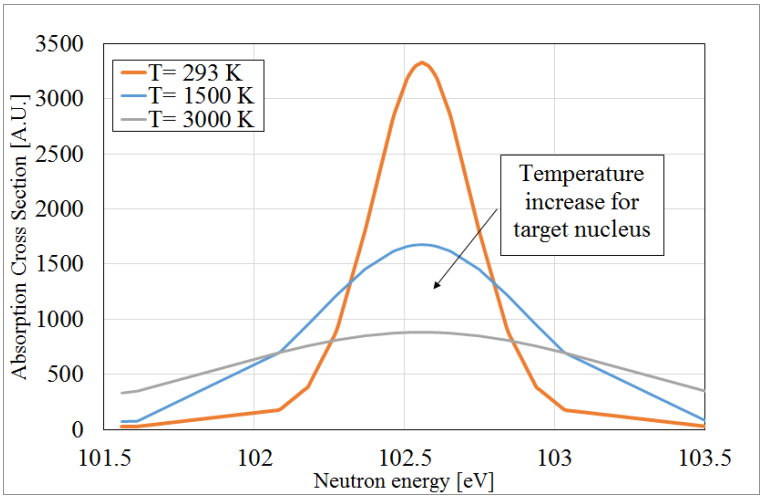

Figure 2.9: Schematic Doppler broadening of an absorption resonance due to changes in temperature of target nuclei. Calculated using Doppler-broadened Breit-Wigner formula (Duderstadt and Hamilton, 1976).

It can be seen in Fig. 2.9 that the temperature increase results in an increased probability of the neutron of being absorbed in this resonances. Modeling this effect is key to depict the neutron physics within the core of a reactor, since it provides one of the most important negative power feedback factors for a PWR and VVER design types.

As a consequence, the accurate modeling of the diverse physics involved within a nuclear reactor that modify the temperature and density fields in the core is mandatory. Further sections discuss the main options to obtain a detailed representation of these distributions, which allow to obtain the required feedbacks to the neutronic problem.

2.6 Thermal-hydraulic description

Disregarding the changes on composition with time, a critical mass of fissile material can operate theoretically at any power level if sufficient cooling can be provided (see Eq. 2.4). Nevertheless, the power generated due to the fission processes within a reactor core must be removed efficiently to avoid conditions where integrity of components can be compromised. The thermal-hydraulic analysis of the reactor thus plays a key role in the overall design, since it provides the feedback required by the neutronics and ensures that no safety-related limit is exceeded. This TH analysis can be considered as a combination of a conduction and a convection problem (the radiation contribution within the fuel-cladding gap is commonly considered altering

the gap conductivity (Imke and Sanchez, 2012)). Therefore, a conduction problem is solved within the fuel rod and a convection problem for the coolant, as is it schematically depicted in Fig.2.10 for a single fuel rod surrounded by coolant (Duderstadt and Hamilton, 1976).

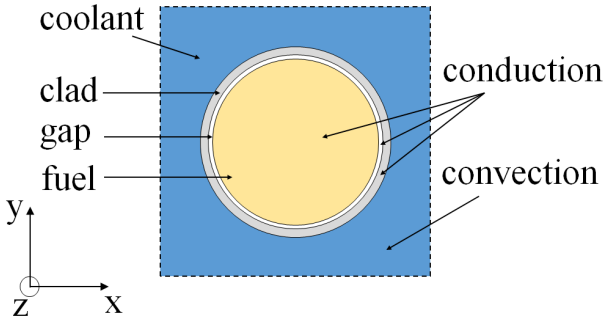

Figure 2.10: Schematic xy cut of a PWR fuel rod and coolant. See Fig. 2.10.

The conduction problem can be modeled through the Fourier's law of thermal conduction to obtain the generic form dependent on time (Duderstadt and Hamilton, 1976):

$$\begin{aligned} &\frac{\partial}{\partial t}(\rho(\bar{r},t)c(\bar{r},t)T(\bar{r},t)) - \nabla \cdot k(\bar{r},t)\nabla T(\bar{r},t) = q'''(\bar{r},t); \\ &\text{with boundary conditions: } - k_s \frac{dT}{dr}\rfloor_s = h_s(T_{clad} - T_{fluid}); \end{aligned} \tag{2.26}$$

where $T(\bar{r},t)$ $[K]$ is the temperature scalar field, $\rho(\bar{r},t)$ $[kg/m^3]$ corresponds to the density, $c(\bar{r},t)$ $[J/(kgK)]$ is the specific heat capacity, $k(\bar{r},t)$ $[W/(mK)]$ is the thermal conductivity and $q'''(\bar{r},t)$ $[W/m^3]$ is the volumetric heat source. Here a boundary condition is considered as a convection surface s (i.e. the coolant that surrounds the fuel pin), where h_s $[W/m^2K]$ is the heat transfer coefficient and T_{clad} and T_{fluid} correspond to the clad and fluid temperatures $[K]$, as discussed in the following paragraphs. The solution of this differential problem is straightforward for stationary cases with constant ρ, c and k parameters, while numerical integration arises as the most used option for more complex cases.

Regarding the convection problem, a forced upward coolant flow with highly turbulent regime is common for most LWR (as for the PWR and VVER designs). Solving this problem is analytically not feasible without approximations, since a reactor core is typically composed of more that fifty thousands of fuel rods almost 4 m long, grouped by spacers, nozzles, and other components that affect the flow (see Fig. 1.1a). The common approach is to take advantage of the main characteristics of the problem and rely on various empirical correlations to finally develop integral analyses over representative portions of the geometry, such as fuel rods and its surroundings. As an example, we can consider an axial portion of a single fuel rod surrounded by coolant and analyze the heat transfer to the fluid. For such purpose we consider the Newton's law of cooling (Duderstadt and Hamilton, 1976):

$$q'' = h_s(T_{clad} - T_{fluid}); \tag{2.27}$$

where q'' $[W/m^2]$ represents the heat flux through the clad and h_s $[W/(m^2K)]$, T_{clad} and T_{fluid} [K] correspond to Eq. 2.26. The problem now is shifted to the calculation of the heat transfer

coefficient. For this purpose correlations are considered, commonly expressed in terms of the hydraulic diameter (D_h) of the problem. As an example, Fig. 2.11 shows typical square and hexagonal lattice arrays (used for PWR and VVER) and its hydraulic diameters.

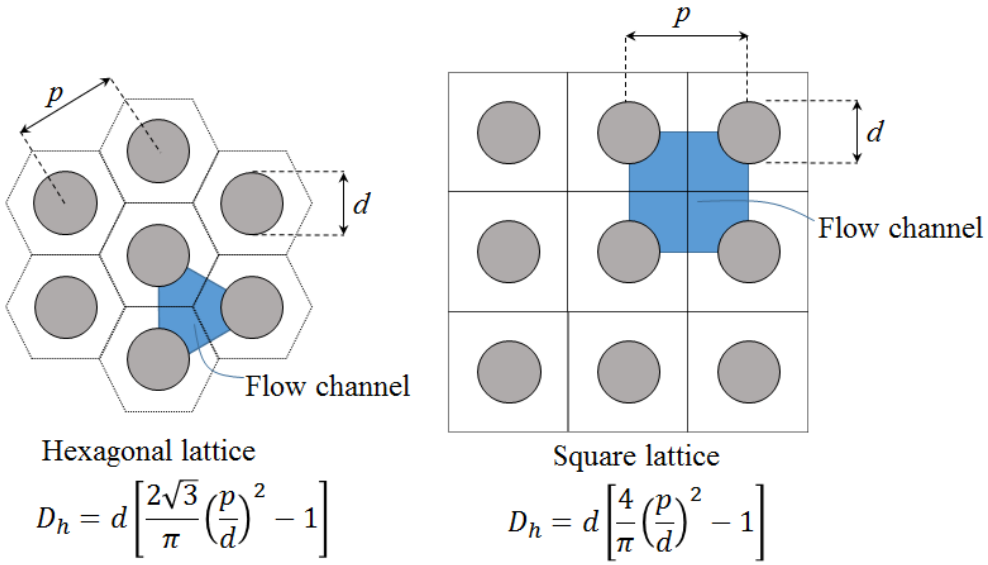

Figure 2.11: Definition of hydraulic diameters D_h for LWR type fuel assemblies; VVER (left) and PWR (right).

The heat transfer coefficient can be expressed in terms of the dimensionless *Nusselt* number, which represents the ratio of the convective to conductive heat transfer, together with the thermal conductivity of the fluid k_f (Duderstadt and Hamilton, 1976) as:

$$h_s = \frac{k_f}{D_h}\mathrm{Nu}. \tag{2.28}$$

To obtain this *Nusselt* number for our problem, several correlations are available. The common approach for non-boiling light water cooled reactors is to use the *Dittus-Boelter* one (or slight modifications). This correlation is expressed in terms of two additional dimensionless numbers, i.e. the *Prandtl* (Pr) and *Reynolds* (Re) numbers. The former can be interpreted as the ratio of the momentum diffusivity to the thermal diffusivity, while the latter can be conceived as the of the inertial forces to viscous forces within a fluid. For fluids with Pr ~ 1 (such as water in a PWR), the *Dittus-Boelter* correlation is expressed as:

$$\begin{aligned} &\mathrm{Nu} = 0.023\mathrm{Pr}^{0.4}\mathrm{Re}^{0.8}; \\ \text{where:}\quad &\mathrm{Re} = \frac{\rho_{fluid}\bar{V}_{axial}D_h}{\mu}; \\ &\mathrm{Pr} = \frac{\mu c}{k}; \end{aligned} \tag{2.29}$$

where μ is the dynamic viscosity of the fluid $[Ns/m^2]$, $\bar{V}_{axial}$ is the average axial velocity $[m/s]$, ρ_{fluid} its density $[kg/m^3]$ and c $[J/kgK]$ its specific heat capacity. If all these parameters are known, the TH problem can be solved with the approximations stated and taking advantage of the correlations from eqs. 2.28 and 2.29, at least for a single FR and its surrounding coolant.

But this analysis has not considered the phenomena that occurs between the channels, nor the axial dependence of the problem. Besides, most of these parameters are function of the pressure and temperature of the fluid, that change both between channels and in the axial dimension.

2.6.1 Subchannel codes

To solve the whole TH problem stated above, a direct discretization of the 3D equations for the conservation of mass (continuity), energy, and momentum of the fluid, coupled with the conduction problem for the fuel rod using a highly detailed discretized grid that takes into account all the details of the core is a valid option. Nevertheless this approach, termed as Computational Fluid Dynamics (CFD), has a limited application within reactor calculations. There are several reasons for that, e.g. its intensive computational requirements likewise the difficulty to model critical phenomena and the acceptance of its results by nuclear regulatory bodies. A common alternative is to take advantage of the physical characteristics of the problem and consider empirical correlations for the pressure drop, heat transfer, void generation, and so forth collected over the last decades for the LWR configurations (Imke and Sanchez, 2012).

This is the approach of the so-called *subchannel TH* codes, which exploit the extruded geometry of the LWR core designs, where the fluid flow is constrained by the surfaces of closely spaced fuel rods oriented parallel to the primary axial flow direction. A control volume that represents a finite fraction of the total cross-sectional area of the nuclear reactor core is considered, connected to its surroundings by a gap, where it is assumed that any lateral flow is directed by this gap losing its sense of direction. This assumption provides the character of the so-called *subchannel* equation system, allowing these to be connected arbitrarily since no fixed lateral coordinate is required. As an example, we can consider the geometry for the PWR described in Fig. 2.11 and define an axial portion Δz of the problem, as shown in Fig. 2.12.

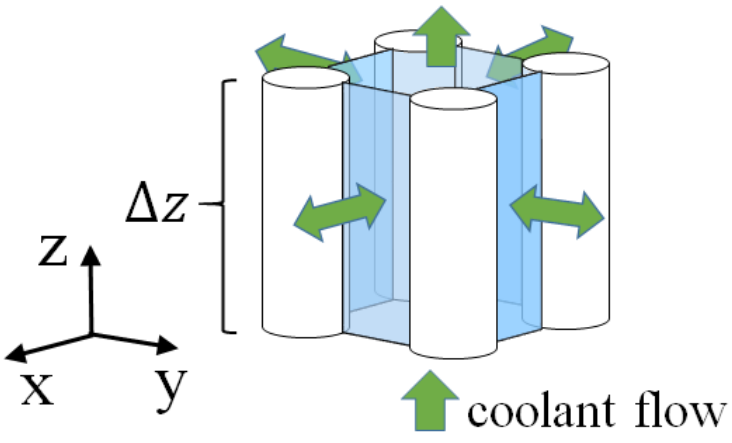

Figure 2.12: Scheme of the axial portion of a common subchannel cell for a PWR-type configuration. Corresponds to a coolant-centered model.

The idea is to solve the equation for the transport of mass, momentum, and energy along the axial direction and between the neighboring channels through the gap formed by the fuel rods (i.e. the lateral direction, cross-flow), identified with green arrows in the plot in an integral manner. Each of these axial cells will be connected to a surrounding channel in the lateral

directions, as shown in 2.13 for the same PWR-type case. The 3D problem is then basically reduced to 1D fluid problem plus the lateral components, losing the directional information (Wheeler et al., 1976; Imke and Sanchez, 2012; Salko and Avramova, 2015).

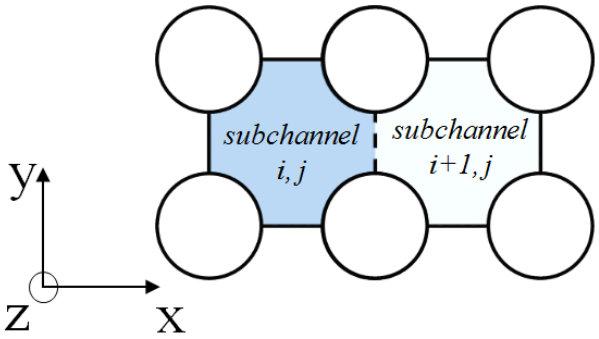

Figure 2.13: Scheme of the xy cut of two consecutive subchannels for a common PWR-type configuration for an axial zone j. Corresponds to a coolant-centered model.

In the Fig. 2.13 the channel representing the fluid is selected to be representative of the fluid flowing through four pins, defining a so-termed *coolant-centered* model. Other options are also available, such as a channel centered in a single fuel pin (i.e. *fuel-centered*), which can represent also a useful approach for some geometries (García et al., 2019b). Finally, for each of these channels the equations of continuity, energy and momentum are derived by applying the conservation equations to this control volume that consists of a segment of subchannel i, j connected to an arbitrary subchannel $i + 1, j$. For each of this adjacent channels (separated by a gap) a direction of the crossflow is considered positive if the flow is from i, j to $i + 1, j$ and negative otherwise. With this convention, a matrix operator $[DC]$ of size Nk (connections) by Nc (channels) is defined, which performs the difference operation across each connection. The general conservation equations can be written as (Wheeler et al., 1976):

Continuity:

$$A\frac{\partial \rho}{\partial t} + \frac{\partial m}{\partial z} + [DC]^t w = 0. \tag{2.30}$$

Energy:

$$A\frac{\partial \rho h}{\partial t} + \frac{\partial mh}{\partial z} + [DC]^t h^* w = q\prime. \tag{2.31}$$

Axial momentum:

$$\frac{\partial m}{\partial t} + \frac{\partial mu}{\partial z} + [DC]^t u^* w + \frac{\partial P}{\partial z} = F\prime. \tag{2.32}$$

Lateral momentum:

$$\frac{\partial w}{\partial t} + \frac{\partial u^* w}{\partial z} - [DC]P = c; \tag{2.33}$$

where A represents the axial flow area, m the mass flow rate, P the subchannel pressure, w the cross flow between adjacent channels per unit length, u the axial subchannel velocity, h the subchannel enthalpy and t the time. Furthermore, $[DC]$ is the matrix operator which performs the lateral finite difference operation, $[DC]^t$ is the transpose of $[DC]$ and performs a summing operation instead of differencing, $F\prime$ is the axial friction and gravity force, c is the lateral friction and $q\prime$ is the heat transfer from all sources. Depending on the case, these equations are applied to the fluid and vapor (e.g. (Salko and Avramova, 2015)) or only to a fluid representing a

mixture of liquid and vapor (e.g. (Imke and Sanchez, 2012)).

These equations are then solved numerically within subchannel codes using a finite-difference scheme, as presented in eqs. 2.34 to 2.37 for the case where a mixture of liquid and vapor is considered (Imke and Sanchez, 2012):

Continuity for the mix:

$$A_{i,j}\frac{\Delta z_j}{\Delta t}(\rho_{i,j}-\rho_{i,j}^{\text{old}})+(m_{i,j}-m_{i,j-1})+\Delta z_j\sum_k w_{k,j}=0. \tag{2.34}$$

Energy for the mix:

$$\frac{A_{i,j}}{\Delta t}[\rho\prime\prime_{i,j}(h_{i,j}-h_{i,j}^{\text{old}})+h_{i,j}(\rho_{i,j}-\rho_{i,j}^{\text{old}})]+\frac{1}{\Delta z_j}(m_{i,j}h_{i,j}-m_{i,j-1}h_{i,j-1})+\sum_k w_{k,j}h_{k,j}= Q_{i,j}-\sum_k w\prime_{k,j}\left(h_{i,j}-h_{n(k),j}\right). \tag{2.35}$$

Axial momentum for the mix:

$$\frac{\Delta z_j}{\Delta t}(m_{i,j}-m_{i,j}^{\text{old}})+m_{i,j}U\prime_{i,j}+\Delta z_j\sum_k w_{k,j}U\prime_{k,j}=-A_{i,j}(p_{i,j}-p_{i,j-1})-gA_{i,j}\Delta z_j\rho_{i,j}-\frac{1}{2}\left(\frac{\Delta z f\Phi^2}{D_h\rho_{\text{liq}}}+K\nu\prime\right)_{i,j}|m_{i,j}|\frac{m_{i,j}}{A_{i,j}}-\Delta z_j\sum_k w\prime_{k,j}(U\prime_{i,j}-U\prime_{n(k),j}). \tag{2.36}$$

Lateral momentum for the mix:

$$\frac{\Delta z_j}{\Delta t}(w_{k,j}-w_{k,j}^{\text{old}})+(\bar{U}\prime_{k,j}w_{k,j}-\bar{U}\prime_{k,j-1}w_{k,j-1})=\frac{s_k}{l_k}\Delta z_j\Delta p_{k,j-1}-(K_G\frac{\Delta z v\prime_k}{s_k l_k})_j|w_{k,j}|w_{k,j}; \tag{2.37}$$

where $A_{i,j}$ represents the subchannel areas $[m^2]$, g the gravity $[m/s^2]$, K and K_G the axial and lateral pressure loss coefficients, l the distance between subchannels $[m]$, m the flow rate [kg/s], p the pressure [Pa], $Q_{i,j}$ the linear power released to the subchannel [W/m], s the inter-channel gap [m], w and $w\prime$ the linear mass and turbulent mass flow rates [kg/(ms)], f the single phase friction coefficient (from correlations), Δz_j the axial length [m], x the steam quality, α the void fraction, h_{fg} the evaporation enthalpy [J/kg], ρ the density [kg/m3] and Φ^2 represents the empirical correlation for the two-phase friction multiplier. Besides, k identifies gaps (and $n(k)$ its channel neighbor), *old* the values at a previous step and *liq* and *vap* values for liquid and vapor. The enthalpy derivative in Eq. 2.35 considers an average for liquid and vapor as:

$$\rho\prime\prime=(\rho^{\text{old}}-h_{fg}\frac{\partial\Psi}{\partial h});\quad \text{where}\quad \Psi=\rho_{\text{liq}}x(1-\alpha)-\rho_{\text{vap}}\alpha(1-x). \tag{2.38}$$

Finally, the specific volume $v\prime$ for the momentum transfer is defined as:

$$v\prime=\frac{x^2}{\alpha\rho_{\text{vap}}}+\frac{(1-x)^2}{(1-\alpha)\rho_{\text{liq}}}; \tag{2.39}$$

whereas the effective momentum velocity $U\prime$ is then defined as:

$$\begin{aligned} U\prime &= \frac{m}{A} v\prime; \\ \text{with} \quad \bar{U}\prime_{kj} &= \frac{1}{2}(U\prime_{i,j} + U\prime_{i+1,j}) \quad \text{for subchannels } i,j \text{ and } i+1,j \text{ connected by gap } k. \end{aligned} \tag{2.40}$$

Besides, it is necessary to specify fluid properties and constitutive equations to form a closed set of equations for solution, such as axial and lateral friction losses, heat transfer coefficients, coefficients for turbulent exchange and fluid properties. These *closure correlations* are available for a wide range of configurations and fluids, where for PWR and VVER experimental background is vast, including correlations for key safety-related parameters (Doroschuk et al., 1976). Finally, to solve numerically these set of equations, the *donor cell* method is applied to compute convected quantities terms, using the positive convention stated for $[DC]$. This method (also known as upwind) considers the direction of the flow to obtain the required variables in the interface (e.g. gap) between channels. For example, the enthalpy carried by crossflow w from two adjacent subchannels i, j and $i+1, j$ is $h_{i,j}$ if w is positive and $h_{i+1,j}$ otherwise. This approach is proven to have physical grounds, it is easy to compute and enhances computational stability. Conversely it produces some numerical diffusion which tends to smear out sharp gradients across the computation mesh (Stewart et al., 1977).

This *subchannel* approach has major simplifications (Wheeler et al., 1976; Imke and Sanchez, 2012). As an example, the turbulent transport of momentum and energy between neighbouring channels is described by a simple empirical mixing model, based on an equal mass exchange. Besides, the thermal equilibrium between vapor and fluid is considered, together with its mechanical equilibrium (i.e. their velocities are set to be equal). No variation of density with time inside the subchannel is allowed, so no sonic propagation can be modeled and the fluid drag forces are represented by a wall friction and form drag, so fluid-fluid shear is neglected (turbulent momentum exchange is modeled, however). Besides, if a transient calculation is developed and explicit schemes are applied, the maximum time step is limited to $\Delta t < \Delta z/u$ (i.e. the *Courant number (C)* lower than 1, being $C = \frac{u\Delta t}{\Delta z}$).

All these approximations are inherently simplifying the complexity of the problem. Nevertheless, this approach is proven to be suitable for reactor core calculations and has been applied for more than four decades with diverse level of geometrical detail (Stewart et al., 1977; Wheeler et al., 1976; Salko and Avramova, 2015). Including more detailed TH eliminates these simplification and can potentially provide a higher resolution and better modeling of the phenomena that occurs between subchannel, but their impact on the coupled solution is limited for most of the cases. Being for the LWR the average neutron path lengths within the core much higher that the level of detail that can be gained solving the complete 3D fluid problem within a fine mesh, the potential gain is rapidly vanished. Obviously inherent limitations from this TH approach will arise if the assumption done to obtain both eqs. 2.30 to 2.33 or 2.29 are not valid, such as cases where pressure waves exist or vapor collapse occurs, which can not be modeled by this approach.

2.6.2 Safety parameters associated to the TH

One of the main goals of the TH analysis is to ensure that no limit is exceeded regarding the coolability of the fuel rods. Otherwise the integrity of the fuel rod can be compromised, leading to a failure and therefore a release of radioactive substances. Several limiting conditions arise from the TH side of the problem, which are dependent on the specific TH design of the core. In particular, for both PWR and VVER designs limitations are imposed both for normal operations and accidental conditions, mostly related to phenomena that compromise the fuel clad integrity.

Maximum allowable values for the centerline fuel rod temperature and for the clad temperature (Duderstadt and Hamilton, 1976) are stated in order to avoid events such as melting. Besides, additional limits are set for the maximum allowable heat flux from the fuel rods. As an example, within a PWR, the clad surface is allowed to exceed the saturation temperature of the coolant. Although small vapor bubbles form on the clad surface, they rapidly collapse as they leave this surface. This phenomena, termed as *subcooled boiling*, represents an extremely efficient heat transfer mechanism. If the heat flux is still increased, the saturation temperature is reached and a bulk boiling begins in the coolant. From this point, some heat transfer instabilities may arise, since the heat flux can become sufficiently large that the small bubbles coalesce into a vapor film that covers the surface. This phenomena represents a critical value for the heat flux, identified as the *departure of nucleate boiling - DNB*. It implies a dramatic drop of the heat transfer efficiency, increasing abruptly the clad surface temperatures by several hundreds degrees and, consequently, the fuel temperature. As a consequence, for PWR and VVER designs the minimum departure of nucleate boiling ratio (*MDNBR*) is stated as a limit, where the departure of the boiling ratio (*DNBR*) is defined as the ratio of the critical heat flux $q''_{\mathrm{DNB(z)}}$ to the heat flux achieved in the core $q''(z)$:

$$\mathrm{DNBR} = \frac{q''_{\mathrm{DNB}}(z)}{q''(z)}. \tag{2.41}$$

As an example, for PWR a limit of MDNBR > 1.3 is usually set for a PWR overpower of 115 [%]. Finally, when dealing with reactor *transients* generated by rapid insertion of reactivity (i.e. Reactivity Initiated Accidents, termed as RIA), the maximum enthalpy rise within the fuel rods is a common parameter to characterize the fuel integrity. The limit value is dependent on the fuel design, whereas a maximum of ~ 711 [W/g] for PWR fuel rods is considered (USA NRC, 2007).

2.7 Coupled neutronics-thermal-hydraulics

2.7.1 Coupling options

The coupled neutronic and TH problem is nonlinear as far as the neutron flux (and eigenvalue) depends on the nuclide field cross sections, and thus, in the temperatures and densities distribution arising from the TH solution. To solve this issue, the most common approach is to use a fixed-point iteration scheme, where the different solvers are executed consecutively keeping the

coupled physics constant. This scheme, known as *Picard* iteration, can be expressed in terms of the Eq. 2.42 (Gill et al., 2017):

$$X^{n+1} = H(X^n); \tag{2.42}$$

where X^n represents the solution for an iteration step n (in this case both the neutronic and TH scalar fields) and $H(X^n)$ is the fixed-point map (in our case the neutronic and the TH problems). As a result, the process has the advantage of allowing the coupled iteration to use independent neutronic and TH solvers (i.e. operator splitting) for the required inputs (e.g. powers for the TH or temperatures and densities for the neutronics), setting a proper convergence criteria between X^{n+1} and X^n. The disadvantage is that, in principle there are no guarantees that the Picard iteration will converge. This scheme is usually applied not only when dealing with MC-based neutronics, but also as industry-standard due to its simplicity, where a practical convergence test is mandatory. Besides, the relaxation of the interchanged TH fields is commonly applied to improve the convergence stability, as explained in the next Chapter. This scheme is considered within this work, where details of the application for both *steady-state*, *burnup* and *transient* cases are described.

More advanced methods have been also investigated within reactor physics, where those based on gradient-based approaches (such as the Jacobian methods, (Gill et al., 2017)) have been also applied with some success within the deterministic neutronics and TH problems. These have the advantage of an improved convergence rate but its complexity arises as a limiting factor, as far as several additional non-standard parameters have to be calculated, leading to important restructuration of calculation codes. In particular, these methods are not available for MC-based neutronics due to several inherent drawbacks, such as the difficulty to estimate Jacobian elements using MC, and the presence of stochastic noise in the results. Finally, another class of methods nowadays available for MC-based neutronics are based on stochastic approximation approaches (Leppänen et al., 2020), which rely on the use of independent (and less converged) MC calculations to obtain of independent TH solutions which will be averaged to then proceed to the new neutronic fields estimation (Faucher et al., 2019). The advantage of this method is that it is inherent stable, but the main drawback arises from the fact that patologic power distributions arising from statistically poorly converged MC solutions can lead to non-converging TH fields, which is usually a common problem when full-core calculations are tackled.

2.7.2 The industry-standard approach and its limitations

In view of this dissertation goals, a short discussion over the inherent limitations imposed by the standard-industry approach described in previous sections is mandatory. The usual technique within the neutronic side is to divide the problem in a series of successive steps where the physics are solved at different levels. This *cell-core* scheme, schematically depicted in Fig. 2.14 is applied in almost all standard calculation lines, regardless of the involved calculation codes (Duderstadt and Hamilton, 1976).

This scheme depicted in Fig 2.14 starts with the processing of the evaluated nuclear data using dimensionless codes (e.g. NJOY (MacFarlane, 2019)) in order to build a working Nuclear Data

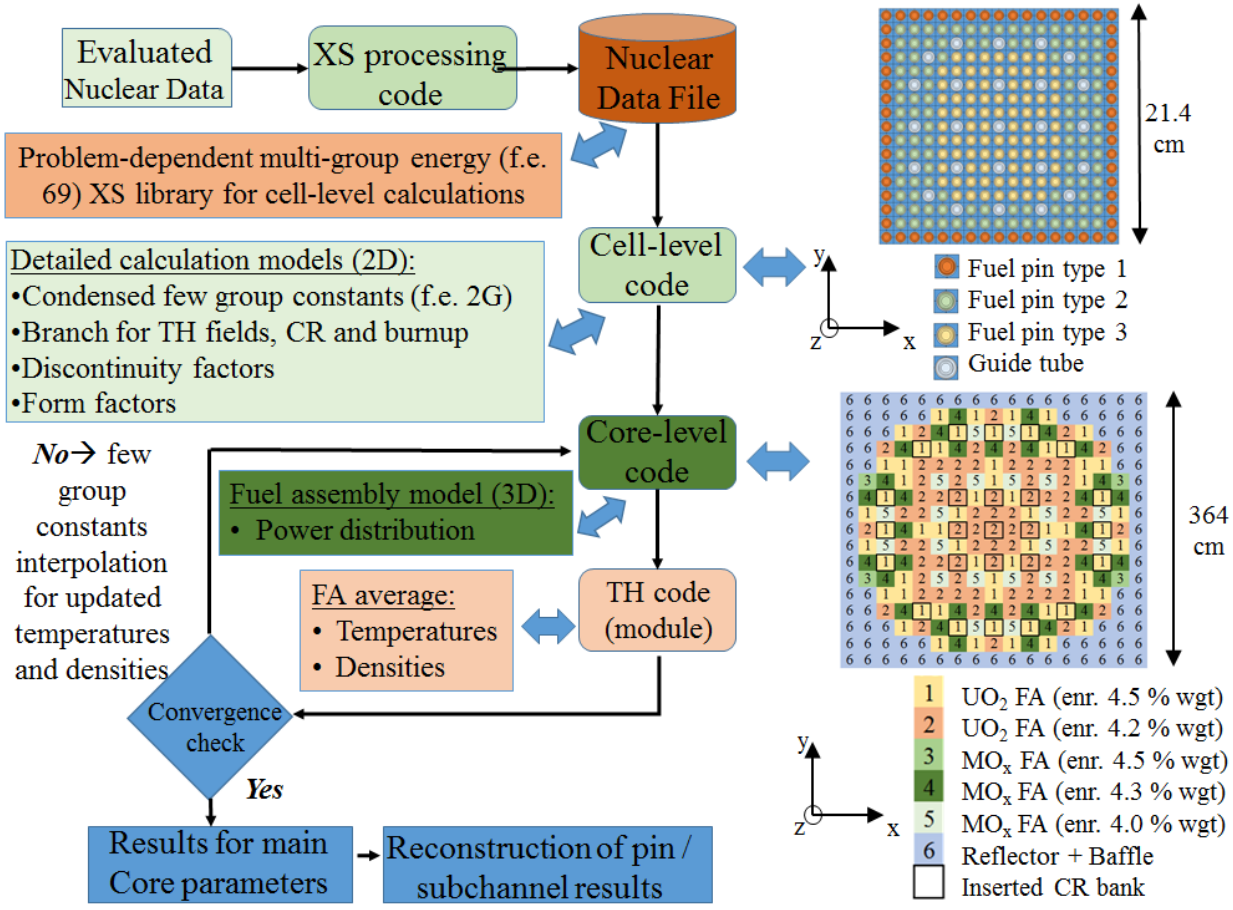

Figure 2.14: Sketch of the standard industry calculation scheme for a coupled N-TH problem.

Library (NDL) suitable for further codes. In this process, several physical models are taken into account to obtain a working library. This obtained NDL can be pointwise continuous in energy (usually referred as ACE) or formed by a series of so-called energy groups, where number of groups depend on the further use, but commonly 69 and 172 groups are standard values.

Once the NDL is available, the standard approach is to solve a representative problem of the diverse components of the core (such as FA or reflector) using a detailed treatment of the physics and spatial details (Lewis and Miller, 1984). These *cell-level* codes develop some approximations over Eq. 2.1 that preserve the physics and geometric heterogeneity as far as possible, leading to methods already mentioned, such as *Collision Probabilities* (e.g. CASMO code (Grandi et al., 2010)) or S_n in 2D geometries. The *cell-level* calculation yields a condensed and homogenized few-group library for diverse zones of the reactor core to be used by further *core-level* codes. This condensed and homogenized library provides problem-specific average parameters (such as macroscopic cross sections, diffusion coefficients, etc.), usually divided in 2 or 3 energy groups. Furthermore, this library must be built considering branches representing changes in condition of the considered zones (such as temperature changes, insertion of control rods, the burnup of the fuel, etc.).

The last step on the neutronic calculation represents the whole core. Mainly the diffusion approximation of Eq. 2.9 is used with the few group constants obtained in the previous step, but also applications of higher-order angle approximations such as the simplified spherical harmonic

approach (namely SP3, see (Lee et al., 2015)) is sometimes found (Cacucci, 2010). For LWR geometries nodal-approximation techniques are preferred over finite-differences ones in order to limit the required spatial discretization (Lewis and Miller, 1984). Several codes are industry standard for such purpose (e.g. Nestle (Turinsky et al., 1994), PARCS (Kozlowski and Downar, 2007) or Simulate (Bahadir and Lindahl, 2009)), that include several advanced processing capabilities to perform relevant analysis such as fuel-management, reactivity worths, etc. In addition, if *transient* calculations are to be considered, the time dependence and the precursor data is solved as for Eq. 2.10.

As a final step, these *core-level* codes usually count with thermal-hydraulics modules to calculate with diverse level of detail the average temperature and density profiles over the calculation nodes, as shown in Fig. 2.14. These profiles are used to interpolate the values from the few-group library and update the *core-level* calculation, where is important to note that no pin-by-pin feedback is developed, since the data for core calculation is already homogenized representing a portion of a fuel assembly. This iteration is developed with some convergence criteria, generally stated over the system reactivity and the power distribution. When this iteration is ended, the final prediction for neutronic and TH parameters is then available. Here the detailed neutron flux is not available thus to obtain pin-wise power distributions a process of convolution of *core-level* with *cell-level* is mandatory (known as pin power reconstruction).

Regarding the TH analysis of the core, the most accurate approach would be first perform a detailed 3D calculation of the core taking into account all neutronic aspects such as burnup or control rods positions for the whole core life to then proceed to determine the coolant flow and temperatures distributions throughout the core. This scheme is expensive from the computational point of view, so it is commonly replaced for a so-called *hot channel* methodology, mainly used to analyze the TH design limits. For such simplified approach the most relevant limiting factors for the safety point of view are analyzed just considering a single channel that represents a conservative description of the most demanded portion of the reactor core.

As a result, this standardized process allows to solve the complex coupled problem with accessible computational effort. In contrast, an inherent loss of the solution detail arises, which inevitably leads to higher design margins. Some of the aspects that can be easily identified are (not exhaustive):

- Specific detailed neutron spectral effects are lost by the *cell-core* approach due to the successive condensations held.
- Spectral shifts due to fuel heterogeneity are not properly modeled for some burnup cases in the *cell-core* approach.
- The pin-wise power distribution within the core is lost, and partially reconstructed through the convolution of *core-level* with *cell-level* (i.e. *pin power reconstruction*).

Moreover, when dealing with transient calculations, the combination of the first two effects is known to produce a big impact on the solution, as has been already analyzed by (Daeubler et al.,

2015b; Lee et al., 2015). As an example, a series of reported results developed in the past years for a full-scope PWR transient numerical benchmark (Kozlowski and Downar, 2007) generated by a sudden CR withdrawal are depicted together in Fig. 2.15. The reported total power evolution obtained using different core-level codes (PARCS, DYNSUB), geometrical discretization (i.e. nodal or pin-by-pin), energy group condensation (i.e. 2, 4 or 8 energy groups) and physical approximations (diffusion or SP3) by the different authors is depicted, identifying the code and its main considerations.

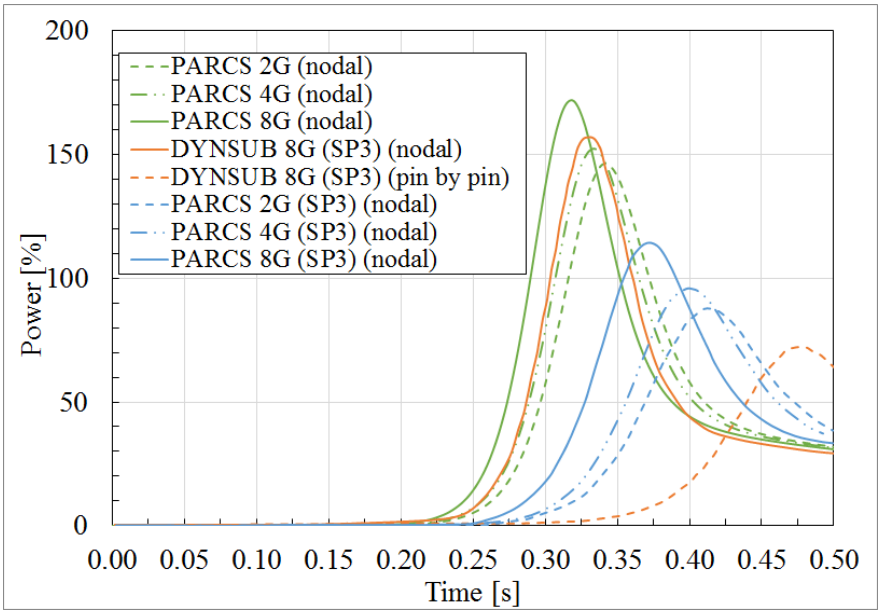

Figure 2.15: Example span of results for transient calculation using cell-core approach. Results for a PWR sudden CR withdrawal scenario, obtained from (Daeubler et al., 2015b) and (Lee et al., 2015).

It is key to observe the impact in the results of Fig. 2.15 is noticeable, where the analysis of the contribution of each of the modeling aspects and approximations within the cell-level approach in the global behavior is not straightforward (Lee et al., 2015). Besides, the efforts to develop a pin-level coupling using an improved description of the neutronics problem (i.e. SP3) showed inconsistencies, reflected by an incompatible power peak description for this case (Daeubler et al., 2015b).

All the aspects above formulate the starting point for the scientific and technological question to be treated within this work. The objective of the investigation is to couple a *highly-detailed* MC-based neutronic methodology with a pin-wise TH, thus avoiding almost all approximations arising from the homogenization and condensation process. Being the scope oriented to industry-like applications (i.e. real LWR configuration), follow a consistent investigation path this alternative promising approach becomes mandatory. The suitability of the approach using state-of-the-art codes has to be assessed to then implement, test, verify and validate its implementation to draw conclusions over its aptness to tackle the *steady-state*, *burnup* and *transient* problems stated.

"The kind of Being which equipment possesses -in which it manifests itself in its own right-, we call readiness-to-hand."

—Martin Heidegger describing a hammer

3 Development of a versatile MC-based multi-physics tool for LWR

Developing coupled MC neutronics plus subchannel TH allows to get rid of most of the approximations arising from the neutronic physical description considered in the industry-standard approach, likewise it proposes a direct thermal-hydraulic calculation of the whole problem. It allows to directly obtain pin-level solutions that can be used, e.g. to obtain safety-related parameters. In more detail, it enables to:

- Avoid the *cell-core* approach, eliminating thus the potential issues arising from successive homogenization and condensation process (e.g. problems related to high heterogeneity of the novel reactor cores, spectral shifts, etc.)
- Avoid the pin power reconstruction methods required to obtain detailed parameters (i.e. convolution of *core-level* with *cell-level* parameters), thus providing a direct calculation of local safety parameters, both for *steady-state*, *burnup* and *transient* calculations.

The cell-core approach from Fig. 2.14 is then avoided, providing a direct full-scope calculation, as schematically described in Fig. 3.1.

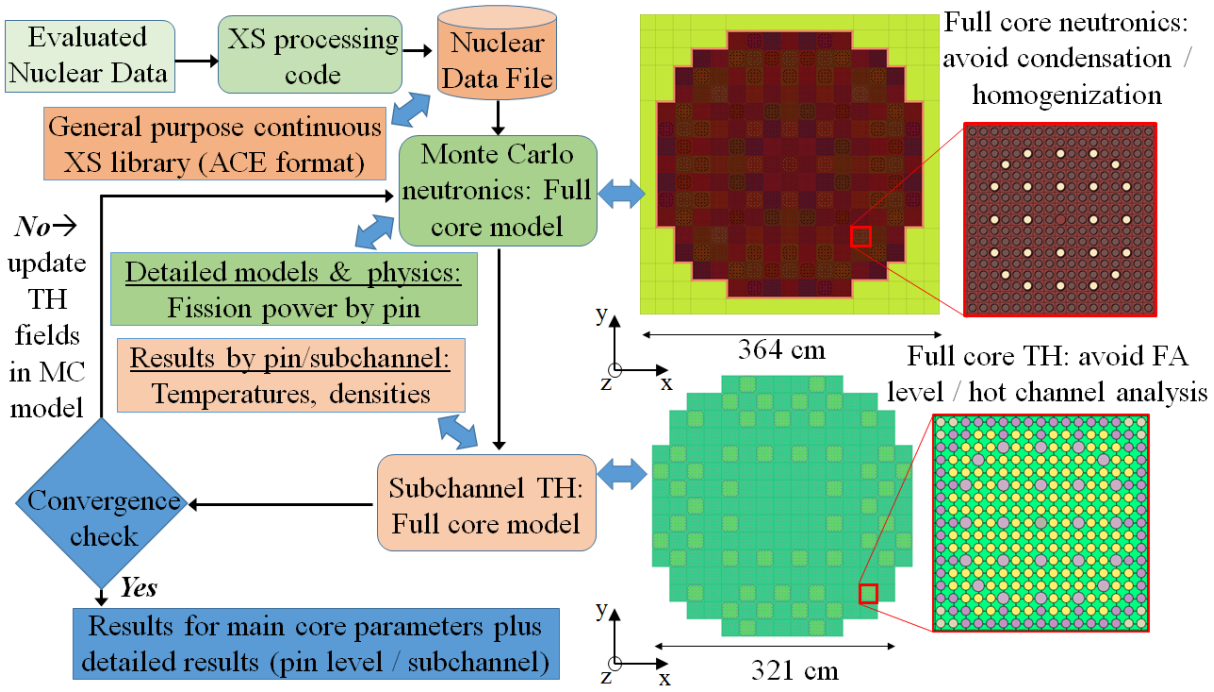

Figure 3.1: Proposed MC-based plus subchannel TH calculation line.

As shown in Fig. 3.1, this proposed scheme uses continuous nuclear data (in ACE format, non-problem dependent (Santamarina et al., 2009)) to develop a full-core MC neutronic modeling of

the reactor, where the level of detail for materials remains at pin and subchannel levels for the fuel rods and the coolant. This pin-wise (and subchannel-wise for the coolant) information is interchanged with a subchannel TH code. The MC code provides the pin-wise powers, whereas the subchannel TH code uses them to solve the TH problem and then provide the resulting temperatures and densities. It is clear that the *homogenization* and *condensation* steps in the neutronic calculation are completely avoided and no power reconstruction is required at the expense of increasing the complexity of the modeling and its computational requirements.

3.1 The proposed MC neutronic code

The Serpent 2 MC code is taken to deal with the neutronic side of the coupled problem. It is a multi-purpose 3D continuous-energy Monte Carlo transport code, developed since 2004 at VTT Technical Research center of Finland Ltd. (Leppänen et al., 2015). It is capable to perform static, burnup and transient 3D calculations using standard ACE format NDL. It can handle diverse geometry definition alternatives, including the 3D constructive solid geometry model and unstructured mesh geometries, giving enough flexibility to model almost all reactor geometries. Besides, it provides an user-oriented input definition, that allows to define universe-based geometries in a flexible manner with the aid of predefined surfaces and lattice structures (e.q. hexagonal and square arrays). Different neutronic boundary conditions are accepted for the external limits of the model, such as *reflective* (i.e. the particle is reflected), *periodic* (i.e. the particle is moved to the opposite surface) or *black* (i.e. the particle is killed), allowing infinite lattice configurations for 2D and 3D. Massive parallelization of the code is allowed, where the possibility to manage a hybrid compilation considering OMP (*Open Multi-Processing*, a shared memory multiprocessing programming interface) plus MPI (Message Passing Interface, a communications protocol for parallel architectures without shared memory) makes it specially suited for its use in HPC architectures, commonly composed by several calculation nodes (each of them with multiple processors).

Regarding the particle transport, Serpent handles a combination of the conventional surface-tracking (i.e. a particle is tracked as in Eq. 2.19 until reaches a surface) and the so-called *Woodcock delta-tracking method* (Leppänen et al., 2020). The concept behind this second method is to use *virtual collisions*, i.e. interactions in which the neutron is not absorbed and both the incident energy and the direction of flight are preserved. If an appropriate virtual collision cross section is added to each material in such a way that the modified total cross section has the same value in all materials, the result is that the total interaction probability is the same for all materials. This modified cross section, termed as *majorant* (Σ_m) is defined for the whole system depending on the neutron energy. The tracking procedure is then reduced to the sample of the free path length as in Eq. 2.19, but using this *majorant* cross section, to then move the particle to the tentative collision site and define if the collision is either real or virtual (just using the ratio of Σ_t to Σ_m). This approach constitutes a rejection technique, since some of these events will be rejected (Leppänen, 2007). This *Woodcock delta-tracking method* considerably simplifies the geometry routines and speed-up the calculation in complicated geometries, thus providing a major advantage over other MC codes in terms of computational efficiency. The major draw-

back arises from the undersampling of small zones in the geometry with high absorption cross sections. For such purpose Serpent develops a combination of these two techniques to balance the computational performance maintaining a good statistical behavior.

To handle material temperatures, Serpent includes the on-the-fly temperature treatment termed as *target motion sampling - TMS* routine, (Viitanen and Leppänen, 2014), which tackles the Doppler resonance broadening (see Fig. 2.9) just taking into account the thermal motion of target nuclei explicitly. To do this a coordinate transformation is made considering the nuclei target at rest frame before handling the collision physics. Besides, to handle the neutron thermal scattering cross section dependence for low neutron energies (i.e. the $S(\alpha, \beta)$ information), interpolation between tabular data is allowed also on-the-fly. Besides, these methods can be also combined with the rejection techniques described above to handle variations in materials density (Leppänen, 2013b), which makes the code specially suited for multi-physics coupling. These capabilities to handle the temperatures and density in the materials can be easily applied with the use of a nested array of meshes that superimposes the values for the TH fields on the geometry model. These meshes, define a set of interfaces aimed for multi-physics couplings (termed as IFC (Valtavirta, 2017)), where densities and temperatures are inputs and the power constitutes the output.

Within *criticality* calculations, Serpent provides weighted point kinetic parameters (see Eq. 2.11) through diverse techniques available within MC neutronics, such as *Iterated Fission Probability* method - IFP (Leppänen et al., 2014, 2020), which allows to count with realistic values for key parameters that govern transient behavior of the reactor configuration modeled (e.g. β_{eff} or Λ_{eff}).

Finally, for *transient* calculations, Serpent develops a traditional two-step approach, where the consideration of *delayed* neutrons has been recently implemented using the approach described in Section 2.4.5. To handle modifications in the geometry with time, Serpent allows to develop time-dependent *transformations* (i.e. linear transforms) over portions of the geometry (e.g. transformations at constant velocity or acceleration or combination of them), which permits the easy modeling of standard LWR *transient* scenarios such as control rod movements.

3.2 The proposed subchannel TH code

The SUBCHANFLOW code (Imke and Sanchez, 2012; Imke, 2019), named here as *SCF*, is considered for the TH side of Fig. 3.1. It is a versatile subchannel-level TH code suited for steady-state and transient calculations, developed at KIT, extensively validated for LWR. *SCF* solves the problem stated in Section 2.6.1 for a mixture of two-phase flow (see eqs. 2.34 to 2.39), using four conservation equations. The basic flow variables such as the axial and lateral flow rates, the pressure, the enthalpies, and the void fractions are calculated in each time step axially layer by layer, where the momentum conservation is used in the mass conservation equation to solve the axial pressure gradients. From the enthalpy of each axial cell, the steam quality and volume fraction are obtained using correlations to compute the coolant density, repeating the

procedure during each time step up to convergence is reached. For steady-state calculations, the time step is set to a very large value (see eqs. 2.34 to 2.39). Regarding the heat conduction problem within the fuel rods, they are divided into a number of radial rings to solve the heat conduction equation in radial direction by a finite volume method.

In *SCF* the geometry is defined as a set of channels and rods with given hydraulic parameters and interfacial areas (i.e. connectivities) without assuming a particular geometry type such as square or hexagonal lattices. Besides several correlations are available for the critical heat flux, the subcooled boiling, the single and two-phase friction, single-phase heat transfer. *SCF* also provides safety-related parameters as standard output, such as the departure of nuclear boiling ratio (*DNBR*), the cladding temperatures, the central fuel temperatures and the fuel enthalpy increase, among others. To enhance the geometrical model development, a preprocessor is available, which allows to build inputs for PWR and VVER geometries through a high-level definition of lattices and geometry aspects (García et al., 2019b), facilitating the accurate full-core modeling of LWR at subchannel level.

SCF is regularly updated to enhance its capabilities and facilitate its coupling with other calculation codes. Recently, the management of its main calculation routines (i.e. *steady-state* and *transient* cases) is allowed to be controlled by a series of *high-level - C Programming Language* functions interface (García et al., 2019b,a). These series of functions permit to use *SCF* as an external (precompiled) library, to exchange all the data necessary for coupled calculations and switch from *steady-state* to *transient* calculations . All these capabilities make *SCF* specially suited for the coupling approach proposed in Fig. 3.1,

3.3 Coupling approach for *Serpent-SCF*

The coupling of Serpent and *SCF* was analyzed as proof-of-concept in previous works for *steady-state* calculations, showing its aptness for such approach (Daeubler et al., 2015a). Besides, preliminary studies were performed to assess the capability of the codes to handle the expected level of accuracy for *steady-state*, *burnup* and *transient* calculations within realistic LWR geometries and operational configurations. The main outcome of these analyses demonstrated that these codes are suited to tackle the stated goals likewise the coupling scheme (see Section 2.7.1) behaves stable, but also spotted some constrains, where details can be gathered in the Appendix sections A and B.3.

Here a versatile implementation of this N-TH coupling is developed, where features such as the flexibility and suitability for use within high performance computing architectures (HPC) are observed. To develop a neutronic-TH coupling, several work paths are feasible. These options can be generalized as *external-coupling*, *master-slave* or *object-oriented*, whose main aspects are summarized in Table 2, where it should be noted that several hybrid-approaches are also found.

During the investigation of this N-TH scheme, calculations and implementations have been done between Serpent and *SCF* using the three approaches presented in Table 2. Coupled

Approach / Parameter	**External coupling**	**Master-slave**	**Object-Oriented**
Main aspects	· Both codes are executed by an external script (e.g. Python). · Interchange of fields with standard output files (generally ASCII). · Coupled flow control using semaphores.	· Codes are integrated in a single tool. · Interchange of fields internally by memory. · Coupled flow control managed by master code.	· Codes are modularized · Interchange of fields internally by memory. · Coupled flow control managed by top-level supervisor.
Main advantages	· Easy to implement and test. · No source code required. · Portability. · Codes are not modified.	· Take advantage of internal memory structures. · Only slight modifications to main codes flow. · Easy to build a portable executable. · Easy to run, even in HPC environments. · No external ASCII files are required to manage field interchange. · Geometrical versatility (up to code limitations). · Inherent capabilities of codes easily maintained.	· Take advantage of internal memory structures. · Easy to incorporate several codes to the coupling. · Changes in the coupling flow managed by the supervisor. · No external ASCII files are required to manage field interchanges. · Geometrical versatility (up to code limitations).
Main disadvantages	· Limited capabilities due to external flow control. · Managing big coupling files limits HPC applications. · Geometrical versatility is limited to standard output available.	· Source codes are required. · The "open doors" for slave need to be foreseen in master. · Coupling flow options are fixed.	· Source codes are required. · Several modifications to codes due to the modularization process. · External libraries are required to manage the code interactions. · Not easily portable.

Table 2: Main aspects for alternatives to develop a Serpent-SCF coupling scheme

calculations by means of *external-coupling* can be found in the Appendix A and examples of *object-oriented* can be gathered in (García et al., 2019a, 2020a,c). Here, the *master-slave* approach is selected as implementation scheme. The main justification for this decision is that *transient* calculations are the main focus and by this potential overheads and in-depth modularization of the MC code shall be avoided, likewise it is possible to take advantage of the standard codes calculation flows. Nevertheless, the main insights from the analysis developed using *external-coupling* likewise features from the *object-oriented* approach are here intensively used for the *master-slave* scheme, as described in the following sections.

3.4 The master-slave *Serpent-SCF* coupling

A new master-slave coupling approach between Serpent v.2.1.31 (as master) and *SCF* v.3.6.1 (as slave) is implemented. This tool is written from scratch into an embedded code that is here briefly described. Within this implementation all capabilities from Serpent and *SCF* are maintained, where aspects such as *easy-to-compile* and *user-friendly* are specially considered (i.e. simple problems should be reflected in simple inputs for the user). The code calculation flow for Serpent and *SCF* has not been altered, where all the interaction is managed by *high-level* functions, as explained in the following sections.

3.4.1 Main implementation aspects

The coupling approach relies in the extensive use of features available in both codes, which are used as starting point for this development (Ferraro et al., 2020c). The most relevant aspects to be mentioned are:

- The capability of Serpent to efficiently handle variable material densities fields within the geometry (Leppänen, 2013b).
- The capability of Serpent to internally manage variable temperature fields (i.e. (Viitanen and Leppänen, 2014) plus the interpolation of $S(\alpha, \beta)$ data).
- The availability of diverse options for the multi-physics Interface Files (IFC) suitable to tackle LWR geometries. This superimposed nested meshes permit handle both the square and hexagonal geometries of the LWR considered in this work. Besides, the way these data is internally stored can be rearranged through external mapping files.
- The capability of *SCF* to deal with *steady-state* and *transient* calculations, whereas the time advance and the TH fields interchange can be done handled directly by the *high-level - C Programming Language* functions interface as an external library (García et al., 2019b,a).
- The Serpent code calculation flow, which foresees the updating of the TH fields for *steady-state*, *burnup* and *transient* calculations through the processing of the IFC files (Valtavirta, 2017).

As a result, the coupling scheme is developed in *C Programming Language*, as for the Serpent code (i.e. master). For such purpose a series of simple, robust and small functions are considered for the coupling tasks, putting an effort in the commenting and main readability, in view of potential further improvements. Aspects such as the initialization, the correct definition of coupling parameters and values (i.e. sanity checks), the convergence calculation analysis, the interchange of fields, the relaxation of interchanged fields are tackled by these coupling routines, etc. are clearly separated from both codes routines. The implementation is conceptually shown in Fig. 3.2, where it can be seen that the codes interact through these specific *high-level* routines defined for such purpose.

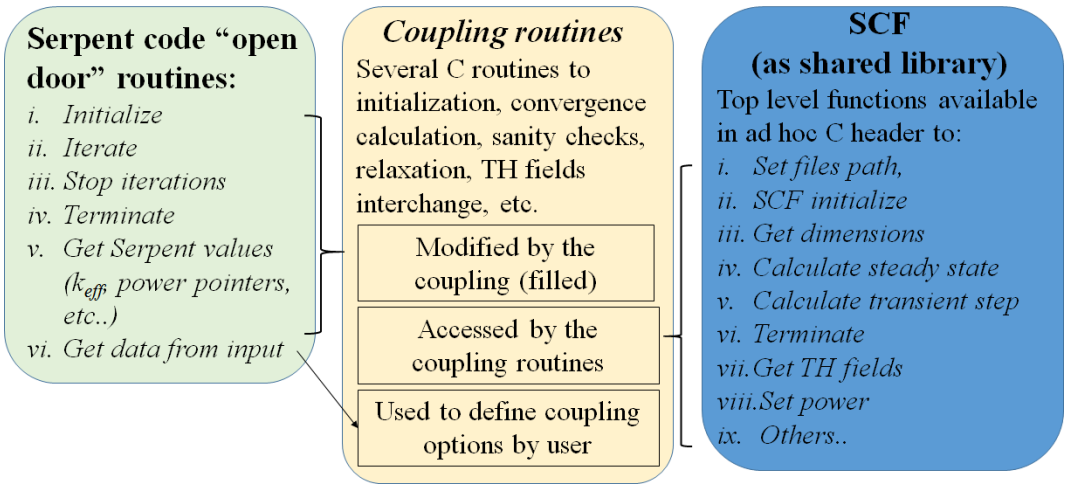

Figure 3.2: Schematic implementation of the new internal coupling approach.

This scheme is possible since both Serpent and *SCF* codes count with the appropriate capability. Serpent offers a series of *open door* functions, which allows to manage all main aspects of a coupled scheme within the code flow (such as detect a coupling request in user input, initialize, iterate, terminate, deallocate, etc.). For its part, the *SCF* code is compiled as a shared library. Linking these two sides, the developed routines can handle the interaction between the codes and provide all the coupling options to be available. As a result, both codes are independently maintainable and can be updated with further codes releases (as far as these *high-level* interfaces are maintained). Furthermore, no restrictions to the inherent capabilities are imposed to any code.

3.4.2 The time dependence handling within the coupling

The implementation maintains the code flow from Serpent, where the coupling routines identified in Fig. 3.2 handle the *TH* calculation selecting the correspondent *SCF high-level* function to be accessed (i.e *steady-state* or *transient*), depending on the type of case to be run. This is schematically depicted in Fig. 3.3, where details of the algorithm can be gathered in the Appendix B.

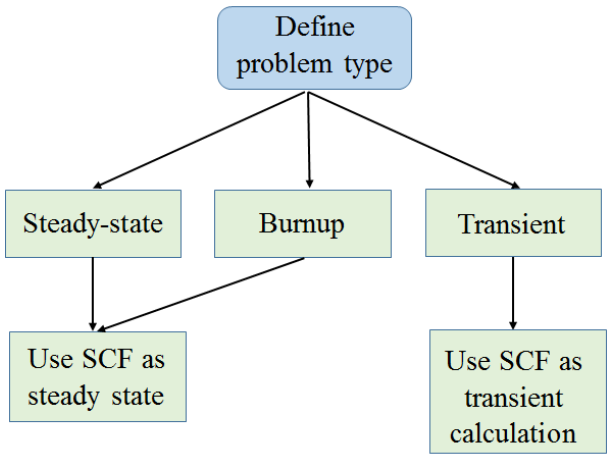

Figure 3.3: Scheme of the options available in the developed master-slave coupling.

Each neutronic-TH iteration in the coupled code is a typical implementation of the Picard scheme (see Eq. 2.42), where successive neutronic and TH calculations are applied (i.e. operator spitting is considered) using a defined convergence scheme and a relaxation of the interchanged fields (defined by the user as an average of the fields in the iteration n and $n+1$), as depicted in Fig. 3.4.

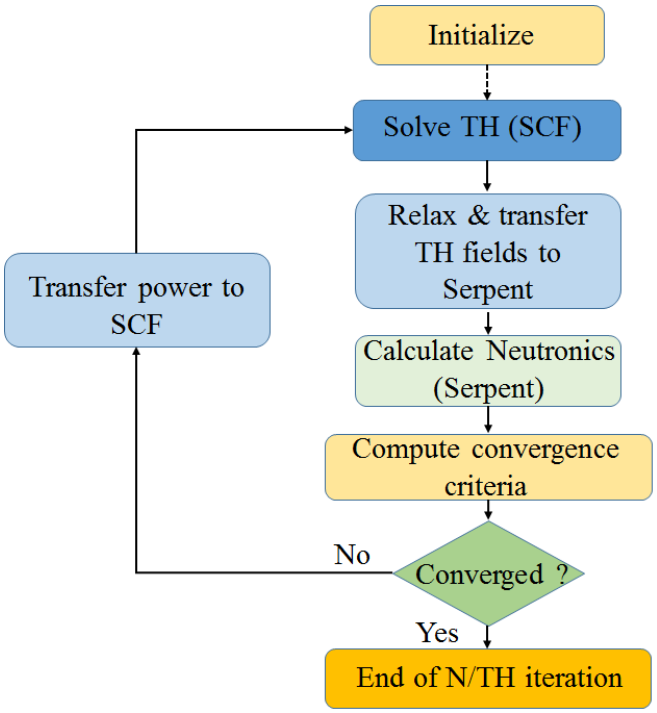

Figure 3.4: Schematic Picard iteration scheme.

This scheme in Fig. 3.4 can be turned into a fully-explicit one in time if the convergence criteria is fully avoided. Conversely, it should be regarded that an additional iteration is applied by Serpent when dealing with *burnup* calculations, depending on the scheme selected to solve the Bateman problem described in Eq. 2.7, where additional iterations arise between two successive burnup steps. This process is schematically described in Fig. 3.5, where Serpent code flow for burnup schemes applies (Leppänen et al., 2020), whereas the *SCF* calculations corresponds to a series of *steady-state* ones.

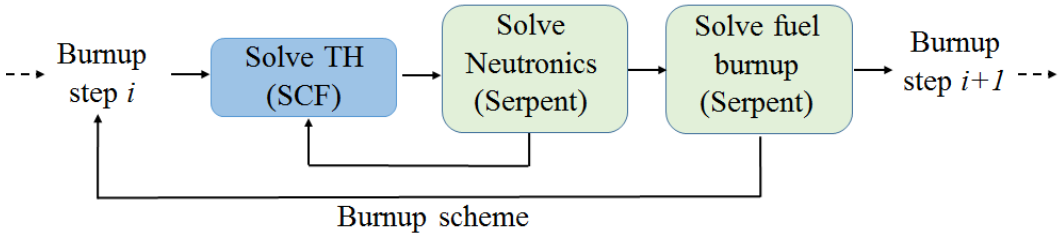

Figure 3.5: Scheme of the code flow for burnup calculations in the developed master-slave coupling.

If *transient* calculations are selected, an explicit coupling is applied, as depicted in Fig. 3.6, where a *transient* calculation is considered for *SCF* (see Fig. 3.3). The advance in time is controlled by Serpent which demands *SCF* to evolve the time variable from a time step i to

$i + 1$, whereas intermediate calculation steps are allowed inside *SCF* for numerical stability. The update of TH fields provided by *SCF* is considered after each time step, which is handled internally in Serpent as an adjustment of cross sections due to density and temperature fields through the IFC defined by the user for the coolant and fuel. Both the IFC containing the temperatures and densities at the beginning and end of interval are internally stored. Finally, a linear interpolation between the two fields with respect to time is done to obtain the actual temperature and density at the interaction moment.

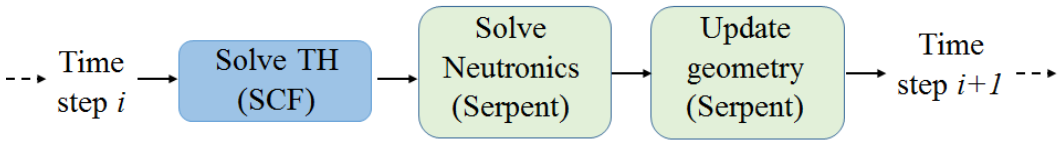

Figure 3.6: Scheme of the code flow for transient calculations master-slave coupling.

3.4.3 The TH field exchange

To exchange the TH fields between Serpent and SCF, the IFC structures from Serpent are connected to the correspondent subchannels and pins in *SCF*, as schematically shown in Fig. 3.7 for a square lattice array. These superimposed meshes can also handle diverse geometrical configurations into a nested scheme, allowing to easily deal with square and hexagonal lattice structures from PWR and VVER. The TH fields from *SCF* are mapped to these IFC as a combination of subchannel and pin average variables, where the possibility of rearrangement of fields through a mapping file is also offered. Besides, to map the power from Serpent to *SCF*, the fission power output from the IFC arrays is linked to the correspondent array in *SCF* through the the *high-level* functions that allows to set the power by node.

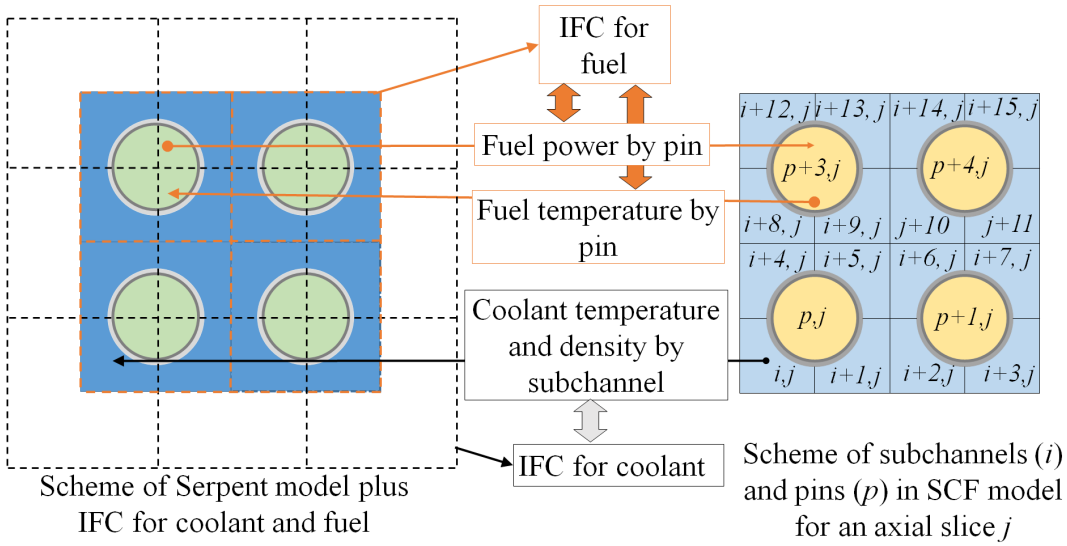

Figure 3.7: Scheme of the variables interchange within the code coupling. Example for square geometry.

The mapping of fields between Serpent and *SCF* is done through the direct copy of pointers from code to code (namely from/to the IFC values in Serpent and the channels and rods arrays in SCF). All these fields are stored in RAM (Random Access Memory, i.e. they are not dumped

into files), which ensures a fast interchange suitable for HPC applications. Several options are available for the user:

- Transfer *SCF* fields to Serpent arrays using the values averaged at rod in *SCF* (for coolant and fuel): This option can be used if Serpent model considers a fuel-centered IFC that agrees with *SCF* (namely square lattices) and the indexing are coherent.
- Transfer *SCF* fields into Serpent arrays using the values averaged at channel in *SCF* (for coolant, for fuel the values are still averaged at rod): This option can be used if Serpent model considers a coolant-centered IFC that agrees with *SCF* (namely square lattices) and the indexing are coherent.
- Transfer *SCF* fields to/from Serpent with a rearrangement of arrays by the use of an external mapping file (provided by user): This is a general option that by the aim of an external file rearranges the Serpent vectors (power and IFC), where this mapping indicates which IFC bin maps to which *SCF* node.

With the options listed above, all potential models can be mapped from code to code. Regarding the mapping aspects, the canonical case is the one where no remapping is required (i.e. the *SCF* and Serpent models are indexed with the same convention), while the more complicated one corresponds to the case where the mapping cannot be easily developed. For this second case, the capabilities from *SCF* preprocessor are used, which provides these mapping files (García et al., 2019a,b). As a result this *Serpent-SCF* can handle a wide range of geometries that cover the required models for the LWR analysis, namely:

- Single pins models.
- FA square arrays of pins, with and without inter FA gaps.
- FA hexagonal arrays of pins, with and without inter FA gaps.
- Core arrays of FA (at pin level) - using nested square lattices.
- Core arrays of FA (at pin level) - using nested hexagonal lattices.
- Abstract models: as far as the mapping is correct, no limitation between models are imposed, so the models can represent abstract geometric configurations.

3.4.4 The coupling options available

Regarding the feedback of fuel temperatures from SCF, several options are available, where a detailed description is provided in the Appendix B. To manage the fuel temperature, a volume average within the pin or a *Doppler* weighted average can be selected. This second case defines a temperature for the feedback as:

$$T_{fuel}^{doppler} = \alpha T_{fuel}^{surface} + (1.0 - \alpha) T_{fuel}^{center}; \tag{3.1}$$

where $T_{fuel}^{doppler}$ is the temperature used by Serpent, $T_{fuel}^{surface}$ and T_{fuel}^{center} are the temperatures calculated by *SCF* for the fuel pellet centerline and surface and α is a value defined by user.

The main physical background to consider these options relies in the fact that the Doppler temperature effect (see Fig. 2.9) in a LWR is driven by the absorption in ^{238}U, which has a considerable spatial self-shielding, thus mostly occurs near the surface of the fuel pin, where the temperatures are lower than in the centerline. As a consequence, these weighted averages try to capture the fact that most of this absorption occurs at a temperature closer to the pellet surface than to the pin centerline one (Goltsev et al., 2000). Several options can be used, such as $\alpha = 0.7$ or $\alpha = 5/9$ (i.e. the Rowlands approach (de Kruijf and Janssen, 1996)), where its accuracy depends on the case analyzed (Grandi et al., 2010). In addition, it should be noted that the extension to direct coupling of radial description of this temperatures is straightforward, which can be handled directly by the remapping capabilities.

Regarding convergence criteria both L_2 and L_∞ norms are available for the fuel and coolant as user options, as shown in eqs. 3.2 and 3.3, using the fuel temperature as example.

$$\epsilon^{L_2}_{T_{fuel}} = \frac{\sqrt{\sum_{i,j,k}(T^t_{fuel}[i,j,k] - T^{t-1}_{fuel}[i,j,k])^2}}{\sqrt{ijk}}; \tag{3.2}$$

$$\epsilon^{L_\infty}_{T_{fuel}} = \max_{i,j,k}\{\mid T^t_{fuel}[i,j,k] - T^{t-1}_{fuel}[i,j,k] \mid\}; \tag{3.3}$$

where t identifies the iteration step, i, j, k identifies the position and ϵ is the scalar to converge. The same criteria is applied for the coolant temperature and density fields, while the reactivity convergence is just obtained as the reactivity difference between two successive steps.

The option to relax the TH fields is also available for a user-given relaxation factor to improve the convergence when necessary (Gill et al., 2017), as shown in Eq. 3.4:

$$\tilde{T}^t[i,j,k] = T^{t-1}[i,j,k]\omega + (1-\omega)T^t[i,j,k]; \tag{3.4}$$

where $T[i,j,k]$ is the TH field (namely T_{fuel}, T_{cool} and ρ_{cool}) and ω is a value between 0 and 1. These relaxation schemes are commonly used to ensure the convergence of the Picard iteration. The potential instabilities for such fixed-point mapping are well understood, being the primary mechanism the physical relation between the power and the fuel temperatures (Gill et al., 2017). For LWR, large peaks in the power from neutronic solution result in large temperature peaks in the TH side, which produce subsequent local increase in neutron absorption through the Doppler effect, resulting into a local depression in flux. The simplest technique to prevent this type of undesired behavior is to relax the TH fields, where commonly $\omega = 0.5$ is applied.

3.5 Specific aspects of *transient* coupled calculations

The two-step process described in Section 2.4.5 remains as a mandatory path for *transients*. But when dealing with coupled *steady-state* calculations, a slight modification is compulsory. This is due to the fact that not only the initial sources (both for the *live* neutrons and precursors) have to be obtained through a coupled calculation, but also the initial *SCF* calculation must be started from the converged power distribution. As a result, the two step approach is modified

as depicted in Figure 3.8 for this coupled case.

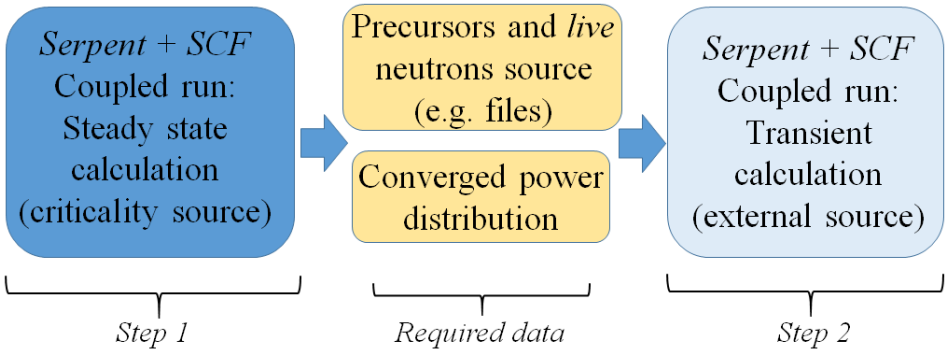

Figure 3.8: Transient two–step approach for coupled calculations for Serpent-SCF.

To obtain these initial distributions for *live* neutrons and delayed neutron precursors, a *steady-state* coupled criticality source simulation is first executed and once a critical configuration is reached, the distributions are recorded into dedicated files (Leppänen et al., 2020). The second step (i.e. the *transient* simulation itself) is then started by setting up the initial *live* neutron and delayed neutron precursor distributions using the corresponding options.

Finally, the time dependent geometry transformations available in Serpent standalone can be used (Leppänen et al., 2020). As an example, RIA-kind scenarios driven by the withdrawal of control rod can be modeled, defining the movement of this portion of the geometry in the Serpent model.

3.6 Final comments on the implementation approach

The consistency check of the developed internal master-slave coupling is included in Appendix sections A and B.2 for PWR and VVER geometries. The following steps to tackle the stated goals are to develop a verification and validation for *burnup* and *transient* calculations, described in the following chapters.

"All code is guilty, until proven innocent."

— Software testing precept

4 Verification of the approach for *steady-state* and *burnup* coupled calculations

All Serpent capabilities regarding *burnup* calculations are within this *master-slave* coupling available, where the handling of the neutronic-TH iterations is done as well as the solution of the isotopes evolution problem (see Eq. 2.8 and Fig. 3.5). This Chapter is devoted to the verification of this approach for *steady-state* and *burnup*, a mandatory step prior to the consideration of *transient* calculations. It has to be regarded that the capabilities to develop *burnup* calculations is key regarding industry-like applications of the approach. This statement arises from the fact that several safety-related analysis for LWR are developed departing from burned cores (commonly calculated at end of cycle, EOC), since the associated kinetic parameters lead to more severe scenarios due to the presence of ^{239}Pu. Despite inherent tools constraints have to be tackled to be able to provide such a complete approach (i.e. full-core scope neutronic-TH coupled burnup plus a transient calculation), this Chapter shows the viability of such path.

4.1 Dealing with full-scope *burnup* problems

This Chapter tackles the verification process through the development of selected benchmarks that allow to assess the consistency of the coupling and its features, namely:

- The capability to reproduce neutronic-TH coupled *burnup* results, using pin-by-pin calculations with TH feedback.
- The capability to develop a full core pin-by-pin TH feedback for a LWR, including a simplified burnable materials management.

In view of Serpent computational constraints when dealing with a high number of zones where the isotopes evolution problem has to be solved (see Appendix Section B.3), a full-core *burnup* calculation within a LWR core requires the application of the so-called Domain Decomposition Techniques (García et al., 2018). The implementation and testing of such technique is beyond the scope of this work, thus only a simplified scheme is considered for the full-core calculations, while the fully-detailed burnup (i.e. considering a detailed subdivision of fuel zones) is developed considering a radially-reflected 3D FA model.

4.2 Pin-by-pin burnup calculations for a radially-reflected FA

As a first step, the pin-by-pin coupling including burnup is assessed for a single 3D radially-reflected FA case. For such purpose, coupled burnup calculations for two VVER-type FA are developed and compared with results reported in open publications (Bikeev et al., 2017; Aleshin et al., 2015). These reference results provide the system reactivity evolution within a typical

burnup scope in VVER reactors. Consequently, this global comparison allows to verify the implementation of the scheme when burnup capabilities are used. Besides, in view of the stated objectives, analysis of the obtained pin-by-pin results are also developed.

The reference results correspond to a MC neutronic calculation (i.e MCU code (Bikeev et al., 2017)), which is coupled to diverse TH modules to handle both the conduction and convection problems (namely the *TPA* code to model the coolant side and a fuel pin behavior code named TOPRA-s code (Aleshin et al., 2015)). In this approach, the feedback of the coolant density and the coolant temperature is approximated at a FA level model, partitioned into 30 equidistant layers along the axial length. Besides, the feedback on the fuel temperature is directly taken from the fuel pin behavior code. As a result, the coolant temperature and density, the fuel temperature, and equilibrium concentration of xenon in each height layer are determined for the whole burnup scope.

Two cases are considered in this comparison, both using enriched UO_2 pins, where the main difference is the presence of a burnable poison within the fuel rods (in the form of Er oxide mixed with the UO_2). These are identified as *U-Er* and *U* for the design with and without poison, both representing cases without control rod (CR) inserted. The main geometrical data and TH characteristics are reproduced in Table 28 and Table 29 in Appendix Section D.3. The geometrical setup for Serpent is depicted in Fig. 4.1 for the *U* fuel case as an example.

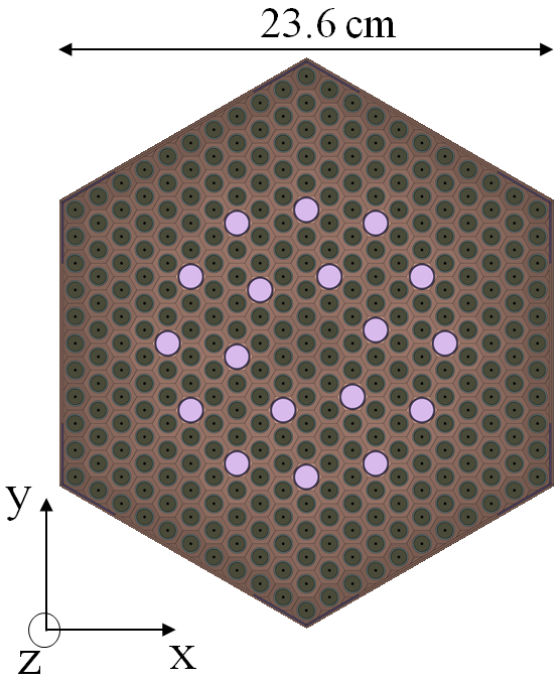

(a) Plot of the Serpent model for U-Er, xy cut at z=0cm, where (x,y,z)=(0,0,0) corresponds to the center of the FA and AL. Model is reflected in the faces of the hexagon. Guide tubes (GT) in pink.

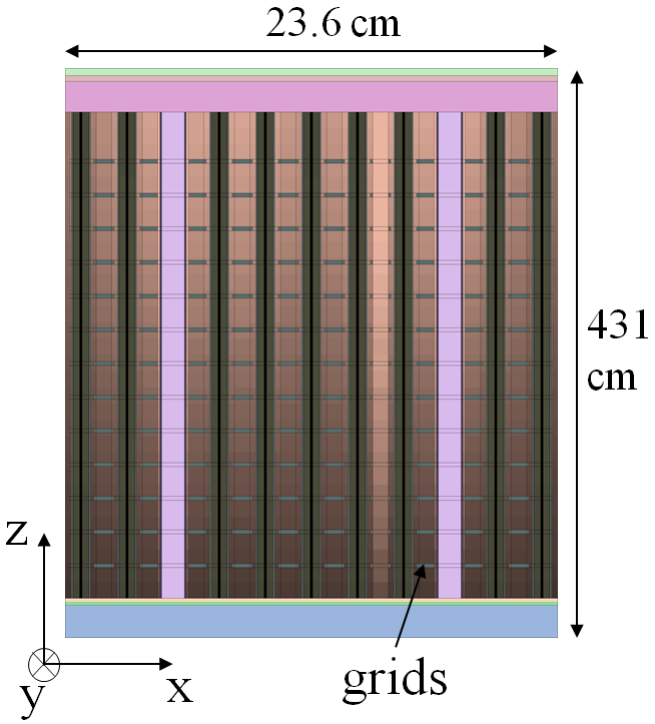

(b) Plot of the Serpent model for U-Er, xz cut at y=0 cm, where (x,y,z)=(0,0,0) corresponds to the center of the FA and AL. Top and bottom surfaces are black boundaries. Not at scale.

Figure 4.1: Plots for the Serpent geometrical model developed for radially-reflected U VVER FA.

This neutronic model in Serpent includes guide tubes (GT) and details such as stiffeners and grid spacers, where generic values are used in case of an incomplete specification. Besides, reflected boundary conditions are set for the radial dimensions, while for the bottom and top zones an homogenized composition has been included as reflector, followed by black boundary conditions, as shown in Fig. 4.1b. For both cases, the JEFF3.1.1 NDL is considered (Santamarina et al., 2009). Besides, the *burnup* calculation is developed with equilibrium xenon calculation to avoid burnup instabilities (Ferraro et al., 2018; Leppänen and Isotalo, 2012). To tackle the burnup of the fuel materials, a division of fuel zones by pin is considered, setting two radial zones for the *U-Er* model. These totaled $\sim 8.4e3$ and $\sim 1.7e4$ burnable zones for *U* and *U-Er* cases. Besides, a *Predictor-Corrector* scheme was selected to handle the burnup of such zones (Leppänen and Isotalo, 2012).

To handle the TH, a pin-wise model is considered in *SCF*, as shown in Fig. 4.2 for the *U* FA.

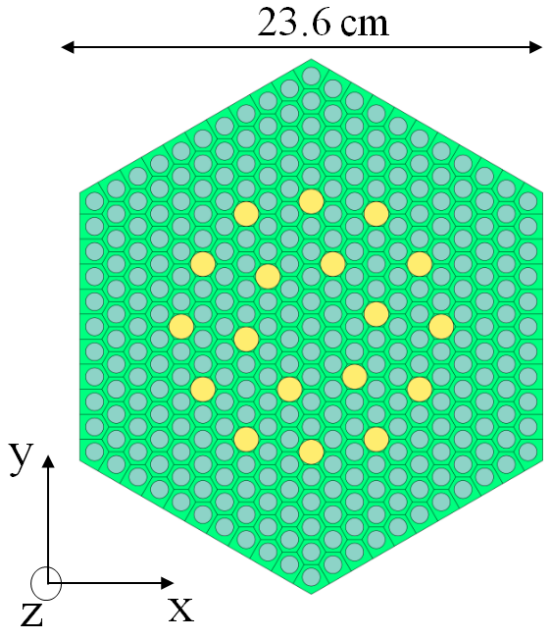

Figure 4.2: Plot of the SCF model for radially-reflected U VVER FA, xy cut at z=0 cm, where (x,y,z)=(0,0,0) corresponds to the center of the FA and AL.

The *SCF* model shown in the Fig. 4.2 represents a *fuel-centered* approach. To ensure the consistent behavior of the coupled problem, the convergence of the internal *SCF* iteration over temperature and density fields has been set to be at least two orders of magnitude below the neutronic-TH coupling convergence (e.g. 0.1 [K] for the fuel temperature). As for the reference case, 30 equidistant axial zones are considered, which is the same axial discretization considered within Serpent IFC files for both the coolant and fuel, where mapping files are considered to develop the one-to-one mapping of the TH fields to the nested hexagonal IFC (see Fig. 3.7).

Neutronic calculations in Serpent consider $2e3$ active cycles with $5e4$ particles each, thus totaling $1e8$ active histories per step, which allows to obtain a statistical convergence of ± 10 [*pcm*] per step. In accordance with these values, the convergence of reactivity between neutronic and TH iterations is set to ± 35 [*pcm*], which applies for each predictor and corrector *burnup step*,

together with a convergence goal for the TH of 10 $[K]$ and 2.5 $[K]$ for fuel and coolant temperatures respectively, while a 0.01 $[g/cm^3]$ was set for the maximum coolant density variation. Besides, a relaxation of TH fields is considered with $\omega = 0.5$ (see Eq. 3.4) to avoid convergence instabilities, while a volume average of fuel temperatures is considered within the fuel pins.

For this *Serpent-SCF* approach, the expected level of agreement for the reactivity comparison with the results reported is in the range of $\sim 500-1000$ $[pcm]$. There are several reasons for this statement, where the approximations on the physical phenomena and models and the NDL choice are the most relevant. The level of agreement for a reflected FA within neutronic calculation codes using the same physical approximations and NDL can be as good as ~ 100 $[pcm]$ if no TH feedback is considered (Wilderman et al., 2015), but for cases including TH coupling differences of $\sim 200-500$ $[pcm]$ can be found. There are many reasons for such differences, including the treatment of the feedbacks (see Appendix A) and the specific-calculation codes characteristics (Luo et al., 2017). On top of that, if different NDL are considered and *burnup* calculations are developed, differences up to ~ 1000 $[pcm]$ can be found (Loetsch et al., 2010), mainly arising from the impact of the fission product inventory (Ceresio, C. et al., 2012).

As a first step, the system multiplication factors k_{eff} reported in (Bikeev et al., 2017; Aleshin et al., 2015) (named as *MCU-TOPRA*) are compared with the obtained *Serpent-SCF* results in Fig. 4.3 for *U* and *U-Er* FA, including also the differences in terms of reactivity.

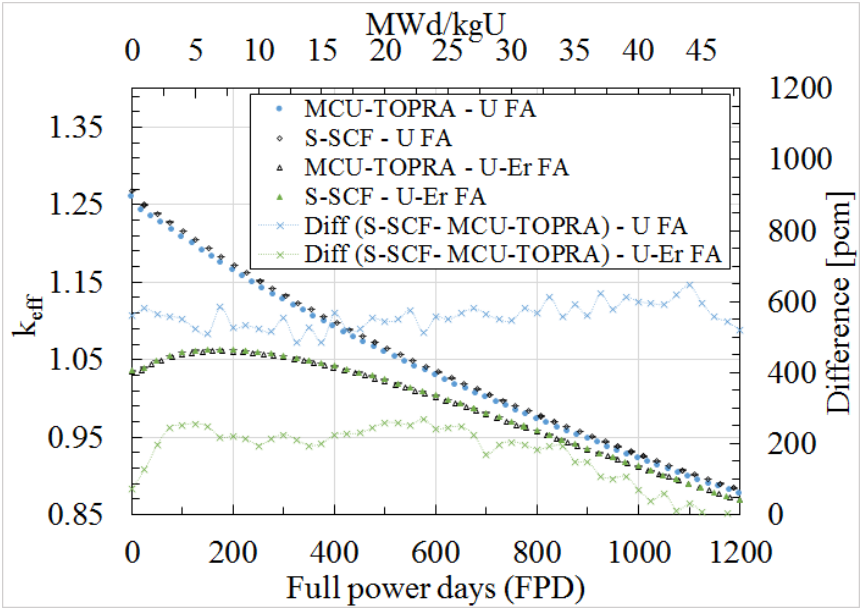

Figure 4.3: Comparison of effective multiplication factors for U and U-Er radially reflected fuels with reported values as a function of burnup.

In the Fig. 4.3, the fuel burnup for both cases is presented in terms of the accumulated energy released per kg of Uranium (i.e. $[\frac{MWd}{kgU}]$ and its equivalent days at nominal power (i.e. Full Power Days - FPD). The effect of the fuel burnup is appreciated, which generates a decrease of the reactivity due to the depletion of ^{235}U of the fuel. Besides, the impact of the burnable poison is also observable for the *U-Er* FA, which initially decreases the system reactivity due to additional non-fission absorptions in the *Er*. This BP is consumed after ~ 400 FPD, leading to a behavior

similar to the *U* FA, where the difference in reactivity is due to the lower Uranium content of the *U-Er* FA. The comparison of these results with the reported ones show a good agreement, where average differences below $\sim$ 600 pcm are observed for both cases. This represents a consistent result for reflected 3D FA calculations involving TH feedback and burnup with different codes and NDL. On top of that, the global behavior of the multiplication factor is consistent for the whole burnup scope for both cases, where the peak reactivity of the *U-Er* FA agrees with reported values, assessing that the burnup of the burnable poison is correctly reproduced and no instabilities arise.

The analysis of consistency of the coupled calculations is commonly restricted to the interchanged parameters between codes (i.e. the power, temperatures and densities). Nevertheless, for this case, the analysis of the neutron flux allows to depict the grounds of the key physical phenomena, which is common to all further analysis within this dissertation. Therefore, the thermal neutron flux is shown in Fig. 4.4 for the *U-Er* case in the first burnup step.

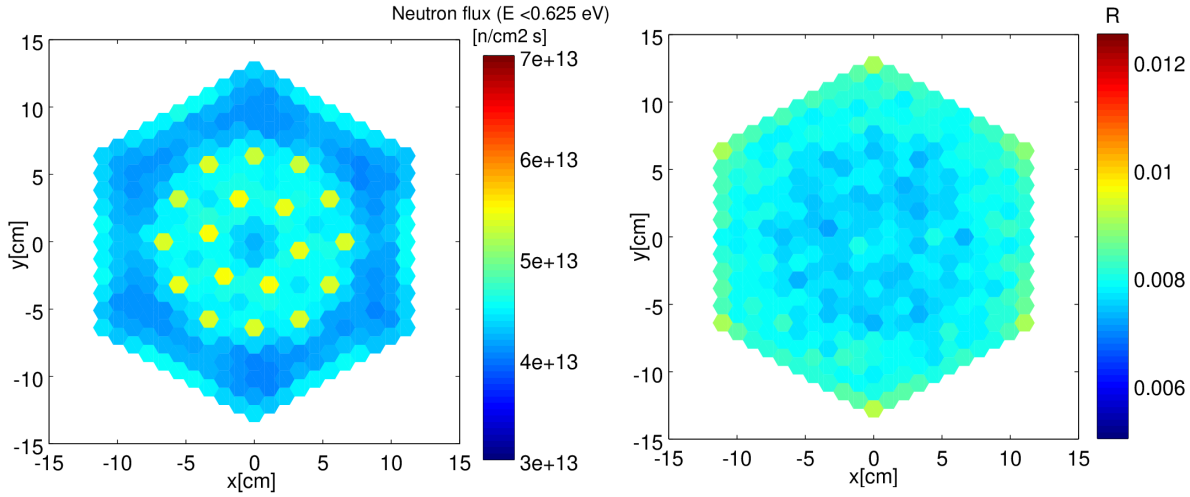

(a) Thermal neutron flux ($E < 0.625$ eV) in a 12 cm axial xy slice from $z = 0$ cm (center of AL) at 0 MWd/kgU.

(b) Relative statistical uncertainty in the thermal neutron flux ($E < 0.625$ eV) in a 12 cm axial xy slice from $z = 0$ cm (center of AL) at 0 MWd/kgU.

Figure 4.4: Calculated Serpent-SCF neutron flux for an axial slice of the radially-reflected U-Er FA model at 0 MWd/kgU.

The results for the thermal neutron flux in the Fig. 4.4a correspond to spatially-integrated values in an hexagonal mesh, where the FR heterogeneity is averaged to bear with a description equivalent to the fuel IFC. The effect of different components in the thermal neutron flux distribution can be appreciated, where higher values are observed in the inner zone. The water in the GT leads to an increase of moderation, seen as peaks of thermal flux in these positions, that affects also the sorrounding pins. This in turn causes higher fissions rate and thus higher power for such pins (the CR absorbers are in fact designed to produce an opposite effect when inserted). These spatial dependence also affects the statistical convergence depicted in the Fig. 4.4b, where lower flux values correlate with higher relative uncertainty since a lower amount of particles are interacting in those zones. But for both PWR and VVER the presence of FR that produce an excesive amount of power must be avoided. This is the physical ground for the heterogenous FA designs observed in LWR reactors, where diverse pins containing *burnable*

poisons are included, aimed both to flatten the power distribution and the global system excess reactivity. All this physical phenomena is explicitely modeled by *Serpent-SCF*, whereas this is only considered in the *cell-level* calculation step in the industry-standard approach. To observe the effect on the power distribution, pin-by-pin results are presented in Fig. 4.5.

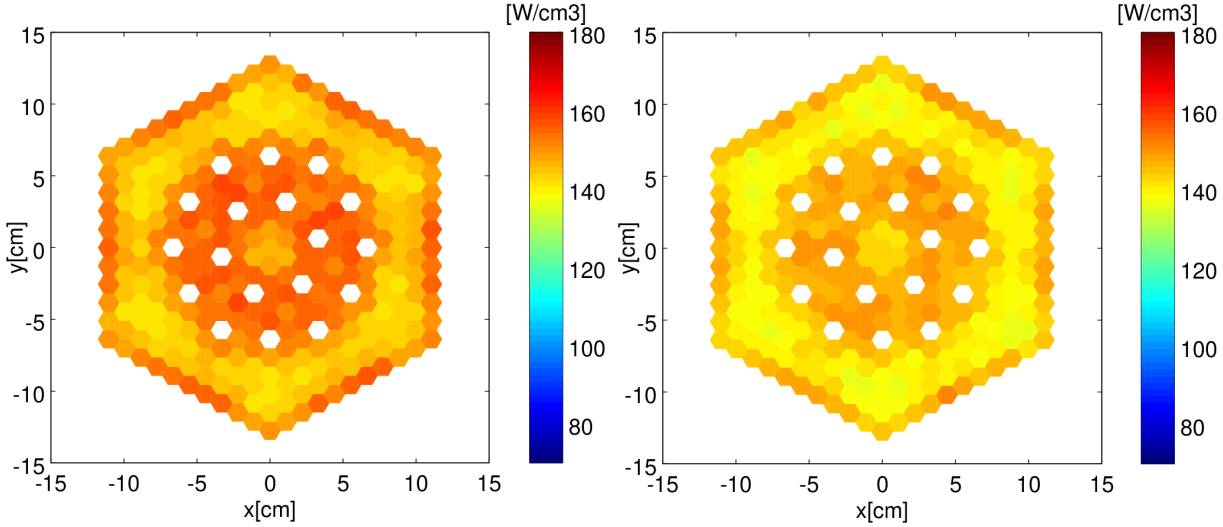

(a) Power density by pin in a 12 cm axial xy slice from z = 0 cm (center of AL) at 0 MWd/kgU.

(b) Power density by pin in a 12 cm axial xy slice from z = 0 cm (center of AL) at 11 MWd/kgU.

Figure 4.5: Calculated Serpent-SCF power for an axial slice of the radially-reflected U-Er FA model for two burnup steps. Statistical convergence is shown in Fig. 4.8.

The Fig. 4.5a shows the power density for initial burnup, where thermal neutron flux depicted in the Fig. 4.4a is reflected as an increase of power in the central zone. This power radial dependence is smoothed with the *burnup* of the system due to the increased fuel consumption in the central zone, as seen in 4.5b. The corresponding temperatures are depicted in Fig. 4.6.

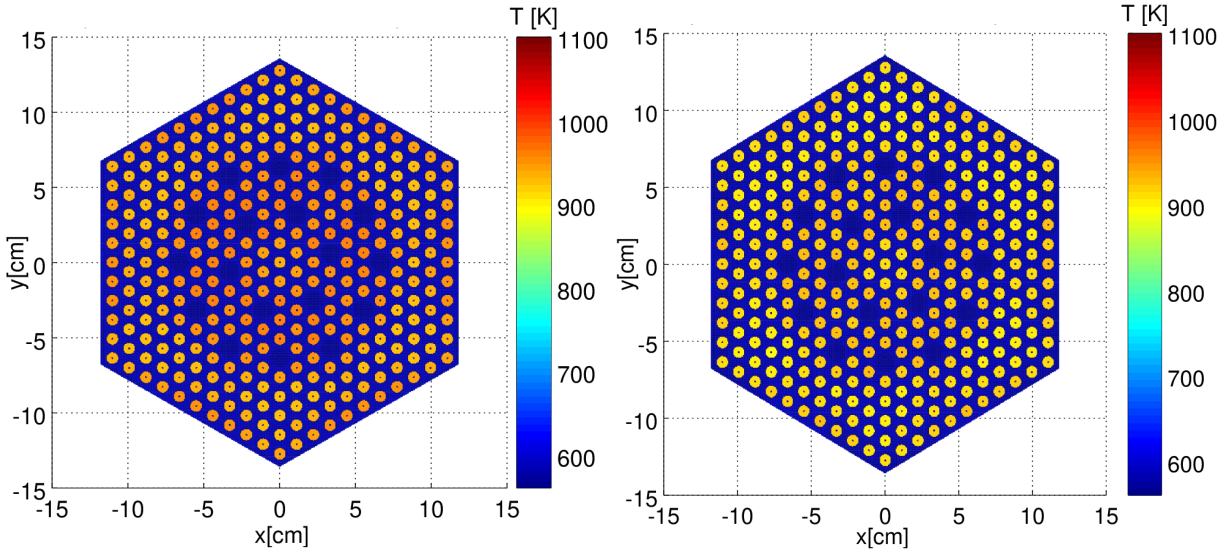

(a) Temperatures in a 20 cm xy slice from z = 0 cm (center of AL) at 0 MWd/kgU.

(b) Temperatures in a 20 cm xy slice from z = 0 cm (center of AL) at 11 MWd/kgU.

Figure 4.6: Calculated Serpent-SCF temperatures for an axial slice of the radially-reflected U-Er FA model for two burnup steps.

The Fig. 5.5 depicts the temperatures for an xy slice for the same burnup steps. The higher temperatures in the inner zone of the FA in Fig. 4.6a correspond to the power density of Fig. 4.5a, whereas the decrease in power density with burnup leads to lower temperatures in the Fig. 4.6b. Moreover, the axial power density is depicted in the Fig. 4.7.

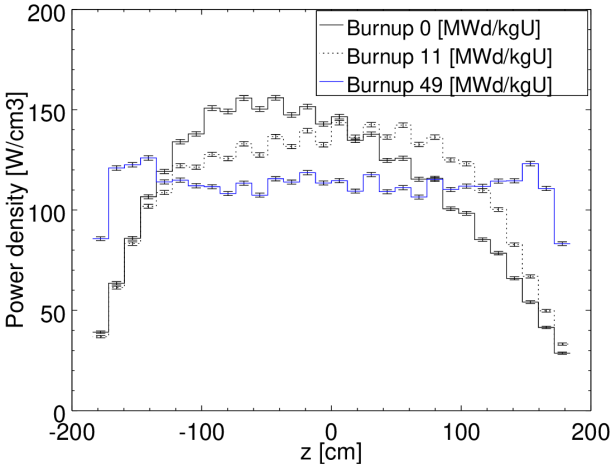

Figure 4.7: Serpent-SCF result for the axial power density as a function of burnup for the central pin in U-Er FA (x,y)=(0,0) [cm]. Error bars for statistical uncertainty at 1σ

The Fig. 4.7 shows the evolution of the axial power profile for the central pin for the *U-Er* FA within the burnup scope analyzed. The first think to notice is the effect of the ^{235}U consumption for those zones where the power density is higher, leading to a decrease of power in the central axial zone with burnup, thus a flattening of the axial shape with the successive *burnup steps* can be identified. Other appreciable effect is the presence of structural materials (i.e. FA grids, see Fig. 4.1b and Table 28), reflected as a depression in the power density, since these components remove water and increase non-fission absorptions, e.g. for the first bins that surround the center of the AL. This effect is common for all LWR reactor designs, being *Serpent-SCF* capable to do an explicit modeling (see also Appendix A, where a PWR FA is analyzed, e.g. Fig. A.5).

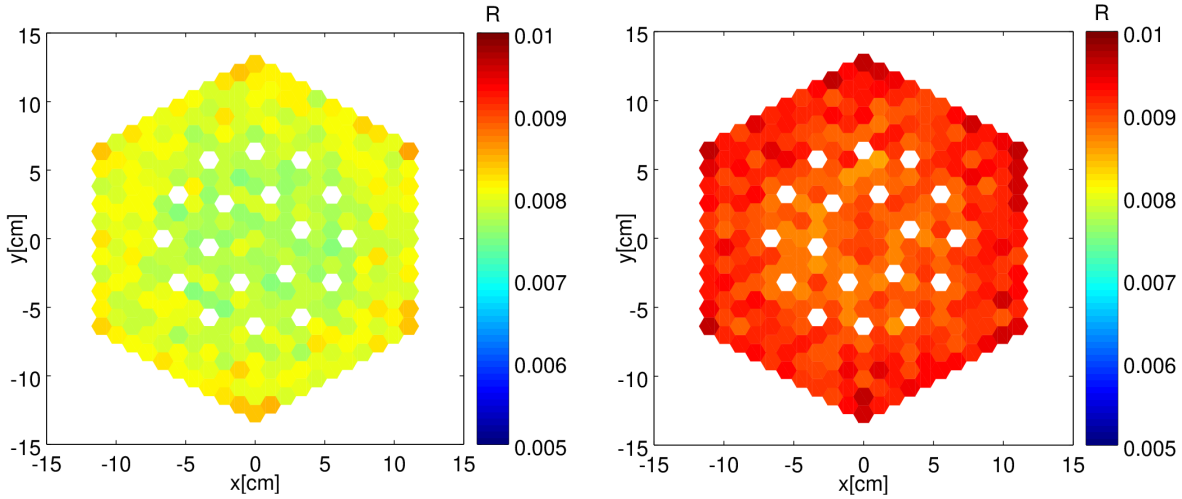

(a) Relative statistical uncertainty in the power density by pin, burnup 0 MWd/kgU.

(b) Relative statistical uncertainty in the power density by pin, burnup 49 MWd/kgU.

Figure 4.8: Evolution of the relative statistical error in power for a 12 cm axial xy slice from z = 0 for U-Er FA.

Finally, the change in the power profile with the burnup for a given axial slice is also reflected in the level of the resulting statistical convergence of the power shown in the Fig. 4.8, that corresponds to the same axial slice presented the Fig. 4.5. If the evolution of the relative statistical error from the Fig. 4.8a to the Fig. 4.8b is analyzed, it can be seen that an increment is observed. This is due to the fact that lower power (and neutron fluxes) are obtained in these zones for higher burnups, thus indicating that a lower amount of particles are sampled, resulting into an increase of the relative statistical error. Nevertheless the range of statistical convergence presented in Fig. 4.5a is within the confidence levels stated in Table 1 for a well-behaved MC calculation, regardless of the burnup step.

The aptness of *Serpent-SCF* to develop coupled *burnup* calculations is assessed through this radially-reflected FA case, where further key aspects are presented in Table 3. The analysis of Table 3 shows that the the high amount of computational resources is directly related to the MC approach of the neutronics, where the CPU and RAM memory must be regarded. Besides the average number of neutronic-TH iterations is the order of ~ 2 for the predictor and the corrector steps, which represents a lower value than those observed when no burnup is considered (see Appendix A and Section B.2). This effect is related to the fact that the TH profiles are suffering only minor changes between *burnup* steps, but the neutronic-TH feedback is asked to converge for all burnup steps (see Fig. 3.5). Despite being this behavior problem-dependent, it is a strong indicator that shows that the accurate results can be obtained doing the neutronic-TH iteration only for selected burnup steps.

Running time per iteration [CPUmins]		**Serpent average *stdev* at 1σ**		**Av. N-TH iterations per burnup step**		**RAM [GB]**
Serpent	*SCF*	Reactivity [pcm]	Power by pin (max/ave) [%]	Predictor	Corrector	~ 30
1.25*e*4	1e-1	12	1.7 / 0.8	2.4	2.2	

Table 3: Main running aspects for the radially-reflected FA case with burnup - using Intel(R) Xeon(R) Gold 5118 CPU @2.30GHz

4.3 Full core pin-by-pin neutronic-TH coupling for a VVER core

As a second step, a pin-by-pin coupling for a full-core scope is conducted to verify the coupling capabilities within a highly-heterogeneous VVER core. Therefore, a *Serpent-SCF* calculation is developed using a VVER experimental benchmark as basis (Loetsch et al., 2009) (a verification for a single radially-reflected FA can be gathered in Appendix Section B.2). Here, the full-core is modeled, considering a simplified burnup scheme due to computational constraints (see Appendix Section B.3). The comparison is done with the experimental results for diverse reactor states with low fuel burnup, where the reported system reactivity is compared for cases with and without equilibrium xenon from the first operation cycle (Loetsch et al., 2010, 2009). As far as detailed experimental results are not provided within the benchmark, the pin-by-pin results are analyzed in terms of consistency.

This experimental benchmark provides data for a full-core VVER-1000 reactor, namely the

Khmelnitsky NPP 2nd unit. Despite its successive updates and corrections during last years, this benchmark still present some inconsistencies, but it nevertheless represents the most complete set of open information available for a real VVER core. The selected core configuration corresponds to the first operation cycle, constituted of 163 FA with diverse enrichments and burnable poisons configurations (see Fig. D.1 in the Appendix Section D.2). These FA are *TVSA-type*, which main characteristics can be gathered in tables 25 and 26 in the same appendix. A brief summary of the main aspects of this first core is presented in Table 4.

Parameter	**Value**
Reactor type	VVER-1000/320
Core lattice type	Hexagonal - FA pitch 23.6cm
Total Core Power	3000MWth
Type of FA in core	*TVSA-type* FA *390GO*, *39AWU*, *22AU*, *30AV5* and *13AU*
Number of FA	163

Table 4: Main reactor data for the VVER core experimental data benchmark (Loetsch et al., 2010).

This benchmark also provides Control Rod (CR) positions and critical soluble boron concentrations (as acid boric - $C_{H_3BO_3}$ and boron concentration C_b) for diverse reactor states during the first four operation cycles. For the comparison and assessment of the coupled scheme only two specific reactor states from the first cycle are selected, listed in Table 5, with a low FA burnup, thus a simplified modeling of the burnup zones can be assumed.

Case	T_{inlet} [° **C**]	**Burnup [FPD]**	$C_{H_3BO_3}$ **[g/kg]**	C_b **[ppm]**	**CR10 [% ext]**	**Power [MWth]**	**Xenon**
1	281.0	0	6.55	1146	70.8	275	No
2	282.6	$0 - 4.5$	5.2	909	85.34	1490.7	Eq.

Table 5: Reactor states considered for the full-core VVER experimental benchmark (Loetsch et al., 2010). Both correspond to the first cycle.

For this benchmark, the accepted level of agreement for the reactivity comparison with the experimental results is slightly increased with respect to those from the previous case, since the benchmark does not provide detailed data for each state and some inconsistencies are identifiable (Loetsch et al., 2010, 2009). As a result, the satisfactory level of agreement for the *Serpent-SCF* results is $\sim 0.7 - 1.0$ in $C_{H_3BO_3}$ [g/kg] (that is $\sim 122 - 175$ C_b [ppm], and thus $\sim 1200 - 1700$ [*pcm*] for a VVER), which represents the span of results available in reports (Loetsch et al., 2011).

A full-core pin-by-pin *Serpent-SCF* model is developed for the states of the first core loading listed in Table 5. The neutronic model in Serpent is depicted in Fig. 4.9, where the origin of coordinates system is set in the center of the active length of the core. For this case two different runs using the ENDF/B VII.0 (Chadwick et al., 2011) and JEFF 3.1.1 (Santamarina et al., 2009) NDL are considered to determine the impact of these in the results. Besides, the core reflector and the upper and lower zones are modeled as homogenized compositions, accordingly to benchmark specifications. Main plots from the Serpent neutronic model are shown in in figs. 4.9a and 4.9b, where the external zones correspond to black boundary conditions.

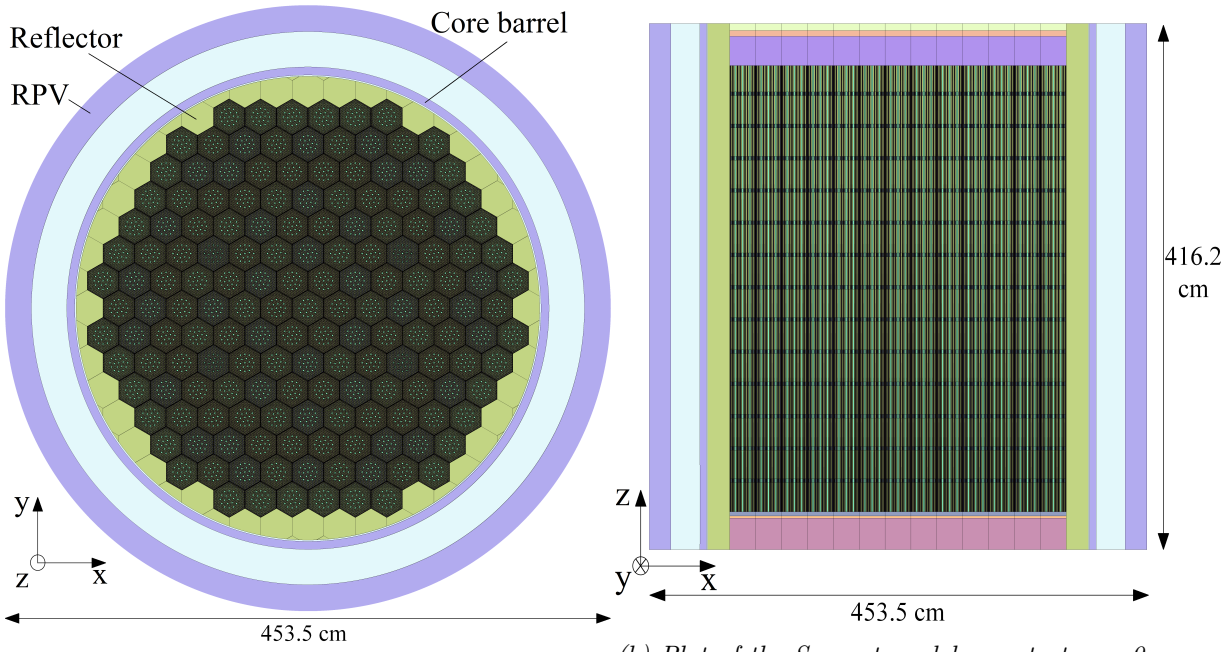

(a) Plot of the Serpent model, xy cut at z = 0 cm, where (x,y,z)=(0,0,0) corresponds to the center of the core and AL. Radial external surface is a black boundary.

(b) Plot of the Serpent model xz cut at y = 0 cm, where (x,y,z)=(0,0,0) corresponds to the center of the core and AL. Top and bottom surfaces are black boundaries. Not at scale.

Figure 4.9: Plots for the Serpent geometrical model for the full core VVER.

Detailed plots for these Serpent models are presented in Fig. 4.10, where it has to be considered that this core loading heterogeneity is expected to be reflected in the resulting power and temperature distributions (see Fig. D.1 and Table 4 in the Appendix Section D.2).

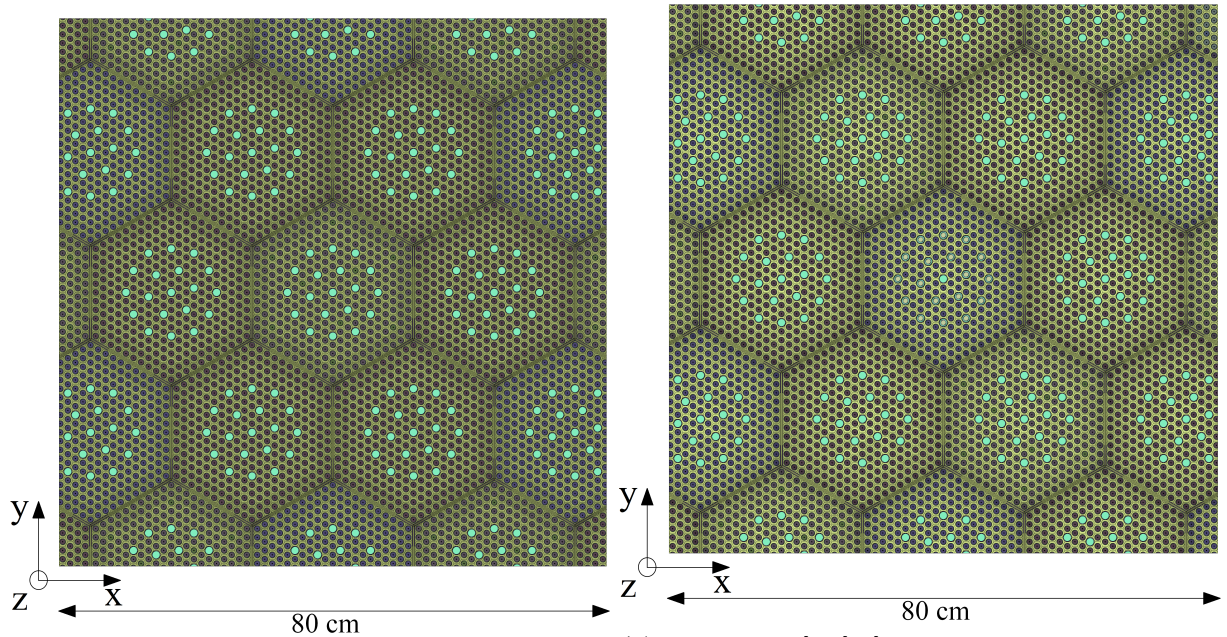

(a) Detail for [x,y]=[-40 to 40 cm,-40 to 40 cm].

(b) Detail for [x,y]=[30.8 to 110.8 cm, 0.87 to 80.87 cm].

Figure 4.10: Plots for the Serpent geometrical model for the full core VVER - detail at center of AL (z = 0 cm).

For the TH side of the problem a full-core *fuel-centered SCF* model is considered, as shown

in Fig. 4.11. This model considers 30 axially equispaced zones, with a total number of $\sim 5.4e4$ rods and channels. Besides, the convergence within temperatures and densities inside *SCF* is set to be at least two orders of magnitude below the neutronic-TH coupling convergence of the fields.

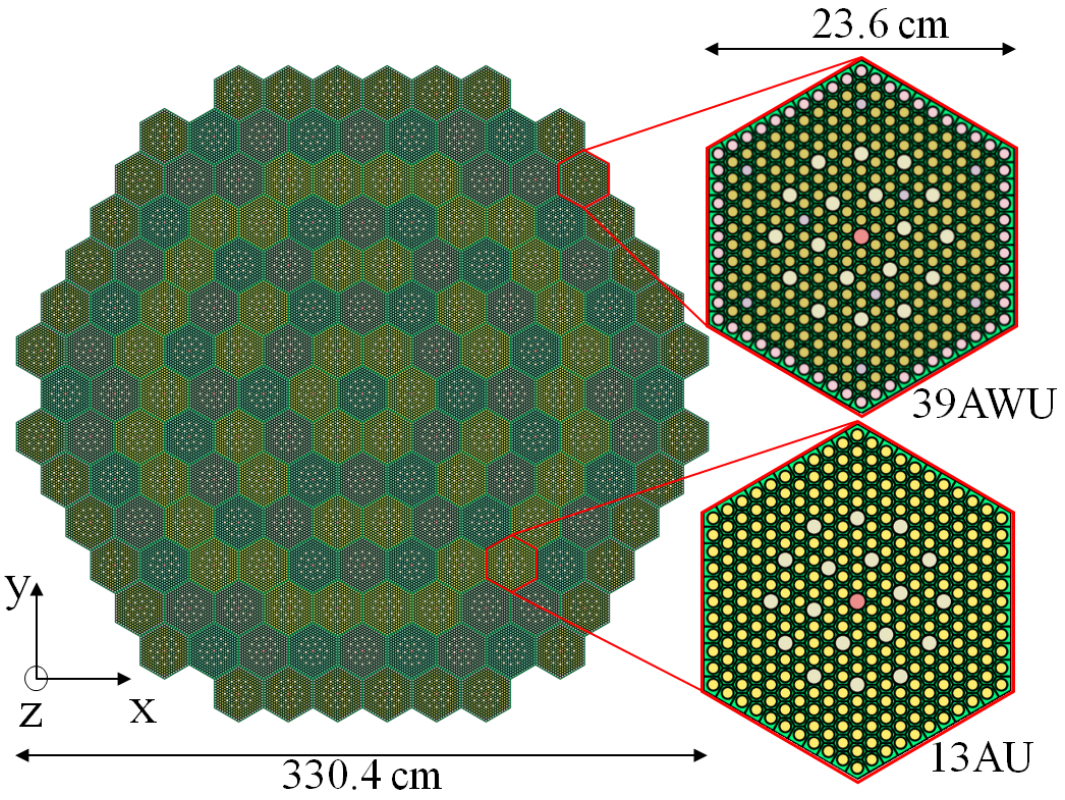

Figure 4.11: Plot of the SCF geometrical model for the full core VVER - xy cut at z=0 cm, where (x,y,z)=(0,0,0) corresponds to the center of the core and AL. Details of FA are included. Different colors represent different FR types (see tables 4) and 26.

Regarding the coupling between Serpent and *SCF*, a mapping file is also considered to map the TH fields to the corresponding nested hexagonal IFC on Serpent for the fuel and the coolant, where a volume average for fuel temperatures is considered within the fuel pins. Finally, to avoid instabilities in the neutronic-TH convergence, a relaxation of TH fields was considered with $\omega = 0.5$ (see Eq. 3.4).

The cases listed in Table 5 are considered adjusting the inlet temperature, the boron concentrations and total power as specified. To model the equilibrium xenon concentration for the case 2, a series of two burnup steps up to 4.51 [FPD] are developed using a *Predictor-Corrector* scheme. As far as the detailed (i.e. pin-by-pin) division of the full-core depletion zones implies high resources requirements and the pin-wise modeling of the xenon distribution is not required for this low burnup case, a simplified material division is considered. Therefore, a division by type of pin on each fuel assembly with 30 axial zones is considered (totaling 8160 burnup zones) for this case number 2. Besides, for both cases, $2e3$ active cycles of $2e5$ particles each (totaling $4e8$ active histories per iteration step) are considered, leading to a statistical convergence of ± 5 $[pcm]$ in reactivity. Regarding the neutronic-TH iteration, the convergence of the TH fields was set to 30 $[K]$ and 2.5 $[K]$ for fuel and coolant temperatures respectively, while a 0.01 $[g/cm^3]$

was set for the coolant density variation. Finally, to tackle the computational requirements, both cases in Table 5 were run in a HPC (i.e. ForHLR II cluster (SCC, 2020)).

The converged system multiplication factor from *Serpent-SCF* calculations for both cases are presented in Table 6, where it should be regarded that the experimental values are for critical positions (i.e. keff=1.0). As it can be seen, a good agreement is observed in terms of global parameters, with differences in reactivity below 1200 pcm both for cases at high and low power (with equilibrium xenon and without xenon respectively). This difference corresponds to a deviation of ∼100/200 ppm and ∼50/100 ppm of C_b with the measured values for cases 1 and 2 respectively, which is in line with the level of agreement stated (Loetsch et al., 2011). Besides, the impact of the considered NDL (i.e. changing from JEFF 3.1.1. to ENDF/B VII.0) is found to be ∼100 pcm.

Case		k_{eff}	**Reactivity [pcm]**
1 ($\sim 300MWth$, no Xe)	ENDF/B VII.0	$1.01078 \pm 3E-5$	1067±3
	JEFF3.1.1	$1.01174 \pm 3E-5$	1160±3
2 ($\sim 1500MWth$, eq. Xe)	ENDF/B VII.0	$1.00323 \pm 6E-5$	322±6
	JEFF3.1.1	$1.00248 \pm 6E-5$	247±6

Table 6: Serpent-SCF results for the full-core VVER benchmark cases in Table 5.

The analysis of the pin-wise power density profiles is done for xy slices below and above the core center, as presented in figs. 4.12 and 4.13, where the Case 2 from Table 6 (using JEFF 3.1.1 NDL) is selected, since it represents the higher reactor power. For completeness, the corresponding statistical convergence for these slices is presented in Fig. 4.14.

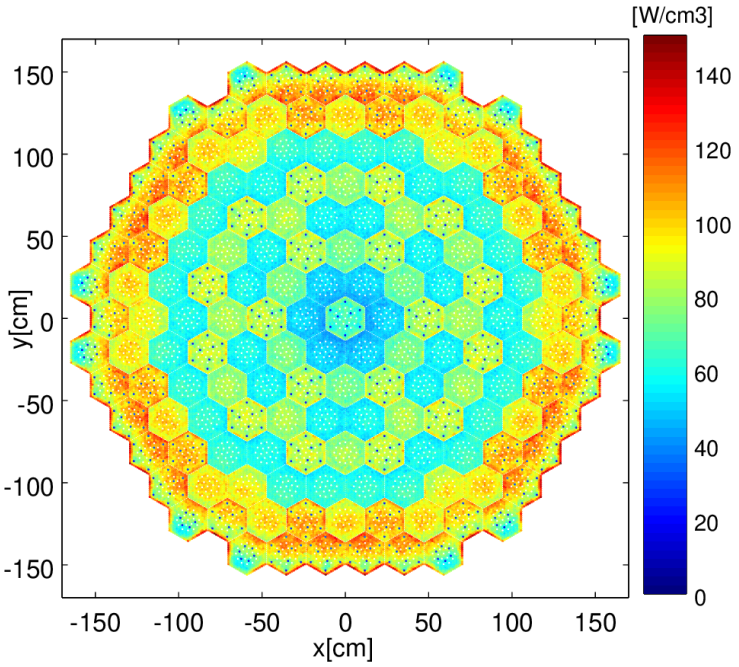

Figure 4.12: Serpent-SCF converged pin power density profiles for the case 2 of the full-core VVER benchmark (using JEFF 3.1.1 NDL); xy cut for a 12 cm slice starting at $z \sim -12$ cm from core center, where (x,y,z)=(0,0,0) corresponds to the center of the core and AL.

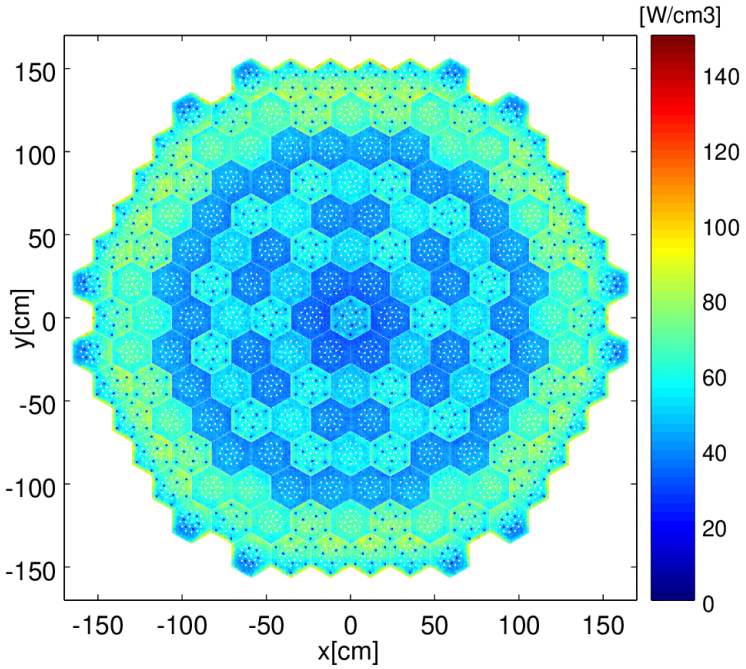

Figure 4.13: Serpent-SCF converged pin power density profiles for the case 2 of the full-core VVER benchmark (using JEFF 3.1.1 NDL); xy cut for a 12 cm slice starting at $z \sim 105$ cm from core center, where (x,y,z)=(0,0,0) corresponds to the center of the core and AL.

The core heterogeneity is noticeable in the pin-wise power density slices presented in figs. 4.12 and 4.13 (see Fig. D.1 and Table 4). A depression in the power surrounding the central FA is appreciated, since it is encircled by FA with a lower ^{235}U enrichment (i.e 30AV5 enclosed by 13AU). The same effect occurs in the FA rings at 3 and 5 FA pitchs from the center, where these zones also exhibit a lower power density. The effect of the radial reflector (i.e. an increase of power in the outer pins) is also observed, producing hot spots for positions where FA with higher enrichment are present. Besides, the axial dependence of the power density is also seen, showing the Fig. 4.12 higher values than those from Fig. 4.13.

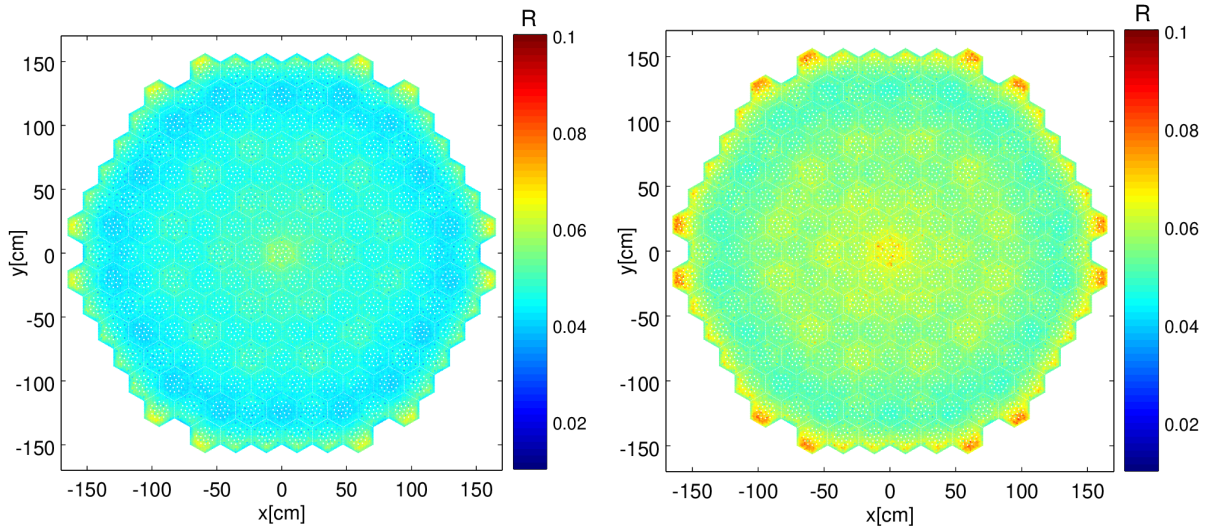

(a) Xy cut for a 12 cm slice at $z \sim -12$ cm from core center. Corresponds to Fig. 4.12.

(b) Xy cut for a 12 cm slice $z \sim 105$ cm from core center. Corresponds to Fig. 4.13.

Figure 4.14: Serpent-SCF relative statistical convergence in power for the case 2 of the full-core VVER benchmark (using JEFF 3.1.1 NDL); (x,y,z)=(0,0,0) is the center of the core and AL.

The statistical convergence in Fig. 4.14 shows relative errors consistent with the confidence levels stated in Table 1 for an MC neutronic calculation, where a lower convergence is obtained for the second slice due to the lower flux levels there. Finally, the associated temperatures distribution for this case are presented in figs. 4.15 and 4.16.

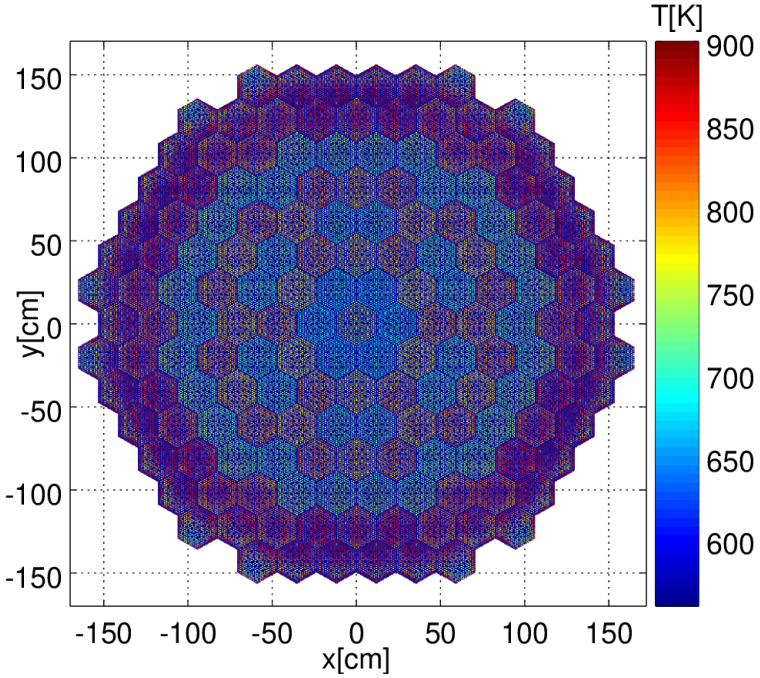

Figure 4.15: Serpent-SCF converged temperature profiles for case 2 of the full-core VVER benchmark (using JEFF 3.1.1 NDL) - xy cut for a 12 cm slice at $z \sim -12$ cm from core center ($z = 0$ cm).

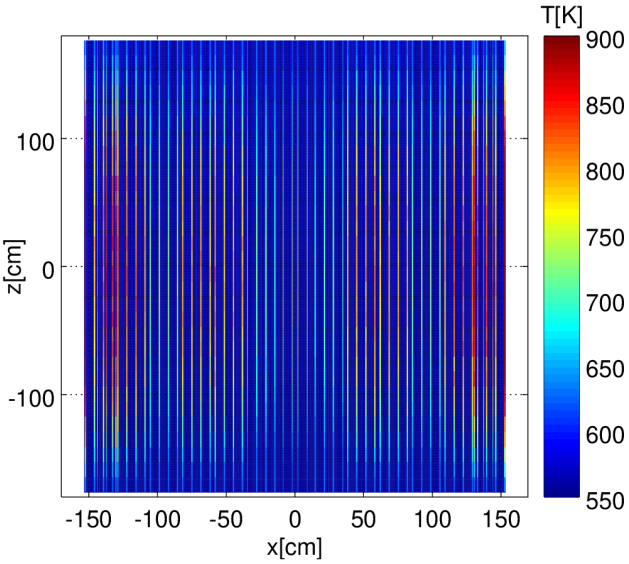

(a) Xz cut for a 0.1 cm slice in the core center ($y = 0$ cm).

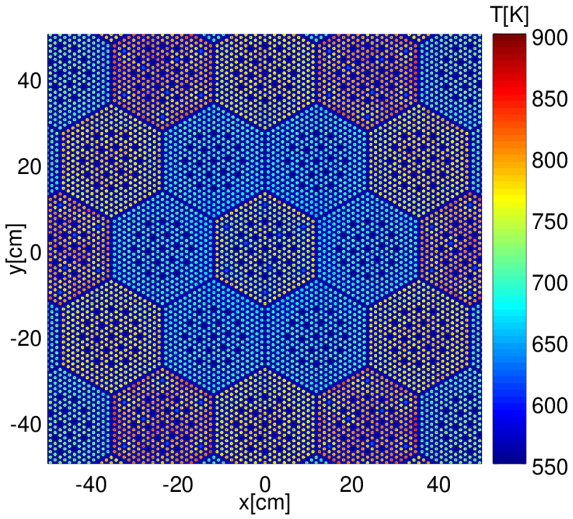

(b) Detail of the xy cut in Fig. 4.15, a 12 cm slice at $z \sim -12$ cm from core center ($z = 0$ cm).

Figure 4.16: Serpent-SCF converged temperature profiles for case 2 of the full-core VVER benchmark (using JEFF 3.1.1 NDL).

The Fig. 4.15 depicts a 12 cm slice at z ~ -12 cm from core center that corresponds to Fig. 4.12. Moreover, an xz slice in the core center (i.e. y = 0 [cm]) is shown in Fig. 4.16a to

depict the axial dependence and a detail for the same xy slice as in Fig. 4.15 is provided in Fig. 4.16b. The radial dependence of the temperatures in figs. 4.15 and 4.16b exhibit an qualitative accordance with the power densities from Fig. 4.13, where the effect of the different FA present in the core load is identifiable (see Fig. D.1 and Table 4). The increse in the temperatures for the FA in the second ring that surrounds the central one can be appreciated, reinforcing the importance of the detailed modeling, developed in *Serpent-SCF* in a direct manner. Besides the axial dependence of the problem is appreciated in Fig. 4.16a, consistent with the differences observed between the power density values of figs. 4.12 and 4.13, reflecting that the power is tilted to the bottom axial zone of core due to the TH feedbacks.

To summarize, the proposed neutronic-TH scheme shows also a convergent behavior for this pin-wise analysis for a highly heterogenous full core VVER case composed of more than fifty thousands rods. The agreement of the system multiplication factors with experimental data is as accurate as intended, whereas the consistency of the main physical phenomena is also assessed. Finally, a brief summary of involved computational resources can be gathered in the Table 27 in the Appendix Section D.2.

4.4 Final comments for *Serpent-SCF steady-state* and *burnup* calculations

The analysis developed above assess the aptness of the proposed approach to tackle pin-by-pin neutronic-TH *steady-state* and *burnup* calculations. The verification of the system reactivity results together with the consistency of the modeled physical phenomena and the convergence stability of *Serpent-SCF* represents a first step towards the validation process and allows to be confident in further steps regarding *transient* calculations.

"If it ain't broke, don't fix it."

— Engineering proverb

5 Verification for coupled *transient* calculations

This Chapter is devoted to provide a verification of the *Serpent-SCF* capabilities regarding coupled *transient* calculations and to study its features. Therefore, a simplified geometry is here considered, namely a PWR minicore from (How et al., 2018), where coupled calculations from a HFP state are developed for a series of relevant RIA-type scenarios.

5.1 The coupled *transient* calculations for the PWR Minicore

The verification case is based on a 3 by 3 PWR FA minicore numerical benchmark, reflected by water on all sides from (How et al., 2018). A control rod is placed in the central FA (fully inserted in nominal conditions), allowing the development of a coupled *transient* generated by its withdrawal. The FA are a TMI-type (i.e. a 15 by 15 array with Zircalloy cladding), that includes four burnable poison (BP) pins containing Gd_2O_3+UO_2. This FA and the minicore array are illustrated in figs. 5.1a and 5.1b, where a summary of the benchmark specifications can be gathered in the Table 22 in the Appendix Section D.1. For this configuration, a fresh (i.e. no burnup), clean (i.e. no xenon) and Hot Full Power (HFP) condition is modeled. The TH parameters, that represent scaled operation parameters from a full-size PWR, are summarized in the Table 23 in the same Appendix.

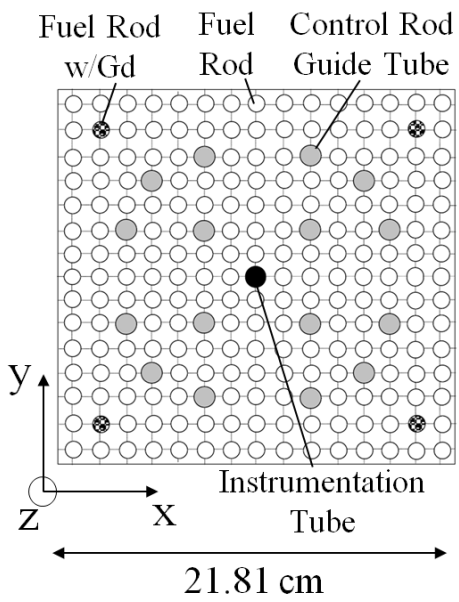

(a) Fuel assembly description

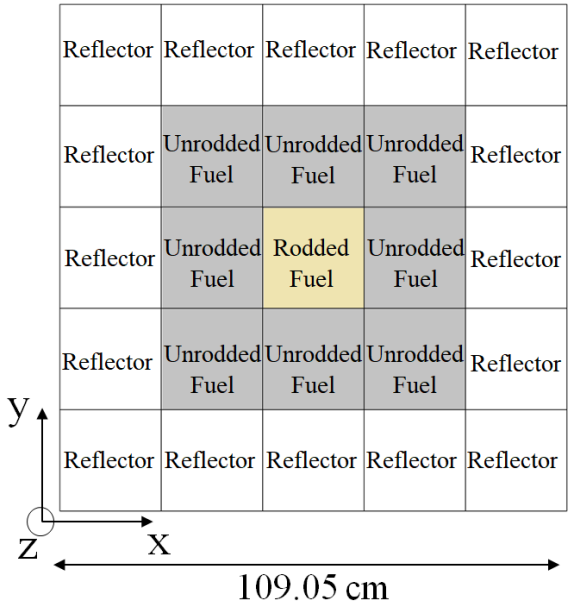

(b) Minicore array composed of 8 unrodded and 1 rodded FA.

Figure 5.1: TMI type Fuel and minicore description. Further details can be obtained in (How et al., 2018).

The analyzed *transients* represent a RIA-kind scenario, caused by sudden insertion of reactivity in the system (i.e. Rod Ejection Accident). The initial condition is a critical HFP state with

the central CR fully inserted, whereas the *transient* scenario is driven from the withdrawal of the CR during a certain period of time. Two sequences are here considered, presented in Table 7, where the CR is extracted at fixed velocity for 1 second. Then this movement is abruptly stopped and the temporal system response is analyzed up to 5 seconds.

Scenario	Description
#1	Extraction 30 [cm/s] from 0.2 to 1.2 s
#2	Extraction 35 [cm/s] from 0.2 to 1.2 s

Table 7: Coupled transient scenarios analyzed with Serpent-SCF for the TMI minicore.

The target is to develop a pin-by-pin neutronic-TH coupling and evaluate the total power, together with the pin-wise (or subchannel) distribution of the power density and the TH fields for the cases in Table 7. For such purpose, a fixed time binning is used (i.e. a 50 milliseconds binning, 100 bins in total). It should be considered in this point that no reference results are available, but code-to-code comparisons with other MC-based plus subchannel TH schemes for these same scenarios can be found in (Faucher et al., 2020).

From the neutronic point of view, a detailed Serpent 3D model is considered, including axial and lateral reflectors, where the external faces represent *black boundary* conditions. Details of this model are presented in figs. 5.2 and 5.3, where the first one identifies two pins that will be used to provide detailed axial profiles in further sections (i.e. *Pin A*, in the core center and *Pin B*, next to the lateral reflector).

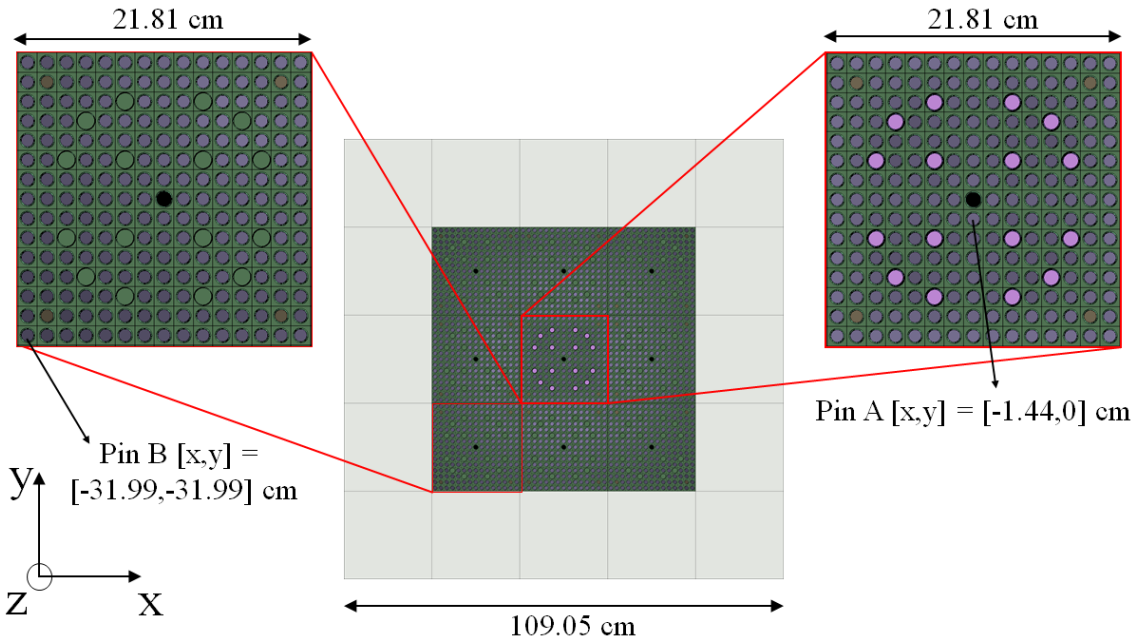

Figure 5.2: Plot of the Serpent model xy cut at z=0 cm, where (x,y,z)=(0,0,0) corresponds to the center of the core and AL. Lateral surfaces are black boundaries. Pins A and B are identified for further analysis.

The JEFF3.1.1 NDL is used (Santamarina et al., 2009), which counts with eight family precursor groups. To consider the TH feedback, IFC pin-by-pin and subchannel-by-subchannel are

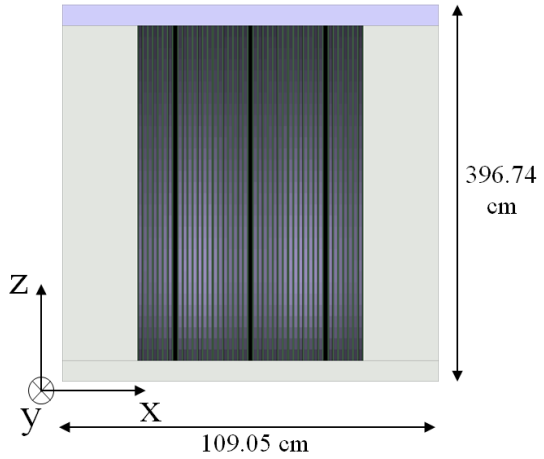

Figure 5.3: Plot of the Serpent model xz cut at y=0 cm, where (x,y,z)=(0,0,0) corresponds to the center of the core and AL. Top and bottom surfaces are black boundaries. Not at scale.

included for fuel and coolant materials, using regular cartesian meshes that cover the whole active length with 30 equidistant axial zones. Additional superimposed power detectors by pin with 10 axial zones are also included to obtain diverse power density plots, as discussed in further sections. Finally, to consider the CR movements, time-dependent translations for the CR geometry are defined with a constant velocity as defined in the Table 7.

The TH side of the problem is treated with a pin-by-pin (and subchannel for coolant) *SCF* model for the full minicore with the same 30 axial zones as for Serpent IFC. A *coolant-centered* model is considered, as depicted in Fig. 5.4, where the indexing of rods and subchannels is chosen to agree with these from the IFC in Serpent, thus avoiding the need of mapping files. For the *CHF* correlations, the table lookup option is selected (Doroschuk et al., 1976). Besides, the convergence criteria for temperatures and densities inside *SCF* solver is selected to be at least one order of magnitude below the neutronic-TH coupling convergence criteria for the *steady-state* calculation. Regarding the fuel temperature feedback, a volume average is considered for the fuel pins (see Section 3.4.4).

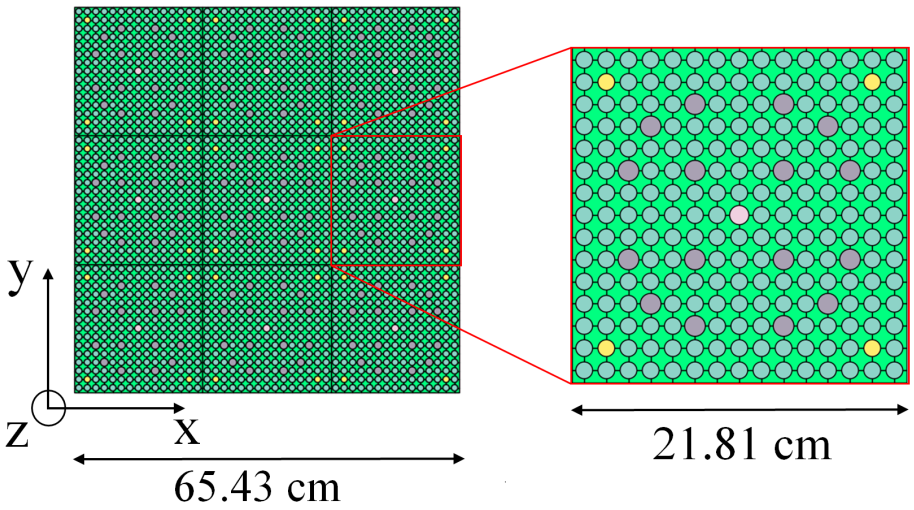

Figure 5.4: SCF model xy cut at z=0 cm, where (x,y,z)=(0,0,0) corresponds to the center of the core and AL. Detail of the FA model included.

To deal with the coupled *transient* calculations the two-step approach has to be followed (see

Section 3.5), where details can be gathered in the Table 24 in Appendix Section D.1. Here, the initial state is a HFP state, hence the following steps are followed:

1. A preliminary search is conducted through successive coupled *steady-state* iterations to obtain the critical boron concentration for the starting configuration (with the CR fully inserted). It yields a $C_b = 1272$ [ppm]. A separate calculation is developed to get the equivalent static reactivity introduced by the CR extraction with this C_b (i.e. the CR worth).
2. A critical coupled *steady-state* calculation with $C_b = 1272$ [ppm] is executed to obtain the required source data for the *live* neutrons and point-wise precursors (see Section 3.5). These are obtained using $2.4e9$ active particles divided in $3e3$ active cycles.
3. Finally, the *transient* calculations are executed using the previous step as source, using $2e6$ particles for each time interval.

The *Serpent-SCF* verification for these coupled *transient* calculations is developed through the consistency check of both core-level (e.g. total power and averaged TH parameters) and local results (e.g. pin-wise power densities). Moreover, the capability to provide relevant safety-related parameters is also discussed (see Section 2.6.2).

5.2 Results for coupled *steady-state* calculation at HFP

The *steady-state* configuration obtained with *Serpent-SCF* is critical (k_{eff}=1.00010±$2E-05$) where the convergence of the TH parameters by pin is lower than 5 $[K]$ for fuel temperature and 1 $[K]$ for coolant temperature (with less than $1E-03$ $[g/cm^3]$ for coolant density). As an example, the obtained temperatures are depicted in the Fig. 5.5.

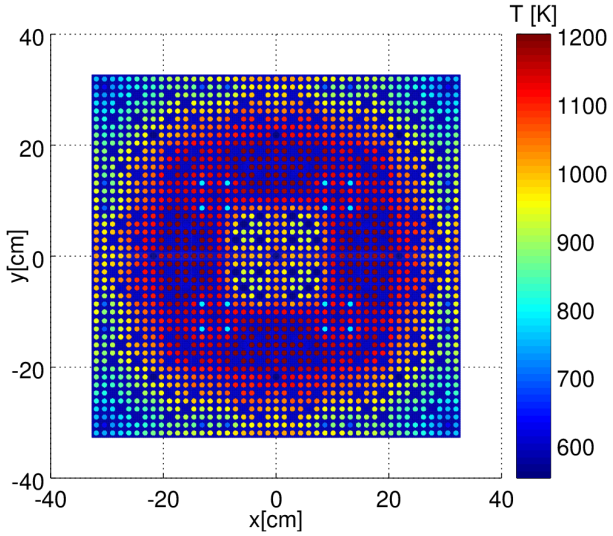

Figure 5.5: Serpent-SCF steady-state calculated temperatures for the TMI minicore at HFP - cut for a xy slice of 20 cm above the core center (i.e. $z = 0$ [cm]).

The Fig. 5.5 depicts the obtained temperatures for a xy slice of 20 cm above the core center (i.e.

$z = 0$ [cm]), where the capability of *Serpent-SCF* to model the strong spatial dependence of this minicore can be appreciated. This allows to depict the important effect of the pins distribution in this minicore, as observed in the Fig. 5.5, together with the strong power depresion in the central FA caused by the inserted CR, which leads to lower temperature values. The pins with BP (see Fig. 5.1) exhibit lower temperatures, as a product of a lower power generation. Besides, this depression of power generated by the CR (fully-inserted here) is also accompanied by increase of the power in the outer FA ring, resulting into an increase of the temperatures there. These strong gradients play a key role in the analyzed *transient* scenarios, as discussed in the following sections.

Finally, the inserted CR reactivity for the scenarios in Table 7 is estimated through critical calculations for the extracted CR positions, as presented in Table 8 (0 cm of withdrawal represents the fully-inserted CR case). It can be seen that both scenarios represent a reactivity insertion below the prompt-supercritical condition, where β_{eff}=755±10 [pcm] (calculated with Serpent for the coupled *steady-state* case using the *IFP* method (see Section 3.1).

Scenario	**CR withdrawal [cm]**	**Static reactivity [pcm]**	**Static reactivity [$]**
#1	30	354 ± 7	0.469 ± 0.015
#2	35	610 ± 7	0.808 ± 0.027

Table 8: Static reactivity as a function of the CR withdrawal for the TMI minicores for the two scenarios to be analyzed.

5.3 Results for coupled *transient* calculations

The *Serpent-SCF* calculated results for the extraction of the control rod at constant velocity of 30 [cm/s] from 0.2 to 1.2 [s] are presented in figs. 5.6 and 5.7. Moreover, the results for the second scenario are depicted in figs. 5.8 and 5.9.

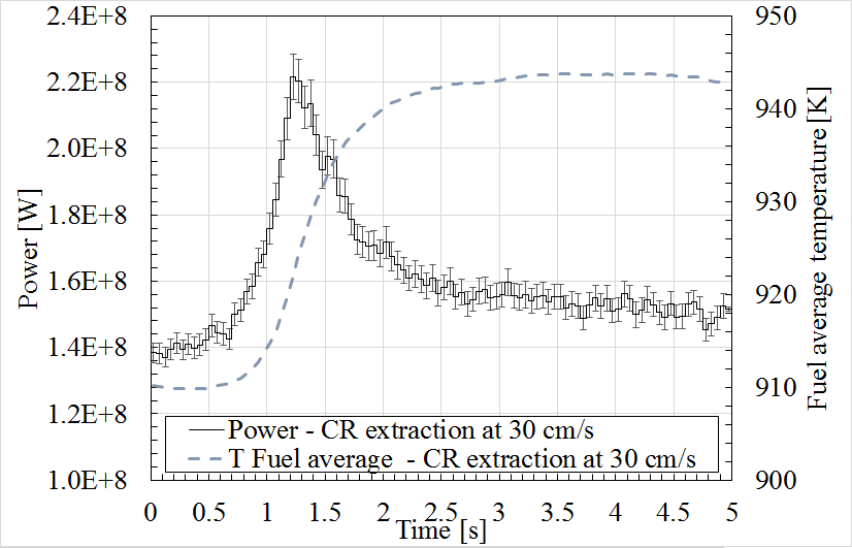

Figure 5.6: Serpent-SCF total power and average fuel temperature evolution solutions for the TMI minicore - CR extraction at 30 cm/s. Error bars represent statistical uncertainty at 2σ.

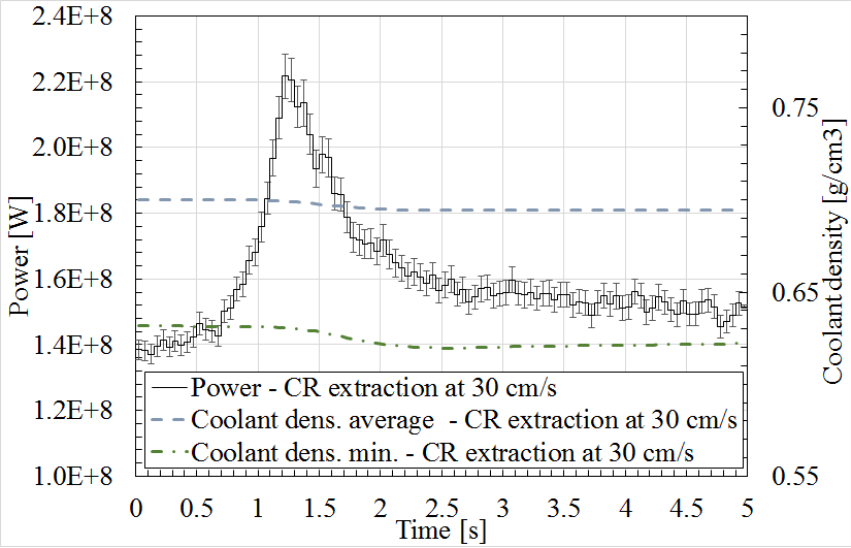

Figure 5.7: Serpent-SCF total power and coolant density evolution solutions for the TMI minicore - CR extraction at 30 cm/s. Error bars represent statistical uncertainty at 2σ.

The Fig. 5.6 shows the total power temporal evolution together with the fuel temperature (from the Serpent IFC, calculated by *SCF*), averaged in the whole minicore. Likewise, the Fig. 5.7 depicts the average value for the coolant density, together with its minimum value, also from the IFC. A power peak is observed, due to the sudden CR extraction that generates a positive reactivity insertion and thus generates an initial power increase (as seen in Fig. 2.2). This increase in power leads to a temperature increase in the fuel and coolant (and density decrease in the latter, observed after the power peak). This TH feedback compensates the inserted reactivity due to the negative fuel temperature and coolant density reactivity coefficients (estimated in separate steady-state calculations to be $\sim -1.8[pcm/K]$ and $\sim -240[pcm/\%\Delta\text{Coolant}_{\text{density}}]$). As a result this power overshoot results into higher temperatures (and a lower coolant density), where a further decrease is observed for fuel temperature, following the total power evolution.

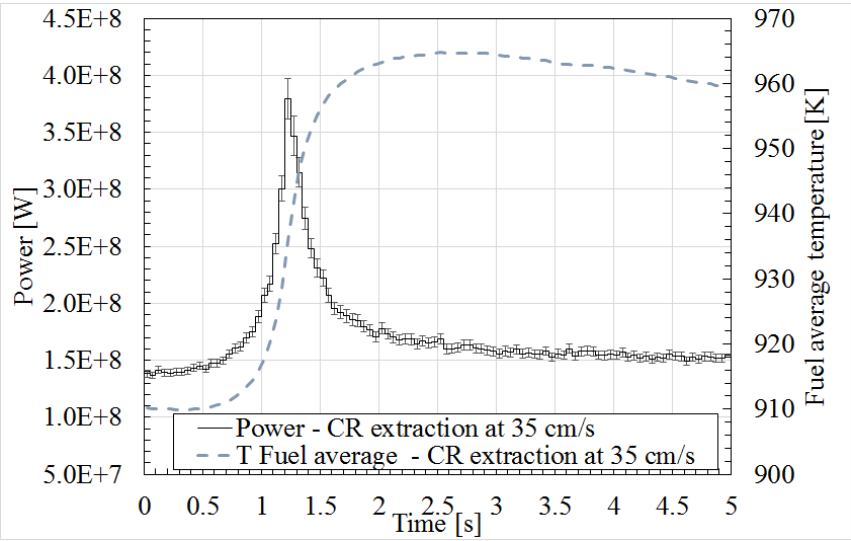

Figure 5.8: Serpent-SCF total power and average fuel temperature evolution solutions for the TMI minicore - CR extraction at 35 cm/s. Error bars represent statistical uncertainty at 2σ.

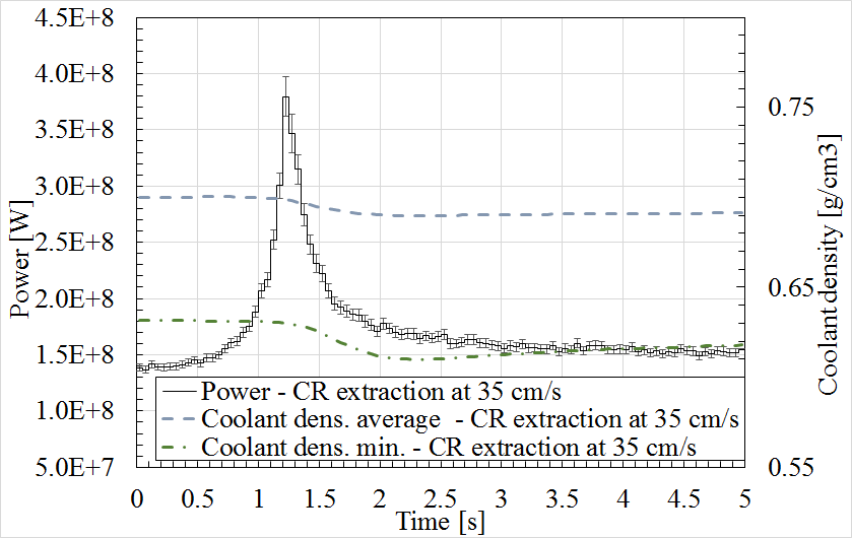

Figure 5.9: Serpent-SCF total power and coolant density evolution solutions for the TMI minicore - CR extraction at 35 cm/s. Error bars represent statistical uncertainty at 2σ.

The second scenario depicted in figs. 5.8 and 5.9 increases the CR withdrawal, leading to a higher reactivity insertion (see the Table 8). The same analysis is developed, where the Fig. 5.8 includes the power and fuel temperature average evolution (obtained as an average of the Serpent IFC values) and the Fig. 5.9 provides the evolution for the coolant average and minimum values (also from the Serpent IFC). Increasing the amount of reactivity generates a bigger power overshoot and thus higher average fuel and coolant temperatures increments (and coolant density decrements). In this case, after the initial peak in fuel temperature a further decrease is observed, due to rapid decrease in the total power resulting from the TH feedbacks. This effect can be clearly observed if we compare both scenarios, shown in Fig. 5.10.

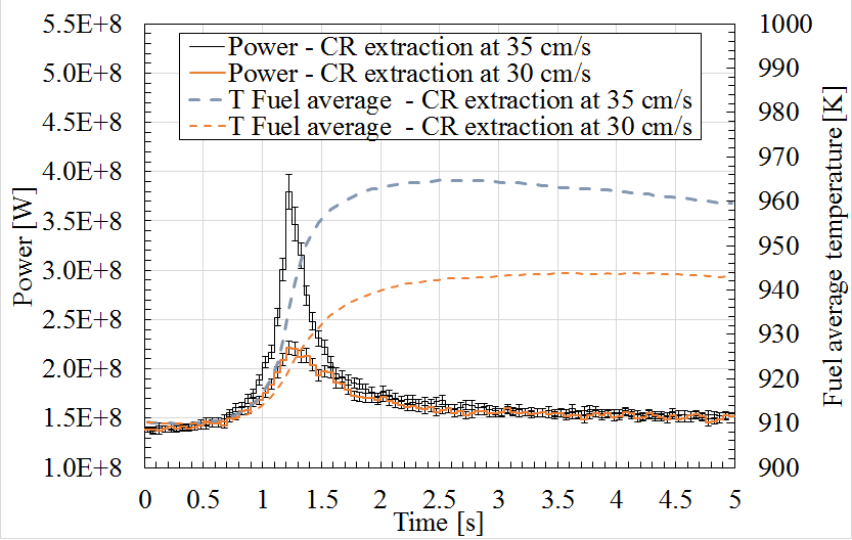

Figure 5.10: Serpent-SCF total power and fuel temperature evolution for the TMI minicore - comparison for scenarios. Error bars represent statistical uncertainty at 2σ.

The effect of the increased amount of inserted reactivity is appreciable in the Fig. 5.10,

reflected as a higher power overshoot and thus a increase of fuel temperatures. The system thus achieve higher temperatures, providing a stronger feedback that compensate this increased reactivity. Finally, regarding pin-by-pin results, the time evolution is analyzed for the scenario # 1 for a xy slice of 35 [cm] starting $\sim 140cm$ below the center of the core, as shown in Fig. 5.11.

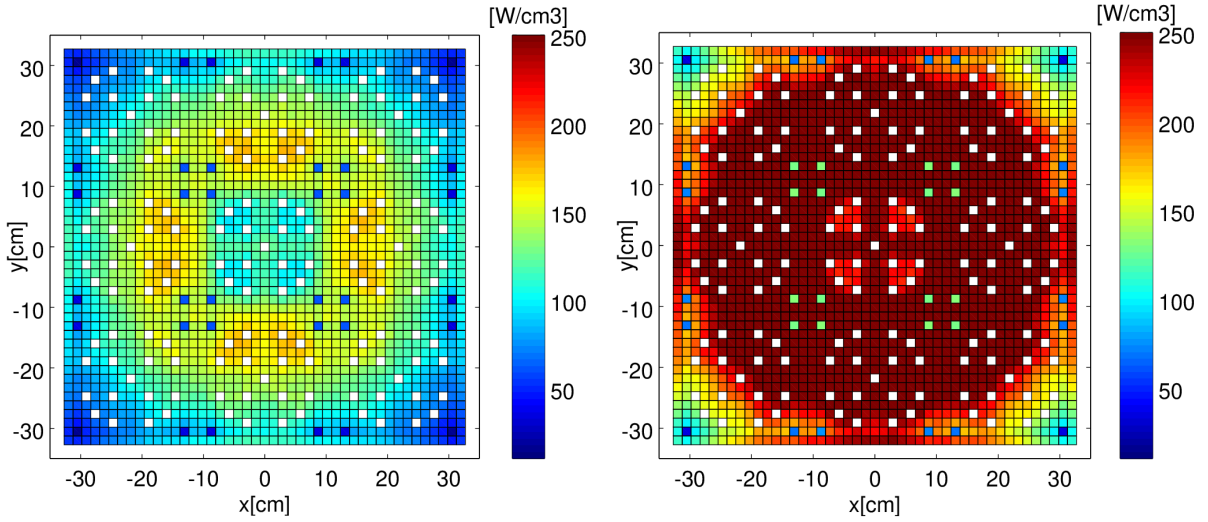

(a) Initial time bin. *(b) Time bin starting at 1.3 s (power peak).*

Figure 5.11: Serpent-SCF results for power density for the TMI-minicore for a xy slice of 35 cm $\sim 140cm$ below the core center ($z = 0$ [cm]) - results for CR extraction at 30 cm/s. Relative statistical errors $< 3\%$ (1σ).

The evolution of the power in Fig. 5.11 shows the effect of the CR withdrawal, which leads to a power increase within the whole core, but more noticeable for the central zone, where the power is highly depressed for the initial time step. Moreover, the effect in the TH parameters is shown in figs. 5.12 and 5.13.

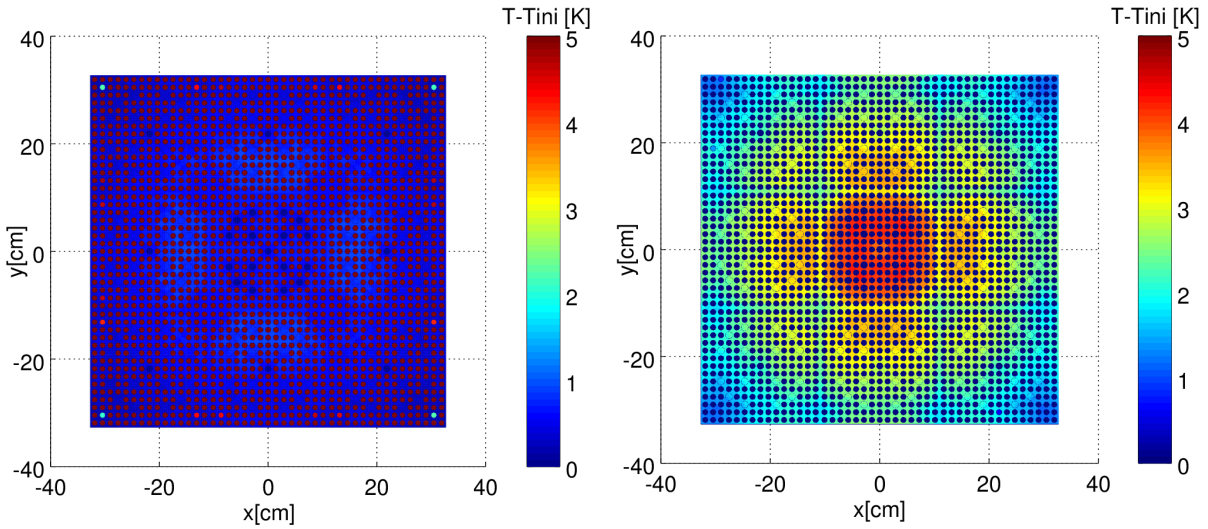

(a) Difference with time bin at 1.3cm. *(b) Difference with final time bin.*

Figure 5.12: Serpent-SCF results for the increase in temperature in the TMI-minicore for a xy slice of 20 cm above the core center ($z = 0$ [cm]) - results for CR extraction at 30 cm/s.

The Fig. 5.12 presents the change in the temperature distribution for a xy slice of 20 [cm] above the core center (i.e. $z = 0$ [cm]) at times 1.3 [s] and 4.9 [s], which represents a position ~ 1 [m] above the Fig. 5.11, and above the zone where the CR is extracted, allowing to analyze the effect of this localized increase of the power in the TH. For the first step shown in the Fig 5.12a (i.e. the power peak time) the global increase of power is seen as a generalized increase in the fuel temperatures. This increase of temperatures is then translated to an increase on coolant temperatures in further time steps, as observed in the Fig 5.12b. This temperature increase impacts on the coolant density, as depicted in the Fig. 5.13.

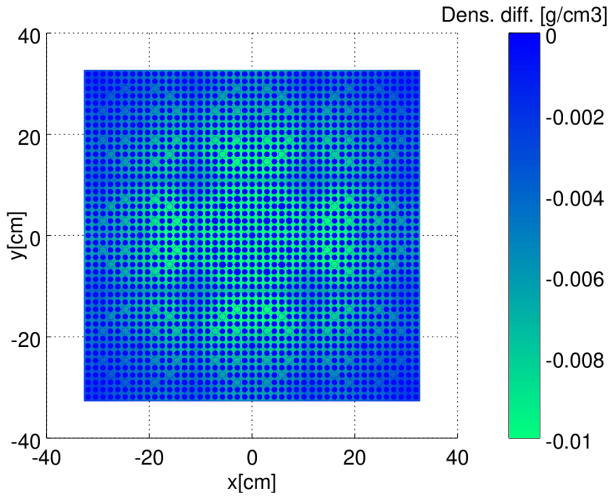

Figure 5.13: Serpent-SCF transient results for the decrease in density at 4.9 [s] in the TMI-minicore for a xy slice of 20 cm above the core center ($z = 0$ [cm]) - results for CR extraction at 30 cm/s.

The Fig. 5.13 shows the change in coolant density change for the same xy slice of 20 cm above the core center (i.e. $z = 0$ [cm]) at 4.9 [s]. It can be seen that the increase of coolant temperatures due to the increase of power (and fuel temperatures) leads to a decline in the coolant densities, which have an important contribution in the reactivity feedback. The combination of all these parameters (i.e fuel temperatures, coolant temperatures and coolant densities) is thus providing the negative reactivity required to compensate the one inserted by the CR movement, where the heavily localized effect is noticeable, modeled explicitely by *Serpent-SCF* at pin-wise level (and subchannel for the coolant).

5.4 Safety-related parameters calculation within coupled *transients*

The capability to provide pin-by-pin axial profiles temporal evolution during this coupled *transient* calculation represents an added value for this dissertation objectives (see Section 1.2). The presence of strong local effects caused by the CR within this minicore *transients* can be tackled by the proposed approach, unlocking a wide range of analysis unattainable in the industry-standard approach. Hence, the evolution of the axial power profiles for pins A and B identified in Fig. 5.2 are here analyzed for the scenario #1 in figs. 5.14a, 5.14b.

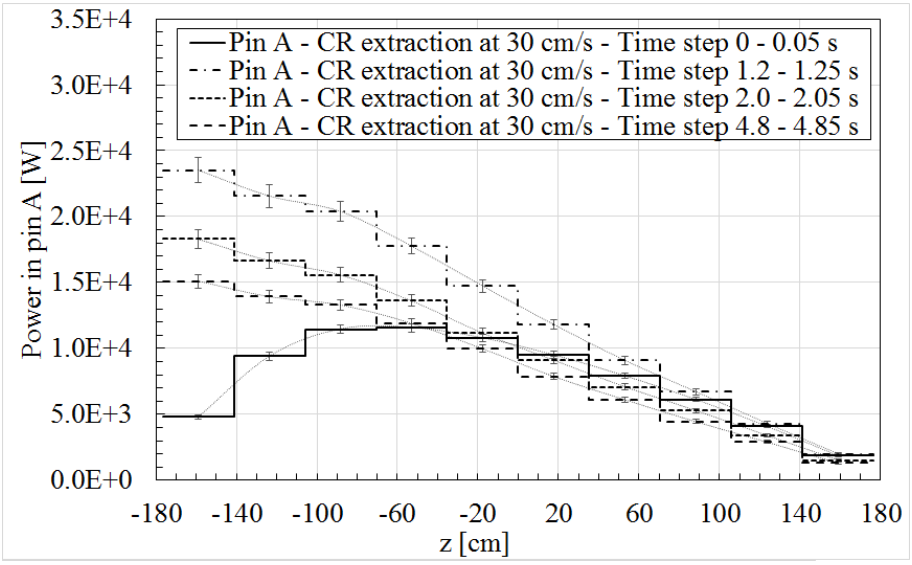

(a) Axial profile evolution during transient for pin A - Scenario #1.

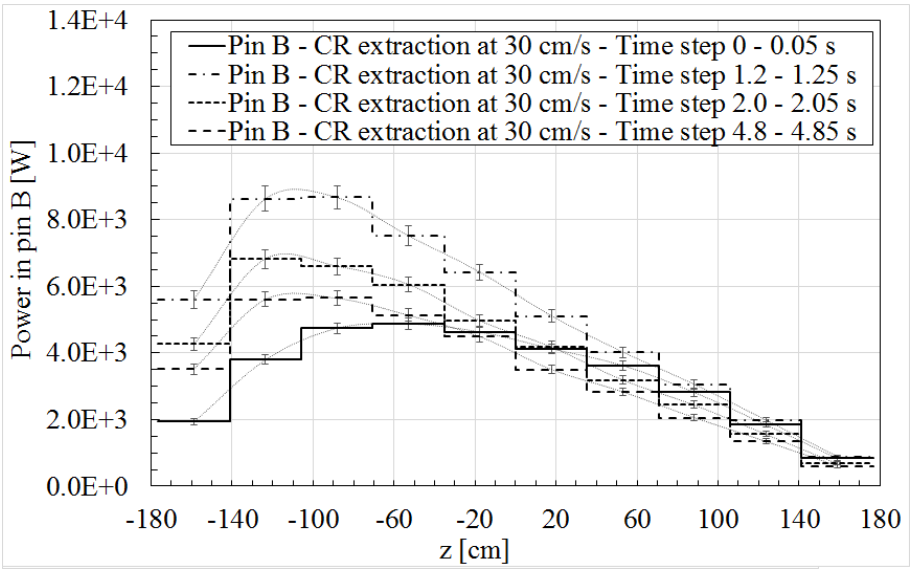

(b) Axial profile evolution during transient for pin B - Scenario #1.

Figure 5.14: Serpent-SCF transient results for the TMI minicore for the axial profile evolution for pins in Fig. 5.2 - results for CR extraction at 30 cm/s. Error bars represent statistical uncertainty at 2σ.

The results presented in the Fig. 5.14 show the capability of *Serpent-SCF* to model the complex merger of the axial dependence and temporal evolution of the problem. The combined effect of the slender geometry of the minicore and the TH feedback makes the axial profile to be tilted to the bottom zone of the core, which also corresponds to the zone where the CR in the central FA is withdrawn. This is reflected in the axial profiles evolutions, since the pin *A* in Fig. 5.14a is heavily perturbed with the CR movement, altering its axial shape with time. Conversely, this effect is not seen in the pin *B* in Fig. 5.14b by reason of its larger distance to the CR (i.e. it is placed inside an unrodded FA and next to the reflector). Besides, both pins show a power overshoot around 1.3 s. As a result, the axial power profiles remain shifted to the lower zone, where the effect is more important for the pin *A* (in the central rodded FA).

Having a pin-wise (and subchannel level for the coolant) description of the problem, *Serpent-SCF* can provide the associated safety-related parameters, as shown in the Fig. 5.15.

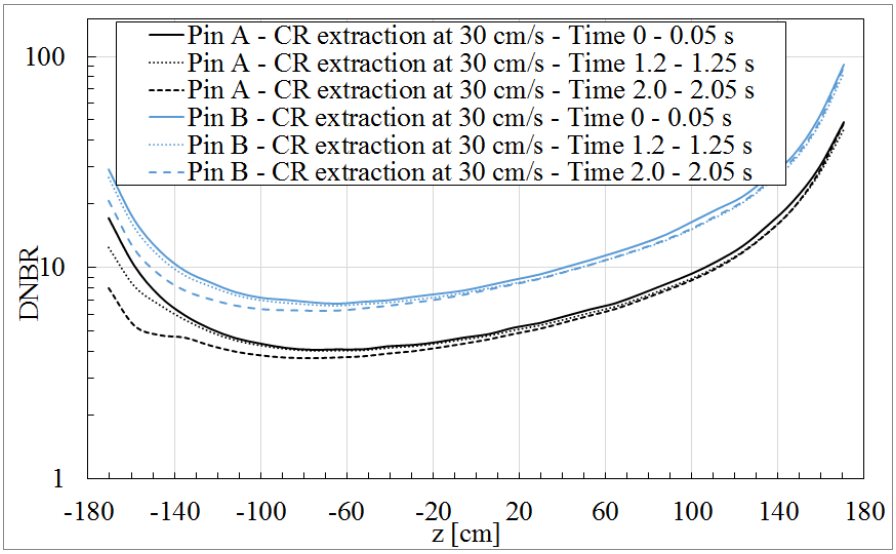

Figure 5.15: Serpent-SCF transient results for the TMI minicore for the DNBR axial profile evolution for pins A and B in Fig.5.2 - results for CR extraction at 30 cm/s.

The Figure 5.15 presents the results for the DNBR for the same pins *A* and *B*. Despite not being these two pins the most demanded ones in the core, the analysis of the axial dependences as a function of the time is key to understand the behaviour of this parameter during *transients*. The DNBR is a parameter that takes into account both the power and the TH conditions (since it is a ratio of the critical heat flux to the actual heat flux, thus dependent on the coolant conditions, see Eq. 2.41). For this slender minicore case the axial power shape is heavily tilted to the lower zone of the core, generating the minimum values minimum in the lower core zone for both pins. In the coolant inlet the lower temperatures dominate the behavior and generate a high DNBR, while in the outlet zone the high DNBR is due to the low power densities, leading to the axial shape in the Fig. 5.15. Moreover, the same strong spatial effects with time already observed in Figs. 5.14 are appreciated, where the local effect of the CR is clearly observable for pin *A* (located in the central rodded FA), that disturbs the axial shape. Furthermore, the pin *A* exhibits higher power and temperatures than pin *B* (see Figs. 5.11 and 5.12), that leads to a lower DNBR, corroborating the consistency of the *Serpent-SCF* results.

5.5 Consistency of the Serpent-SCF solution for coupled *transients*

A comparison of the *Serpent-SCF* results for this TMI minicore with other MC-based plus subchannel TH is provided in (Faucher et al., 2020), where a qualitative and quantitative consistent behavior is reported, showing differences in power evolution within the statistical convergence of the considered MC codes. On top of that, the robustness of the solution obtained with this MC-based approach is here briefly discussed. Regarding the amplification of the statistical uncertainty from MC in the TH within *transient* calculations, the physical characteristics of the neutronic-TH problem stabilizes this effect for these cases, since the feedbacks with power are

negative within LWR configurations (Sjenitzer, 2013; Ferraro et al., 2019a). Moreover, the numerical stability of the solution with the time bin size must be also checked for these MC-based calculations. It has to be regarded here that the time step size does not behave in this *Serpent-SCF* scheme as for the Eq. 2.10, since there is no approximation of the time derivative (e.g. a finite difference (Turinsky et al., 1994)), but rather a direct calculation of population within each time bin. Besides, the potential limitations arising from the TH side of the solution can be discarded since the time step in *SCF* is defined to avoid potential numerical instabilities, where a finer time steping than the imposed to the neutronic side is allowed (see Fig. 3.6). To prove this statement, the same *transient* scenario # 1 is re-run doubling the time bin size (i.e. considering 50 time bins instead of 100, but maintaining the total number of particles and total time), as depicted in the Fig. 5.16.

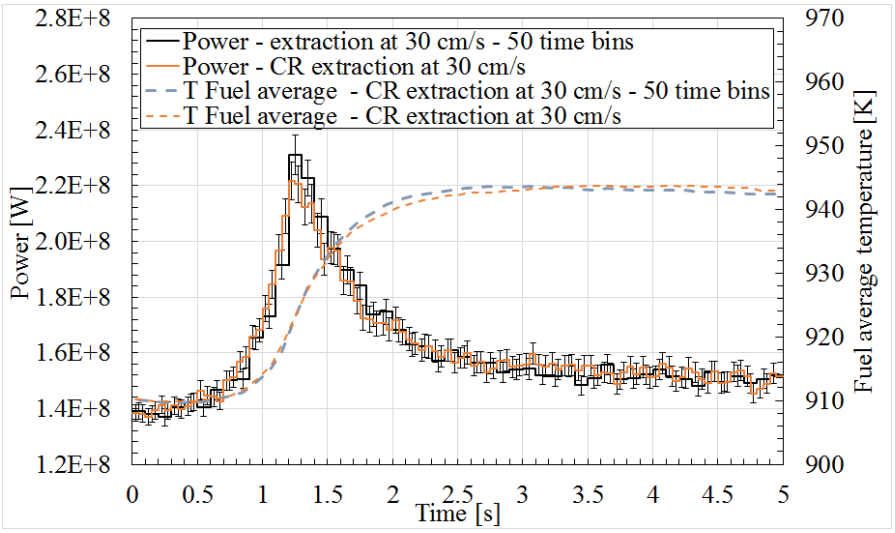

Figure 5.16: Serpent-SCF transient results for the TMI minicore for two different time bin sizes - Scenario #1. Error bars represent statistical uncertainty at 2σ.

The Fig. 5.16 shows consistent results for the total power and average fuel temperatures when the time step is doubled. The powers are statistically the same (i.e. the results are within the statistical error bars) and the temperature differences are below 1 $[K]$ (i.e. ~ 0.1 [%]). For the bigger time steps (i.e. 0.1 [s], which represents a value considerably larger than those required within industry-standard methods (Kozlowski and Downar, 2007)), the only appreciable effect is a decrease in the statistical convergence, which is due to the fact that the same amount of particles are distributed in a bigger time bin.

5.6 Final comments from the *Serpent-SCF* coupled *transients* verification using TMI minicore scenarios

The aptness to develop these *pin-by-pin* coupled *transient* calculations within a reduced LWR geometry is assessed, showing that the *Serpent-SCF* coupling can represent the key neutronic and TH physical phenomena. Moreover, the capability to obtain *safety-related* parameters in a direct manner is also shown. Conversely, the major constraints arise from the computational requirements (see Table 24 in Appendix Section D.1).

"Reality is the only truth."

— Argentine proverb

6 Validation and verification for transient calculations within real PWR configurations

In this Chapter the validation of the approach with experimental data from LWR-kind configurations (and operational ranges) is developed to assess its aptness for the stated objectives. For such purpose, a series of coupled *transients* are here analyzed. Firstly, RIA-kind scenarios from the SPERT IIIE reactor experimental campaign (McCardell et al., 1967) are studied with *Serpent-SCF*, validating the aptness of this approach and showing its capability to provide safety-related parameters. Finally, its suitability to tackle full-core size *transients* is also here studied using as basis a full-core numerical benchmark for PWR loaded with mixed-oxide *burned* FA, which represents the highest complexity foreseen (Kozlowski and Downar, 2007).

6.1 Validation using SPERT-IIIE experimental data

A series of transient experiments conducted in the SPERT III reactor using the E-Core (McCardell et al., 1967) have been selected for comparison with the *Serpent-SCF*. This SPERT-IIIE was a 40 MW pressurized water research reactor, designed in the 1960s as part of the U. S. Atomic Energy Commission's reactor safety program, devoted to experimental and theoretical investigations of the kinetic behavior and safety of nuclear reactors. Several tests were held during 60s and 70s in this facility, where the selected set of experiments to be considered here provide RIA-kind scenarios within a PWR-type core starting from a HFP condition. These experiments were initiated with a sudden withdrawal of an transient control rod designed for such purpose, which leaded to reactivity insertions ranging from 0.5 to 1.3$. As a result, these experiments provided data for non-damaging power excursions with reactor periods from from 10 to 1000 msec. It should be noted that these experiments were not deemed to provide detailed pin-by-pin results, but they represent the most-relevant set of experimental for RIA-kind scenarios within a PWR-type core at initial conditions other than cold-startup. Hence, the quality of the available reported data within (McCardell et al., 1967; Olson, A. P., 2015) represents a source of discrepancies, as has already been discussed by several authors (Zoia and Brun, 2016; Olson, A. P., 2013; Cao et al., 2015; Levinsky et al., 2019).

This reactor was devoted to conduct core behavior and safety studies under operating conditions typical of a PWR. The core configuration was a square lattice type, where three different rodded-type fuel assemblies (FA) could be loaded. The fuel assemblies could either be standard (SFA), control fuel type (CFA) or central (16FA), schematically depicted in figs. 6.1a and 6.1b for the first two cases, where details are provided in the Table 30 and 31 in Appendix Section D.4.

For the reactivity control, the SPERT-IIIE reactor had eight CFA (arranged in four pairs) and

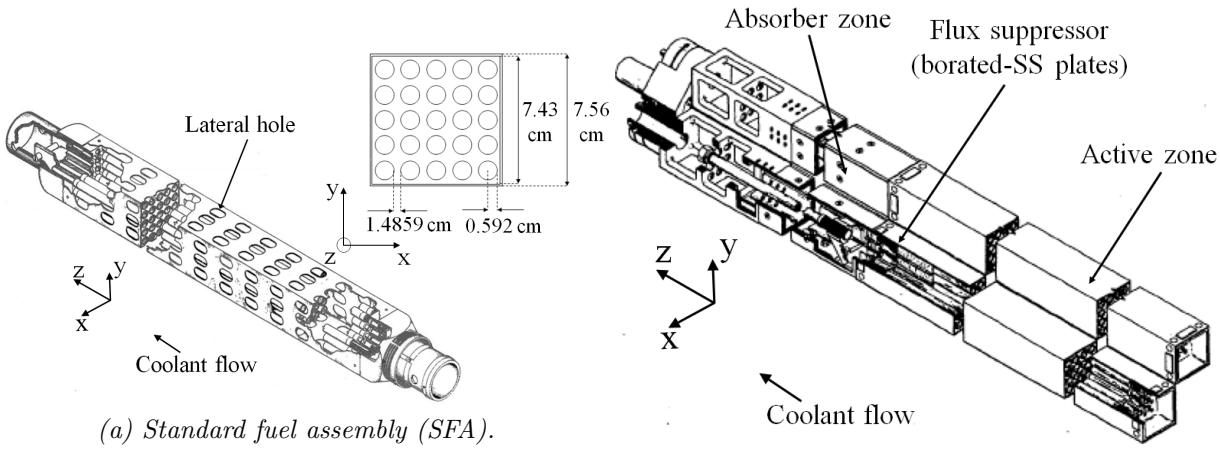

(a) Standard fuel assembly (SFA).

(b) Control fuel assembly (CFA).

Figure 6.1: Scheme of the fuel assemblies in SPERT-IIIE (obtained from (Olson, A. P., 2015))

a central cross-shaped absorber (namely transient rod - TR), used to generate the fast transients to be analyzed here. The FA were rodded-type, formed by fresh fuel pins of low enriched uranium oxide with Stainless Steel (SS) cladding, having all the same FR pitch. These rods could be either in a 5x5 pin array (SFA), an axially movable 4x4 array (CFA, where the neutron absorber box is located above the fuel pins) or in a 4x4 fixed array (16FA) that surrounded the TR, where intermediate spacer grids ensure the geometrical stability, as for the PWR designs (see Fig 1.1a). They were canned and placed into a square lattice array grid at core level, which included Zircalloy-2 guide tubes for the CFA and the central 16FA to avoid potential structural damage from the CR or TR movements. An scheme of the standard 60 FA core configuration is shown in the Fig. 6.2, where the positions of the described components are depicted.

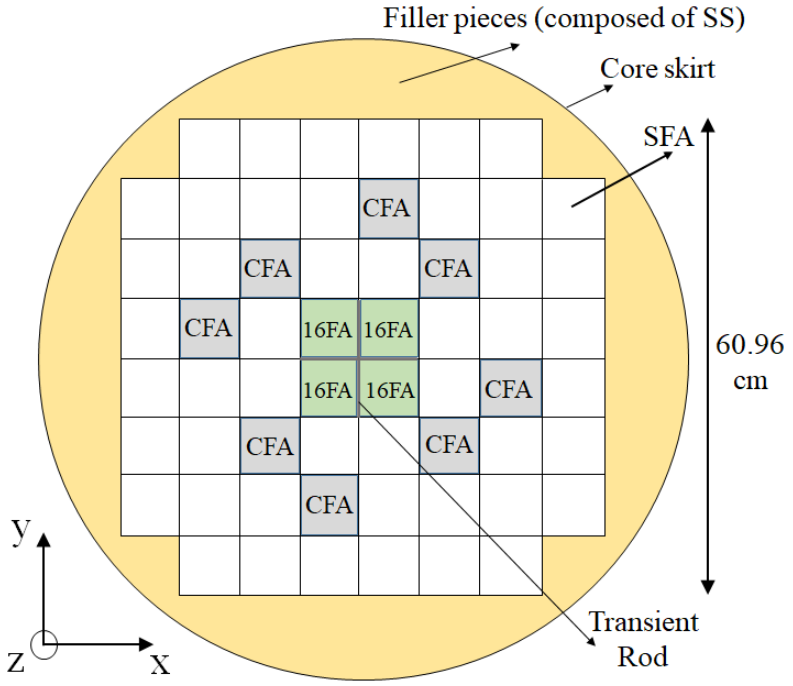

Figure 6.2: Scheme of the SPERT-IIIE core, identifying main components. See also figs. D.2 and D.3.

As depicted in Fig. 6.1a, the can of the SFA included lateral holes that could be configured to allow coolant flow between SFA in the core, which were not present in the other FA types. Besides, for the CFA, the zone between the active fuel and the absorber included neutron flux suppressors (i.e. thin plates of SS poisoned with Boron-10 attached to the upper fuel zone). The central TR depicted in Fig. 6.2 included a SS follower that was present in core for the fully extracted position, thus no extra water gaps are present in the central zone of the core during its withdrawal. Besides, the outside zone of the core counted with thermal shields and special SS filler boxes that filled the space between the core and the core skirt (see figs. D.2 and D.3 in the Appendix Section D.4).

From the whole set of experiments developed (McCardell et al., 1967), those starting at a hot full-power state at 20 MW have been selected for the validation. These scenarios are named as T-84 and T-85, from which no initial CR positions are reported. Main aspects are summarized in Table 9, where the reported experimental uncertainty is included.

ID	**Peak reactivity [$]**	**Inlet T [°C]**	**Flow rate $[m^3/h]$**	**Initial power [MW]**	**Peak power [MW]**	**Peak time [s]**
T-84	0.46±0.02	263±2	2725	19±1	39±4	0.18±0.02
T-85	0.87±0.04	262±2	2725	19±1	130±10	0.155±0.005

Table 9: Main TH and reactivity parameters from the selected experiments to be analyzed for the SPERT-IIIE reactor.

As a result, to tackle this validation process, the following steps are here developed:

1. An initial validation of the Serpent stand-alone model is assessed, where all parameters that govern the *transient* evolution are analyzed, both at Cold Zero Power (CZP) and Hot Zero Power (HZP).
2. A rough estimation of the impact of specification uncertainties on the results is held.
3. Specific reported RIA-experiments are selected, calculated with *Serpent-SCF* using a pin-by-pin coupling and globally compared with experimental data, assessing the capability to reproduce the main behavior reported in (McCardell et al., 1967).

6.1.1 Serpent and *SCF* models

The lack of detailed material and geometrical information for this reactor has to be considered if accurate neutronic and TH models are required. These inconsistencies include core compositions (namely impurities of structural materials), guide tubes sizes and can thickness. Moreover, the experimental results for stationary core parameters (such as global reactivity, control rod worth, etc.) also show a big discrepancy between diverse reported experimental measurements (Zoia and Brun, 2016). A graded approach is executed to establish consistent Serpent and *SCF* models, where the following considerations are done:

1. The material compositions as available in (McConn et al., 2011) are considered, except for the fuel, where composition from (Olson, A. P., 2015) are used. Besides, as recommended

in (Olson, A. P., 2015), SS348 were considered instead of SS347 for fuel cladding.

2. A mass of 50 g of SS348 was considered for the intermediate spacer grids of the SFA, positioned according to (McCardell et al., 1967). A scaled mass was used for the CFA and 16FA.
3. The gap between outer Zircalloy 2 guide tubes and FA preserve the same gap as for the FAs (see Table 31).
4. The thickness of Zircalloy-2 guide tubes for the central FA is obtained considering a 0.0635 [cm] gap between outer FA can and the guide tube and 0.3175 [cm] between the guide and the CR. This approach preserves the reported FA gaps (see Table 31) and resulted in ~ 0.3 [cm] thickness of Zircalloy for the central FA.
5. The thickness for the control fuel assemblies Zircalloy 2 guide tubes is obtained considering a 0.1905 [cm] gap between the CFA fuel zone and the guide tube, also preserving the FA gap (see Table 31) resulting in a thickness of ~ 0.4175 cm.
6. The thickness of the SS can for all fuel assemblies is calculated from the outer size and the reported flow area, resulting in 0.0639 [cm], 0.0626 [cm] and 0.1837 [cm] thickness for the 5x5 fuel assembly (SFA), the 4x4 (16FA) and the CFA respectively, thus ensuring the correct fuel-moderator ratio.
7. The lateral can holes of the SFA are homogenized in the Serpent model for geometrical simplicity (see Fig. 6.1a), resulting in ~ 75 [%] SS and ~ 25 [%] of coolant in volume. The same approach is considered for the zone between the active fuel and the hollow absorber of the CFA, where the homogenization considers the volume of pins, cans and neutron flux suppressors.
8. A constant gap heat transfer coefficient is considered (of $10e3$ $[W/m^2/K]$) in the *SCF* model (typical value for PWR).
9. To handle the neutronic-TH feedback, the fuel temperatures and coolant temperatures and densities are modified using nested IFC meshes, considering a pin-by-pin coupling with 20 equidistant axial zones (see Section 3.4.3). Besides, independent coolant materials for the core inlet and outlet are also considered.
10. JEFF3.1.1 ACE NDL is considered (Santamarina et al., 2009), where it should be noted that the delayed neutron data is condensed to 8 precursors groups.

An scheme of the Serpent neutronic model is presented in Fig. 6.3, which includes the core skirt, thermal shields and RPV (see Fig. D.3 in Appendix Section D.4) and considers a *black boundary* condition for the radial and axial directions (Ferraro et al., 2020d).

Main components within the core in the Serpent model are identified in Fig. 6.3b, where the axial modeling of the CFA is depicted in figs. 6.3c and 6.3d. This TH feedback for this neutronic model comes from the a *coolant-centered* model in *SCF*, as presented in Fig. 6.4.

Regarding the axial discretization of this TH model, the same number zones as for the Serpent model IFC are considered (i.e. 20 axial zones). Being all FA canned, no cross-flow between FA is

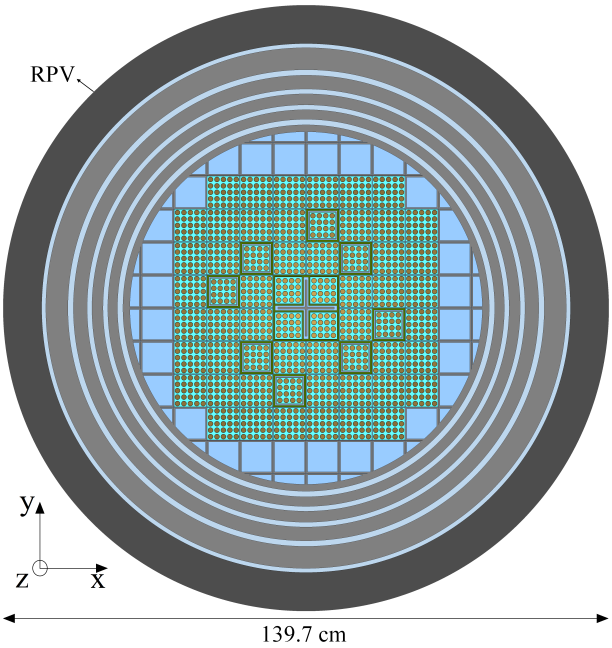

(a) Plot of the Serpent model for xy cut at $z = 0$ cm, CR extracted. Radial surface is a black boundary.

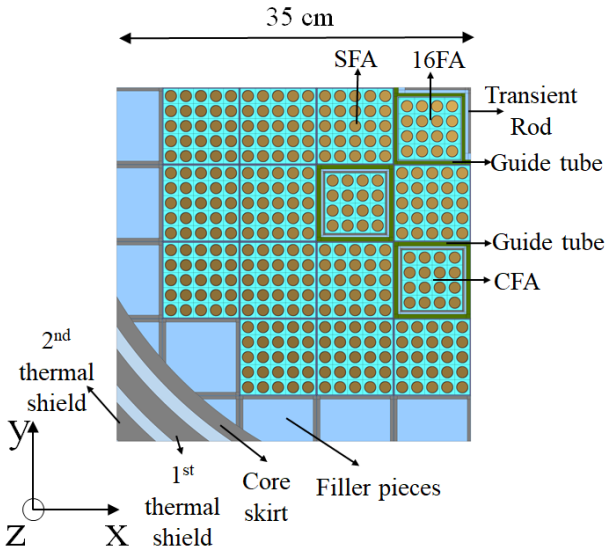

(b) Plot of the Serpent model for xy at $z = 0$ cm, detail for the bottom left quarter of core, showing CR and TR.

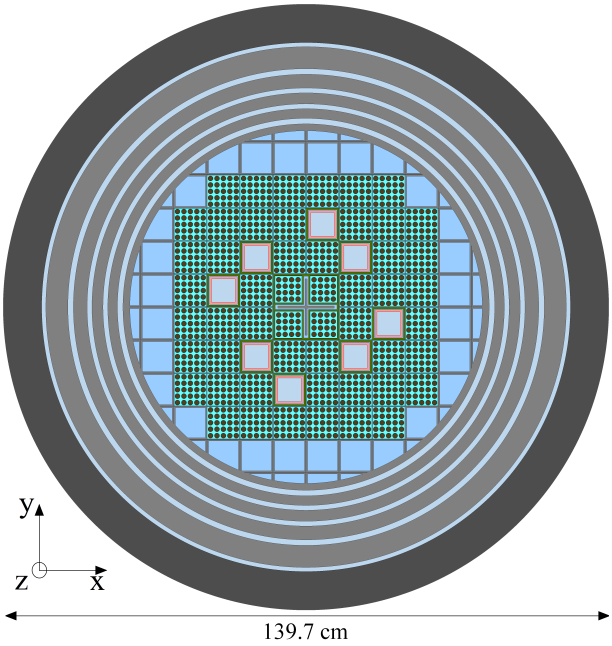

(c) Plot of the Serpent model for xy cut at $z = 0$ cm, CR inserted. Radial surface is a black boundary.

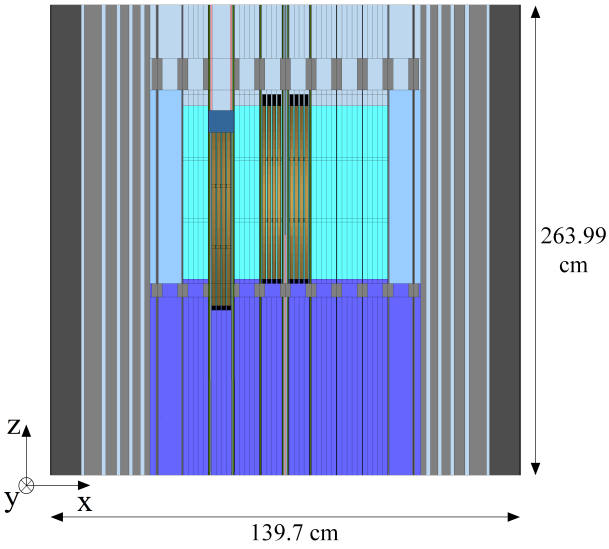

(d) Plot of the Serpent model for xz cut at $y = 6$ cm, CR extracted. Xz cut 6cm from center of core, the CR inserted 25cm. Radial, top and bottom surfaces are black boundaries.

Figure 6.3: Schematic plot of the Serpent model for the SPERT-IIIE, (x,y,z)=(0,0,0) [cm] corresponds to the center of the FA and AL.

considered (it was considered that SFA were arranged in such way, as far as no specification was available in (McCardell et al., 1967)) thus *SCF* model considers that no mass, momentum or energy is transferred between FA (see details in Fig. 6.4). The convergence criteria for the *SCF* TH solution have been selected to be at least one order of magnitude below the neutronic-TH coupling convergence criteria for the steady-state calculation. Finally, for the coupling between Serpent and *SCF* models, a volume averaged fuel temperatures is considered for the TH feedback

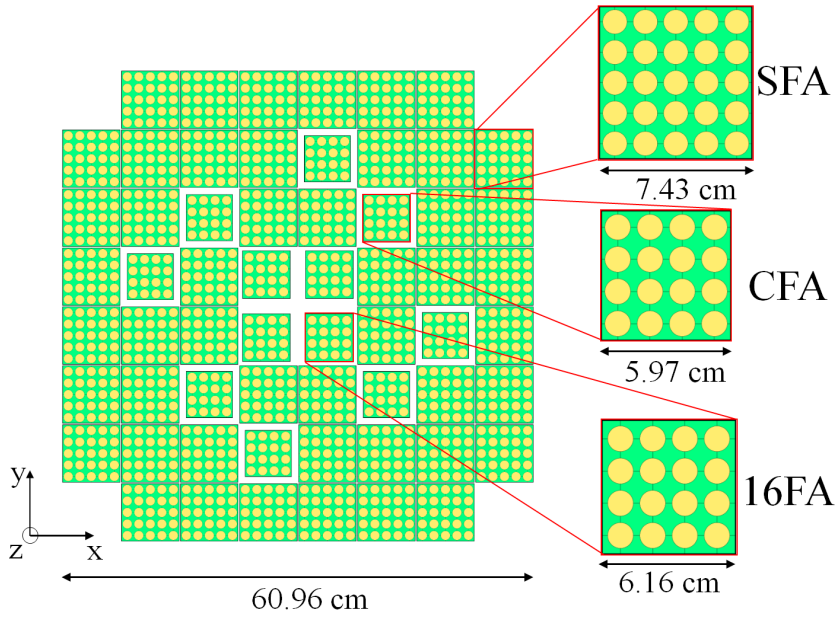

Figure 6.4: Scheme of the SCF model for the SPERT-IIIE, (x,y,z)=(0,0,0) [cm] corresponds to the center of the FA and AL. Details for FA types are included.

and convergence in L_2 norm and a relaxation of TH fields is set for *steady-state* calculations (i.e. 20 [K] and 2.5 [K] for fuel and coolant temperatures and to 0.01 $[g/\text{cm}^3]$ for the variation in density, and a $\omega = 0.5$ for the relaxation of TH fields between iterations, see section. 3.4.4). Besides, the *transient* calculations are developed fully-explicit (see Fig. 3.6). In view of the computational requirements, an HPC is considered for the runs (i.e. ForHLR II (SCC, 2020)), where details can be gathered Table 32 in the Appendix Section D.4.

To develop a consistent validation the accepted level of agreement for the different parameters has to be clearly stated. Hence, for core reactivities calculations in *steady-state* CZP and HFP (such as TR reactivity worth, excess reactivities, etc.) differences in the order of ∼1-1.5 β_{eff} are accepted, as already studied by (Zoia and Brun, 2016; Olson, A. P., 2013; Cao et al., 2015; Levinsky et al., 2019), mainly related to the quality of the specifications available. Besides, for the main parameters governing the time evolution of the coupled case (such as kinetic parameters and isothermal reactivities), differences in the order of ∼5-10 [%] are accepted, in line with the reported experimental uncertainty (Olson, A. P., 2015). Finally, for the *transient* scenarios presented in Table 9, the accurate modeling of the whole time evolution is required within both experimental and calculation statistical uncertainty, where the correct modeling of power peak is considered a key factor. It should be regarded here that the reported experimental error for these cases only provide precise values for the initial and peak powers, where the values are ∼5 [%] and ∼10 [%] respectively (as shown in Table 9). Thus, it is considered a good agreement the correct representation of the power peak within the reported experimental error, together with the full time scope agreement with differences between ∼5 [%] to ∼10 [%].

6.1.2 Validation results for the SPERT-IIIE without TH feedback

As a first step, the *Serpent* standalone results for CZP are presented in Table 10, including the kinetic parameters obtained with the *Iterated Fission Probability* method (IFP), while the

comparison with reported experimental values is presented in Table 11. A good agreement is encountered for all parameters (i.e. differences below 1.5 β for core reactivities and 5 and 6 [%] for TR worth and kinetic parameters).

Case	k_{eff}	β_{eff} **[pcm]**	ρ**[pcm]**	ρ **[$]**
ARO	1.0962±6E-5	748.8±3.0	8775±5	11.7±6E-3
TR in	1.0594±6E-5	762.0±3.2	5603±5	7.4±7E-3

Table 10: Serpent calculated results for the integral neutronic parameters of SPERT-IIIE at CZP (Uncoupled). Statistical uncertainty for Serpent at 1σ.

Parameter	**Measured**	**Calculated**	**Difference**
Excess ρ [$]	13.1±0.7	11.7±6E-3	1.4
TR Worth [$]	4.6	4.4	0.2
$\beta_{eff}/\Lambda_{eff}$ [ms]	2.15±0.2	2.03±0.01	0.12

Table 11: Serpent calculated results for the integral neutronic parameters of SPERT-IIIE CZP results comparison with reported values from (Olson, A. P., 2015). Statistical uncertainty for Serpent at 1σ.

As a second step, a comparison of Serpent results for different operational temperatures and TR positions is presented in Fig. 6.5 including the experimental reported values.

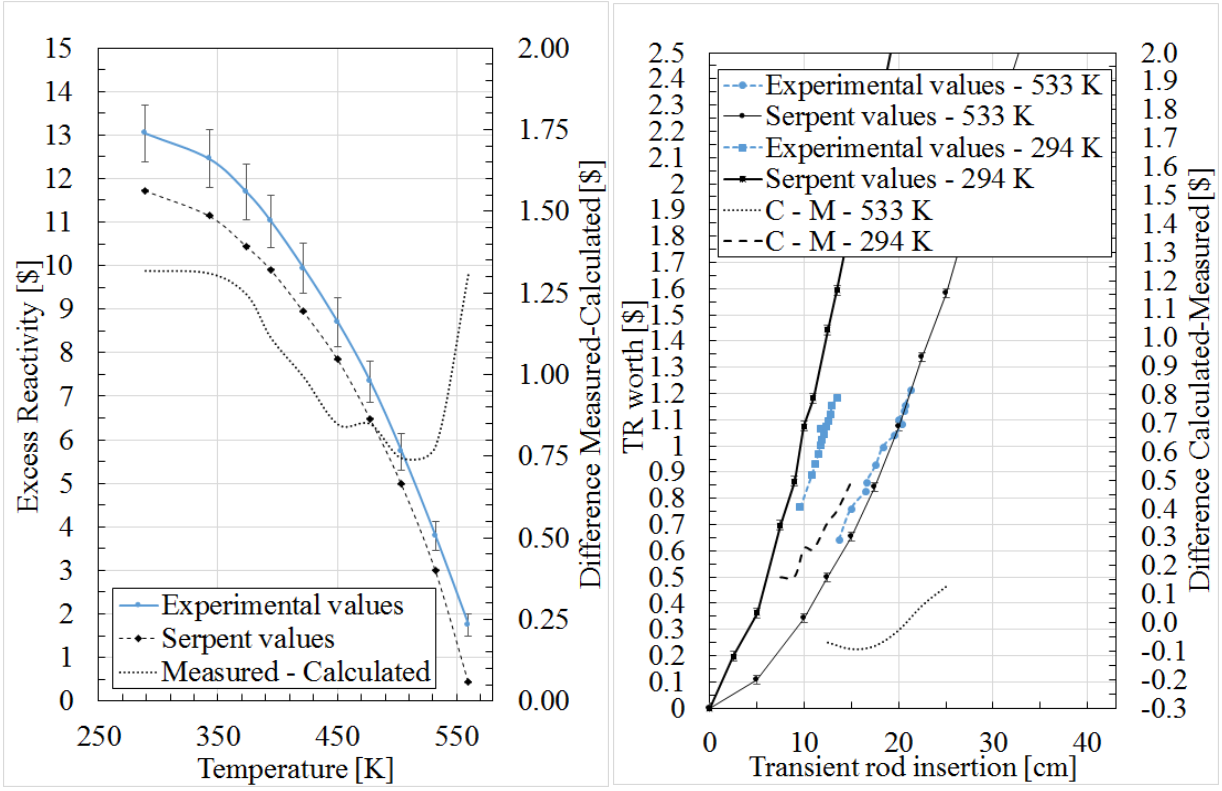

(a) Results for isothermal reactivity effect. *(b) Results for TR worth at CZP and HZP.*

Figure 6.5: Stand alone Serpent calculation results comparison with reported data for the SPERT-IIIE reactor. Error bars represent the statistical uncertainty for Serpent at 2σ.

The Fig. 6.5a presents the comparison of results for the isothermal reactivity, obtained considering the whole core at the same temperature. Morever, the results for the transient rod

reactivity worth are compared with the reported ones both for CZP and HZP cases obtained from (McCardell et al., 1967) in Fig. 6.5b), where for both cases an initial CFA position near critical was considered. All these parameters represent differential quantities, since both the excess reactivity and the TR worths are not measured in a reactor by direct means (i.e. they are obtained from the integration of the experimental differential control rod worths (McCardell et al., 1967)).

The decrease of excess reactivity for higher temperatures is appreciated in the Fig. 6.5a, due to the negative feedback coefficients for this PWR-kind configuration. A good agreement is observed for the isothermal behavior, with differences in Fig. 6.5a between 0.8 to 1.3 β_{eff} (i.e. between $\sim$ 650 to $\sim$ 990 [pcm]). This results into a $\sim$ 6 [%] of difference for isothermal feedback coefficient (calculated as the change in reactivity divided by the delta of temperature, i.e. experimental value of $\sim$ -0.038 [$/K] and a calculated one of $\sim$ -0.036 [$/K] for the temperature range shown in Fig 6.5a). Besides, for the transient rod results in Fig. 6.5b the effect of the CFA axial position is appreciable (i.e. more inserted for the CZP due to the effect of the temperature described), which leads to an increase in the TR worth for the CZP case. For these comparisons, the agreement with experimental values is also good, with differences between 0.1 to 0.5 β_{eff}. Hence, the parameters that govern the *transient* behavior (i.e. TR reactivity shape, isothermal reactivity change and core kinetic parameters) calculated by this Serpent model agree with the experimental values within the required accuracy.

As a final step, the lack of detailed specification for relevant core components is here addressed to provide a quantification of the impact of each of these on the neutronic modeling. For such purpose, a rough analysis of the effect is done within the Serpent neutronic model through modifications in specific components. Therefore, the impact of the consideration of the intermediate grids in the FA, the neutron flux suppressors for CFA, the Zircalloy guide tubes for the 16FA and CFA (see Fig. 6.3b) and the impurities on SS348 (i.e. the concentration of Tantalum) are studied. The results obtained are presented in Table 12, where an additional CZP ARO case using ENDF/B VII.0 NDL (Chadwick et al., 2011) is also included to provide a gross assessment of the impact of the nuclear data.

#	**Case description**	ρ **[pcm]**	ρ **[$]**
a	No intermediate grids modeled	315	0.41
b	No flux suppressors (ARO) modeled	30	0.06
c	Model 1mm less Zr in central guide tubes	40	0.09
d	Model 1mm less Zr in CFA	400	0.64
e	Model SS348 without Tantalum	690	0.81
f	Consider ENDF/B VII.0 NDL	-76	-0.1

Table 12: Impact of the experimental configuration lack of specifications for the SPERT-IIIE in the Serpent model - system reactivity results for CZP.

Regarding results from Table 12, the sum of all reactivity changes can provide a reactivity offset of $\pm$1.5$ only due to the specification uncertainty, which is in line with the reported discrepancies in (Zoia and Brun, 2016; Olson, A. P., 2013; Cao et al., 2015; Levinsky et al.,

2019). Nevertheless, it is important to note that the starting positions during the transients are not reported (McCardell et al., 1967), thus reactivity offset attributed to lack of specification have no impact on the further *transient* calculations.

6.1.3 *Serpent-SCF steady-state* results for the SPERT-IIIE at HFP

The coupled *steady-state* critical case required as starting point for *transient* calculation is here described (see Section 3.5). A total power of 20MWth is considered, where the CR and TR critical configuration is obtained through successive iterations where the TR was adjusted to be able to introduce a maximum reactivity of ∼1 β_{eff}. The resulting extraction positions in the axial dimension z for the CR is ∼15 cm, compensated with a insertion of ∼25 cm of the TR (in the same axial dimension). This configuration is considered to obtain the source files with the precursors and *live* neutrons to be used for further transient calculations. The resulting converged power densities and temperatures are presented in the figs. 6.6 and 6.7.

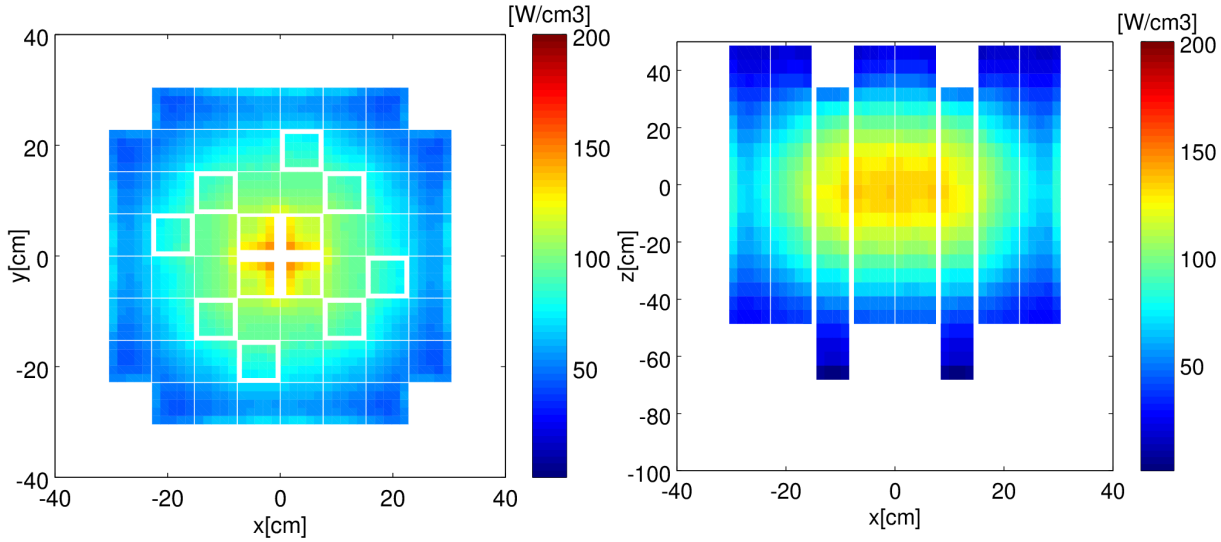

(a) Xy cut for a slice of 4.9 cm, starting 19.5 cm above core center (z = 0 cm, see Fig. 6.3).

(b) Xz cut for a slice of 1.5 cm, starting at y = -13.7 cm (see Fig. 6.3).

Figure 6.6: Serpent-SCF steady-state calculated results for the SPERT-IIIE reactor at 20MW - results for power density.

The Fig. 6.6a shows the power density for an xy slice of 4.9 [cm] starting 19.5 [cm] above core AL center (i.e. z = 0 [cm]), while the Fig. 6.6b depicts an xz slice of 1.5 [cm] starting at y = -13.7 [cm] (i.e. showing the two CFA positions in the second row in bottom side of the core plot, see Fig. 6.2). These power density profiles show the effect of the different components within the core. The effect of the central TR (inserted 25 [cm] from top to bottom) is appreciated in the Fig. 6.6a as a power density depression instead a peak in this inner radial zone. The core reflector can be also noted, where an increase in the power for pins in the FA placed in the outer radial core zone positions is seen. Besides, the axial displacement of the CFA placed at x = ±11.4 [cm] is appreciated in Fig. 6.6b (i.e. 15 [cm] extracted from core, allowing the insertion of the absorber CR from the upper part).

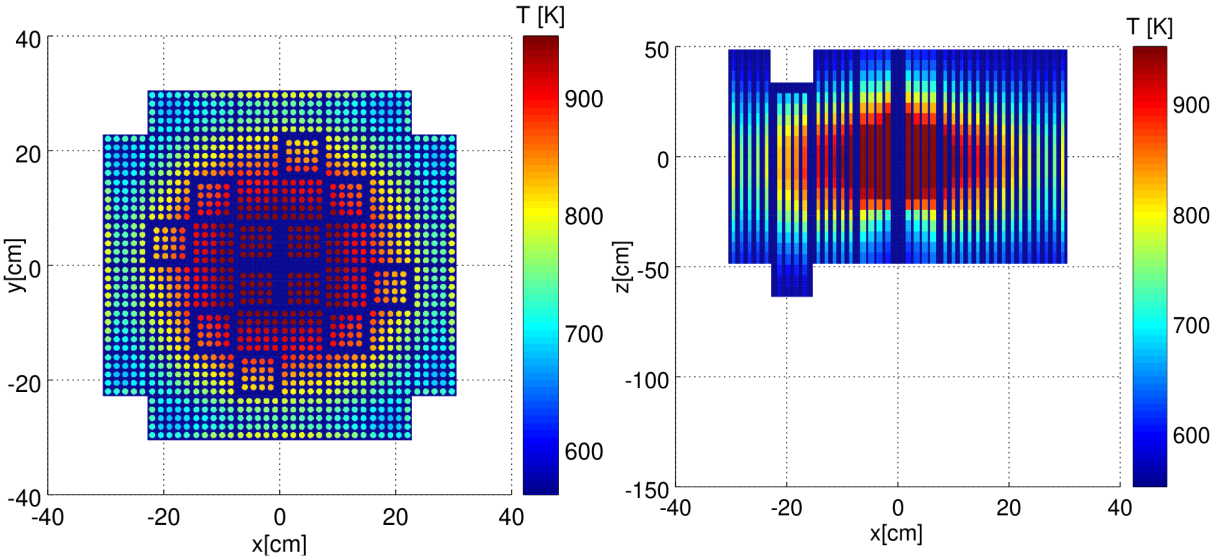

(a) Xy cut for a slice of 10 [cm], starting in the core center (z = 0 [cm], see Fig. 6.3).

(b) Xz cut for a slice of 0.01 cm, starting at y = 3.8 cm (see Fig. 6.3).

Figure 6.7: Serpent-SCF steady-state calculated results for the SPERT-IIIE reactor at 20MW - results for power density.

The Fig. 6.7a depicts the calculated temperature for a 10 cm xy slice starting in the core center (i.e z = 0 [cm]) and in the Fig. 6.7b for a xz cut of 0.01 [cm] starting at y = 3.8 [cm] (i.e. showing the CFA in the first row of the left-top side of the core plot, see Fig. 6.2). These temperature profiles reflect the power distributions, where increments in higher power density zones are translated into higher temperatures. It is also noticeable the effect of the position of the CFA in Fig. 6.7b (i.e. 15 cm extracted), which generates an axial shift in the temperature profile to the lower zone of the core, resulting from the power distribution.

Additional key coupled criticality calculations at HFP are presented in Fig. 6.8.

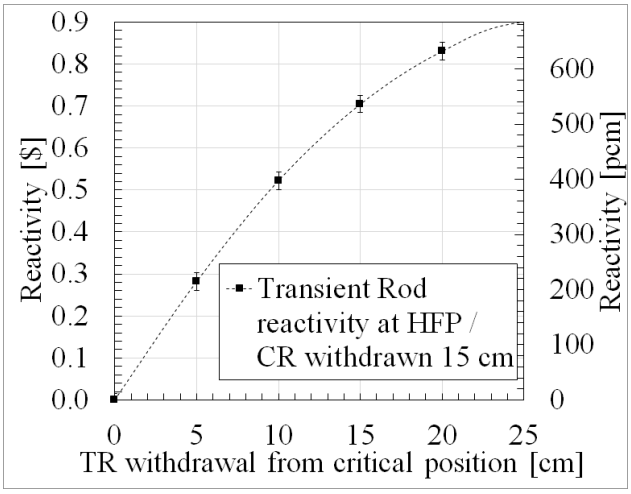

Figure 6.8: Serpent-SCF results for the TR reactivity worth in SPERT-IIIE from critical position at HFP - Error bars represent statistical uncertainty for Serpent-SCF at 2σ.

The results presented in Fig. 6.8 correspond to reactivity worths calculated for diverse TR

positions, required to define the TR movement to introduce the reported reactivity listed in Table 9. The dependence of this TR reactivity is not linear in the axial dimension since its neutronic worth diminishes when it is almost extracted, due to the higher probability of leak from the core for neutrons there (Duderstadt and Hamilton, 1976).

6.1.4 *Serpent-SCF transient* validation results for the SPERT-IIIE

For each case in the Table 9, a coupled *transient* calculation of 1 s with 100 time bins is considered (i.e. 10 ms per time bin, with 2e6 particles each), as summarized in Table 13. A constant speed of the TR withdrawal is assumed, since no experimental specification is provided (McCardell et al., 1967).

Case	TR movement [cm]	Speed [cm/s]	Time scope [s]
T-84	8.7	-67.1	0.04-0.17
T-85	22.9	-190.8	0.04-0.16

Table 13: Modeled TR withdrawal scenarios in Serpent-SCF for the SPERT-IIIE.

The reported experimental errors are included in the power and reactivity experimental results plots for both cases. For the reactivity, a relative 4 % is considered for each time value (as proposed in (Olson, A. P., 2015)), while the power plots are presented including the initial reported experimental relative error (∼5 %), where it should be regarded that the relative error near the power peak is reported to be ∼10 % for both cases. The results for T-84 are shown in figs. 6.9, 6.10 and 6.11, while the second scenario (i.e. T-85) is depicted in figs. 6.12, 6.13 and 6.14.

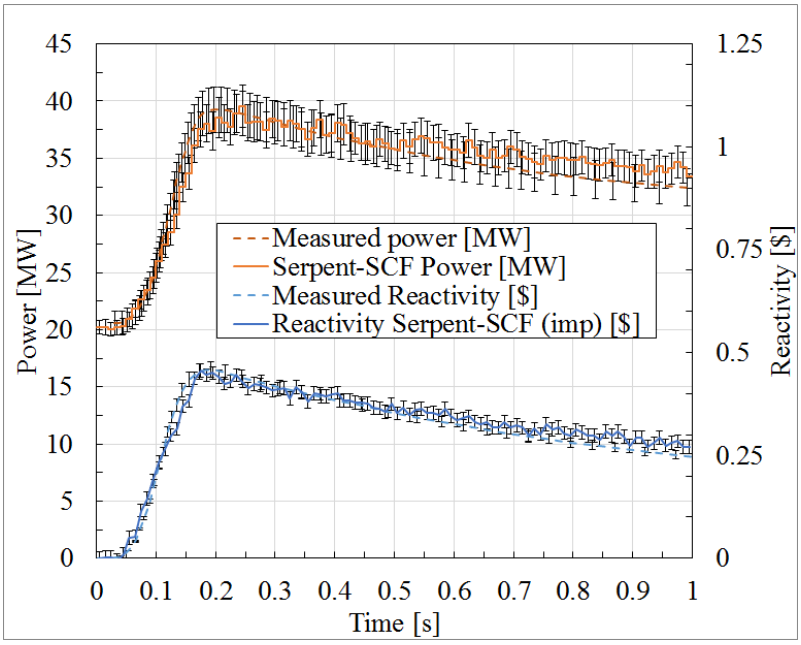

Figure 6.9: Serpent-SCF evolution of total power and system reactivity for the SPERT-IIIE reactor, comparison with experimental reported data - Test 84 - Error bars represent statistical uncertainty for Serpent-SCF at 2σ.

The Fig. 6.9 presents *Serpent-SCF* results for the total power evolution and system reactivity obtained for case T-84, together with the experimental reported values. A consistent behavior is observed in the results, where the aspects of the *transient* are modeled correctly by *Serpent-SCF*. The TR withdrawal generates a sudden reactivity insertion, which leads to a supercritical configuration associated with the power increase. This increase of power leads to an increment of fuel and coolant temperatures that provide the negative feedback that compensates the reactivity insertion. When comparing the calculated *Serpent-SCF* results, the evolution for reactivity and power results is found to be within the experimental uncertainty. A slight difference in the reactivity is observed near the power peak, which is reflected as a slight offset of the power evolution near this time. This slight difference is indicating that a more detailed TR movement should be used to obtain an exact match. In spite of that, no further adjustment of the CR movement was held since the main scope here is to validate the global evolution and assess the consistency of the feedbacks.

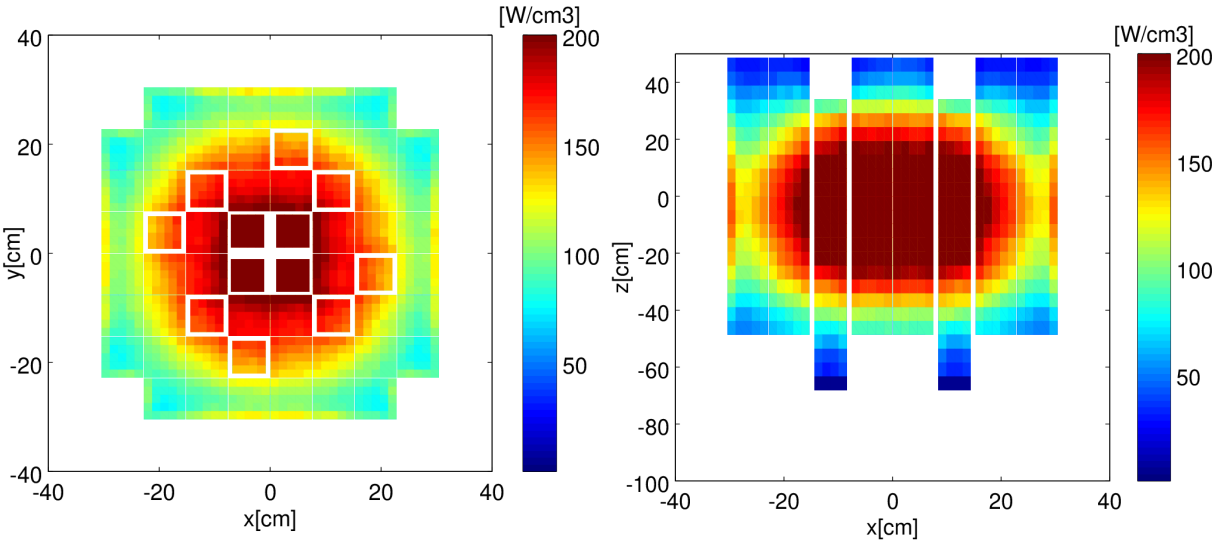

(a) Xy cut for a slice of 4.9 cm, starting 19.5 cm above core center (z = 0 cm, see Fig. 6.3), time 0.2 s.

(b) Xz cut for a slice of 1.5 cm, starting at y = -13.7 cm (see Fig. 6.3), time 0.2 s.

Figure 6.10: Serpent-SCF pin-wise power density results for the SPERT-IIIE reactor - Test 84, time 0.2 s. Average relative statistical error ∼1.5 [%].

The corresponding power evolution at pin-level is shown in figs. 6.10a and 6.10b for the same slices presented in Fig. 6.6 for a time of 0.2 [s] (i.e. in the peak power), where the average relative statistical error is reliable as defined in Table 1 (average ∼1.5 [%], maximum < 9 [%], located in the bottom of CFA). It can be seen in Fig. 6.10 that this power increment reproduces the power distribution already observed in the Fig. 6.6, where the increment in the central zone due to the TR withdrawal is noticeable.

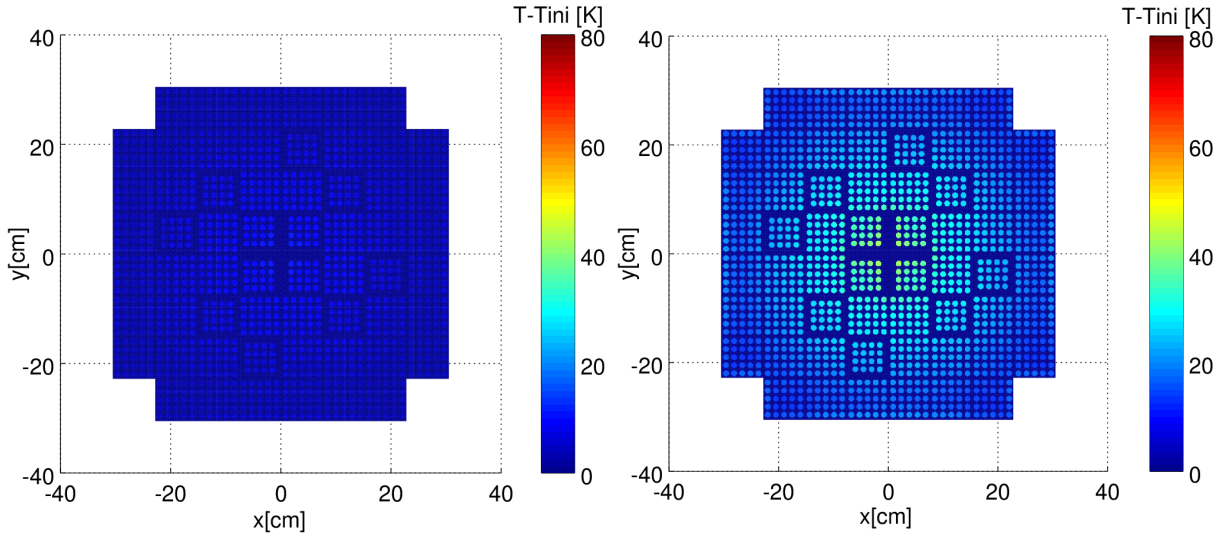

(a) Xy cut in a 10 cm slice from center of AL (z = 0 cm), 0.2 s vs initial time.

(b) Xy cut in a 10 cm slice from center of AL (z = 0 cm), 0.5 s vs initial time.

Figure 6.11: Serpent-SCF results for the SPERT-IIIE reactor - difference in the temperature for Test 84 at 0.2 and 0.5 s.

The Fig. 6.11 presents the differences in the temperatures calculated by *Serpent-SCF* with respect to the initial time at 0.2 and 0.5 s for an xy slice of 10 cm above center of the AL of the core (i.e. z = 0 cm). These reflect the increase of power seen in Fig. 6.10a due to the CR withdrawal, where the effect in the central zone is reflected as a higher temperature increase. Besides, higher values for the temperatures are observed for the second instant shown in 6.11b (i.e. after the power peak), since the temperatures evolution reflect the integration of the excess of power released in the system, as discussed in the following Section.

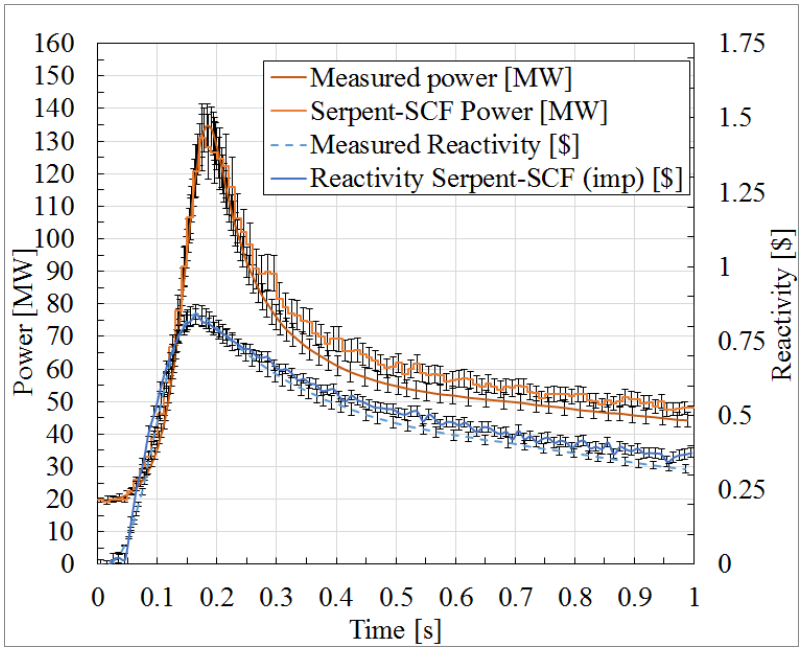

Figure 6.12: Serpent-SCF evolution of total power and system reactivity for the SPERT-IIIE reactor, comparison with experimental reported data - Test 85 - Error bars represent statistical uncertainty for Serpent-SCF at 2σ.

The T-85 case has a bigger reactivity insertion (see Table 9), thus the power and temperatures must be affected to a greater extent. The Fig. 6.12 shows the total power and reactivity evolutions calculated by *Serpent-SCF*, including the experimental reported data. The physical phenomena described for the former test is also observed in Fig. 6.12, where the reactivity inserted leads to a power increase which produces a temperature increment and compensates the effect due to the negative feedbacks. This higher power peak is thus correctly reproduced by *Serpent-SCF*, where the comparison with experimental results shows a good accuracy. A slight difference in the reactivity introduced is observed, where the same remarks apply as for the case T-84. Besides, a slight increase of the difference is observed for the power after the peak. Despite being this difference below 10 [%] with respect to the experimental results, it is important to note that several aspects produce slight modifications to this behavior, such as the fuel gap conductivity and the fuel temperature average that is considered (Grandi et al., 2010), unfortunately not defined within the experimental specification.

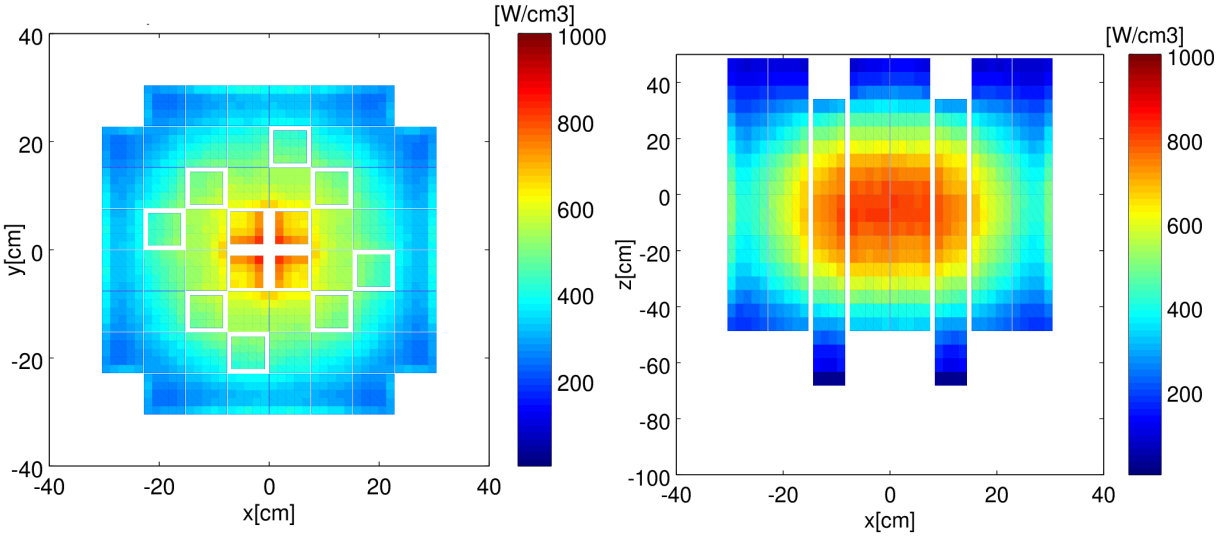

(a) Xy cut for a slice of 4.9 cm, starting 19.5 cm above core center (z = 0 cm, see Fig. 6.3), time 0.2 s., time 0.2 s .

(b) Xz cut for a slice of 1.5 cm, starting at y = -13.7 cm (see Fig. 6.3), time 0.2 s.

Figure 6.13: Serpent-SCF pin-wise power density results for the SPERT-IIIE reactor - Test 85, time 0.2 s. Maximum limits of color bar increased respect to Fig. 6.11. Average relative statistical error ∼ 1.5 [%].

The pin-wise power density calculated by *Serpent-SCF* are presented for this T-85 test case in Fig. 6.13 for the same slices presented in Fig. 6.6 for a time of 0.2 s (i.e. in the power peak), also statistically reliable (average and maximum values for the relative uncertainty of ∼1.5 [%] and < 9 [%]). These results are analogous to the former case, but with a much higher power increment (seen in Fig. 6.12 as a power peak with a factor of ~ 4 to the initial power), also accurately modeled by *Serpent-SCF*. This higher amount of power deposited within the reactor core leads to more noticeable temperature increments, as depicted in the Fig. 6.14.

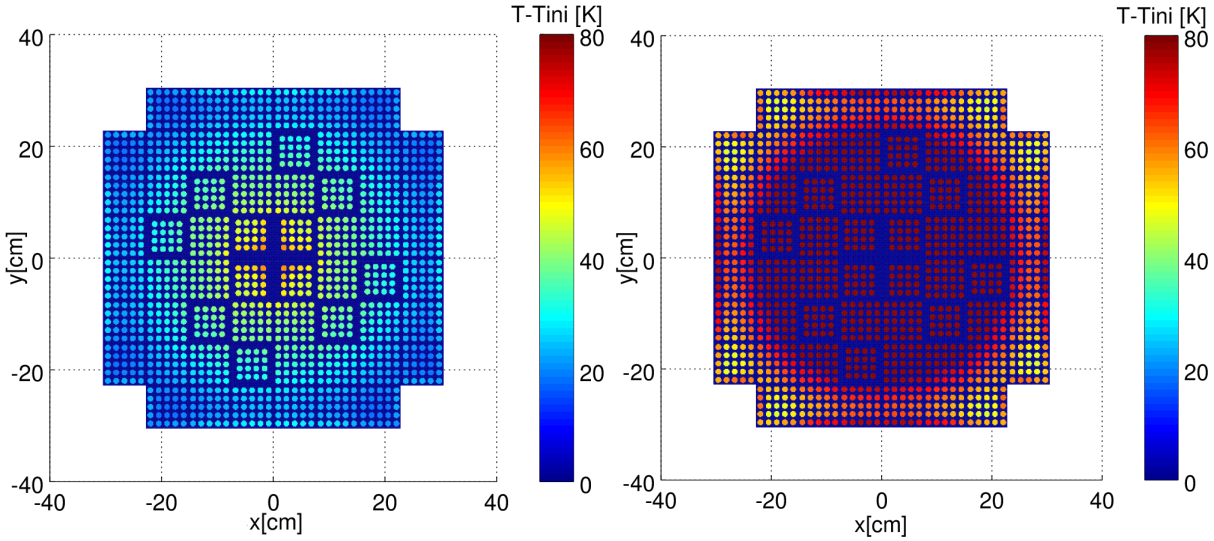

(a) Xy cut in a 10 cm slice from center of AL (z = 0 cm), 0.2 s vs initial time.

(b) Xy cut in a 10 cm slice from center of AL (z = 0 cm), 0.5 s vs initial time.

Figure 6.14: Serpent-SCF results for the SPERT-IIIE reactor - difference in the temperature for Test 85 at 0.2 and 0.5 s.

The Fig. 6.14 depicts the temperature differences with respect to initial time at 0.2 and 0.5 s respectively for an xy slice of 10 cm above core center of AL (i.e. z = 0 cm) for this case with increased power overshoot. Again the effect on the temperature is seen, where the power increase generates temperature differences that reproduce the spatial dependence and also provide the negative feedback, that are in this case much higher than those from T-84 due to the amount of reactivity introduced by the TR withdrawal.

As a summary, the comparison of experimental and calculated results for the maximum power for cases T-84 and T-85 shown in figs. 6.9 and 6.12 is presented in Table 14, where it is important to note that the differences encountered are within the reported experimental uncertainty.

Case	Reported [MW]	Calculated [MW]
T-84	39±4	39.6±1.2
T-85	130±10	131.1±6.8

Table 14: Serpent-SCF results for the SPERT-IIIE, comparison of power peak with experimental reported values McCardell et al. (1967); Olson, A. P. (2015) - Statistical uncertainty for Serpent-SCF at 2σ.

6.1.5 Main remarks from gross validation of *Serpent-SCF* using the SPERT-IIIE

The obtained *Serpent* values for the CZP and HZP calculations for the parameters that govern the phenomena within *transients* (such as kinetic parameters, isothermal coefficients and TR reactivity worths) are found to be within the reported experimental uncertainty, thus allowing to discard any inaccuracy in the models. Moreover, the *Serpent-SCF transient* calculations results for the selected HFP tests T-84 and T-85 results are also within the experimental error both for the power and system reactivity, being key parameters (i.e. power and reactivity

peaks) accurately reproduced both in shape and temporal position. Hence, the approach can be considered validated for these RIA-kind *transients*. Besides a consistent representation of the involved phenomena is found, showing the aptness of the proposed approach to reproduce the physics within real PWR configurations, thus reaching the stated objective in the Section 1.2.

6.2 *Serpent-SCF* safety-oriented calculations for the SPERT-IIIE

Key safety-related parameters can be also analyzed in a direct manner for this case, since the *Serpent-SCF* models consider a pin-wise representation. Two observables are selected for analysis in Fig. 6.15, which represent limiting parameters regarding the fuel integrity during RIA scenarios within PWR (see Section 2.6.2).

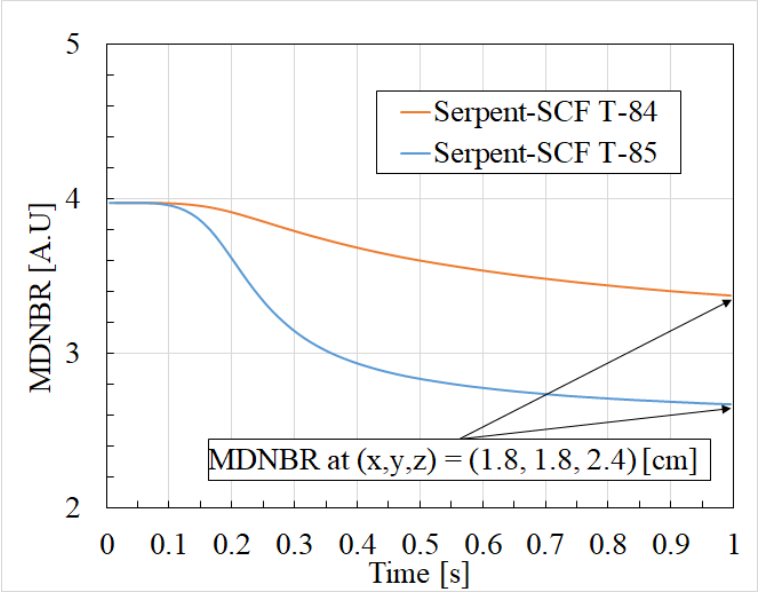

(a) Minimum DNBR evolution.

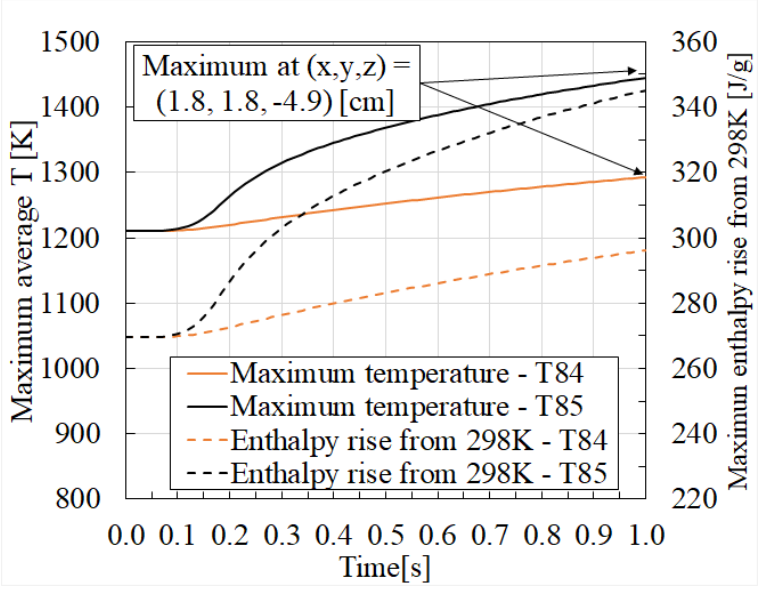

(b) Maximum fuel temperature and enthalpy rise.

Figure 6.15: Serpent-SCF calculated temporal evolution of key safety-related parameters for the SPERT-IIIE Tests 84 and 85.

The evolution of minimum value of the DNBR (i.e. MDNBR) is presented in Fig. 6.15a for the same tests T-84 and T-85, obtained using CHF correlations from (Doroschuk et al., 1976). Besides, the maximum enthalpy rise is also studied, using the correlations for fuel from (Oak Ridge National Laboratory, 2001) for both coupled *transients*, depicted in the Fig. 6.15b. Despite the unavailability of reference values for these cases, the behavior from figs. 6.15a and 6.15b can be quantitative analyzed to assess the consistency of the physical behavior. The MDNBR temporal evolution in Fig. 6.15a presents a decrement due to increased amount of power released to the system, where the mimimum values are observed after the power peak, spatially located in the 16FA, below the TR and above the core axial center (i.e. (x,y,z) = (1.8, 1.8, 2.4) [cm]) for both cases. The position corresponds to zones with the higher radial power for both cases, shown in figs. 6.10a and 6.13a. Besides, the axial location is above the axial zone where the higher power is observed, since the critical heat flux (numerator of the DNBR) decreases with the coolant temperatures, thus the minimum values are in the core upper axial zone (Duderstadt and Hamilton, 1976). The additional power released to the core is also reflected into the fuel enthalpy in Fig. 6.15b, where the temporal behavior shows the increasead amount of energy being deposited in the core with respect to the initial time. For this parameter the T-85 is also the most demanded case, since the involved increase of power and temperatures is higher due to the higher amount of inserted reactivity. Besides, the maximum values for the fuel temperature increase are slightly below the core axial center, corresponding to the higher power zones. The results for these parameters are consistent, being both key indicators used to study potential fuel failure. Here, they are obtained with *Serpent-SCF* for this PWR-kind reactor configuration with a direct-scheme (see Fig. 3.1), thus avoiding several neutronic approximations and the whole reconstruction process (i.e pin power reconstruction) discussed in Section 2.7.2, thus achieving the additional goals stated in this dissertation.

6.3 Towards full-core modeling of PWR *transients*

As a final step, the aptness of the proposed *Serpent-SCF* to tackle full-core size *transients* is evaluated. The safety analyses for real PWR consider burned compositions for the FA, since the kinetic parameters that govern the time evolution of a *transient* change with core burnup (due to the increase of ^{239}Pu , that generate a decrease in β_{eff}, see Eq. 2.11). For this purpose, a full-core numerical benchmark for a burned PWR configuration is here considered, which represents the higher complexity foreseen for industry-like applications. Therefore, the MOX/UO_2 PWR OECD/NRC benchmark (Kozlowski and Downar, 2007) is here considered (Ferraro et al., 2020e). This benchmark proposes a step-by-step approach for the calculation of *transients* within full-core PWR burned core, providing also reference values obtained by independent participants using a diverse range of calculation tools. Here RIA-kind (i.e. a *transient* generated by a sudden CR withdrawal, namely a REA) from HZP state is analyzed to show the feasibility of this approach. The core geometry is based on a four-loop Westinghouse reactor design, as shown in Figure 6.16.

This core configuration is composed by a series of 17x17 square lattice FA with simplified dimensions (e.g. details such as FA grids or spacers are not included), loaded with burned UO_2

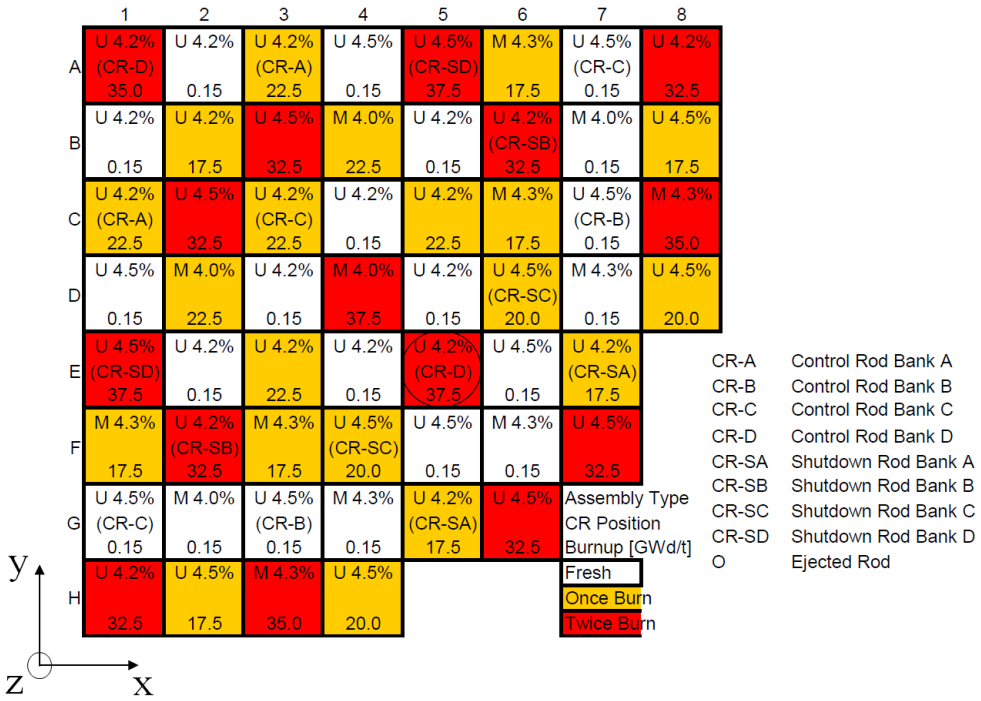

Figure 6.16: MOX/UO_2 PWR transient benchmark - sketch of the core loading pattern (quarter core - obtained from (Kozlowski and Downar, 2007)).

and MOX fuels composed by FR with ^{239}Pu (details of the specification can be gathered in Table 33 in Appendix Section D.5). For this configuration, a pin-by-pin *Serpent-SCF* approach is developed, as shown in Fig. 6.17.

From the neutronic side, a Serpent 3D model is developed, as depicted in Fig. 6.17a. The core is modeled with the compositions provided within (Kozlowski and Downar, 2007), including independent IFC meshes for the fuel (at pin-by-pin level) and coolant (at subchannel level) for the coupling, where 30 axial zones are considered for both cases. The JEFF3.1.1 (Santamarina et al., 2009) ACE NDL is used, which considers eight precursors family groups. Regarding the TH model from *SCF*, a *coolant-centered* model is applied, as shown in Fig. 6.17b. The key aspects such as gap conductivity, thermal conductivities and heat capacities both for the cladding, the UO_2 and MOX fuels provided in the benchmark are included in the *SCF* models as interpolation tables. For the coupling the same criteria for convergence of the TH solution in *SCF* is applied (i.e. one order of magnitude below the neutronic-TH convergence for the *steady-state case*). Besides, for this case an effective fuel Doppler temperature is considered (with $\alpha = 0.7$, see Eq. 3.1), as stated in the benchmark specification. The accuracy of these *Serpent-SCF* models is assessed through diverse preliminary HFP and HZP calculations (Ferraro et al., 2020e), where a good agreement with reported data is found for these *steady-state* cases.

Regarding the coupling for these *transient* calculations, a fully-explicit scheme is also considered, where a previous *steady-state* calculation is done to obtain the required sources for the two-step approach. The proposed *transient* (i.e. Part IV of benchmark (Kozlowski and Downar, 2007)) states a sudden extraction of CR-D in Figure 6.16, occurring from 0.0 s to 0.1 s at HZP condition (i.e. initial power 10^{-4} % of full power), where a time frame of 1 s is to be modeled providing results each 10 ms. This time bin size is considered, setting 1e7 particles on each.

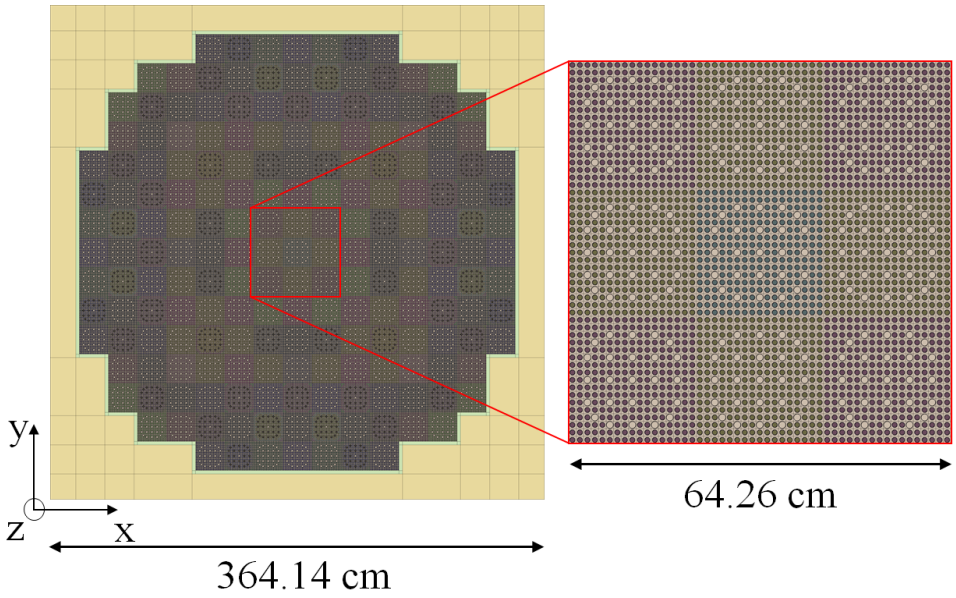

(a) Plot of the Serpent model for xy cut at z = 0 cm, where (x,y,z)=(0,0,0) corresponds to the center of the core and begin of AL. Lateral surfaces are black boundaries (bottom and top also, not shown here).

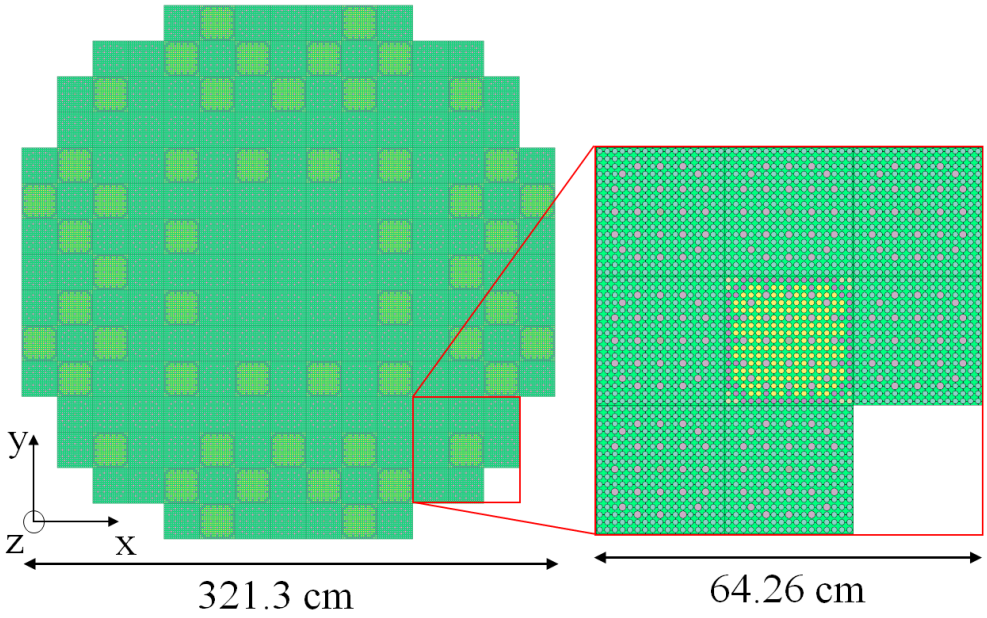

(b) Plot of the SCF model, xy cut at z = 0 cm, where (x,y,z)=(0,0,0) corresponds to the center of the core and AL. Detail of the FA included.

Figure 6.17: Schematic description of the Serpent-SCF models developed for the MOX/UO_2 PWR transient benchmark.

For this *transient* case, the benchmark does not set a reference result. Instead of that it provides a diverse set of results for quantitative comparison, obtained using diverse core-level codes such as CORETRAN, PARCS, EPISODE (diffusion nodal codes) and BARS (heterogeneous lambda matrix) (Kozlowski and Downar, 2007) for a diverse number of energy groups G. Results obtained using a SP3 (see Section 2.7.2) are also included in the comparison for PARCS and DYNSUB codes (Lee et al., 2015; Daeubler et al., 2015b). Besides, for the DYNSUB case, a nodal and a pin-by-pin modeling is included in the comparison. Hence, the consistent modeling of the time evolution plus the achievement of main parameters within the reported results is expected.

The Table 15 compares the *Serpent-SCF* calculated results for the peaks in time, power and reactivity together with the integrated power for this RIA transient (as proposed in the benchmark, using power in [%] integrated during the 1 s *transient*). These results are consistent, being the power peak captured in time and heigth, except for the BARS and DYNSUB 8G SP3 (pin-by-pin) cases, where differences are noticeable (attributed to modeling deficiencies in the ejected CR reactivity worth (Kozlowski and Downar, 2007; Daeubler et al., 2015b)). If these two cases are not considered, the peak powers are within 0.32 to 0.41 [*s*] in time and between 88 to 179 [%] of full power, with integral powers ranging from 22.1 to 29.1 [% s]. The *Serpent-SCF* results are included in this range, being this approach the only one that avoids the cell-core scheme (and the homogenization-condensation process described in Section 2.7.2). Moreover, the temporal evolution of the main parameters is analyzed in figs. 6.18 to 6.21

Code	**Peak time [s]**	**Peak power [%]**	**Peak ρ [$]**	**Integral power [% s]**
CORETRAN 2G (diffusion)	0.35	140	1.08	24.8
EPISODE 2G (diffusion)	0.33	160	1.13	26.9
PARCS 2G (diffusion)	0.34	142	1.12	27.2
PARCS 4G (diffusion)	0.33	152	1.12	27.8
PARCS 8G (diffusion)	0.32	172	1.14	29.1
PARCS 2G SP3	0.41	88	(not reported)	22.10
PARCS 4G SP3	0.40	96	(not reported)	22.90
PARCS 8G SP3	0.37	114	(not reported)	24.60
BARS 5G	0.21	522	1.29	41.7
DYNSUB 8G SP3	0.33	158	(not reported)	27.3
DYNSUB 8G SP3 (pin-by-pin)	0.48	71.8	(not reported)	17.9
Serpent-SCF (pin-by-pin)	0.355	179 ± 26	1.18±0.02	27.7±3

Table 15: Serpent-SCF results comparison for the MOX/UO_2 PWR transient benchmark (Part IV (RIA case), CR-D withdrawal, see Fig. 6.16). Statistical uncertainty for Serpent-SCF at 1σ.

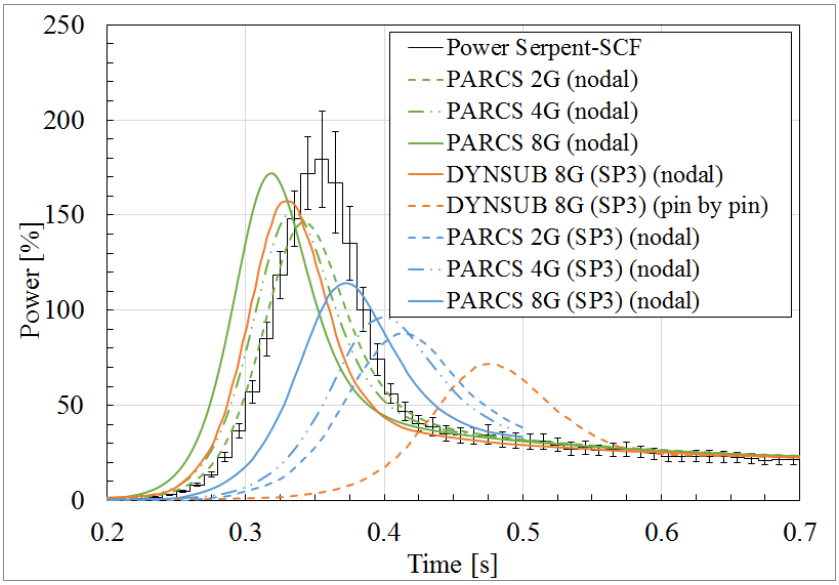

Figure 6.18: Serpent-SCF total power evolution comparison for the MOX/UO_2 PWR transient benchmark (Part IV (RIA case), CR-D withdrawal, see Fig. 6.16). Statistical uncertainty for Serpent-SCF at 1σ.

The comparison of the evolution of the total power is presented in the Fig. 6.18, including the *Serpent-SCF* total power plus the PARCS (using different group numbers and approximations) and DYNSUB (using SP3 both at nodal and pin-by-pin approach) ones. The initial power increase due to the positive reactivity insertion from the CR ejection generates a fuel and coolant temperature increase (and coolant density decrease) that counterbalance this reactivity, thus leading to a further power decrease. The results from *Serpent-SCF* show a consistent representation of this physical phenomena, where it is key to note that a change of more than five orders of magnitude in the power is correctly captured. The span in the reported values in Fig. 6.18 is known to be from a series of factors, including the energy group condensation, the CR worth differences and the TH handling (Lee et al., 2015; Daeubler et al., 2015b), reinforcing the relevance of this alternative MC-based plus subchannel TH approach.

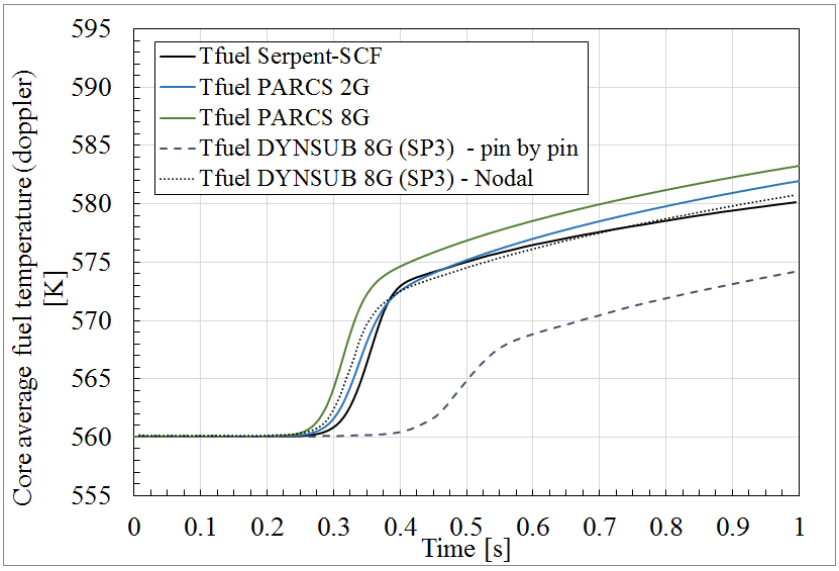

Figure 6.19: Serpent-SCF average fuel temperature evolution comparison for the MOX/UO_2 PWR transient benchmark (Part IV (RIA case), CR-D withdrawal, see Fig. 6.16).

The Fig. 6.19 depicts the evolution of the core averaged values for the fuel *Doppler* temperatures, including the comparison with the available reported data from PARCS (diffusion) at nodal level and DYNSUB (SP3) using pin-level description. These *Serpent-SCF* results for the average Doppler fuel temperature are obtained as an average of the fuel IFC values. The power increase from Fig. 6.18 is then reflected as a rise in the fuel temperatures evolution, therefore providing a negative reactivity feedback. The *Serpent-SCF* results show differences < 3 [K], where a noticeable offset is observed in the other pin-by-pin solution (i.e. DYNSUB), related to the CR worth miscalculation (reported in (Daeubler et al., 2015b)). Besides, the resulting evolution of the coolant can be also analyzed, as depicted in Fig. 6.20.

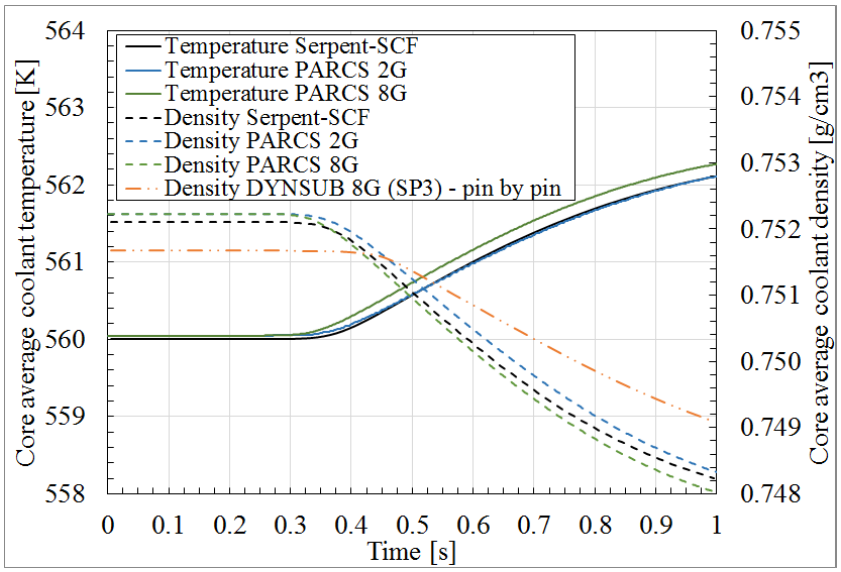

Figure 6.20: Serpent-SCF average coolant evolution comparison for the MOX/UO_2 PWR transient benchmark (Part IV (RIA case), CR-D withdrawal, see Fig. 6.16).

The Fig. 6.20 complements the analysis of the fuel temperature, showing both the evolution of the average coolant temperatures and densities. The power and fuel temperatures increase are also reflected as an increment in the coolant temperature and therefore a decrease of its density, which combined provide additional negative reactivity feedback. Again the *Serpent-SCF* results reproduce the physics in a consistent manner, with differences < 1 [K] to the reported values (DYNSUB differences are attributed to deviations in water properties (Daeubler et al., 2015b)).

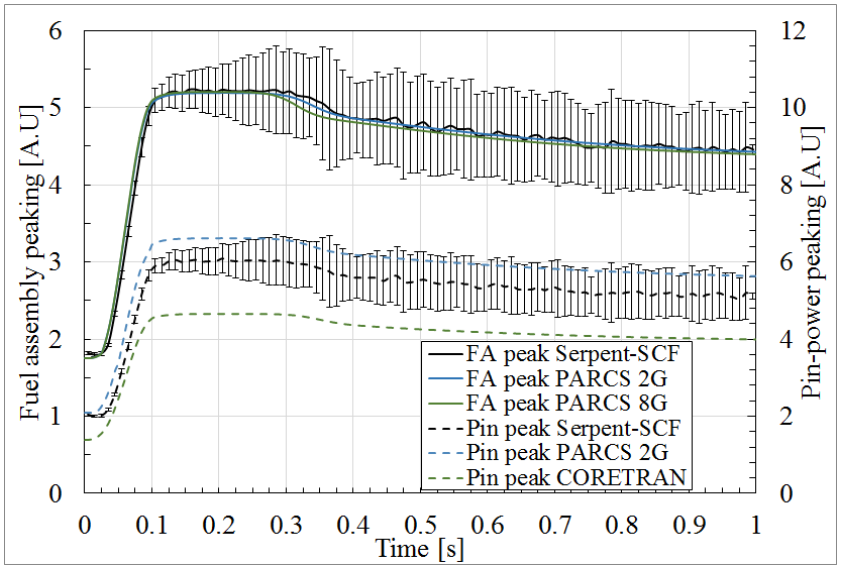

Figure 6.21: Serpent-SCF peaking factors evolution comparison for the MOX/UO_2 PWR transient benchmark (Part IV (RIA case), CR-D withdrawal, see Fig. 6.16). Statistical uncertainty for Serpent-SCF at 1σ.

The Fig. 6.21 presents the pin power peaking evolution both at FA and pin level, comparing the obtained *Serpent-SCF* with the reported values. These are defined as the ratio of the

maximum axially-integrated FA power to the core mean power value (FA peaking) and maximum axially-integrated pin power to the core average power value (pin peaking). For the pin power distribution, only the PARCS 2G results are available in reports. Hence, CORETRAN results are included, where for both cases pin-power reconstruction methodologies are applied by authors. Again the initial increase is balanced the TH feedbacks, showing *Serpent-SCF* a consistent representation of the phenomena. The sudden rise of both parameters also indicate that the local effects are noticeable, being the power peaking heavily altered during the *transient* (both at pin and FA). The strong spatial dependence of the power increase due to the CR-D can be analyzed in the pin-wise results, as depicted in the Fig. 6.22.

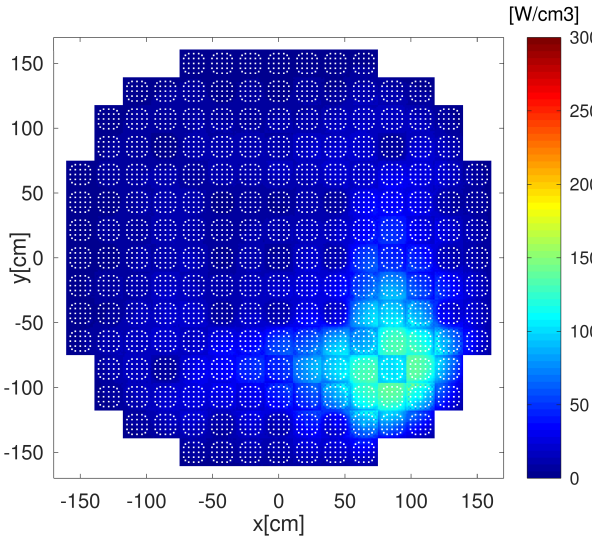

(a) Power density results for a 40 cm xy slice starting 20 cm below center of AL (z = 0 cm) , time 0.27 s. Average relative statistical error of ∼ 10 [%].

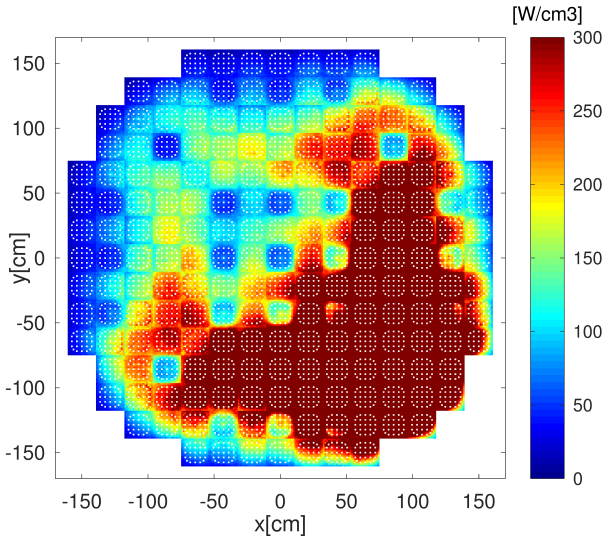

(b) Power density results for a 40 cm xy slice starting 20 cm below center of AL (z = 0 cm), time 0.34 s. Average relative statistical error of ∼ 14 [%].

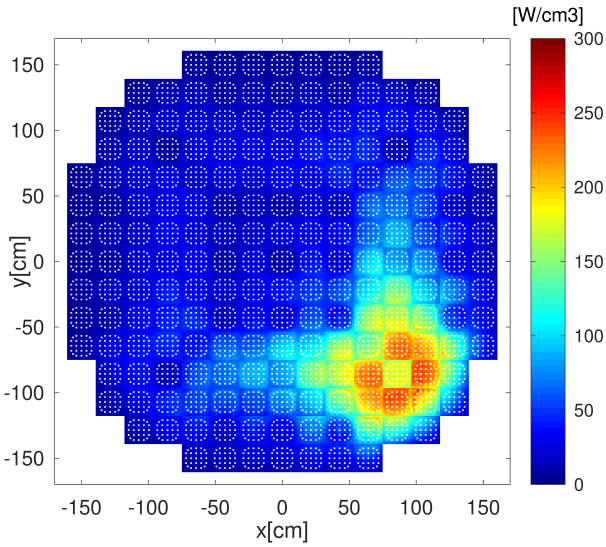

(c) Power density results a 40 cm xy slice starting 20 cm below center of AL (z = 0 cm), time 0.55 s. Average relative statistical error of ∼ 11 [%].

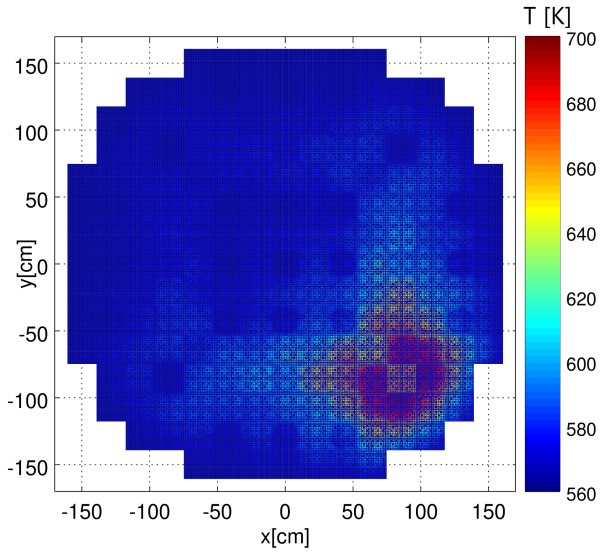

(d) Temperature results for a 20 cm xy slice starting at center of AL (z = 0 cm), time 0.55 s.

Figure 6.22: Serpent-SCF detailed results for the MOX/UO_2 PWR transient benchmark (Part IV (RIA case), CR-D withdrawal, see Fig. 6.16).

The Fig. 6.22 depicts the power density evolution calculated by *Serpent-SCF* and its corresponding temperature effect, shown for xy slices in the center of the active core length. The local effect of the sudden CR withdrawal in this full-core case is seen in the evolution of power depicted in figs. 6.22a to 6.22c, which produces a localized increase of the temperatures in the zone that surrounds the CR-D, as seen in Fig. 6.22d. The combined effect of the heterogeneous core loading and the CR position produces a power peak in the FA next to CR-D (see Fig. 6.16), reflected also in the temperature distributions in the 6.22d. It is worth to note that these results show a statistical convergence slightly above the insights described in Table 1 due to computational resources constraints (see Table 34).

One of the most important aspects of the RIA analyzed in the Fig. 6.22 arises from its strong assymetry, which difficults its integral study by industry-standard methods. Besides, it leads to power hot-spots in core zones that are not highly demanded in normal operational conditions, which must be studied in detail. Conversely, the *Serpent-SCF* capability to model explicitely this effect is a key feature, since it allows to directly obtain local key-safety parameters. To depict this, the minimum DNBR (i.e. MDNBR) is also analyzed for this *RIA-kind* case starting from HZP and compared with the values obtained for the same core operating *steady-state* at HFP, presented in Fig. 6.23.

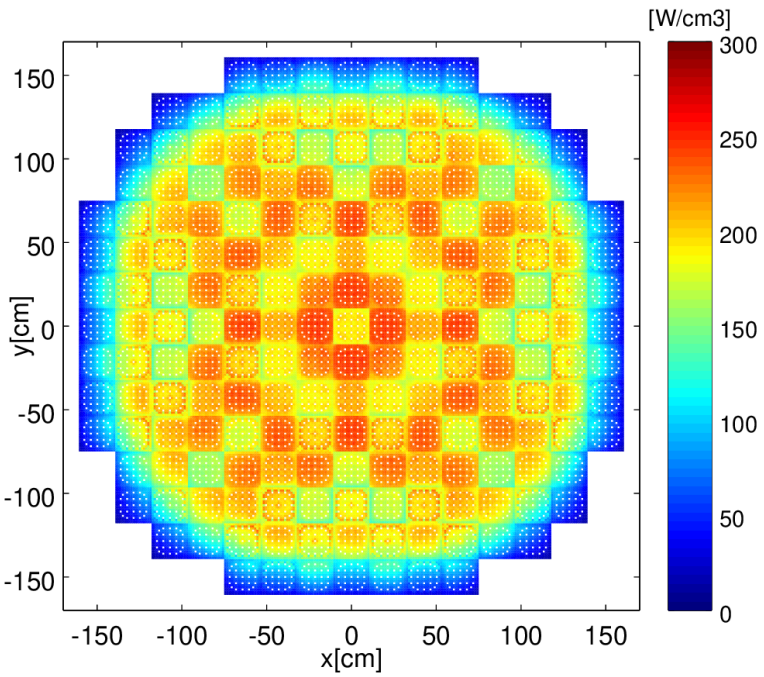

Figure 6.23: Power density results for the MOX/UO_2 PWR transient benchmark at HFP steady-state (ARO) for a 40 cm xy slice starting 20 cm below center of AL (z = 0 cm). Average relative statistical error of ~ 1 *[%].*

The Fig. 6.23 presents the *Serpent-SCF* power density *steady-state* results for the reactor configuration at hot full power (with all control rods extracted), for the same xy slice analyzed in the Fig. 6.16. The core heterogeneity is noticeable, leading in this case to higher power densities in the positions with FA with low burnup near the inner radial zone (e.g. position A2 in Fig, 6.16). This heterogeneous core loading heavily influences the associated TH limits of the

core both at nominal (HFP) and accidental conditions (e.g. RIA), where the most demanded FR is not neccesary the same for both cases, as depicted in the Fig 6.24.

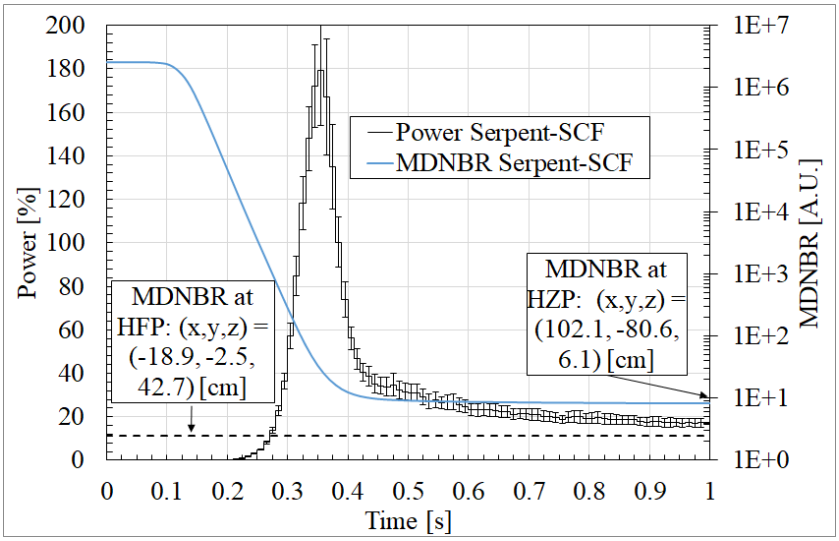

Figure 6.24: Serpent-SCF total power evolution for the MOX/UO_2 PWR transient benchmark (Part IV (RIA case), CR-D withdrawal and MNDBR . Results for HFP MDNBR are included. Statistical uncertainty for Serpent-SCF power at 1σ.

The Fig. 6.24 presents the evolution of DNBR calculated by *Serpent-SCF* for the analyzed *RIA-kind* case, including in the plot the total power evolution and the corresponding value for the *steady-state* HFP case depicted in the Fig. 6.23. For both cases the same CHF correlation is considered (i.e. (Doroschuk et al., 1976)) and no pin-power reconstruction is required. If the *transient* case starting at HZP is analyzed, it can be seen that the TH margins are initially very high (i.e. values of MDNBR >> 1.3, the stated limit for a PWR), due to the the low power and temperatures involved. Then the power increase leads to a strong decrease of the MDNBR, which reaches its minimum values in the hot-spot zone that surrounds the CR-D (i.e. (x,y,z) = (102.1, -80.6, 6.1) [cm]). Conversely, for the HFP case the most-demanded rod is placed in the FA that surrounds the central one (i.e. (x,y,z) = (-18.9, -2.5, 42.7) [cm]), corresponding to the higher power seen in the Fig. 6.23. Moreover a higher axial position is obtained for this HFP case, reflecting the decrease of the critical heat flux with the increase of coolant temperature. The main physical phenomena for this key parameter are thus captured by *Serpent-SCF* within this full-core model in a consistent manner for these cases with different TH conditions.

6.4 Final comments on verification and validation within real PWR geometries

The previous sections showed the capability of the proposed MC-based neutronics plus subchannel TH approach to achieve the stated objectives within this dissertation. The aptness of the developed *Serpent-SCF* tool to tackle full-core LWR coupled *transients* is assessed, where these results provide a novel approach for the problem, as far as all the major approximations from Section 2.7.2 are reduced in a large fraction. The use of the developed tool to safety-kind analysis within full-core LWR real scenarios is proven to be feasible, opening the gate towards

industry-like applications. The only evident inherent constrains are related to computational requirements, which are noticeable for these pin-by-pin coupled *transient* calculations. To handle this drawback the options are to develop a massive parallelization of the problem (if this infrastructure is available) or to improve the FOM of the MC side of the calculation (see Eq. 2.23). Fortunately these options can be combined for RIA-kind problems (see Appendix Section B.4 and C), which added to the increasing computing power nowadays available foresees further applications of this novel approach for PWR and VVER.

"All models are wrong, but some are useful."

— G. Box, British statistician

7 Summary and conclusions

The main scientific question stated in this dissertation is the investigation of advanced methodologies to develop the coupled neutronic-TH calculations within LWR, focusing mainly in the study of MC-based neutronics plus subchannel TH within coupled *transient* scenarios. A series of objectives are accomplished to provide a concise answer to this question, where the main findings and conclusions are here summarized.

7.1 Main findings summary

The stated scientific question leads to the selection of appropriate calculation codes, the verification of their aptness, the implementation of a versatile coupling between them and the verification and validation within real geometries and operational conditions. To avoid the main physical approximations from the industry-standard approach, the cell-core scheme has to be replaced by a direct approach, where a direct full-core pin-wise neutronic and TH representation is proposed. In particular, the application of MC-based neutronics plus subchannel TH eschew main neutronic approximations at the same time that allows to develop a direct pin-by-pin (and subchannel level) feedback of temperatures and densities, thus providing a more accurate representation of the involved spatial dependence of the involved physical phenomena. Specifically, the combination of Serpent code to handle the neutronic side of the problem plus *SCF* to deal with the TH is shown to be a suitable approach within this dissertation, where the *transient* scenarios are studied likewise the *steady-state* and the *burnup* ones. For all cases, the associated computational resources are analyzed, which represent the major drawback of the proposed approach.

Regarding *steady-state* calculations, the verification of the *Serpent-SCF* capabilities is developed for real PWR and VVER geometries both considering radially-reflected 3D FA cases and full-core problems. For these cases the comparison with calculated and experimental reported data is developed, defining the accepted level of agreement for the global parameters (such as system multiplication factors, soluble Boron concentrations and integrated power profiles) and detailed ones (such as axial dependence for power in specific fuel rods or coolant temperature in subchannels). The encountered agreement is in the order of $100 - 300 \sim [pcm]$ for the reflected-FA cases, whereas for full core cases differences in Boron concentration of $\sim 50 - 100$ $[ppm]$ are found. Besides differences in detailed power distributions up to ~ 5 [%], whereas differences about $\sim 2 - 3$ $[°C]$ are observed for subchannels axial coolant temperature results. Better agreement is found for non-axial dependent values (i.e. ~ 1[%] for axially integrated pin powers and $\sim 1°C$ for coolant outlet temperatures), since the differences are smeared when the axial dependence is eliminated. The results are encouraging, where differences are within the intended accuracy and the behavior of all the involved physics is shown to be consistent.

Besides the versatility of the proposed tool in terms of geometry and operational conditions is also demonstrated within this process.

An analogous approach is developed for *burnup* cases, where the importance of these capabilities lies in the fact that safety-related analyses within LWR require the consideration of depleted cores. In this sense, if the cell-core scheme is to be avoided, the approach must be capable to handle coupled *burnup* calculations. For such purpose *Serpent-SCF* results are also compared with reported and experimental results involving change in the system compositions. The accuracy of the approach is corroborated through the comparison of global parameters and the consistent behavior of the involved physics, where differences in system reactivity between $\sim 500 - 1000$ $[pcm]$ are found for typical PWR *burnup* ranges.

Finally, regarding *transient* cases, the aptness of *Serpent-SCF* approach is demonstrated by a verification and validation process using numerical benchmarks and experimental data that reflects real RIA-kind PWR scenarios (i.e. fast reactivity insertions, due to a CR sudden withdrawal). Again a series of global and detailed parameters are calculated and compared for these real LWR geometries and operational conditions, where it is found that the results accurately reproduce the reported experimental and calculated results. The resulting power peaks are correctly modeled by *Serpent-SCF* (i.e. differences below ~ 3 [%] in peak power with experimental data), while the comparison for a MOX/UO_2 burned full-core numerical benchmark shows its aptness to obtain pin-wise results without any power reconstruction method (showing differences in the order of $\sim 10 - 15$ [%] with reported values from industry-standard approaches). The consistency of the modeled physical phenomena is assessed for diverse geometries sizes (i.e. a minicore, a test reactor and a full-core PWR), reactor states (i.e. Hot Full Power, Hot Zero Power) and reactivity insertions (from ~ 0.4 to ~ 1.2 β_{eff}), where the time evolution of the spatial dependence is correctly replicated. Finally, safety-related parameters calculated with *Serpent-SCF* are qualitative studied for these cases, finding a coherent evolution with time for all cases analyzed.

7.2 Main conclusions

The selected MC-neutronic (i.e. Serpent) and subchannel TH (i.e. *SCF*) codes are proven to be suitable for the intended objectives stated to answer the associated scientific question, showing that full-core pin-level coupled calculations within real LWR can be accurately developed for *transient*, *steady-state* and *burnup* cases. This novel approach provides an independent path that avoids most relevant physical approximations in the neutronics and its associated TH feedback within the standard-industry approach. On top of that, its aptness to provide safety-related parameters without any reconstruction technique is also assessed, which represents a novel and compelling path for coupled *transient* RIA-kind scenarios. On the contrary, the major drawback arises from the computational resources involved. The consistency of results obtained encourage further work in this path, paving the way for industry-like applications. In this sense, some potential further steps are discussed in the next Chapter, where it should be noted that the further use of the developed tool shall certainly lead to additional interesting work paths.

"We have just crossed the Rubicon river."

— Roman proverb

8 Outlook

Based on the analyses developed within this this dissertation, diverse insights for further developments are here provided.

8.1 Extension of the methodology for other reactor designs

The aptness of the approach is ensured for the typical LWR designs described in Chapter 1. The extension to other reactor designs (e.g. Material Testing Reactors, Heavy Water Pressurized Reactors, Advanced Gas Cooled Reactors, sodium-cooled reactors etc.) represents a compelling path. In principle no major limitations are foreseen if the particular neutronic and TH aspects involved are taken into account, where the major expected effort is related to the validation of the *SCF* code for these cases. Conversely, the implementation approach for *Serpent-SCF* allows to easily extend the geometry handling to tackle these alternatives (only proper IFC and mapping files should be addressed).

8.2 Investigations related to the impact of TH parameters

For RIA-kind scenarios, parameters such as the fuel gap conductivity and the consideration of different temperatures average schemes are known to affect the evolution of the global behavior, since the TH feedback is affected (and thus the reactivity compensation) (Grandi et al., 2010). In this work path, further investigations can be developed with *Serpent-SCF* for the already analyzed PWR cases, where the study impact of the uncertainty in the fuel gap conductivity represents an interesting outlook.

8.3 Further investigations related to the MC-intrinsic characteristics

The *Serpent-SCF* approach can be extended to handle not only neutronic-TH calculations, but also the gamma heating (arising from the fission reactions and decay of activated materials) (Tuominen et al., 2020). The study of the impact of these contributions (that produce a slight distortion of the power distribution within the core) for the full-scope geometries analyzed represents an interesting novel work path where some insights can be addressed.

Finally, the in-depth study and development of VR techniques specially tailored to *transient* calculations can boost industry-like applications (Sjenitzer, 2013). The main object of these techniques is to diminish of the associated computational resources, where the suitability of each potential alternative has to be assessed to define a suitable work path, since the effectiveness of a VR is highly dependent on the problem characteristics (e.g. core size and heterogenity, time scope, etc.).

8.4 Further investigations related to subchannel TH

For full-core applications at subchannel level the *SCF* running times are not negligible (see Appendix D.5). This fact represents a problem, as far as when using massive HPC architectures the *SCF* part is not parallelized as Serpent, thus the allocated resources for the coupled calculation are not used. The investigation of coarsening methods arises as an alternative, in which the subchannels within the *SCF* models are combined for regions of low interest into larger zones comprising several subchannels and rods, modeled with condensed hydraulic parameters (García et al., 2020b). In particular for *transient* calculations this process has to be done between time steps which represents a challenging (and novel) application.

Finally, the impact of including additional physics within the *SCF* models (such as more detailed gap conduction models with burnup and material dependence) likewise the inclusion of ad-hoc fuel pin mechanics codes in the coupling (García et al., 2020c) when dealing with pin-by-pin coupled *transient* calculations represents a interesting scientific topic.

8.5 Additional verification and validation of the tool

Testing, verification and validation is a mandatory process when dealing with novel tools or approaches. Further in-depth comparison of pin-wise parameters with experimental results that extend the span of LWR geometries and scenarios represents a compelling path. For such purpose, suitable sets of experimental data that reproduce LWR-kind geometrical and operational conditions must be identified, collected, compiled and systematized to then develop a further validation of the proposed tool. On top of that, the comparison with similar calculation tools can also provide important insights, since detailed experimental results (i.e. axially dependent pin-wise values) are not commonly available, thus a qualitative code-to-code comparison can be useful. In this sense the comparison with approaches that consider a lower number of approximations in the TH side represents an interesting theme.

Finally, the analysis results of a complete-independent calculation approach to obtain RIA safety-related parameters within real PWR geometries represents an interesting goal. For this purpose, the coupled *Serpent-SCF burnup* capabilities can be used to obtain a depleted core (e.g. at the end of the cycle) to then develop a coupled *transient* calculation for specific initiating events, where the major drawback arises from the required calculation resources.

References

Aleshin, S., Bikeev, A., Bolshagin, S., Kalugin, M., Kosourov, E., Pavlovichev, A., Pryanichnikov, A., Sukhino-Khomenko, E., Shcherenko, A., Shcherenko, A., and Shkarovskiy, D. 2015. *Calculations of 3D full-scale VVER fuel assembly and core models using MCU and BIPR-7A codes.* In *Kerntechnik*, volume 80, pages 326–338.

Aviles, B. N., Kelly, D. J., Aumiller, D. L., Gill, D. F., Siebert, B. W., Godfrey, A. T., Collins, B. S., and Salko, R. K. 2017. *MC21/COBRA-IE and VERA-CS multiphysics solutions to VERA core physics benchmark problem #6. Progress in Nuclear Energy*, 101:338 – 351. ISSN: 0149-1970.

Bahadir, T. and Lindahl, S.-O. 2009. *Studsvik's next generation nodal code SIMULATE-5.* In *Advances in Nuclear Fuel Management IV (ANFM 2009)*, Hilton Head Island, South Carolina, USA. ISBN: 978-0-89448-068-3 / Pages 992-1004.

Bateman, H. 1910. *The solution of a system of differential equations occurring in the theory of radio-active transformations.* In *Proceedings of the Cambridge Philosophical Society, Mathematical and physical sciences.* Vol. 3 / Pages 423-427.

Bell, G. I. and Glasstone, S. 1970. Nuclear Reactor Theory. Van Nostrand Reinhold Company, New York, USA. ISBN: 978-0-442-20684-0.

Bikeev, A., Kalugin, M., Oleinik, D., Shcherenko, A., Shkarovsky, D., and Tomilov, M. 2017. *MCU Code Precision Calculation of a Full-Scale VVER-1000 Model Considering Feedbacks.* In *In proceedings of M&C 2017 - International Conference on Mathematics and Computational Methods Applied to Nuclear Science and Engineering*, Jeju, Korea. ISBN: 978-1-5108-5645-5 / Paper ID: P090.

Cacucci, D. G. 2010. Handbook of Nuclear Engineering. Springer, Boston, MA, USA. ISBN: 978-0-387-98149-9.

Cao, L., Gerlach, A., Xu, Y., Downar, T., and Lee, J. C. 2015. *Neutronics modeling of the SPERT III E-Core critical experiments with MPACT and KENO. Annals of Nuclear Energy*, 80:207 – 218.

CASL 2010-2020. *The Consortium for Advanced Simulation of Light Water Reactors (CASL), a DOE Energy Innovation Hub for Modeling and Simulation of Nuclear Reactors* . `https://www.casl.gov/`. Accessed: 11.12.2020.

Ceresio, C., Cabellos, O., Martínez, J.S., and Diez, C.J. 2012. Importance of nuclear data uncertainties in criticality calculations. *EPJ Web of Conferences*, 27:00004.

Chadwick, M., Herman, M., Obložinský, P., Dunn, M., Danon, Y., Kahler, A., Smith, D., Trkov, A., Hoblit, S., Young, G., et al. 2011. *ENDF/B-VII.1 Nuclear Data for Science and Technology: Cross Sections, Covariances, Fission Product Yields and Decay Data. Nuclear Data Sheets*, 112(12):2887 – 2996. Special Issue on ENDF/B-VII.1 Library. ISSN: 0090-3752.

Cullen, D. E., Clouse, C. J., Procassini, R., and Little, R. C. 2003. *Static and Dynamic Criticality: Are They Different?* Technical Report UCRL-TR-201506 , Lawrence Livermore National Laboratory. Available at `https://www.osti.gov/biblio/15009756`. Accessed: 11.12.2020.

Daeubler, M., Ivanov, A., Sjenitzer, B., Sanchez, V., Stieglitz, R., and Macian-Juan, R. 2015a. *High-fidelity coupled Monte Carlo neutron transport and thermal-hydraulic simulations using Serpent 2/SUBCHANFLOW. Annals of Nuclear Energy*, 83:352 – 375.

Daeubler, M., Trost, N., Jimenez, J., Sanchez, V., Stieglitz, R., and Macian-Juan, R. 2015b. Static and transient pin-by-pin simulations of a full PWR core with the extended coupled code system DYNSUB. *Annals of Nuclear Energy*, 84:31 – 44.

de Kruijf, W. J. M. and Janssen, A. J. 1996. *The Effective Fuel Temperature to Be Used for Calculating Resonance Absorption in a 238UO2 Lump with a Nonuniform Temperature Profile. Nuclear Science and Engineering*, 123(1):121–135.

Doroschuk, V., Levitan, L., and Lantzman, F. 1976. Tabular data for calculating burnout when boiling water in uniformly heated round tubes. *Teploenergetika*, 23:90–92.

Duderstadt, J. J. and Hamilton, L. J. 1976. Nuclear Reactor Analysis. John Willey & sons Inc., New York, USA. ISBN: 0-471-22363-8.

Faucher, M., Mancusi, D., and Zoia, A. 2020. *Multi-physics transient simulations with TRIPOLI-4.* In *International Conference on Physics of Reactors 2020*, Cambridge, UK. ISBN: 978-1-5272-6447-2 / Paper ID: 1684.

Faucher, M., Mancusi, D., Zoia, A., Ferraro, D., Garcia, M., Imke, U., Leppänen, J., and Valtavirta, V. 2019. *Multi-physics simulations with TRIPOLI-4® and Serpent 2: coupling neutron transport with the sub-channel code SUBCHANFLOW.* In *ICAPP - International Congress on Advances in nuclear Power Plants*, Juan-les-pins, France. Paper ID: 159.

Ferraro, D., Faucher, M., Mancusi, D., Zoia, A., Valtavirta, V., Leppänen, J., and Sanchez-Espinoza, V. 2019a. *Serpent and TRIPOLI-4® transient calculations comparisons for several reactivity insertion scenarios in a 3D PWR minicore benchmark.* In *International Conference on Mathematics and Computational Methods applied to Nuclear Science and Engineering (M and C 2019)*, Portland, Oregon, USA. ISBN: 978-0-89448-769-9 / Vol. 3 / Pages 1734-1743.

Ferraro, D., García, M., Imke, U., Valtavirta, V., Leppänen, J., and Sanchez-Espinoza, V. 2019b. *Serpent/SCF pin-level multiphysics solutions for the VERA Fuel Assembly benchmark. Annals of Nuclear Energy*, 128:102–114.

Ferraro, D., García, M., Imke, U., Valtavirta, V., Tuominen, R., Bilodid, Y., Leppänen, J., and Sanchez-Espinoza, V. 2020a. *Serpent / SUBCHANFLOW coupled calculations for a VVER core at hot full power.* In *International Conference on Physics of Reactors 2020*, Cambridge, UK. ISBN: 978-1-5272-6447-2 / Paper ID: 1190.

Ferraro, D., García, M., Imke, U., Valtavirta, V., Tuominen, R., Leppänen, J., and Sanchez-Espinoza, V. 2020b. *Serpent / SUBCHANFLOW coupled burnup calculations for VVER fuel assemblies*. In *International Conference on Physics of Reactors 2020*, Cambridge, UK. ISBN: 978-1-5272-6447-2 / Paper ID: 1189.

Ferraro, D., Garcia, M., Mercatali, L., Sanchez-Espinoza, V. H., Leppänen, J., and Valtavirta, V. 2018. *Foreseen capabilities, bottlenecks identification and potential limitations of serpent MC transport code in large-scale full 3-D burnup calculations*. In *26th International Conference on Nuclear Engineering*, London, UK. American Society of Mechanical Engineers ASME. ISBN: 978-0-7918-5145-6 / Vol. 3 / Paper ID: V003T02A049.

Ferraro, D., García, M., Valtavirta, V., Imke, U., Tuominen, R., Leppänen, J., and Sanchez-Espinoza, V. 2020c. *Serpent/SUBCHANFLOW pin-by-pin coupled transient calculations for a PWR minicore. Annals of Nuclear Energy*, 137:107090.

Ferraro, D., García, M., Valtavirta, V., Imke, U., Tuominen, R., Leppänen, J., and Sanchez-Espinoza, V. 2020d. *Serpent/SUBCHANFLOW pin-by-pin coupled transient calculations for the SPERT-IIIE hot full power tests. Annals of Nuclear Energy*, 142:107387.

Ferraro, D., Valtavirta, V., García, M., Imke, U., Tuominen, R., Leppänen, J., and Sanchez-Espinoza, V. 2020e. *OECD/NRC PWR MOX/UO_2 core transient benchmark pin-by-pin solutions using Serpent/SUBCHANFLOW. Annals of Nuclear Energy*, 147:107745.

García, M., Ferraro, D., Sanchez-Espinoza, V., Mercatali, L., Leppänen, J., and Valtavirta, V. 2018. *Development of a Spatial Domain Decomposition Scheme for Monte Carlo Neutron Transport*. In *26th International Conference on Nuclear Engineering*, London, UK. American Society of Mechanical Engineers ASME. ISBN: 978-0-7918-5145-6 / Vol. 3 / Paper ID: V003T02A042.

García, M., Ferraro, D., Valtavirta, V., Imke, U., Tuominen, R., Sanchez-Espinoza, V. H., and Mercatali, L. 2019a. *Development of an Object-oriented Serpent2 - SUBCHANFLOW Coupling and Verification with Problem 6 of the VERA Core Physics Benchmark*. In *International Conference on Mathematics and Computational Methods applied to Nuclear Science and Engineering (M and C 2019)*, Portland, Oregon, USA. ISBN: 978-0-89448-769-9 / Vol. 2 / Pages 1424-1433.

García, M., Ferraro, D., Valtavirta, V., Tuominen, R., Imke, U., Leppänen, J., and Sanchez-Espinoza, V. 2020a. *Serpent2 - SUBCHANFLOW pin-by-pin modelling capabilities for VVER geometries. Annals of Nuclear Energy*, 135:106955.

García, M., Ferraro, D., Valtavirta, V., Tuominen, R., Imke, U., Sanchez-Espinoza, V., and Leppänen, J. 2020b. *A subchannel coarsening method for Serpent2 - SUBCHANFLOW applied to a full-core VVER problem.* In *International Conference on Physics of Reactors 2020*, Cambridge, UK. ISBN: 978-1-5272-6447-2 / Paper ID: 1289.

García, M., Imke, U., Ferraro, D., Sanchez-Espinoza, V. H., and Mercatali, L. 2019b. *Advanced Modelling Capabilities for Pin-level Subchannel Analysis of PWR and VVER Reactors*. In

18th International Topical Meeting on Nuclear Reactor Thermal Hydraulics (NURETH-18), Portland, Oregon, USA. ISBN: 978-0-89448-767-5 / Pages 4299-4309 / Paper ID: 4299.

García, M., Tuominen, R., Gommlich, A., Ferraro, D., Valtavirta, V., Imke, U., Uffelen, P. V., Mercatali, L., Sanchez-Espinoza, V., Leppänen, J., and Kliem, S. 2020c. *A Serpent2 - SUBCHANFLOW - TRANSURANUS coupling for pin-by-pin depletion calculations in Light Water Reactors. Annals of Nuclear Energy*, 139:107213.

Gaston, D., Newman, C., Hansen, G., and Lebrun-Grandié, D. 2009. *MOOSE: A parallel computational framework for coupled systems of nonlinear equations. Nuclear Engineering and Design*, 239(10):1768 – 1778.

Gill, D. F., Griesheimer, D. P., and Aumiller, D. L. 2017. *Numerical Methods in Coupled Monte Carlo and Thermal-Hydraulic Calculations. Nuclear Science and Engineering*, 185(1):194–205.

Godfrey, A. 2014. *VERA core physics benchmark progression problem specifications.* Technical Report CASL-U-2012-0131-004 - Revision 4, Oak Ridge National Laboratory.

Goltsev, A. O., Davidenko, V. D., Tsibulsky, V. F., and Lekomtsev, A. A. 2000. *Computational Problems in the Calculation of Temperature Effects for Heterogeneous Nuclear Reactor Unit Cells. Annals of Nuclear Energy*, 27(2):175 – 183. ISSN: 0306-4549.

Grandi, G., Smith, K., Xu, Z., and Rhodes, J. 2010. *Effect of Casmo-5 cross-section data and doppler temperature definitions on LWR reactivity initiated accidents.* In *PHYSOR 2010 - Advances in Reactor Physics to Power the Nuclear Renaissance*, Pittsburgh, USA. ISBN: 978-0-89448-079-9 / Vol. 3 / Pages 2459-2472.

Horelik, N., Herman, B., Forget, B., and Smith, K. 2013. *Benchmark for evaluation and validation of reactor simulations (BEAVRS).* In *Proceedings of the International Conference on Mathematics and Computational Methods Applied to Nuclear Science and Engineering, M and C 2013*, Sun Valley, USA. ISBN: 978-0-89448-700-2 / Pages 2986-2999 / Paper ID: 7834.

How, J., Blyth, T., Porter, N., Toptan, A., Avramova, M., Ivanov, K., et al. 2018. *Benchmark for uncertainty analysis in modelling (UAM) for design, operation and safety analysis of LWRs - Volume II: Specification and Support Data for the Core Cases (Phase II) - NEA/NSC/DOC(2018) v 19.1.*

IAEA 2006. Fundamental Safety Principles. Number SF-1 in Safety Fundamentals. INTERNATIONAL ATOMIC ENERGY AGENCY, Vienna, Austria. ISBN: 92-0-110706-4.

IAEA 2009. Nuclear Power Objectives: Achieving the Nuclear Energy Basic Principles. Number NP-O in Nuclear Energy Series. INTERNATIONAL ATOMIC ENERGY AGENCY, Vienna, Austria. ISBN: 978-92-0-106209-3.

IAEA 2014. Applications of Research Reactors. Number NP-T-5.3 in Nuclear Energy Series. INTERNATIONAL ATOMIC ENERGY AGENCY, Vienna, Austria. ISBN: 978-92-0-145010-4.

IAEA 2017. Industrial Applications of Nuclear Energy. Number NP-T-4.3 in Nuclear Energy Series. INTERNATIONAL ATOMIC ENERGY AGENCY, Vienna, Austria. ISBN: 978-92-0-101417-7.

Imke, U. 2019. *User manual for SUBCHANFLOW 3.6.1.* Technical report, Karlsruhe Institute for Technology - Institute for Neutron Physics and Reactor Technology. Available by request for code users.

Imke, U. and Sanchez, V. H. 2012. *Validation of the Subchannel Code SUBCHANFLOW Using the NUPEC PWR Tests (PSBT). Science and Technology of Nuclear Installations*, 2012. Hindawi Publishing Corporation, Article ID 465059, 12 pages.

Ivanov, A. 2015. High Fidelity Monte Carlo Based Reactor Physics Calculations. PhD thesis, Karlsruher Institut of Technology, Karlsruhe, Germany. doi: 10.5445/IR/1000050615. Available at `https://publikationen.bibliothek.kit.edu/1000050615/3761631`. Accessed: 11.12.2020.

Kochunas, B., Jabay, D., Collins, B., and Downar, T. 2013. *Coupled single assembly solution with Cobra-TF/MPACT (Problem 6).* Technical Report CASL-U-2013-0280-000 - Revision 0, Oak Ridge National Laboratory.

Kozlowski, T. and Downar, T. 2007. *PWR MOX/UO2 Core Transient Benchmark.* Technical Report NEA/NSC/DOC(2006)20, NUCLEAR ENERGY AGENCY (NEA) - Organisation for Economic Co-operation and Development. ISBN: 92-64-02330-5. Available at `https://www.oecd-nea.org/science/wprs/MOX-UOX-transients/benchmark_documents/final_report/mox-uo2-bench.pdf`. Accessed: 11.12.2020.

Lee, D., Kozlowski, T., and Downar, T. J. 2015. Multi-group SP3 approximation for simulation of a three-dimensional PWR rod ejection accident. *Annals of Nuclear Energy*, 77:94 – 100.

Leppänen, J. 2007. Development of a New Monte Carlo reactor physics code. PhD thesis, Helsinki University of Technology, Espoo, Finland. ISBN: 978-951-38-7018-8 - Available at `http://montecarlo.vtt.fi/download/P640.pdf`. Accessed: 11.12.2020.

Leppänen, J. 2013a. *Development of a dynamic simulation mode in the Serpent 2 Monte Carlo code.* In *Proceedings of the International Conference on Mathematics and Computational Methods Applied to Nuclear Science and Engineering, M and C 2013*, Sun Valley, USA. ISBN: 978-0-89448-700-2 / Pages 117-127 / Paper ID: 7250.

Leppänen, J. 2013b. *Modeling of Nonuniform Density Distributions in the Serpent 2 Monte Carlo Code. Nuclear Science and Engineering*, 174(3):318–325.

Leppänen, J., Aufiero, M., Fridman, E., Rachamin, R., and van der Marck, S. 2014. Calculation of effective point kinetics parameters in the serpent 2 monte carlo code. *Annals of Nuclear Energy*, 65:272 – 279.

Leppänen, J. and Isotalo, A. 2012. *Burnup calculation methodology in the Serpent 2 Monte Carlo code.* In *Proceedings of the International Conference on the Physics of Reactors, PHYSOR*

2012, Knoxville, Tennessee, USA. American Nuclear Society ANS. ISBN: 978-1-6227-6389-4 / Vol. 2 / Pages 924-935.

Leppänen, J., Pusa, M., Viitanen, T., Valtavirta, V., and Kaltiaisenaho, T. 2015. *The Serpent Monte Carlo code: Status, development and applications in 2013. Annals of Nuclear Energy*, 82:142 – 150.

Leppänen, J., Valtavirta, V., Tuominen, R., Kaltiaisenaho, T., Pusa, M., and Viitanen, T. 2020. *Serpent Wiki on-line user Manual for Serpent 2.* `http://serpent.vtt.fi/mediawiki/index.php/Main_Page`. Accessed: 11.12.2020.

Levinsky, A., Valtavirta, V., Adams, F., and Anghel, V. 2019. *Modeling of the SPERT transients using Serpent 2 with time-dependent capabilities. Annals of Nuclear Energy*, 125:80–98.

Lewis, E. and Miller, W. 1984. Computational methods of neutron transport. John Wiley and sons, New York, USA. ISBN: 0-471-09245-2.

Loetsch, T., Khalimonchuk, V., and Kuchin, A. 2009. *Proposal of a Benchmark on core burnup follow calculations for a VVER-1000 reactor core.* In *Proceedings of the 19th Symposium of AER on VVER Reactor Physics and Reactor Safety*, Varna, Bulgaria. Available at `http://www.iaea.org/inis/collection/NCLCollectionStore/_Public/41/035/41035568.pdf?r=1`. Accessed: 11.12.2020.

Loetsch, T., Khalimonchuk, V., and Kuchin, A. 2010. Corrections and additions to the proposal of a benchmark for core burnup calculations for a WWER-1000. In *Proceedings of the 20th symposium of atomic energy research on VVER Reactor Physics and Reactor Safety*, Espoo, Finland. Available at `https://inis.iaea.org/search/search.aspx?orig_q=RN:41131407`. Accessed: 11.12.2020 / Paper ID: 2.8.

Loetsch, T., Khalimonchuk, V., and Kuchin, A. 2011. *Solutions for the TASK 1 and TASK 2 of the benchmark for core burnup calculations for a WWER-1000 reactor.* In *Proceedings of the 21th Symposium of AER on VVER Reactor Physics and Reactor Safety*, Dresden, Germany. Available at `https://inis.iaea.org/collection/NCLCollectionStore/_Public/42/105/42105721.pdf?r=1`. Accessed: 11.12.2020 / Paper ID: 2.6.

Luo, Z., Guo, J., Yu, G., Wang, K., and Liu, S. 2017. *Solutions to VERA Core Physics Benchmark Progression Problems 1 to 6 Based on RMC.* In *Transactions of the American Nuclear Society / Vol. 117 / Pages 1235-1238*, Washington D.C., USA.

MacFarlane, R. E. 2019. The NJOY Nuclear Data Processing System, Version 2016. Number LA-UR-17-20093 in Nuclear Energy Series. Los Alamos National Laboratory.

McCardell, R., Herborn, D., and Houghtaling, J. March 1967. *Reactivity Accident Test Results and Analyses for the SPERT III E-Core.* Technical Report IDO-17281 - Phillips Petroleum Co, USA Atomic Energy Commission (AEC). Available at `https://www.osti.gov/biblio/4792676`. Accessed: 11.12.2020.

McConn, R. J., Gesh, C. J., Pagh, R. T., Rucker, R. A., and Williams III, R. 2011. *Compendium of Material Composition Data for Radiation Transport Modeling.* Pacific Northwest National Lab report No. PNNL-15870 Rev. 1 (USA).

Oak Ridge National Laboratory 2001. ORNL/TM-2000/351: Thermophysical Properties of MOX and UO2 Fuels Including the Effects of Irradiation. Available at `https://www.osti.gov/servlets/purl/777671`. Accessed: 11.12.2020.

Olson, A. P. 2013. *Neutronics Calculations for SPERT-III, E-core.* Nuclear Engineering Division, Argonne National Laboratory - Report No. ANL/GTRI/TM-13/10.

Olson, A. P. 2015. *SPERT III E CORE: FACILITY SPECIFICATION.* IAEA Technical Report Series No. 480. Available at `https://www.iaea.org/publications/10578`. Accessed: 11.12.2020.

PSF 2020. *The Python Software Foundation (PSF) - Python 3.7.0 documentation.* `https://docs.python.org/3.7/`. Accessed: 11.12.2020.

Salko, R. and Avramova, M. 2015. *COBRA-TF Subchannel Thermal-hydraulics Code (CTF) - Theory Manual.* Technical Report CASL-U-2015-0054-000, Pennsylvania State University.

Sanchez-Espinoza, V., Mercatali, L., Leppänen, J., Hoogenboom, E., Vocka, R., and Dufek, J. 2020. *The McSAFE project - high-performance Monte Carlo based methods for safety demonstration: from proof of concept to industry applications.* In *International Conference on Physics of Reactors 2020*, Cambridge, UK. ISBN: 978-1-5272-6447-2 / Paper ID: 1143.

Santamarina, A., Bernard, D., Blaise, P., Coste, M., Courcelle, A., et al. 2009. *The JEFF-3.1.1 Nuclear Data Library.* Technical Report JEFF Report 22, NUCLEAR ENERGY AGENCY (NEA) - Organisation for Economic Co-operation and Development. ISBN: 978-92-64-99074-6. Available at `http://www.oecd-nea.org/dbdata/nds_jefreports/jefreport-22/nea6807-jeff22.pdf`. Accessed: 11.12.2020.

SCC 2020. *High Performance Computing (HPC) Cluster Wiki at Karlsruhe Institute of Technology.* Steinbuch Centre for Computing - `https://wiki.scc.kit.edu/hpc/index.php/Main_Page`. Accessed: 11.12.2020.

Sjenitzer, B. 2013. The Dynamic Monte Carlo Method for Transient Analysis of Nuclear Reactors. PhD thesis, Delft University of Technology, Delft, Netherlands. ISBN 978-90-8891-657-1.

SPC 2018. *The SciPy community (SPC- NumPy v1.15 Manual.* `https://docs.scipy.org/doc/numpy/index.html`. Accessed: 11.12.2020.

Stewart, C., Wheeler, C., Cena, R., C.A., M., J.M., C., and D.S., T. 1977. *COBRA-IV: The model and the method.* Technical Report BNWL-2214, Pacific Northwest Laboratories.

TGCC 2020. *Très Grand Centre de calcul du CEA: description.* `http://www-hpc.cea.fr/en/complexe/tgcc-curie.htm`. Accessed: 11.12.2020.

Tuominen, R., Valtavirta, V., García, M., Ferraro, D., and Leppänen, J. 2020. *Effect of energy deposition modelling in coupled steady state Monte Carlo neutronics/thermal hydraulics calculations.* In *International Conference on Physics of Reactors 2020*, Cambridge, UK. ISBN: 978-1-5272-6447-2 / Paper ID: 1114.

Turinsky, P., Al-Chalabi, R., Engrand, P., Sarsour, H., Faure, F., and Guo, W. 1994. *NESTLE: Few-group neutron diffusion equation solver utilizing the nodal expansion method for eigenvalue, adjoint, fixed-source steady-state and transient problems.* USA DOE Technical Report No. EGG-NRE-11406.

USA NRC 2007. *Standard Review Plan for the Review of Safety Analysis Reports for Nuclear Power Plants, LWR Edition - Chapter 4.2 - Fuel system design.* Technical Report NUREG-0800, USA NUCLEAR REGULATORY COMMISSION. Revision 3. Available at `https://www.nrc.gov/docs/ML0707/ML070740002.pdf`. Accessed: 11.12.2020.

Valtavirta, V. 2017. Development and applications of multiphysics capabilities in a continuous energy Monte Carlo neutron transport code. PhD thesis, Aalto University, School of Science, Department of Applied Physics, Aalto, Finland. ISBN: 978-952-60-7377-4. Available at `http://montecarlo.vtt.fi/download/S150.pdf`. Accessed: 11.12.2020.

Valtavirta, V., Hessan, M., and Leppänen, J. 2016. *Delayed Neutron Emission Model for Time Dependent Simulations with the Serpent 2 Monte Carlo Code - First Results.* In *PHYSOR 2016: Unifying Theory and Experiments in the 21st Century*, Sun Valley, USA. American Nuclear Society ANS. ISBN: 978-0-89448-762-2 / Pages 1568-1583.

Viitanen, T. and Leppänen, J. 2014. *Target Motion Sampling Temperature Treatment Technique with Elevated Basis Cross-Section Temperatures. Nuclear Science and Engineering*, 177(1):77–89.

Wang, K., Li, Z., She, D., Liang, J., Xu, Q., et al. 2015. *RMC - A Monte Carlo code for reactor core analysis. Annals of Nuclear Energy*, 82:121 – 129.

Wheeler, C., Stewart, C., Cena, R., Rowe, D., and Sutey, A. 1976. *COBRA-IV-I: an interim version of COBRA for thermal-hydraulic analysis of rod bundle nuclear fuel elements and cores.* Technical Report BNWL-1962 / TRN: 76-018139, Pacific Northwest Laboratories.

Wilderman, S. J., Martin, W. R., and Brown, F. B. 2015. *Simulation of CASL 3D HFP Fuel Assembly Benchmark Problem with On-The-Fly Doppler Broadening in MCNP6.* In *Proceedings of the ANFM 2015 - Advances in Nuclear Fuel Management V and CASL VERA Workshop*, Hilton Head, South Carolina, USA. Pages 171-178 / Paper ID: 78.

X-5 Team 2008. MCNP - A General Monte Carlo N-Particle Transport Code, Version 5 Volume I: Overview and Theory. Number LA-UR-03-1987 in Nuclear Energy Series. Los Alamos National Security, LLC.

Zoia, A. and Brun, E. 2016. *Reactor physics analysis of the SPERT III E-core with Tripoli-4®. Annals of Nuclear Energy*, 90:71–82.

A Analysis of the suitability of the approach: The VERA problem #6

The aptness of the Serpent plus *SCF* for the stated goals was evaluated developing a numerical benchmark considering pin-by-pin detailed comparison (Ferraro et al., 2019b). The main purpose of this analysis is to ensure the accuracy level, together with the stability of the convergence of the coupled solution. For such purpose, the *VERA* benchmark problem #6 (Godfrey, 2014) was calculated using a external-coupling implementation of the proposed approach. This numerical benchmark problem is based on a standard Westinghouse PWR design, representing a radially-reflected fresh (i.e. no burnup) 3D fuel assembly, to be calculated at Hot Full Power (HFP), without Xenon and considering a pin by pin TH feedback. The main FA, pin and TH aspects of this case are summarized in Table 16.

Parameter	**Value**
Fuel Rods (FR)	
Pellet Radius	0.4096 cm
Clad Radii (inner / outer)	0.418 / 0.475 cm
Rod Pitch	1.26 cm
Rod Height	385.1 cm
Fuel Stack Height	365.76 cm
Plenum Height	16.0 cm
End Plug Heights (x2)	1.67 cm
Pellet Material	UO2, enrichment 3.1 [% wgt]
Clad / Plugs Material	Zircalloy-4
Guide Tubes (GT)	
GT Radii (inner / outer)	0.561 / 0.602 cm
Number of GT / material	24 /Zircalloy-4
Instrumentation Tube (IT)	
IT radii (inner / outer)	0.559 / 0.605 cm
Number of IT / material	1 / Zircalloy-4
Fuel Assembly (FA)	
Assembly Pitch	21.50 cm
Inter-FA half gap	0.04 cm
Top and bottom nozzles and support plates	Stainless Steel 304
Intermediate spacer grids	Zircalloy-4
Top and bottom spacer grids	Inconel 718
Soluble burnable poison	1300 ppm Boron
TH parameters	
Inlet coolant temperature	565 K
Reactor pressure	15.51 MPa
FA fission power	17.67 MW
Coolant mass flow	85.96 kg/s

Table 16: Main geometrical, material and operational parameters for VERA problem #6 data (radially-reflected FA) (Godfrey, 2014).

The object is then to obtain both global parameters (such as reactivity, average power profiles, integrated pin power distributions and outlet coolant temperatures) and local ones (such as axial power profiles and axial coolant temperatures for specific rods and channels respectively) using Serpent plus *SCF*. It should be regarded that no reference results are provided in benchmark specifications, but results from similar *highly detailed* calculation schemes are available in open

publications (Aviles et al., 2017; Kochunas et al., 2013; Wilderman et al., 2015), used here to verify the suitability of the approach. For this analysis, an external-coupling that relies in Serpent IFC files is considered, deemed to provide the main insights, criteria and strategies for the final implementation (i.e. master-slave). A Python3 (PSF, 2020) script was developed for such purpose, which includes the neutronic-TH mapping functions using the mathematical routines provided by the Numpy package (SPC, 2018). A one-to-one mapping of channels and pins with SCF was considered, where the Picard iteration scheme is applied (see Fig. 3.4). A detailed 3D model (radially reflected) is considered in Serpent, schematically presented Fig. A.1a.

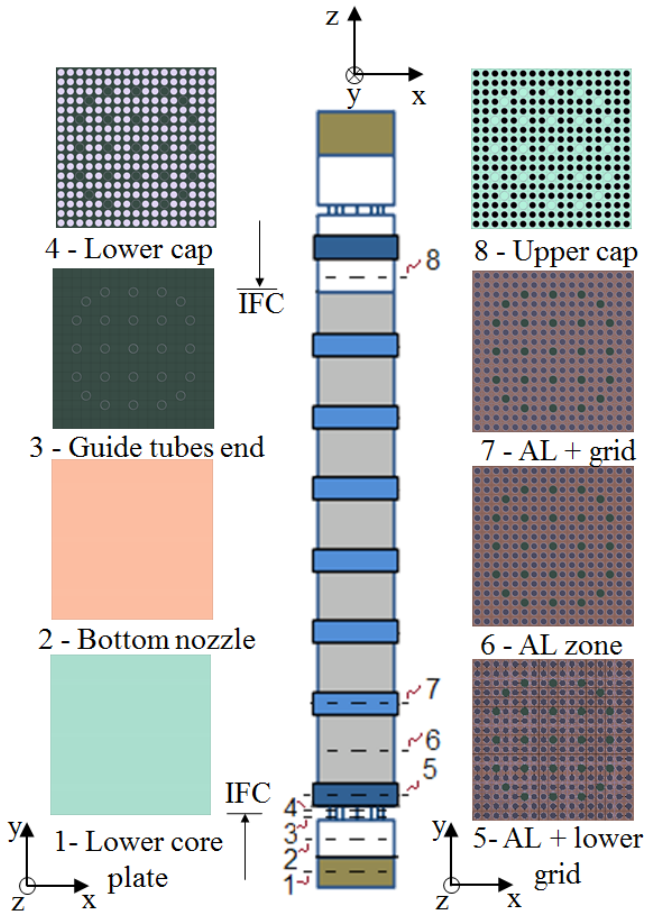

(a) Scheme of the Serpent model. Origin of the axial coordinate is the beginning of the AL (z = 0 cm). Model is reflected in the faces of the square. Top and bottom surfaces are black boundaries.

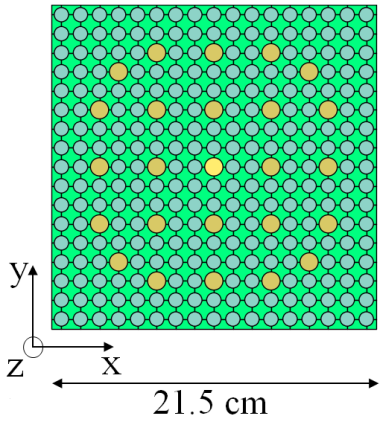

(b) Scheme of the SCF model. Origin of the axial coordinate is the beginning of the AL (z = 0 cm).

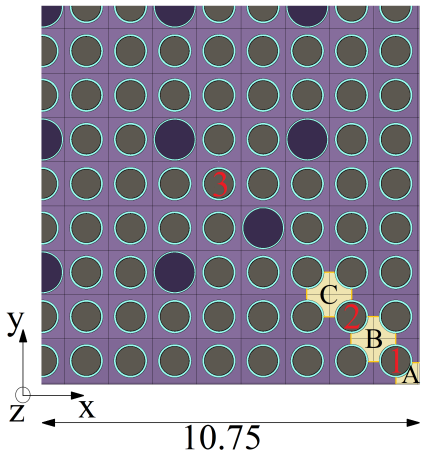

(c) Selected rods and channels for axial comparison (South East quarter of the FA).

Figure A.1: Plots of the Serpent and SCF models developed for VERA problem #6 (Ferraro et al., 2019b)

In the Fig. A.1a, axial cuts from the Serpent model are identified together with the FA scheme, identifying also the axial limits of IFC. Grid spacers and end caps are included, together with homogenized materials for top and bottom nozzles and support plates. Independent IFC (of total size equal to pin positions times axial SCF divisions) are set for fuel and coolant materials, using a regular cartesian mesh that covers the full active length (AL) of the FA. Regarding

the NDL, the JEFF3.1.1 was considered (Santamarina et al., 2009). This neutronic model was coupled with a *coolant-centered SCF* model, depicted in Fig. A.1b. This TH model is composed by 20 axial zones that correspond to the axial discretization of the IFC. Three kinds of pins were considered (i.e. fuel pin, guide tube and instrumentation tube) within the *SCF* model setting the corresponding material properties required by the code (such as material properties). The inlet temperature, exit pressure, coolant flow rate and gap heat transfer conductivity are set using the benchmark data, while the iteration criteria of the *SCF* solver was set to be to obtain a convergence at least two orders of magnitude below the convergence stated for the coupled fields.

The interchanged fields between these two models are the fuel temperatures, coolant temperatures and densities and the power, using a relaxation factor $\omega = 0.5$. All these values are considered by pin (or subchannel for the coolant) with the axial discretization described above. Besides a weighted average fuel temperatures with a $\alpha = 0.7$ is considered. Having this weighted average impact on results (Grandi et al., 2010), additional calculations are developed using alternate fuel temperature averages, such as volume average calculation (identified as Vol_{av}) and a calculation with $\alpha = 5/9$. Regarding the convergence criteria for the neutronic-TH iteration a maximum change in reactivity between iterations was set together with criteria for the coolant, temperatures and density fields and fuel temperature ones, applying the L_2 norm. An inherent complication arises from the goal values for these convergence criteria for the coupled fields within MC approaches, since the statistical variation of its results can be potentially amplified in the TH, resulting in an excess of iterations or even making this process unstable (Gill et al., 2017). A brief study to develop criteria in this sense can be found in (Ferraro et al., 2019b), which allows to define a set of convergence goals for the coupled calculations for a given statistical convergence of power results from Serpent. As a result, the neutronic-TH is developed until all criteria are satisfied, namely for the fuel temperature $\tilde{\epsilon}^t_{T_{fuel}} = 5$ $[^\circ C]$, for the coolant temperature $\tilde{\epsilon}^t_{T_{cool}} = 1$ $[^\circ C]$, for the coolant density $\tilde{\epsilon}^t_{\rho_{cool}} = 0.01$ $[g/cm^3]$ and for the system reactivity (maximum change of 10 [pcm]).

The Serpent neutronic calculation considered 3e8 active histories, achieving a pin-by-pin power statistical convergence of results of ~ 0.4 [%] at 1σ, which represents a statisticable reliable result. Regarding the coupled calculation, a stable neutronic-TH convergence was found, as depicted in figs. A.2a and A.2b for effective multiplication factor k_{eff} and the L_2 norms of TH fields respectively. For such convergence, each neutronic-TH iteration requires $\sim 6e3$ mins of CPU time (for Intel(R) Xeon(R) CPU E5-2697 v2 @ 2.70 GHz) for Serpent, while the SCF running times are below 0.1 mins.

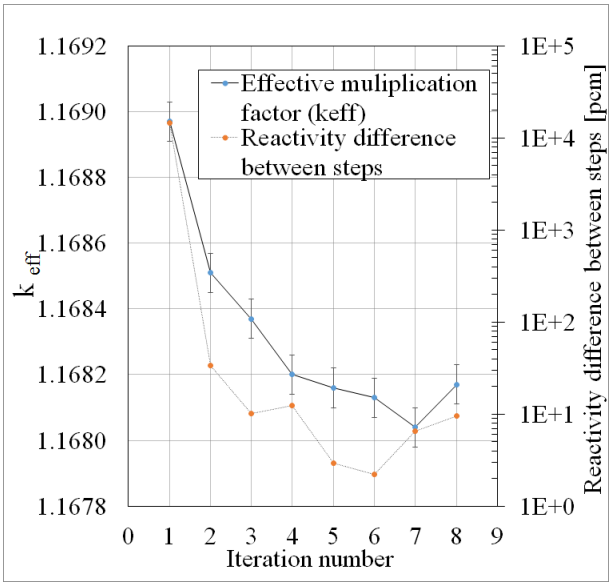

(a) Multiplication factor calculated by Serpent - Statistical error bars at 2 σ.

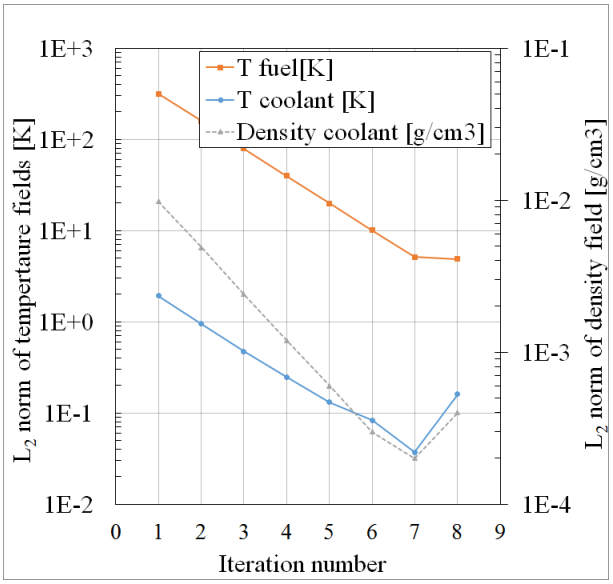

(b) Norms of the TH fields differences resulting from SCF calculations.

Figure A.2: Evolution of convergence of selected parameters for the coupled calculation of VERA problem #6 with Serpent plus SCF (using external coupling).

It can be observed that the global behavior is converging below the threshold set, where after 6 - 7 neutronic-TH iterations an oscillation is observed, resulting from to the inherent propagated statistical noise from MC calculations. It is key thus to avoid unnecessary iterations by setting a consistent convergence criteria and field relaxation, where this insight will be used in the following problems treated in further analysis.

The integral (i.e. global reactivity and integrated power by pin and outlet coolant temperatures) and the axially detailed (i.e. axial profiles by pin or subchannel) results are compared with reported values from similar calculation schemes (Aviles et al., 2017; Wilderman et al., 2015). The solutions from MPACT neutronic code (using the 2D/1D technique with transport-corrected 2D *Method Of Characteristics* in the radial planes and SP3 in the axial direction) plus COBRA-TF (subchannel code with two-fluid models) are considered as reference, identified as *VERA-CS*.

The comparison of the obtained multiplication factors (and associated reactivity) is presented in Table 17. The results for Serpent plus *SCF* obtained using the alternative fuel temperature averaging are included, together with those from other MC-based neutronics plus a subchannel code schemes, such as MCNP6 + CTF (Wilderman et al., 2015), MC21 + C1E (Aviles et al., 2017) and RMC + CTF (Luo et al., 2017), that reported to consider fuel volume averages to develop the TH feedback.

The first aspect to note from Table 17 results is the level of agreement for this global parameter, where it can be seen that a difference of ~ 335 [pcm] is obtained when comparing with results using the $T_{doppler}$ average, while this difference diminishes with other fuel temperature averages.

Case	$k_{eff} \pm \Delta k_{eff}$	Diff. [pcm]
VERA–CS (Aviles et al., 2017)	1.16361	Reference
RMC + CTF (Luo et al., 2017)	1.16239 ± 1E-4	−90
MC21 + C1E (Aviles et al., 2017)	1.16424 ± 3E-5	47
MCNP6 + CTF (Wilderman et al., 2015)	1.16500 ± 6E-5	103
Serpent + SCF	1.16817 ± 3E-5	335
Serpent + SCF Vol_{av}	1.16581 ± 3E-5	162
Serpent + SCF α=5/9	1.16613 ± 3E-5	186

Table 17: Results for the system reactivity after N-TH convergence for the VERA problem # 6. Comparison with reported values. Statistical error at 1σ for the final iteration step for Serpent+ SCF.

This is directly related to the temperature distribution inside the pin, where a volume average leads to higher fuel temperatures for the feedback than for the $T_{Doppler}$ average, thus a higher amount non-fission captures are sampled due to the increased broadening of the absorption resonances. This effect will be translated to a lower global reactivity, reflecting the negative dependence of reactivity with fuel temperature within PWR configuration. This effect is verified when the α=5/9 is considered, which also leads to higher average temperatures than the $T_{Doppler}$ average using α=0.7. It is important to remark that all these averages represent a valid approach to the problem. Moreover, the detailed results comparison is shown in the figs. A.3 to A.6.

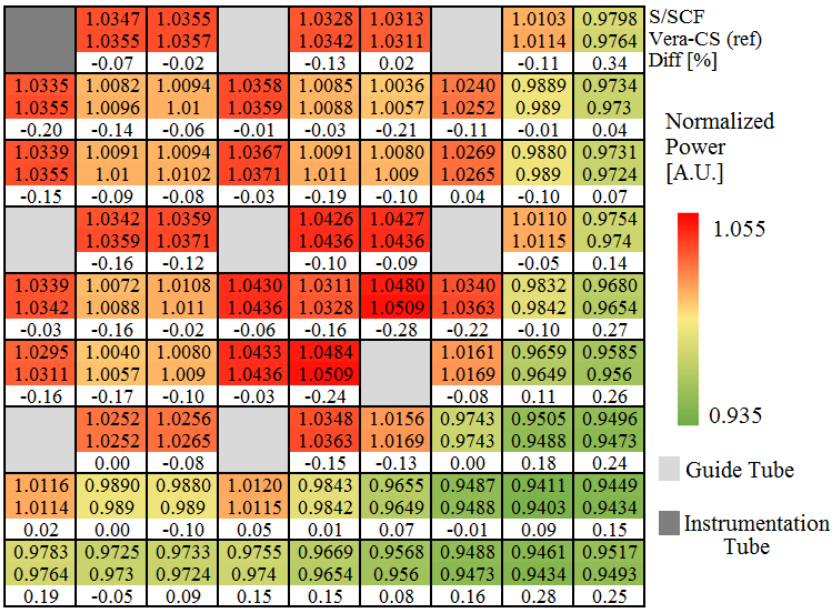

Figure A.3: Comparison of result for VERA Problem #6: Serpent + SCF (external coupling) vs. VERA–CS (Aviles et al., 2017) for the South East quarter of the FA. Axially integrated pin powers (normalized to average values).

The Fig. A.3 depicts the comparison of the axially integrated normalized pin power distribution for the South East quarter of the FA using $T_{Doppler}$ (see Fig. A.1b), indicating the positions of the Guide Tubes (GT) and the Instrumentation Tube (IT). These results show that the obtained pin-wise distributions are physically consistent, where the inner zones of the FA show an increased power due to the presence of GT and IT that leads to higher moderation and thus higher fission in the surrounding pins.

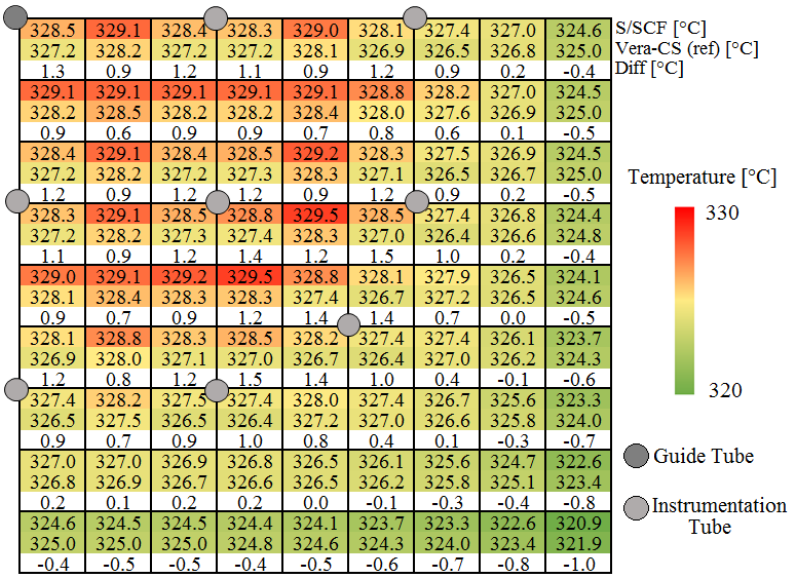

Figure A.4: Comparison of results for VERA Problem #6: Serpent + SCF (external coupling) vs. VERA–CS (Aviles et al., 2017) for the South East quarter of the FA. Outlet coolant temperature by subchannel.

The Fig. A.4 depicts the comparison of the corresponding outlet coolant temperatures by subchannel for the same quarter of FA. The higher power density zones result in higher outlet coolant temperatures, while the incresed inter FA gap is reflected into lower outlet temperatures for these subchannels. The differences with published values are as low as $\sim 0.4\%$ for normalized pin power distributions, likewise as low as $\sim 1.5[^{\circ}C]$ for outlet temperatures by subchannel, which represents the same level of agreement reported when the comparison is made with similar MC-based tools (Aviles et al., 2017).

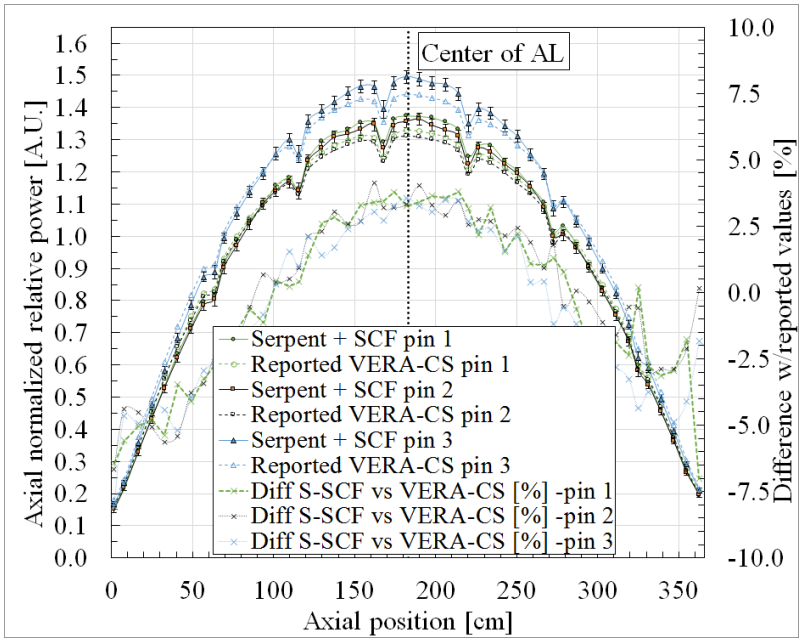

Figure A.5: Serpent - SCF (external coupling) normalized axial profiles comparison for selected pins 1 to 3 from Fig. A.1c. Compared with VERA-CS (Aviles et al., 2017), z = 0 [cm] represents the beginning of the AL. Serpent statistical uncertainty at 3σ.

The Fig. A.5 presents the comparison of the axial normalized power profiles with reported values for the selected pins 1 to 3 in Fig. A.1c. Here the $T_{Doppler}$ average is also used, and z = 0 [cm] is the beginning of the AL. It can be observed that the axial physical behavior of the coupled calculation is accurately modeled, where the cosine-shaped axial distribution obtained for the normalized pin-power profiles is tilted to the bottom zone of the AL due to the increased temperatures in the upper zone (Duderstadt and Hamilton, 1976). Besides the power depresion produced by the presence of FA spacers (due to lower moderation and higher non-fission absorptions generated by these components) is correctly represented.

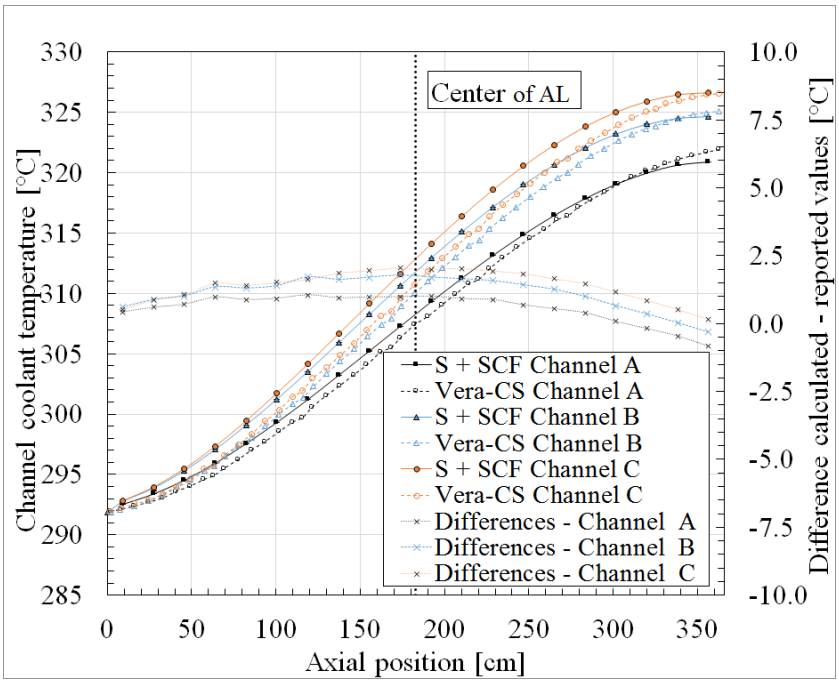

Figure A.6: Serpent - SCF (external coupling) axial coolant temperature profiles comparison for selected subchannels A to C from Fig. A.1c. Compared with VERA-CS (Aviles et al., 2017), z = 0 [cm] represents the beginning of the AL.

Finally, the Fig. A.6 presents the corresponding coolant temperatures comparison with reported values for the selected channels A-C in Fig. A.1c. Again, the power profile is reflected in the coolant temperatures, resulting into an increasing temperature with axial dimension. The comparisons with the reference values shows differences below $\sim 2.5[°C]$ for the subchannels A to C and $\sim \pm 5$ [%] for pin powers in the central zone (average ~ 1 [%]), which is in the same range as the reported in (Aviles et al., 2017; Luo et al., 2017).

To summarize, this analysis developed for the VERA problem # 6 allows to identify several key-aspects relevant for the proposed work path, namely:

1. A convergent coupled behavior is observed for the this MC-base approach, resulting into a consistent representation of the physical phenomena. Besides, it is crucial to avoid unnecessary neutronic-TH iterations (i.e. set convergence criteria below the propagated statistical noise from MC calculations) and develop massive parallel implementations if full-core models are to be tackled.

2. The level of agreement with similar approaches is found to be around $\sim 3-5\%$ for axial pin profiles, and $\sim 2-3$ $[^{\circ}C]$ for axial coolant temperatures. Better agreement is achieved for non-axial dependent values (i.e. $\sim 1[\%]$ for axially integrated pin powers and ~ 1 $[^{\circ}C]$ for coolant outlet temperatures). Besides the agreement in reactivity is in the order of hundreds of pcms. This is in line with available investigations (Aviles et al., 2017), defining an inherent limit on the proposed approach.

B New master-slave coupling approach details and consistency verification

The *Serpent-SCF* coupling represents a standard Picard iteration scheme, where the neutronic and TH problems are divided and solved iteratively, as depicted in the Algorithm 1.

Algorithm 1: Main Picard iteration scheme in *Serpent-SCF*

```
Data: Initial guess for P(r̄) → SCF
SCF Calculate T(r̄), ρ_coolant(r̄) → Serpent
for t_bin = 1 or BU_bin = 1 to n do
    while ε > ε_target or iterations > iterations_max do
        Serpent Calculate P(r̄) → SCF
        if Burnup or steady-state case then
            SCF Calculate as steady state T(r̄), ρ_coolant(r̄) → Serpent
        else
            Serpent time → SCF
            SCF Transient calculation T(r̄), ρ_coolant(r̄) → Serpent
        end
        Calculate ε
        iterations = iterations + 1
        Relax fields P(r̄), T(r̄), ρ_coolant(r̄)
    end
    Result: Tallies from Serpent for time bin / BU step i
    Result: TH fields from SCF for time bin / BU step i
end
```

Managing the convergence criteria ϵ and the maximum number of iterations in Algorithm 1 the scheme can be used as semi-implicit or fully-explicit. whereas the *burnup* scheme from Serpent is maintained. In particular, when dealing with coupled *transient* calculations, the scheme must handle the *live* ($S_{live}(\bar{r},t)$) and *precursors* sources ($S_{prec}(\bar{r},t)$), as depicted in the Algorithm 2.

The specific characteristics of the *Serpent-SCF* coupling are set by the user within Serpent input using a generic card available within Serpent input processing, where a summary of the main options is presented in Table 18.

Combining these options with Serpent ones allows to develop semi-implicit couplings for *steady-state* and *burnup* calculations and fully-explicit couplings for *transient* ones. To indicate to Serpent that the IFCs are to be managed by this internal scheme, an additional option is included (where the remapping files are also identified). Hence, a *steady-state* coupled calculation card within Serpent input is as depicted in the following box:

Algorithm 2: Main *transient* calculation approach in Serpent (Leppänen et al., 2020)

Data: Initial distribution for $S_{live}(\bar{r}, t)$ and $S_{prec}(\bar{r}, t)$
Data: Initial $P(\bar{r})$
Initial SCF calculation: $T(\bar{r}), \rho_{\text{coolant}}(\bar{r}) \rightarrow$ Serpent
for $t_{bin} = 1$ *to* n **do**
1 Create the $S_{live}(\bar{r}, t)$ and $S_{prec}(\bar{r}, t)$ for t_{bin}
Calculate $S_{live}(\bar{r}, t_{bin})$ at the BOI.
Calculate the decay of $S_{prec}(\bar{r}, t_{bin})$ based on the decay law:
Determine the delayed neutron population emitted during t_{bin}.
Determine and store the initial value at EOI.
Divide the initial source points between $S_{live}(\bar{r}, t_{bin})$ and neutrons emitted from $S_{prec}(\bar{r}, t_{bin})$.
Apply population control to $S_{live}(\bar{r}, t_{bin})$.
Sample the emission of the required number of delayed neutrons from existing precursors.
2 Simulate the particles within t_{bin}.
Tally the precursor production during the neutron tracking.
Tally the $P(\bar{r})$
3 Store the neutrons reaching EOI in $S_{live}(\bar{r}, t_{bin+1})$ and surviving precursors to $S_{prec}(\bar{r}, t_{bin+1})$.
4 Develop the TH feedback (e.g. SCF)
Serpent $P(\bar{r}) \rightarrow$ TH module
Serpent $t \rightarrow$ TH module
TH module transient calculation: $T(\bar{r}), \rho_{\text{coolant}}(\bar{r}) \rightarrow$ Serpent
end

Parameter	Description	Expected value
SCF path	Path to *SCF* folder	string
SCF input	*SCF* input name	string
IFC fuel	IFC input for fuel	string
IFC cool	IFC input for coolant	string
Convergence norm flag	Option of Norm2 or Infinite	1 or 2 [1=inf 2=norm2]
Rho convergence [pcm]	Convergence goal for Rho	double
T_{fuel} convergence [C]	Convergence goal for T_{fuel}	double
T_{cool} convergence [C]	Convergence goal for T_{cool}	double
D_{cool} convergence [g/cm3]	Convergence goal for D_{cool}	double
Coolant coupling type	Flag to get values from *SCF*	1=at rods 2=at channel
Remapping file flag	flag to remap (Disables size check)	1=YES 0=NO
Relaxation of TH fields.	$F = F_{i-1}\omega + F_i(1-\omega)$	double (Relax factor ω)
Power vector option	get power from coolant or fuel ifc	1=coolant, 2=fuel, 3=both
T_{fuel} feedback option	get *SCF* temp as volume or *Doppler*	1=Vol, 2=Doppler from SCF
Additional option	Transfer only coolant temperature and density to Serpent	1 = YES, 0 = NO
Additional file	Path to file containing power distribution that is added to the one tallied with Serpent	string ("no" if absent)
Remap added power	Option to remap the power in external file	1 = YES, 0 = NO

Table 18: Main available options in the new master-slave Serpent-SCF coupling scheme

```
ifc "coolant.ifc" internal remap map-scf-coolant-centered.ifc
ifc "fuel.ifc" internal setinmat 1 UO2 remap map-scf-fuel-centered.ifc
set pop 300000 3000 50
set relfactor 0
set ccmaxiter 4
intcoupling SCF 17 "SCF/" "input.txt" "fuel.ifc" "coolant.ifc" 2 50 20
1.0 0.01 2 1 0.5 2 1 0 "no" 0
```

In this example the convergence criteria is stated in for TH fields and the system reactivity,

indicating a maximum number of Neutronic-TH iterations (in a traditional *Picard* scheme), where the TH fields are relaxed, while the power is not. As a result, a semi-implicit scheme is applied. Finally, for *transient* calculations, a coupled scheme coupled calculation is as follows:

```
ifc "coolant.ifc" internal remap map-scf-coolant-centered.ifc
ifc "fuel.ifc" internal setinmat 1 UO2 remap map-scf-fuel-centered.ifc
intcoupling SCF 17 "SCF/" "input.txt" "fuel.ifc" "coolant.ifc" 2 100
20.0 20.0 1.0 2 1 0.0 2 1 0 "no" 0
set relfactor 0
set ccmaxiter 1
set nps 2000000 100 simutime
tme simutime 2 100 0 1.0
set dynsrc "../source-crit/dynsource.bin" 1
```

For this second example, a transient calculation is executed, where no neutronic-TH iterations are performed within the time bins, but the TH fields are updated. As a result, a fully-explicit scheme is applied.

B.1 Consistency verification between approaches

To verify the coupling behavior, the same VERA benchmark problem #6 presented in Fig. A.1 is here calculated using the master-slave approach. The same Serpent and *SCF* inputs are used, where the only modification to the former one is the adding of the cards indicating the coupling. The results are also obtained using a Object-Oriented (García et al., 2019a) approach. The comparison of final reactivity results for this problem are presented in Table 19. All these cases are obtained using a using a *Doppler* temperature average with $\alpha = 0.7$ for the fuel.

Case	k_eff	$\Delta[pcm]$
Serpent-SCF Master-slave	$1.16806 \pm 2.8E-5$	$(reference)$
Serpent-SCF External	$1.16817 \pm 3.E-5$	8
Serpent-SCF Object-oriented	$1.16809 \pm 2.3E-5$	3

Table 19: Comparison for the system reactivity after N-TH convergence for the VERA problem # 6 for different Serpent plus SCF coupling implementations. Statistical error at 1σ for the final iteration step for Serpent+ SCF.

It can be seen from Table 19 that the obtained results are statistically the same, since the differences are included within the statistical convergence. Furthermore, the consistency in the representation of the involved physical phenomena must be also addressed. In this regard a comparison of the integrated pin powers and channel outlet temperatures between the *Serpent-SCF* master-slave and the external coupling approaches are shown in figs. B.1b and B.1a. Here the layout from the figs. A.3 and A.4 from Fig. A.1 in Appendix A is maintained.

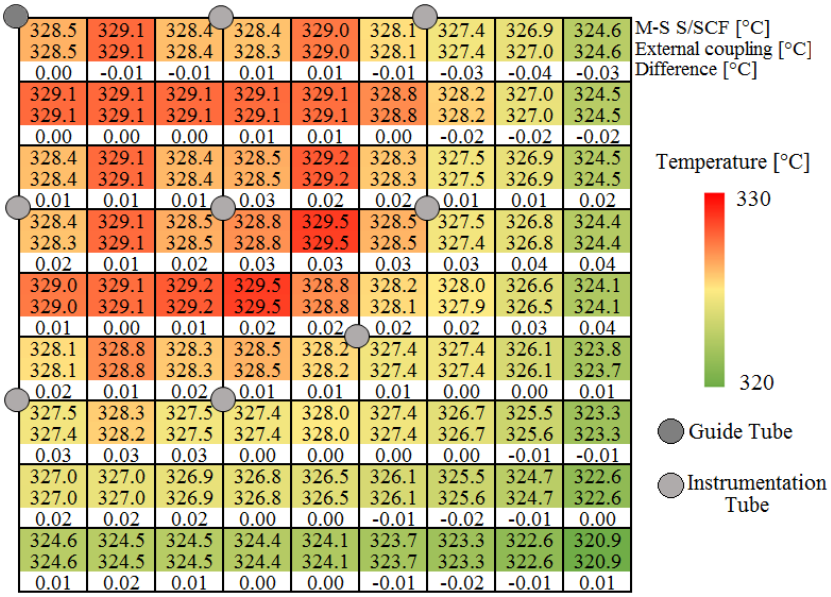

(a) Outlet coolant temperature.

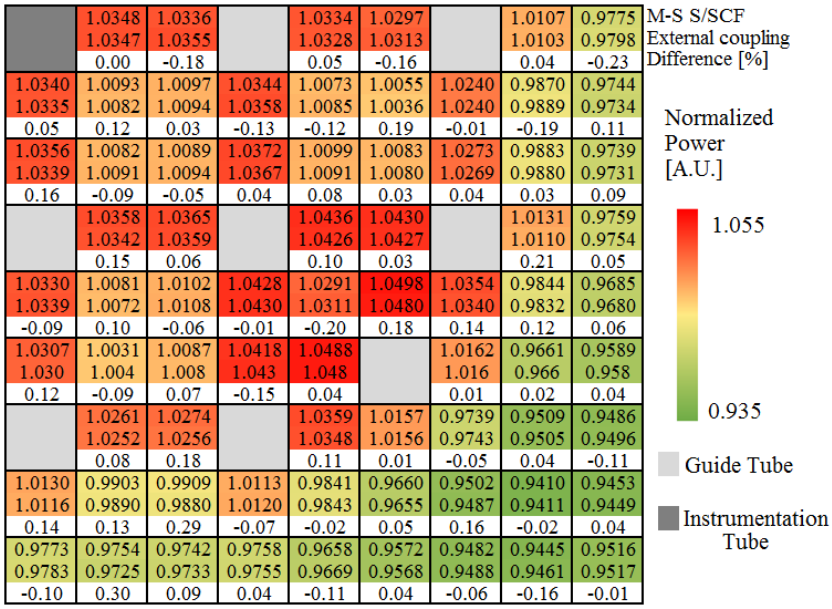

(b) Pin power distribution.

Figure B.1: Comparison of Serpent plus SCF results between master-slave and external couplings results for VERA problem #6.

The level of agreement shows differences below 0.5 [%] in power, which represents results statistically equivalent. This effect is reflected in outlet temperatures differences below 0.1 [$°C$], thus it can be assumed that the results obtained with both implementations are equivalent. Further in-depth analyses that assess this equivalence also with with the Object-Oriented approach can be directly found in (García et al., 2019a).

B.2 Verification of geometrical versatility within hexagonal-type geometries

A consistency test of the geometrical versatility is developed using realistic data from a VVER-1000 benchmark (Loetsch et al., 2010). Therefore, a radially-reflected representative FA (so-called *39AWU* TVSA design, see Table 25) is considered at HFP using a pin-by-pin coupling. This FA is highly-heterogeneous, including three different fuel enrichments and pins with burnable poisons, deemed to depress the neutron flux (and thus power) in specific zones of the geometry. A radially-reflected 3D model is considered Serpent, while a *fuel-centered* model is proposed in *SCF*, where main aspects are depicted in Fig. B.2. The origin of the axial coordinate is set in the center of the AL and the three types of FR are identified (i.e. UO_2 with enrichments of ^{235}U of 4.0 [%wgt], 3.6 [%wgt] and 3.3 [%wgt], this latter one plus 5 [%wgt] of Gd_2O_3 as burnable poison).

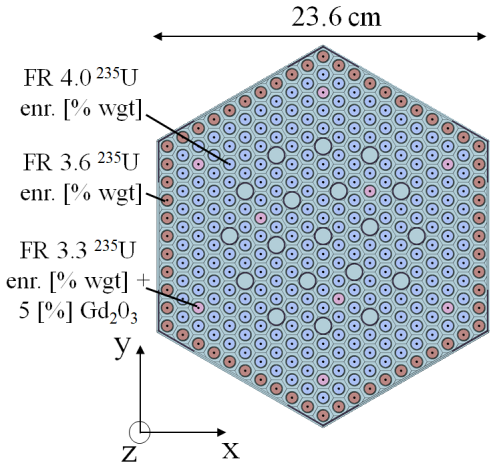

(a) Serpent Model xy cut. The center of the FA AL corresponds to (x,y,z)=(0,0,0). Model is reflected in the faces of the hexagon.

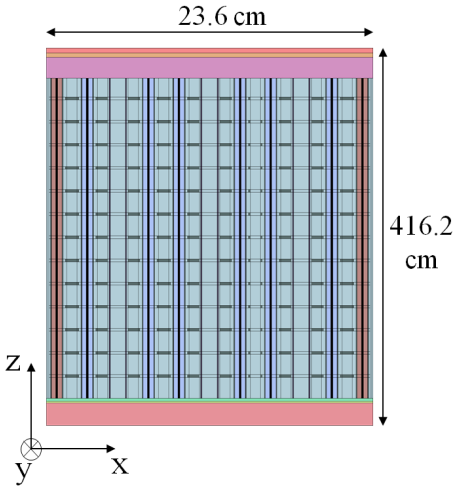

(b) Serpent Model zx cut (not at scale). The center of the FA AL corresponds to (x,y,z)=(0,0,0). Top and bottom surfaces are black boundaries.

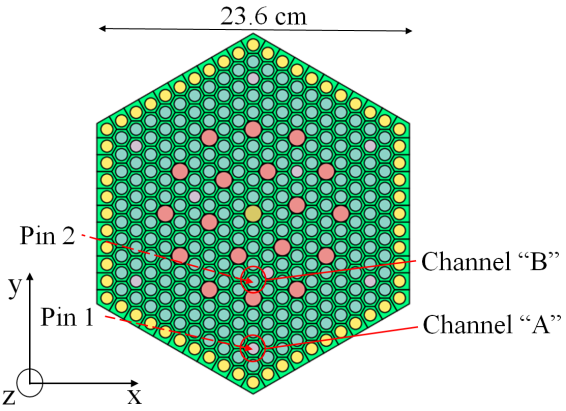

(c) SCF model (scheme). Channels and pins are identified for further analysis.

Figure B.2: Serpent and SCF geometry models developed for radially reflected 39AWU FA.

Regarding the neutronic model, a homogenization of top and bottom zones is done, while the explicit modeling of spacer grids and stiffeners is considered by mass and volume conservation (see figs. B.2a and B.2b). Besides, the JEFF3.1.1 NDL is considered (Santamarina et al., 2009)

and 2e6 active particles distributed in 2e3 cycles are set, which leads to a statistical convergence in the power profiles below 2% at 1σ. A series of pins and channels are selected for further analysis, identified Fig. B.2c. These correspond to distances of 8 and 4 fuel rod pitches in the negative y direction from the center of the FA (i.e. pins 1, 2) and its associated channels A and B. A coupled calculation is developed, using a neutronic-TH convergence criteria of 10 [pcm] for reactivity, 5 [$^{\circ}C$] for T_{fuel}, 2.5 [$^{\circ}C$] for T_{cool} and 0.01 [g/cm^3] for ρ_{cool} and a relaxation of the TH fields (with $\omega = 0.5$). This results into a stable convergence after $\sim 4-5$ neutronic-TH iterations, as it is shown in Fig. B.3.

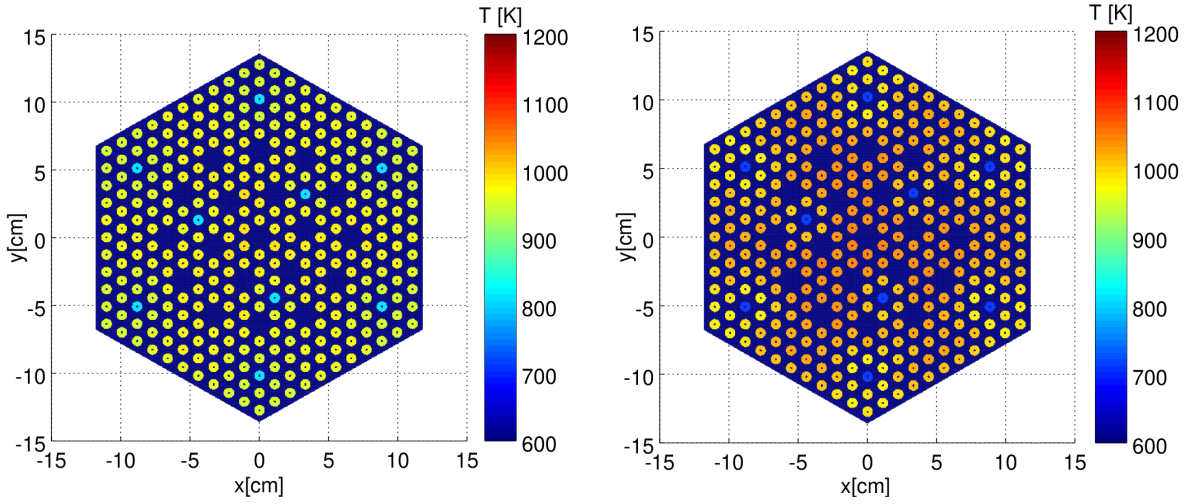

(a) Initial iteration. *(b) Final iteration.*

Figure B.3: Serpent-SCF results for the temperature within N-TH iterations for the radially reflected 39AWU FA - plots for a xy slice from 0 to 20 [cm] (z = 0 [cm] is the center of the AL).

The Fig. B.3 depicts the evolution of temperatures for a 20 [cm] xy slice starting at core center (i.e. z = 0 [cm]), where the radial dependence is reached in the final neutronic-TH iteration. The effect of the feedback of the power distribution to the TH solution is noticeable (i.e. pins with BP can be identified), as shown in the Fig.B.4.

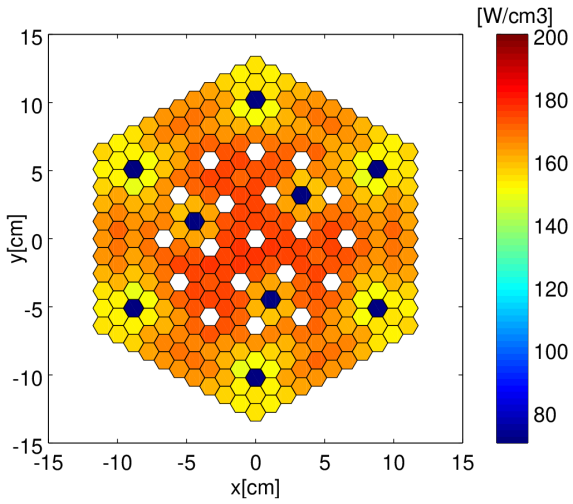

Figure B.4: Serpent-SCF results for the final iteration of power by pin for the radially reflected 39AWU FA - xy slice from 0 to 11.8 cm (z = 0 cm is the center of the AL).

The Fig. B.4 shows the converged power for an xy slice in the center of AL. It can be seen that the temperatures profiles depicted in Fig. B.3b reflect the resulting power distribution. Pins with BP generate lower power, resulting into lower temperatures. The pins that surround these BP ones also show a power depression, which also leads to lower temperatures there. Besides the central zone of the FA shows an increment on the temperature, related to the excess of moderation in the water from the guide and instrumentation tubes. This is also appreciated in the axial distribution the results, depicted in Fig. B.5.

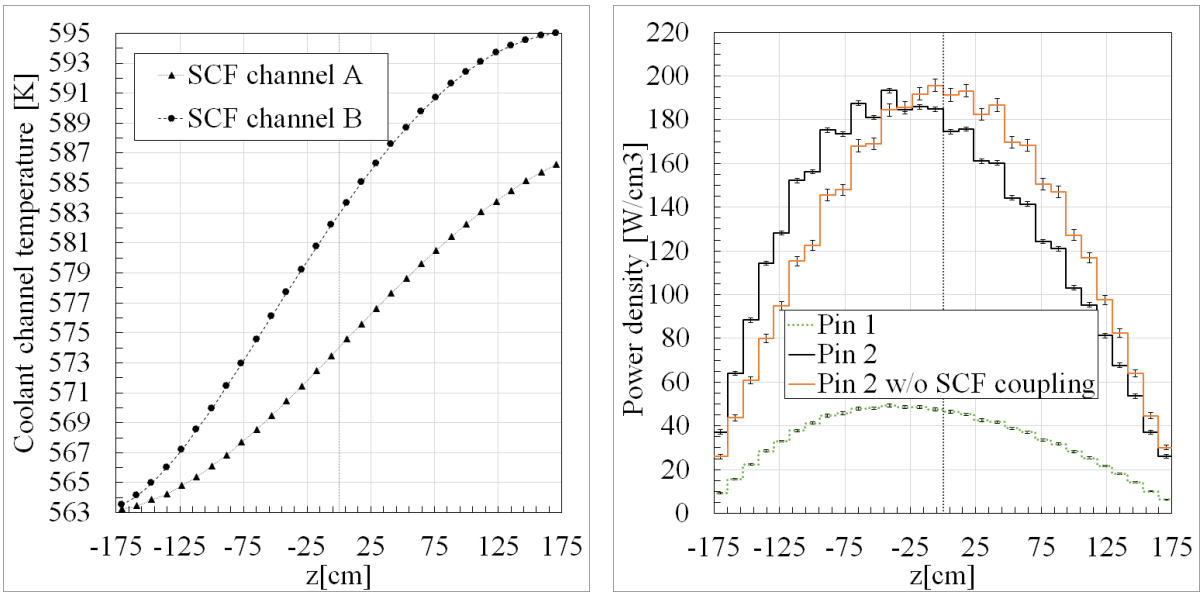

(a) Axial coolant temperatures for fuel 39AWU - channels identified in B.2c

(b) Pin power for selected pins in fuel 39AWU - pins identified in B.2c

Figure B.5: Serpent-SCF results for the pins and channels identified in Fig. B.2 for the radially reflected 39AWU FA.

The Fig. B.5 shows the axial power for the identified in the Fig. B.2c, while the coolant temperatures are presented in Fig. B.5a. It can be seen a coherence with the results from figs. B.3b and B.4. The channels *A* and *B* reflect the differences in power seen in pins 1 and 2, where the first one shows a lower power since it has burnable poison that depress the neutron flux levels. Besides, the increase of temperatures with the axial distance pushes the power axial profiles to the lower half of the FA due to the negative temperature feedbacks. To show this, an additional calculation result is included in Fig. B.5b, which corresponds to the axial result for pin 2 obtained with the same Serpent input without the *SCF* coupling. To summarize, a consistent behavior of the main phenomena is observed for this VVER case, likewise the correct mapping of the neutronic and TH variables between the codes is assessed.

B.3 Associated limitations of Serpent in large-scale *burnup* problems

In view of *transient* scenarios departing from burned configurations, potential constrains must be also analyzed in advance regarding computational issues related strictly to the Serpent code. In particular, in view of the use of HPC architectures, aspects such as RAM memory require-

ments have to be analyzed. To improve efficiency, Serpent develops a pre-loading of several required calculation data (such as material cross sections and other miscellaneous data (Leppänen and Isotalo, 2012)), with the drawback of increasing the demand of RAM memory with the number of materials defined to be burnable. Having most of HPC a limited availability of RAM per node (e.g. 60-100GB), the impact on a full-scope calculation is considerable (Ferraro et al., 2018; Leppänen et al., 2015). As an example, the scalability of this requirement are here analyzed with a simplified Serpent FA model based on the 20BP with 3.1% wt enriched UO_2 fuel from PWR BEAVRS benchmark (Horelik et al., 2013). Regardless of the model details, the key aspect here is that all fuel and burnable poisons are modeled independently, constituting $\sim$1e4 independent *burnable zones*. If we consider a series of minicores composed by an increasing number of these FA maintaining the same *burnable zone* division, an assessment of RAM requirements is obtained, as presented in Fig. B.6.

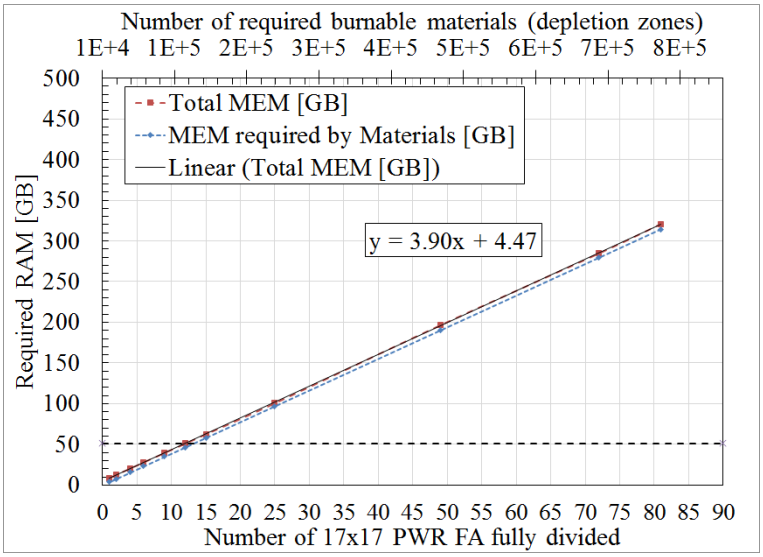

Figure B.6: Analysis of RAM requirements by Serpent as a function of FA fully divided for burnup calculations and total number of burnable zones.

The impact in RAM requirement is noticeable, where it can be observed that for a typical HPC with a limit of $\sim$ 50GB only $\sim$ 10 to 12 FA fully divided can be modeled, which represents a bottleneck to be solved in full-scale simulations with burnup. Several investigations were developed that leaded to the implementation of techniques for the distribution of geometry across nodes (namely Domain decomposition methods) (García et al., 2018; Leppänen et al., 2020).

B.4 Massive parallelization for *transient* calculations

Regarding massive parallelization for the coupled *transient* calculations within HPC infrastructures, scalability checks are necessary. For such purpose, a parametric study was developed in the Irene HPC supercomputer (*Skylake* partition (TGCC, 2020)), using as basis the T-85 coupled Serpent-SCF transient case for SPERT-IIIE reactor from Chapter 6, shown in the Fig. B.7.

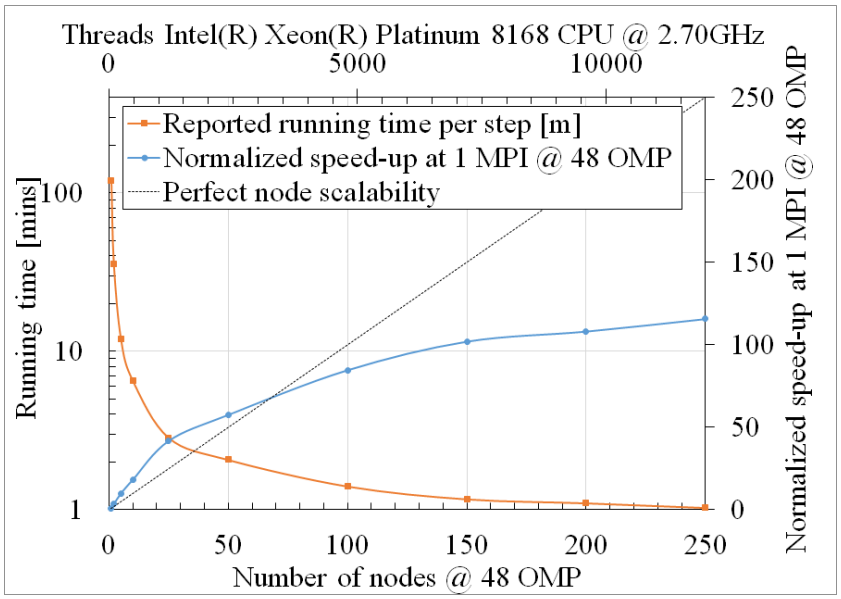

Figure B.7: Serpent 2-SCF results scalability for the SPERT IIIE T-85 (first 3 time bins) within Irene skylab HPC, constituted by 1656 running nodes of 48 Intel(R) Xeon(R) Platinum 8168 CPU @ 2.70GHz each, with up to 180GB.

The Fig. B.7 depicts the scalability (using the normalized speed-up as a ratio to a single node) and the running times for a series of runs done in this HPC for different number of nodes. It can be seen that a very good scalability is observed up to 2000 threads, together with a plateau for a number of MPI above ∼100. For lower number of MPI nodes, some increased performance is observed, attributed to internal MPI barriers programming within Serpent.

C Variance reduction techniques for RIA-kind *transients*

The study of ad-hoc techniques that improve the convergence can contribute to the industry-like applications of the proposed scheme. These VR techniques in MC calculations are devoted to reduce the computer time required to obtain results of sufficient precision. Unfortunately, the successful implementation and use of VR techniques is often difficult, tending to be more art than science (X-5 Team, 2008), since not only the accurate technique has to be selected according to the specific problem, but also the user has to supply appropriate parameters. In particular for *transient* coupled calculations, the problem becomes even harder. In order to provide potential future work paths to deal specifically with RIA-type scenarios, a simple VR technique is here proposed and roughly implemented in the developed tool, mostly oriented to be used for HFP RIA-kind cases. Main aspects of this technique, named as *source scaling* are here described.

For *transient* calculations, Serpent sets an equal number of particles for each time bin (Leppänen et al., 2020). This approach is conservative, stable and commonly applied in MC codes. Unfortunately, for the RIA-kind scenarios a drawback appears. If the power evolution are carefully analyzed (e.g. in figs. 5.6 and 6.12) it can be seen that, being the number of particles simulated on each time bin kept constant, those bins with a sudden increase of power result in lower

statistical convergence. Fortunately, when dealing with a RIA scenario, the rough evolution of the global power can be easily estimated using PK models (see Eq. 2.11). Thus, the idea of the proposed VR is to take profit of a fast preliminary calculation to adjust the size of the source to be modeled. As a consequence, if the total source size is adjusted (by input) using this information, the foreseen effect is to simulate less particles in more converged time bins and put those in less converged ones. This effect becomes more effective if the power peak ends with a power in the same order of magnitude as the initial one (such as RIA starting from HFP). This proposed scheme, schematically depicted in Fig.C.1, is roughly implemented in the master-slave coupling as a proof of concept (introducing an ad-hoc Serpent card - *set sourcescale*).

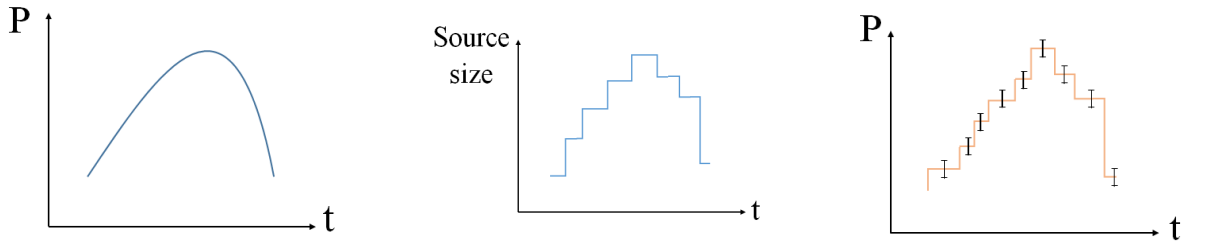

(a) Step 1: Guess for the time behavior from PK (or preliminary runs).

(b) Step 2: Use guess in 1 to shape the amount of particles to be modeled per time bin.

(c) Step 3: Run the case with the scaled source to obtain a "statistically balanced" result.

Figure C.1: Scheme of the proposed VR methodology.

To develop a rough test of the proposed VR technique, the same TMI minicore case from Fig. 5.2 is here considered. The second scenario from Table 7 (with 35 $[cm/s]$ of extraction rate) is considered, where a higher σ is observed for those time bins around the power peak. Consequently, in order to analyze the efficacy of the proposal, a FOM is defined, using the time bin with the maximum relative statistical uncertainty as reference. To provide a fair comparison, two runs are developed, with and without the VR applied, whose main aspects are presented in Table 20.

Case	**Source size**	**Source scale**
Without VR	set nps 2000000	-
With VR	set nps 1450000	*set sourcescale 49 1 1 1 1 1 1 1 1 1 2 4 10 4 3 2 1 1 1 1 1 1 ...*

Table 20: Test details for the VR scheme in the TMI-minicore transient scenario # 2. The nps represent particle per time bins (Leppänen et al., 2020). The number of particles per bin is scaled by the values listed in the second case (first value identifies the total amount of bins).

The key aspect of this VR relies on the a priori knowledge of the problem. In this sense, the scale source per bin is obtained from previous runs, but can be obtained from PK calculations or less converged initial tests. Besides, the total number of particles to be modeled is adjusted to preserve the number after scaling (i.e. if the scale represents a factor of X, the nps is altered by $1/X$). The effect on the *Serpent-SCF* obtained results for both cases in Table 20 is presented in figs. C.2 and C.3.

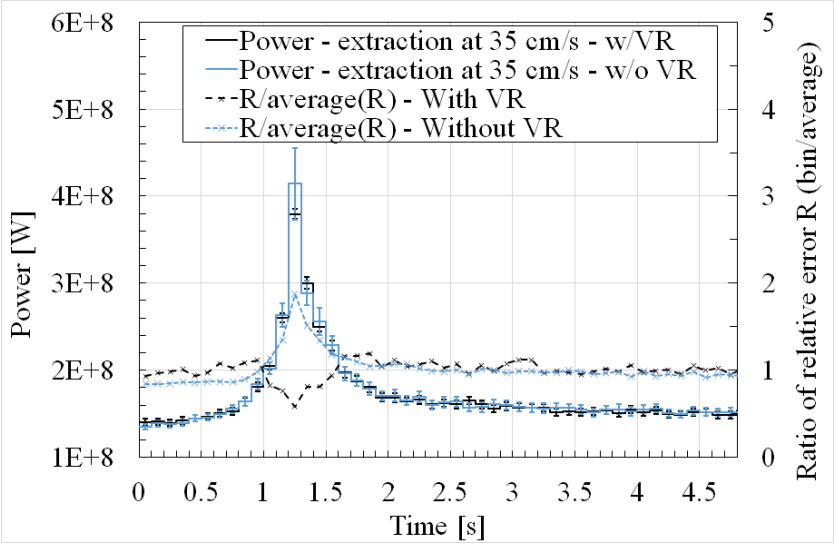

Figure C.2: Serpent-SCF calculations for the TMI-minicore RIA-type scenario # 2. Comparison of results for power evolution with and without VR.

The Fig. C.2 shows the comparison for the total power evolution, including the normalized statistical convergence. It can be seen that the convergence for the time bin representing the power peak is improved, likewise the convergence between time bins is smoothed for the whole time scope. Besides, a slight overshoot in the convergence is seen, meaning that the scaling of the source is here too aggressive. It is clear then that a wise choice of this scaling is mandatory, which represents an iterative process.

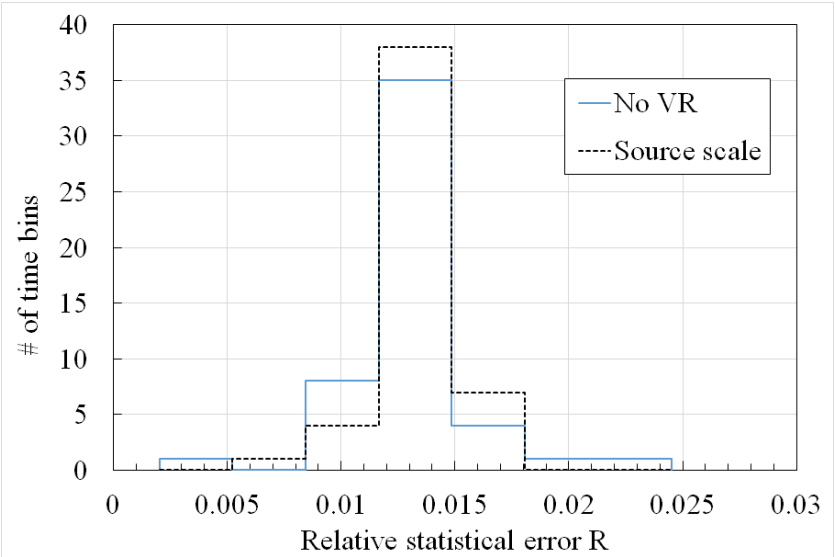

Figure C.3: Serpent-SCF calculations for the TMI-minicore RIA-type scenario # 2. Comparison of time bin convergence distributions with and without VR.

The effect of this technique is more clear in the Fig. C.3, which presents the distribution of the statistical convergence of the time bins for both cases. The result is a redistribution of the statistical uncertainty, where the proposed VR basically pushes the relative error distribution to the left-side of the plot, avoiding low converged time bins. This is summarized in the Table 21,

which presents the FOM for these two cases, together with the maximum and average relative statistical error (R) and the total running time. Despite a slight increment in calculation time, the statistical convergence is balanced and thus the FOM is improved by a factor of ∼6. Thus the aptness of this rough VR scheme to reduce the required calculation time to improve the convergence in a power peak resulting from a RIA-kind scenario is roughly verified.

Case	**FOM**	**Total CPU time [mins]**	**R (max / average) [%]**
Without VR	0.1	∼2*e*5	2.5/1.3
With VR	0.6	∼3.5*e*5	1.6/1.5

Table 21: FOM analysis for Serpent-SCF runs with and without VR for the TMI-minicore RIA-type scenario # 2.

D Summary of problem parameters and modeling details

D.1 PWR-type Minicore based in TMI benchmark for *transient* calculations

The main geometrical and material data for the TMI-minicore benchmark is presented the Table 22 (further details can be gathered from (How et al., 2018)). Besides, the TH parameters for this minicore problem at HFP are listed in the Table 23.

Parameter	**Value**
Unit cell pitch [cm]	1.4427
Fuel pellet diameter [cm]	0.9390
Fuel density [g/cm3]	10.283
Fuel enrichment [Cladding diameter (inner / outer) [cm]	1.0249 / 1.0922
Number of fuel rods per FA	208
Number of guide tubes for CR (GT) per FA	16
Number of instrumentation tubes (IT) per FA	1
Number of Gd pins per FA	4
Active height [cm]	353.06
GT diameter (inner / outer) [cm]	1.2649 / 1.3462
IT diameter (inner / outer) [cm]	1.1201 / 1.2522
IT inner material	void
Fuel assembly pitch [mm]	218.110
Control Rod outside diameter [cm]	1.12014
Absorber material [%]	AgInCd - 80/15/5
Gap conductivity $[W/m^2K]$	1e5

Table 22: Main geometrical and material data for TMI minicore, from (How et al., 2018).

Parameter	**Value**
Inlet coolant temperature	565 K
Reactor pressure	15.51 MPa
Minicore total power	141 MW
Coolant mass flow	773.6 kg/s

Table 23: Main TH parameters considered for the TMI minicore at HFP.

The Table 24 presents the main computational requirements for a given time step of a *Serpent-*

SCF transient calculation for this minicore (see Chapter 5), where it is worth to note here that the initial *steady-state* calculation to build the initial source is not considered in the overall summation. These results show that the CPU resources required are mostly associated to Serpent, where the total amount of CPU time can represent a limiting factor, requiring availability of vast computational resources.

Code	**CPU time per time step [CPU mins]**
SCF	$\sim 6.0E-01$
Serpent	$\sim 5.0E+03$

Table 24: Associated running times per time step for the TMI-minicore, run in hybrid MPI/OMP mode in 50 nodes of 20 threads Intel(R) Xeon(R) CPU E5-2660 v3 @ 2.60GHz in ForHLR II (SCC, 2020).

D.2 Geometrical and TH data for the VVER-TVSA fuels

The main geometrical characteristics and material data for the VVER-1000 TVSA FA is presented the Table 25.

Parameter	**Value**
FR	
Cladding radii (inner / outer)	0.3865 / 0.455cm
Fuel rod pitch	1.275 cm
Pellet radii (inner / outer)	0.075 / 0.3785 cm
Pellet Material	UO_2 / $UO_2 + Gd_20_3$
Clad Material	E110
Guide tube	
Guide Tube radii (inner / outer)	0.545 / 0.63cm
Tube Material	E635
Central tube	
Central Tube radii (inner / outer)	0.55 / 0.65 cm
Tube Materials	E635
Burnable poison pins	
Type	Burnable absorber 5% Gd_2O_3 in UO_2
Configuration	Variable
FA	
Assembly Pitch	23.60 cm
Array	hexagonal
Active length	353 cm
Gap between assemblies stiffener	0.015 cm
Stiffeners thickness	0.1 cm
Number of Grid Spacers	13
Mass of Spacer grid	0.55kg
Material of spacer grid	E110
Soluble burnable poison	Boron

Table 25: Geometrical and material data for the VVER-1000 TVSA FA from (Loetsch et al., 2010).

Moreover, the combinations of different enrichments and burnable poisons within FR in the fuel assemblies is provided in the Table 26 (further details can be gathered from (Loetsch et al.,

2010)).

FA / number of pins	**Fuel pin type [enrichment in % wgt]**								
	1.3	2.2	2.99	3.6	4	2.4+Gd	3.3+Gd	GT	IT
30AV5	-	-	303	-	-	9	-	18	1
39AWU	-	-	-	60	243	-	9	18	1
390GO	-	-	-	66	240	-	6	18	1
22AU	-	312	-	60	243	-	9	18	1
13AU	312	-	-	66	240	-	6	18	1

Table 26: Main characteristics of the VVER-1000 FA TVSA type used within the first core loading, from (Loetsch et al., 2010).

The distribution of these FA within the reactor core is schematically depicted in Fig. D.1 for the first cycle, identifying the different FA types to be considered.

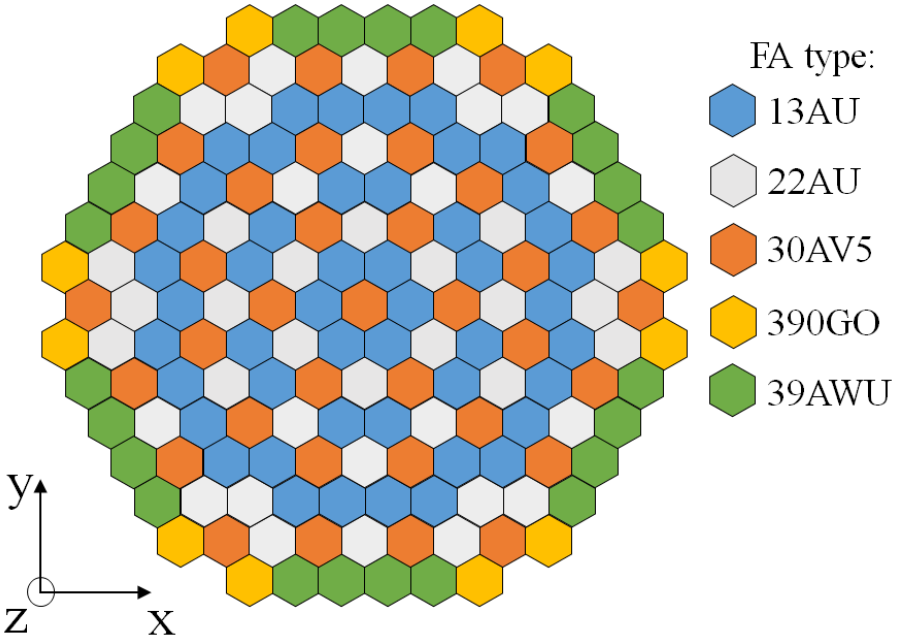

Figure D.1: Scheme of the loading of the first core for the VVER-1000 benchmark.

Finally, a summary of the running aspects for this full-core case is presented in the Table 27. The amount of computational resources is directly related to the MC approach of the neutronics, but for this case the *SCF* running time is not negligible. Moreover, the number of neutronic-TH iterations within the *Predictor-Corrector* steps indicates that the TH fields are not suffering strong changes between the two *burnup steps* considered (i.e. 0 and 4.51 [FPD])

Running time per iteration [CPUmins]		**Serpent average *stdev* at 1σ**		**Average N-TH iterations per bu step**		**RAM [GB]**
Serpent	*SCF*	Reactivity [pcm]	Power by pin (av/max) [%]	Predictor	Corrector	~11
7e4	5	6	6/20	2	1	

Table 27: Main computational requirements for the case 2 in Table 5 of the full-core VVER benchmark. Normalized to a 2.60GHz Intel(R) Xeon(R) CPU E5-2660 v3 CPU

D.3 Geometrical and TH data for the VVER fuels *U* and *U-Er*

The main geometrical and material data for the VVER-1000 TVSA *U* and *U-Er* FA is presented the Table 28.

Parameter	***U***	***U-Er***
Fuel height $[cm]$	368	
Fuel rods number	313	
U Enrichment $[\%wgt]$	4.4	
Fuel assembly pitch $[cm]$	23.6	
Fuel rod pitch $[cm]$	1.275	
Fuel pellet diameter $[cm]$	0.76	
Fuel rod diameter $[cm]$	0.91	
Guide tube diameter $[cm]$	1.26	
BP in pins (Er_2O_3) $[\%wt]$	0.0	1.0
Spacers grids height [cm] / mass [g]	3/ 550	
Number of spacers grids	13	
Separation of spacers grids [cm]	22.5, starting 23.2 above AL	

Table 28: Geometrical and materials data for U and U-Er VVER-1000 TVSA-type fuels, from (Aleshin et al., 2015)

.

The associated TH parameters for this radially-reflected FA cases are provided in the Table 29 (further details can be gathered from (Aleshin et al., 2015)).

Parameter	**Value**
FA power $[kW]$	18405
Coolant flow $[m^3/h]$	534
Pressure $[MPa]$	15.6
T_{inlet} $[K]$	560

Table 29: Main TH data for the VVER-1000 TVSA data for the radially-reflected U and U-Er problem, from (Aleshin et al., 2015).

Moreover, the axial reflector for this model analyzed in Section 4.2 corresponds to the standard mixed compositions defined in (Loetsch et al., 2010) for a full-core VVER.

D.4 Geometrical and TH data for the SPERT-IIIE reactor

The geometrical and material data for the SPERT-IIIE fuel is presented the Table 30, obtained from (McCardell et al., 1967; Olson, A. P., 2015). A summary of the main dimensions of the components in the core is also provided in the Table 31, including relevant TH parameters and the material compositions of key components.

Morever, schemes of the filler pieces placed in the zone between the core and the core skirt are depicted in Fig. D.2. These pieces are composed by stainless steel plates, where the inner zone is filled by water. For completness, an scheme for the components outside the core (i.e. the thermal shields and RPV) is depicted in Fig. D.3.

Parameter	**Value**
Clad material	SS347
UO_2 density	10.5 g/cm3
^{235}U enrichment	4.8 g/cm3
Array	Canned in SS348, 4x4 and 5x5 arrays
Fuel Rod pitch	1.4859 cm (0.585 in)
Fuel outer radius	0.5334 cm (0.21 in)
Clad radii (inner / outer)	0.54102 cm (0.213 in) / 0.59182 cm (0.233 in)
Active length	97.282 cm (38.3 in)
FA pitch	7.62 cm (3 in)
Gap between FA	0.0635 cm (0.025 in)
Nominal moderator density	998.03 kg/m3 at (294K, 101.35 kPa) 947.4 kg/m3 at (394K, 10.34MPa) 790.9 kg/m3 at (533K, 10.34MPa)
Nominal inlet temperature	294 K (Cold) 394 K (Hot Standby-1) 533 K (Hot Standby-2)

Table 30: Main geometrical and material characteristics of the SPERT-IIIE fuel, from (McCardell et al., 1967).

Parameter	**Value**		
Fuel assembly			
Type	Number	External can size	Flow area
SFA	48	7.56 x 7.56 x 133.99 [cm]	27.68 cm^2
16FA	4	6.29 x 6.29 x 133.99 [cm]	20.39 cm^2
CFA	8	6.34 x 6.34 x 115.93 [cm]	18.06 cm^2
Core details			
Nominal power	40 MWth max		
Inlet pressure	14.7 to 1500 psia		
Control system	1 transient rod (cruciform)		
	4 control assemblies in pairs (square tubes)		
Absorber	1.35 [%] ^{10}B in SS304L - thickness 0.476 [cm] (TR) , 0.472 [cm] (CR)		
Shield materials	SS304L		
Support grids			
Position	Material		Thickness
Upper	304L SS		17.78 cm (7 in)
Lower	304L SS		7.62 cm (3 in)

Table 31: Main SPERT-IIIE core geometrical and material parameters, from (McCardell et al., 1967) and (Olson, A. P., 2015).

The computational resources required by *Serpent-SCF* for the SPERT-IIIE *transient* problem (see Chapter 6) are presented in Table 32 for a given time bin of the calculation. It is worth to note here that the initial *steady-state* calculation to build the initial source is not considered. Again these CPU resources are significant and can potentially represent a limiting factor. With the aim of the ForHLR II HPC used in this work, each complete transient scenario requires $\sim 5 - 10$ h using 1000 processors in total to model the complete the 1 s scope.

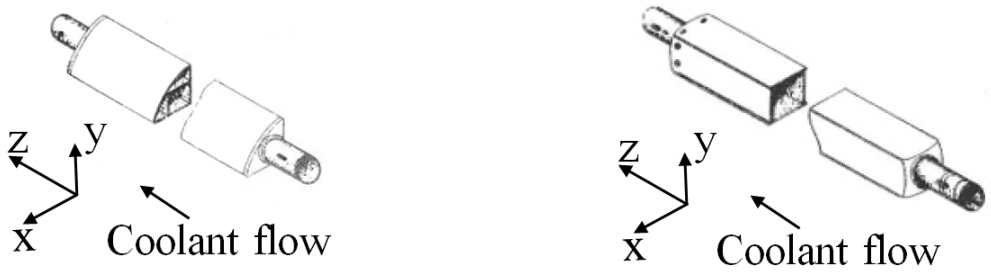

(a) Filler piece type 2F (for core corners). *(b) Filler piece type 4F (for empty FA positions).*

Figure D.2: Scheme of the filler pieces in SPERT-IIIE (obtained from (Olson, A. P., 2015)).

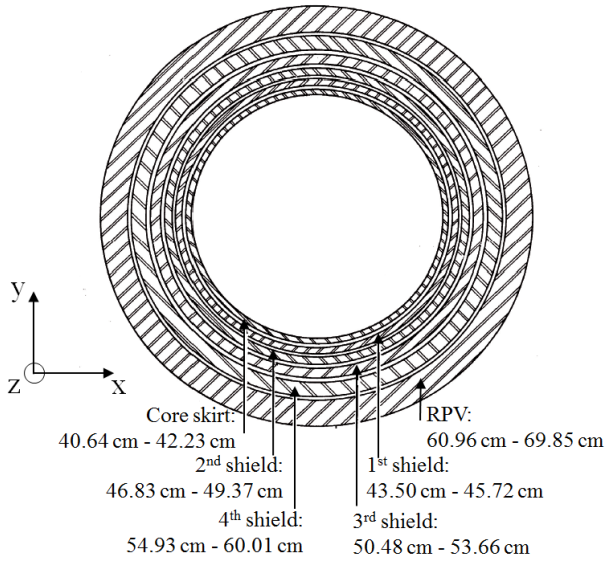

Figure D.3: Scheme of the core skirt, thermal shields and RPV for the SPERT-IIIE reactor (Olson, A. P., 2015).

Code	CPU time per time bin [mins]
SCF	$\sim 4.0E-01$
Serpent	$\sim 4.0E+03$

Table 32: Serpent-SCF running times for SPERT-IIIE transient case. Run in hybrid MPI/OMP mode in 50 nodes of 20 Intel(R) Xeon(R) CPU E5-2660 v3 @ 2.60GHz each (SCC, 2020).

D.5 Geometrical and TH data for the MOX/UO_2 PWR transient benchmark

The geometrical and material data for the MOX/UO_2 PWR transient benchmark is provided in the Table 33, including most relevant TH parameters (further details can be gathered from (Kozlowski and Downar, 2007)).

A brief summary of resources required by *Serpent-SCF* for the MOX/UO_2 PWR transient benchmark analyzed in Chapter 6 is presented in the Table 34 for a given time step of the calculation, where it is worth to note here that the initial steady-state calculation to build the initial source is not considered.

It can be seen from Table 34 that the CPU resources required for these calculation represent

Parameter	Value
Number of fuel assemblies	193
Nominal power (MWth)	3565
Core inlet pressure (MPa)	15.5
Hot full power (HFP) core average moderator temperature (K)	580.0
Hot zero power (HZP) core average moderator temperature (K)	560.0
Hot full power (HFP) core average fuel temperature (K)	900.0
Fuel lattice, fuel rods per assembly	17 x 17, 264
Number of control rod guide tubes	24
Number of instrumentation guide tubes	1
Total active core flow (kg/sec)	15 849.4
Active fuel length (cm)	365.76
Assembly pitch (cm)	21.42
Pin pitch (cm)	1.26
Baffle thickness (cm)	2.52

Table 33: Main geometrical and TH data for the MOX/UO_2 PWR transient benchmark, from (Kozlowski and Downar, 2007).

Code	CPU time per time step [CPU mins]
SCF	$\sim 5.0E+00$
Serpent	$\sim 1.0E+05$

Table 34: Serpent-SCF MOX/UO_2 PWR transient benchmark running times. Run in ForHLR II in hybrid MPI/OMP mode in 64 nodes of 20 Intel(R) Xeon(R) CPU E5-2660 v3 @ 2.60GHz each (SCC, 2020).

a limiting factor. The 1 s transient is run in ∼122 h using 1280 processors, resulting in ∼1.6e5 CPUh (for the given processor characteristics). In spite of this vast amount of resources, the statistical convergence reached for the transient case is ∼10-15 %, where about ∼5 to 10 times more particles must be run to reach convergences ∼5 [%], which was not feasible due to resources availability limitations. Nevertheless, regarding the good scalability in massive parallelization architectures, obtaining highly converged results is feasible if the resources are available.